Dissertation Nr. 28447

Modern computational methods applied to classical long-period seismology

A thesis submitted to attain the degree of
Doctor of Sciences
(Dr. sc. ETH Zürich)

presented by

Johannes Maximilian Kemper

Master of Science, Westfälische Wilhelms-Universität Münster
born on March 20, 1989

accepted on the recommendation of

Prof. Dr. Domenico Giardini
PD. Dr. Amir Khan
Dr. Yann Capdeville

2023

Abstract

Determining the structure of planets is paramount to the understanding of the origin and evolution of planetary systems. As seismic waves propagate freely through planets and interact with discontinuities and material structure, their study, seismology is the predominant discipline to resolve planetary interiors. Density, defined as mass per unit volume, is important in that it is the primary seismic parameter that informs us about the material composition of a planet. In addition, gaining insight into a planet's density structure has many implications for geodynamic, geomagnetic and seismic studies. Earth's mantle flow models are governed by these density differences and thus provide a connection between traditional seismic tomographic models and geodynamics. Moreover, the inner core boundary density contrast drives the convection in the outer core, generating the magnetic field through the geodynamo process. Combining density information with tomographic velocities allows the inference of material properties, such as shear and bulk modulus, that consequently give constrains on the geochemistry. For these reasons, the overarching goal of this thesis is to increase our understanding of density variations.

To achieve this, we use long period seismic signals as they are affected by self-gravitation. This form of gravitation affects waves that, while propagating, change the density structure of their carrier material. This process gives these signals a direct feedback to the gravity potential, which originates from the density distribution. Their detection thus makes it possible to map the long wavelength and therefore large scale density structure. Generally, there are two types of long period signals: tides with a periods of multiple hours, and normal modes or free oscillations with periods from seconds up to one hour for the Earth. To excite free oscillations in planets a powerful seismic energy source is needed. Although the amount of high-quality long-period data has increased significantly in recent decades due to the occurrence of several very large quakes and high precision satellite measurements, there is still little agreement between different density models.

The numerical description of normal modes started together with the emergence of the computer. Several methods based on different forms of numerical integration have been proposed to solve the physically motivated system of differential equations. To resolve density, accuracy of the solutions is of foremost importance as the magnitude of variations is assumed to be in the same order of the error of commonly employed numerical approximations.

The present work describes our advances in long-period seismology with a strong emphasis on our numerical developments which culminated in the open-source publication of a new spectral element based normal mode code called `specnm`. This highly accurate numerical forward code enables us to invert the most recent normal mode measurements to obtain new one-dimensional Earth structure models with higher resolution in density than ever before. To improve on former modelling approaches, we create self-consistently built models of the radial anelastic seismic structure of the Earth. For this, we construct a petrologically and thermodynamically consistent mantle structure which we unite together with a laboratory-based visco-elastic attenuation model that connects dissipation from seismic to tidal periods, whereas core properties are computed using equations-of-state. Lastly, we improve the efficiency of the calculation for three-dimensional simulations in time of gravity affected waves by, among other things, using the crucial fact that the gravity potential outside of the planet has a simple 1/r dependence.

Together, these advances may lead to a better understanding of the density variations in planets.

Zusammenfassung

Die Bestimmung der Struktur von Planeten ist von grösster Bedeutung für das Verständnis des Ursprungs und der Entwicklung von Planetensystemen. Da sich seismische Wellen frei durch Planeten ausbreiten und mit Diskontinuitäten und Materialstrukturen interagieren, ist ihre Wissenschaft, genannt Seismologie, die vorherrschende Disziplin, um das Innere von Planeten aufzulösen. Die Dichte, definiert als Masse pro Volumeneinheit, ist insofern wichtig, als sie der primäre seismische Parameter ist, der uns einen direkten Zugriff auf die materielle Zusammensetzung eines Planeten gibt. Darüber hinaus hat das verbessern der Dichtestruktur eines Planeten starke Auswirkungen auf geodynamische, geomagnetische und seismische Studien. Erdmantelströmungsmodelle werden von diesen Dichteunterschieden bestimmt und stellen somit eine Verbindung zwischen traditionellen seismischen Tomographiemodellen und der Geodynamik her. Darüber hinaus treibt der Dichtekontrast am Grenzübergang zum inneren Kern die Konvektion im äusseren Kern an und erzeugt somit das Erdmagnetfeld durch den Geodynamo-Prozess. Die Kombination aus Dichteinformationen mit tomographischen Geschwindigkeiten ermöglicht die Bestimmung von Materialeigenschaften wie Scher- und Kompressionsmodul, sodass diese dann die Geochemie kontrollieren. Aus diesen Gründen ist das übergeordnete Ziel dieser Arbeit, unser Verständnis von Dichtevariationen zu verbessern.

Um dieses Ziel zu erreichen, verwenden wir langperiodische seismische Signale, da sie von der Eigengravitation beeinflusst werden. Diese spezielle Form der Gravitation wirkt auf Wellen, die bei ihrer Ausbreitung die Dichtestruktur ihres Trägermaterials verändern. Dieser Prozess gibt diesen Signalen eine direkte Rückkopplung mit dem Gravitationspotential, das wiederum die Dichteverteilung als Quelle hat. Der Nachweis dieser Wellen ermöglicht somit die Abbildung der langwelligen und damit grossräumigen Dichtestruktur. Im Allgemeinen gibt es zwei Arten von seismischen Signalen mit langer Periode: Gezeiten mit Perioden von mehreren Stunden und Normalmoden mit Perioden von Sekunden bis zu einer Stunde für die Erde. Um Planeten zu freien Schwingungen anzuregen, wird eine starke seismische Energiequelle benötigt. Obwohl die Anzahl hochwertiger Langzeitdaten in den letzten Jahrzehnten aufgrund des Auftretens mehrerer sehr grosser Beben und hochpräziser Satellitenmessungen erheblich zugenommen hat, gibt es wenig Übereinstimmung zwischen verschiedenen Dichtemodellen.

Die numerische Beschreibung von Normalmoden begann zusammen mit dem

Aufkommen des Computers. Zur Lösung des physikalisch motivierten Systems von Differentialgleichungen sind bisher unterschiedliche Ansätze erprobt worden, die auf verschiedenen Formen der numerischen Integration basieren. Um die Dichte aufzulösen, ist die Genauigkeit der Lösungen von grösster Bedeutung, da davon ausgegangen wird, dass die Grösse der Variationen in der gleichen Grössenordnung liegt wie der Fehler aus üblicherweise verwendeten numerische Näherungen.

Die vorliegende Arbeit beschreibt unsere Fortschritte in der langperiodischen Seismologie mit einem starken Schwerpunkt auf unseren numerischen Entwicklungen, die in der Open-Source-Veröffentlichung eines neuen, auf Spektralelementen basierenden Normalmode-Codes namens `specnm` gipfelten. Dieser hochgenaue numerische Vorwärtscode ermöglicht es uns, die neuesten Normalmoden Messungen zu invertieren, um neue eindimensionale Erdstrukturmodelle mit einer höheren Dichteauflösung als je zuvor zu erhalten. Um bisherige Modellierungsansätze zu verbessern, modellieren wir die radiale, anelastische, seismische Struktur der Erde selbstkonsistent. Dazu konstruieren wir eine petrologisch und thermodynamisch konsistente Mantelstruktur, die wir mit einem laborbasierten viskoelastischen Dämpfungsmodell vereinen, das die Dissipation von seismischen- bis Gezeitenperioden beschreibt, während die Kerneigenschaften mit Hilfe von Zustandsgleichungen berechnet werden. Schliesslich verbessern wir die Effizienz der Berechnung für dreidimensionale Simulationen in der Zeit von Wellen die von Gravitation beeinflusst sind, indem wir unter anderem den wichtigen Fakt nutzen, dass das Gravitationspotential ausserhalb des Planeten eine einfache 1/r-Abhängigkeit hat.

Zusammengenommen tragen diese Fortschritte zu einem besseren Verständnis der Dichtevariationen in Planeten bei.

The stage has now been reached where numerous published papers bearing the Earth's density seem to do little more than fidget around the resolving power of long accumulated observational data.

– The Earth's Density by K.E. Bullen on 29th June 1974

Contents

Chapter 1

Introduction

The term seismology is a composite of the two Greek words *seismos* and *logos* meaning shaking and science respectively. Seismology means, then, the study of waves and their interactions to reveal the structure of their carrier medium or resolving the sources of their seismic energy (*Shearer*, 2009). The analysis of seismic waves is the primary means by which scientists acquire knowledge about planets interior (*Aki and Richards*, 2002). Most seismologists today are interested in exploring higher frequencies to be sensitive to smaller structures or variations in material properties (e.g., *French and Romanowicz*, 2014; *Lei et al.*, 2020; *Simmons et al.*, 2021). The sources used in these explorations are either natural quakes on the Earth, Moon (*Latham et al.*, 1970; *Nakamura*, 2003), Venus (Venera 9, *Ksanfomaliti et al.*, 1982), and Mars (Viking & Insight, *Anderson et al.*, 1977; *Banerdt et al.*, 2020; *Giardini et al.*, 2020)) or man made vibrations due to explosions and various hammering techniques (e.g., Vibroseis, *Crawford et al.*, 1960). In contrast to that, in this work we are interested in very low frequency or long period seismic energy, such as tidal deformations or free oscillation of planets. Free oscillations of planets can be interpreted as standing waves that are produced physically by interference of incoming and outgoing travelling waves such that only certain frequencies will resonate over long time intervals. These resonant frequencies together with their associated displacement in depths are termed normal modes. Normal modes allow for the sensing of lateral heterogeneities at the scale of their wavelength (*Giardini et al.*, 1987), and therefore, are contributing to the field of global seismology. The aim of this project is to improve the computational approach to normal modes to achieve higher accuracy and utilize this to invert novel data sets to attain a higher resolution in radial density than in former reference models. Another aspect is the challenge of incorporating a full gravity description into three-dimensional time simulations, which is a feat that up to this day has not been achieved with sufficient efficiency to make it practicable.

Conceptually, normal modes originate from the solving of the associated eigenvalue problem introduced by transforming the wave equation into frequency do-

main, where the resulting eigenpair consists of the aforementioned eigenfrequency and eigenfunction. Any travelling wave can be expressed as a complete, weighted sum of these modes and they are unique, as a result of orthogonal, in their representation making the normal mode description a fundamentally alternative view on wave propagation. The first major publication on normal modes of a spherical mass was presented by *Poisson* (1829), followed by *Kelvin* (1863); and shortly after, *Lamb* (1881) published his theoretical treatise on the vibrations of an elastic sphere in which he derived closed expressions for normal modes (consisting of eigenfrequencies and eigenfunctions) for three-dimensional Cartesian coordinates. He also identified the spheroidal and toroidal types of modes (see Figure 1.1), which in the toroidal case were known from the work of *Jaerisch* (1880), and calculated the period of 1h 18min for the gravest spheroidal mode of a steel ball the size of Earth. Spheroidal modes alter the external shape of their carrier body by including a radial component. Hence, they are also affected by gravity and for the gravest modes even self-gravitation. Self-gravitation affects long period waves that while propagating change the density structure and therefore the gravity potential forming a feedback loop. Spheroidal modes correspond to P-SV waves in the seismic wave representation and fuse to form Rayleigh waves when they meet the surface. Toroidal modes are much simpler as their propagation and particle motion is constrained to the horizontal plane. They correspond to SH waves when propagating in the bulk material and form Love waves at the free surface. Shortly after the identification of both mode types, *Chree* (1889) transformed the equations from the Cartesian to the spherical coordinate system and gave them the basic structure they are presented in today. Together with this, they introduced spherical harmonics which are functions on the surface of a sphere and form a complete set of orthogonal functions meaning that any function on the sphere can be interpreted as a weighted sum of them. Another major step forward came from the work of *Love* (1927), who extended and clarified earlier results by compiling them in his collection titled "A Treatise on the Mathematical Theory of Elasticity". One important notion that he introduced was the interpretation of the balance between the internal hydrostatic pressure opposing the self-gravitation as the initial state. This allows for the interpretation of a normal mode as additional (small) perturbative stress on top of that equilibrium state (*Love*, 1927). Further improvements in the theoretical description came mainly from the introduction of the variational approach (*Jobert*, 1956, 1957; *Pekeris and Jarosch*, 1958; *Takeuchi*, 1959; *Jobert*, 1961), which produces the frequency solutions bounded below the real eigenfrequencies. The great advantage of this approach is that a first-order error in a trial eigenfunction leads to a second-order error in the derived eigenfrequency making it a robust method (*Lapwood and Usami*, 1981). The variational method as a form of Rayleigh's principle is still used in modern analytical and numerical studies (see chapter 2). A rather complete treatment of the modern

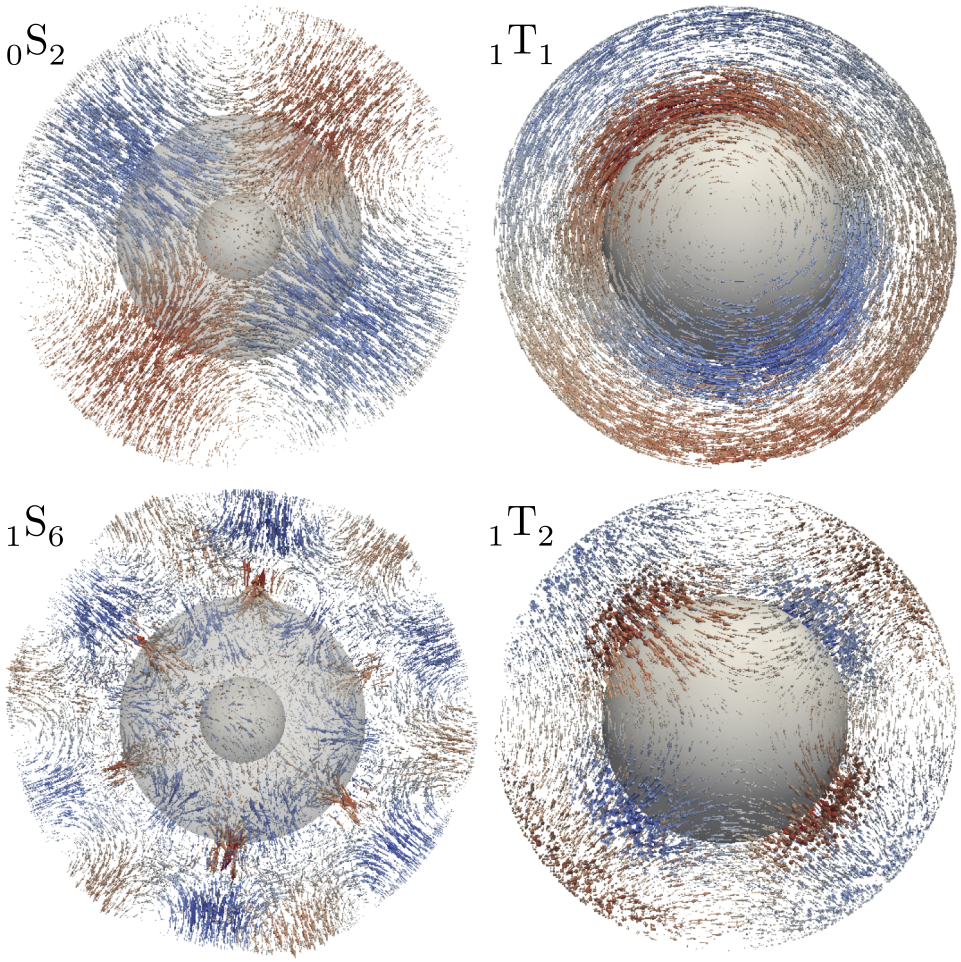

Figure 1.1: Examples of spheroidal S and toroidal T normal modes for a three dimensional, but symmetric Earth (PREM, *Dziewonski et al.*, 1981) model without anisotropy, gravity and rotation. The modes are classified by their positive integer overtone number n and angular degree l as ${}_n\mathrm{M}_l$ with M being the mode type. The overtone number n gives the number of zero crossings in radius, while the angular degree l is the number of zero crossings if we walk from pole to pole on the great circle. The colors from red to blue shown radial magnitude for the spheroidal modes (red=inwards, blue=outwards) and y-magnitude for the toroidal modes (red=negative, blue=positive). The visualizations are vector field snapshots modified from *Shi et al.* (2018).

normal mode theory can be found in the over a thousand page treatise by *Dahlen and Tromp* (1998).

To describe normal modes in a three dimensional setting it is paramount to understand their mathematical structure. The vector spherical harmonics used in the common description of normal modes together with their radial dependence are accompanied by a tuple of three integer indices: overtone number n, angular degree l and azimuthal degree m. An exemplary normal mode of either spheroidal or toroidal type M={S,T} is uniquely defined by the three indices and is denoted by ${}_n\mathrm{M}_l^m$. The overtone number n gives the number of zero crossings in radius, while the angular degree l is the number of zero crossings if we walk from pole to pole on a great circle. In addition, the azimuthal degree m is the number of zero crossings if we walk along the equator. Hence, in a transversely isotropic, symmetric

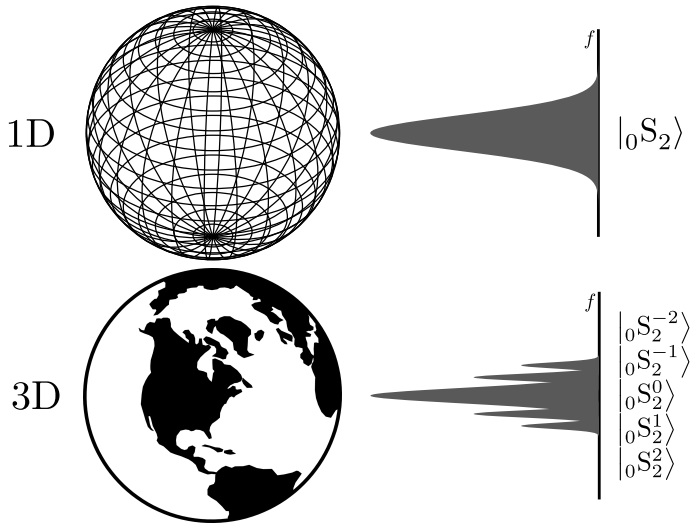

Figure 1.2: Schematic splitting of the spheroidal mode singlet ${}_0\mathrm{S}_2$ due to three-dimensional (3D) structure within the Earth. The single independent, degenerate frequency for the singlet splits into the 3D multiplet structure given by the azimuthal states $m = [-2, -1, 0, 1, 2] = [-l, \ldots, 0, \ldots, l]$.

model the modes become degenerate, which means that they are independent of the azimuthal degree m. A singlet in this sense is given by the normal mode with a unique combination of overtone number n and angular degree l. In the general case, the azimuthal degree can take values between plus and minus the angular degree $l \leq |m|$ of the mode forming the associated multiplet structure (see Figure 1.2). Since the independent, degenerate normal mode singlets couple due to any variation in the three-dimensional spherical symmetry different degree of coupling mechanisms have been developed. The simplest coupling approach is called self-coupling or splitting, which is a coupling between the modes given by their azimuthal degree m within each multiplet. One shortcoming of this self-coupling approximation is that it only depends on even degree spherical harmonics. Since these functions are point symmetric under reflection in the center of the planet, self-coupled modes only sense the average structure between pairs of antipodal points (*Woodhouse and Deuss*, 2015). Data collection is then achieved by large collections of free oscillation splitting function coefficients (*Dahlen*, 1968; *Woodhouse et al.*, 1986; *Giardini et al.*, 1987, 1988), which incorporate the sensitivity of the former degenerate normal mode to the specific lateral heterogeneity (*Akbarashrafi et al.*, 2018). Normal modes naturally can also be clustered and coupled by their distance in frequency. Narrow-band coupling, i.e. coupling within a small frequency interval, of several singlets leads to an approximation called group coupling. The introduction of this coupling type gives unique information in that it allows for the sensing of odd degree structure (*Woodhouse and Deuss*, 2015). The most complete, wide band coupling involves all the modes, including the two different types, below a certain cutoff frequency and is thus called full coupling (*Yang and Tromp*, 2015). It is important to note that the mixing of the singlets of different modes needs to be taken into account in the

generation of synthetic spectra, as through coupling toroidal modes can have effects on the vertical component of seismograms (*Woodhouse and Deuss*, 2015).

For a long time seismologists ignored the early theoretical results, as above 10 mHz the number of eigenfrequencies in a small interval becomes extensive making them nearly indistinguishable in observations. Moreover, the effects of attenuation, as well as lateral heterogeneity smear the peaks even more. The signal-to-noise ratio of the normal mode peaks improves significantly for quakes with large magnitudes, since the amplitudes of the excited waves are higher. For deeper quakes (below the crust), the surface waves have lower amplitude or do not get excited (*Masters and Widmer*, 1995), allowing for the detection of modes that are typically covered in spectra by the fundamental, surface wave modes. Another advantage is that deep quakes are less contaminated by near-source structure (scattering) lowering the noise base level. In contrast to shallow crustal quakes, they seldom excite large-magnitude aftershocks improving the detection of attenuation of the modes (*Frohlich*, 2006). Consequently, deep sources provide an independent source of information by extending the normal mode catalogues. On 22nd of May, 1960 the most powerful earthquake ever, with a magnitude of 9.4–9.6 Mw, occured in Chile. This allowed for the first undisputed observations of normal modes in history (*Ness et al.*, 1961), but it also triggered a tsunami that tragically caused thousands of casualties. The scientific results of the event peaked the interest of researchers in normal modes (*Nolet*, 2008), and over time several studies on the theoretical description, as well as measurements, have been published. The Kamchatka 1952 earthquake (9.0 Mw) was purportedly detected on a three component strain seismogram in Pasadena. This would have made for the first detection of normal modes by *Benioff and Gutenberg* (1952), but the result could not be independently verified (*Kanamori*, 1976). The results were nevertheless reinterpreted and it was concluded that the seismograms include the gravest normal mode ${}_0S_2$ at approximately 54 min period (*Kanamori*, 1976). Since that time a few more large earthquakes, such as the Sumatra 2004 (9.1 Mw) or the Tohoku, Japan 2011 (9.1 Mw), have occurred which excited strong normal modes in the Earth that in turn significantly helped expanding the normal mode data catalogues. One famous example of a deep earthquake is the 1994 Bolivia quake (8.2 Mw) with an estimated focal depth of 647 km that was detected on seismographs all around the world (Section 1.1, *Frohlich*, 2006). Currently, the earthquake database provided by IRIS (*Smith*, 1987) lists 574 earthquakes over magnitude 7 since its establishment in 1984.

In contrast to travelling waves, normal modes are directly sensitive to a planet's density making their study an important tool in constraining density variations in planets (*Resovsky and Ritzwoller*, 1998; *Ishii and Tromp*, 1999; *Romanowicz*, 2001; *Masters and Gubbins*, 2003; *Trampert et al.*, 2004; *Al-Attar et al.*, 2012). The radial density profile of a planet is predominantly constrained by its mass (2nd moment

of radial density), moment of inertia (4th moment of radial density), tides and spheroidal normal modes affected most by self-gravitation ($f \lessapprox 0.3$ mHz) (*Kennett*, 1998) (see Appendix A.1). Although the catalogue of large quake events grows over time, there is currently no consensus in the community on a one-dimensional (1D) density model for the Earth. Density models that are not based on long period signals are usually obtained by scaling a shear-wave velocity model, which is an approximation in that it works only if the heterogeneity has a single cause, such as temperature or composition (*Ishii and Tromp*, 1999). Hence, any improvement on the resolution in density has the potential to gain unique information about the thermal and compositional evolution of the planet. Normal modes do not only constrain density, but in addition help in determining the large scale structure of planets and were essential in the discovery of the solidity of Earth's inner core (*Dziewonski and Gilbert*, 1971). Dispersion data of normal modes and especially surface waves, which are equivalent to normal modes with low overtone numbers in comparison to their angular degree ($n \ll l$), can also be linked to thermochemical parameters through a thermodynamic formalism depending on composition, temperature and pressure for computing mantle mineral phase equilibria and physical properties (*Khan et al.*, 2011, 2013). Long-period spectra can also be used to infer the overall magnitude of very large events, as it was proven that high frequency waves significantly underestimate their true moment (*Park et al.*, 2005).

1.1 Numerical treatment of normal modes

The computational calculation of the free oscillations of a planet started with *Alterman et al.* (1959) who determined not only the period of the gravest spheroidal oscillations, but a whole spectrum of oscillations with the help of the first computer in Israel, and one of the first large-scale computers in the world, the WEIZAC. A numerical treatment of modes starts with the homogeneous wave equation producing orthogonal and complete eigenpairs and uses these to obtain solutions of the inhomogeneous problem containing a source. Indeed the computational effort in the calculation of free oscillations lies in the calculation of the spectrum of eigenfrequencies and eigenfunctions and, over time, several methods to perform this task have been proposed (*Al-Attar and Woodhouse*, 2008). Today, one of the most commonly used, "battle-tested" (p. 163, *Nolet*, 2008), and openly available programs to compute the free oscillations of a planet is `MINEOS` (*Masters et al.*, 2011). Its code base, called `EoS`, was written by F. Gilbert around 1966, who directly integrated the involving ordinary differential equations (see chapter 2) with a variable order and variable step-size Runge-Kutta (up to 8th order). The estimation of the step size in the code roughly depends on the growth rate of the eigenvalues. Shortly after, Adam Dziewonski included transverse isotropy and frequency dependent models into the

code (*Woodhouse*, 1988). At high frequencies the integration of the spheroidal mode ordinary differential equations (ODEs) become challenging as the initially clearly linearly independent set of solutions are projected onto the solution having the most rapid exponential increase making them effectively linearly dependent. This let to the introduction of minor vectors by *Gilbert and Backus* (1966), which in essence solves directly for the relevant solution determinants that emerge in the integration process. Another feature is a rather curious way of counting the modes, using a arccotangent-function of the ratio of eigenfunction and traction that yields integer steps for the number of modes under a certain frequency depending on the radius. To ensure that all modes in the spectrum under a certain cutoff frequency are found these steps can be used in a bisection process to ensure completeness of the spectrum. After the introduction of these methods by *Woodhouse* (1988), the code base was called `OBANI`, which stands for omega-bound-anisotropic. This code was later further modified by G. Masters to include mode counters for toroidal and radial modes and to accurately compute eigenfunctions for Stoneley and IC modes (downward integration needed to match the eigenfunctions) and finally emerged with its current name `MINEOS` (short for Minors-EOS) (*Masters et al.*, 2011; *Woodhouse and Deuss*, 2015). Another important program is DISPER80 (*Saito*, 1988) which is also based on a direct numerical integration method (*Takeuchi and Saito*, 1972).

A different way to tackle the challenge of integrating the differential equations is by employing Ansatz functions for the solutions together with a suitable integration scheme. The method of applying spectral elements for the discretization of the eigenfunctions avoids some of the problems encountered in the aforementioned direct integration codes. Possibly the first work to employ spectral elements for the calculation of normal modes (in the time domain) is that of *Chaljub and Valette* (2004). To improve on the existing normal modes synthetic methods and due to the need of high numerical accuracy to determine density variations in planets we utilize this spectral element method. It combines the flexibility of the finite-element method in accounting for topography in the meshes with the highly desirable convergence properties of Lagrange-basis functions together with the accuracy of Gauss-Lobatto-Legendre integration inside elements (*Igel*, 2017). The possibility to properly align the mesh cells with topographic boundaries is especially important for the calculation of normal modes in contact with internal or free-surface boundaries, i.e. Stoneley modes and fundamental surface wave modes. The spectral element method and in particular the use of the weak, integral form of the equations enables us to implicitly solve for the boundary terms. As we will see in chapter 2, these advantages will enable us to achieve high accuracy, as well as efficiency due to the often diagonal mass matrix that has to be inverted in the solving of the underlying eigenvalue problem.

1.2 Tides

Tidal forces emerge from the gravitational attraction of massive external bodies. They deform planets by changing the gravity potential and thus influencing the spatial distribution of the mass. Earth's tides primarily arise from changes in its gravity potential from the Sun and especially the Moon. The observations of the influence of tides provide independent information on planetary bodies' structure, detecting for example the anelastic structure of Mars (*Bagheri et al.*, 2019) or the thickness of the ice shield on the Jupiter moon Europa (*Wahr et al.*, 2006). Information on the tidal variations also allows for the removal of them from other measurements, for example in normal mode measurements. Tides can also trigger quakes as seen for Earth (e.g., *Schuster*, 1897; *Knopoff*, 1964; *Tamrazyan*, 1968; *Enescu and Enescu*, 1999; *Tanaka et al.*, 2002, 2006; *Thomas et al.*, 2009; *Varga and Grafarend*, 2019) and Moon (e.g., *Goulty*, 1979; *Frohlich and Nakamura*, 2009). In some cases tides induce volcanic activity, as is known for Earth (e.g., *Sparks*, 1981; *Kasahara*, 2002; *Sottili et al.*, 2007) or on the Galilean Jupiter moon Io due to tidal heating (*Peale et al.*, 1979) making it highly volcanically active. In our case, we are primarily interested in the sensitivity of the lowest order tidal perturbation coefficients, called Love numbers, to determine Earth's seismic and anelastic structure (see chapter 3).

The perturbation of the gravitational potential is called deformation potential V_d, and it can be determined from the tidal potential V_t. The associated potential Love number k is then defined by the ratio of these potentials $k = V_d/V_t$ (*Love*, 1927). The Love number h is given by the ratio of the radial displacement of an element of mass of the elastic Earth to the corresponding displacement for a liquid Earth. Moreover, the Shida number l represents the ratio of the transverse displacement of the element of mass of the crust to the displacement for the hypothetical liquid Earth. If the potential of degree n at the surface is V_n, then the distortion of the Earth caused by tidal forces produces an additional gravitational potential $k_n V$, a vertical displacement $h_n(V/g)$, and a horizontal displacement $l_n(\nabla V/g)$ (*Agnew*, 2005).

1.3 Attenuation

Generally, attenuation is defined by loss of signal amplitude over time. For seismic waves, this can be separated into intrinsic attenuation, which involves irreversible anelastic losses due to the viscous behaviour of carrier materials, and scattering attenuation that is given by partitioning or loss of energy into separate waves at scatterers or discontinuities that concur with impedance jumps. Anelasticity is a

property of materials that causes physical dispersion of seismic waves. (*Kanamori and Anderson*, 1977). Hence, the normal modes description of seismic waves is not immune to these effects. Anelastic effects in radial models or global modes are commonly incorporated into quality factors Q that enter as decay factors $\gamma = Q^{-1}$ into the time series of seismic signals by a multiplication with $\exp^{-\gamma t}$. There is a consensus in the community that the intrinsic quality factor Q in the Earth's mantle is nearly period independent at least within the common seismic periods from 1 s to 1 hour (*Knopoff*, 1964). This does not hold for longer periods or shorter periods and also does not give us a free pass to neglect anelasticity altogether. It is good practice to model the behavior of anelastic material with a linear viscoelastic model, such as Maxwell (*Ben-Menahem and Singh*, 1981), extended Burgers (*Faul and Jackson*, 2015), Andrade (*Gribb and Cooper*, 1998), and Sundberg-Cooper model (*Sundberg and Cooper*, 2010). These models are interesting to us because they can be employed in the development of radial shear quality models (e.g., *Bagheri et al.*, 2019). It is necessary to include anelasticity in long period signals as significant discrepancies are found between elastic planet models produced using normal mode and travel time data (*Randall*, 1976). This approach was verified by *Jeffreys* (1967), who was able to reconcile early found differences in using normal modes and travelling-waves for the determination of the Earth's core radius. Figure 1.3 shows the influence of attenuation on the spheroidal modes till 10 mHz using anisotropic PREM(*Dziewonski and Anderson*, 1981) as radial Earth model. The normal mode frequencies most affected by the attenuation are related to crustal surface wave, core sensitive, and especially inner-core boundary Stoneley modes, which are changing up to 2.5% in eigenfrequency. The radial anelastic structure is an important tool to determine the deep structure and composition of planets because of its strong sensitivity to temperature (*Karato and Karato*, 2003). For more information on Earth's anelastic structure see chapter 3.

1.4 Normal mode data

Reliable normal mode measurements are only possible for very large magnitude, preferably deep, quakes. Especially the low frequency normal modes are hard to measure due to noise induced by surface waves, tidal frequencies being in close proximity or traces not being recorded for the required prolonged time at high quality (no glitches or calibration pulses).

In general, strips of several thousand seismic recordings are used to reliably measure the normal mode properties. As a consequence of the diagonal sum rule, the first-order eigenfrequency perturbations of a multiplet split by any three-dimensional effect, such as rotation, ellipticity or lateral heterogeneity, is equal to zero (*Gilbert*,

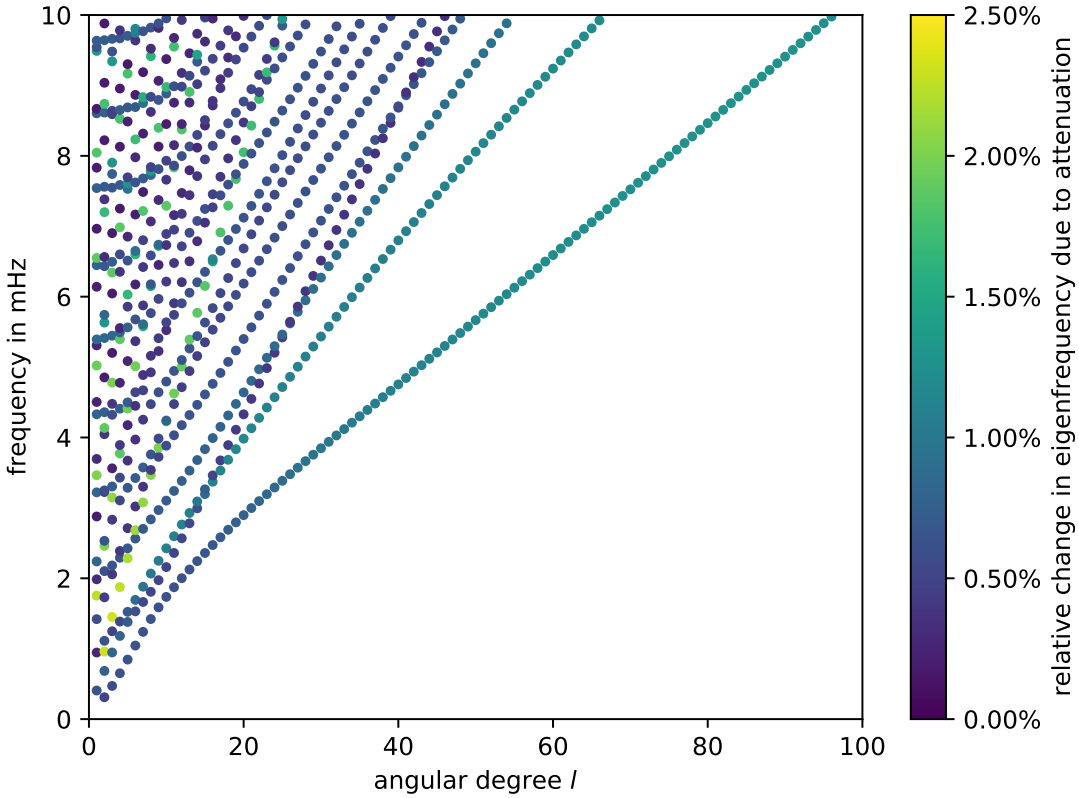

Figure 1.3: Influence of attenuation on spheroidal modes up till 10 mHz calculated with `specnm` (*Kemper et al.*, 2021) for anisotropic PREM (*Dziewonski and Anderson*, 1981). The color scale is indicating the relative eigenfrequency change of the attenuated spectrum to the elastic spectrum. Modes most affected by attenuation are crustal surface wave modes, core sensitive modes and especially inner-core boundary Stoneley modes. This dispersion diagram shows the typical terracing or branching of the modes and one can clearly identify the fundamental branch in the bottom that corresponds to overtone number $n = 0$ and is clearly separated from the other branches. This branch corresponds to Rayleigh surface waves that sense increasingly shallower the higher the angular degree l. Overall, modes with lower angular degree (more left in the diagram) and higher frequency (up in the diagram) are sensitive to deeper structure. A more detailed explanation of the dispersion diagram for Earth can be found in (Section 8.8.10, *Dahlen and Tromp*, 1998).

1971). For this reason the measured center frequencies from different sources and receivers constrain the spherically averaged, unperturbed planet. With the advent of global seismological networks that are professionally maintained and the occurrence of ever more large quakes in the databases the normal mode central frequency catalogues are ever expanding (*Deuss et al.*, 2013). The properties of the normal modes (e.g. center frequencies f_{obs} and quality factors Q) and their associated uncertainties can then be determined with different techniques which we will briefly explain. The raw traces are cut to last roughly the length of one Q-cycle (*Dahlen*, 1982), which is the time in which the amplitude of the signal decays to $e^{-\pi}$ of its original amplitude. The first hours after the event are removed to allow for the decay of fundamental and other mantle sensitive modes that are affected by higher damping. Known tidal signals, glitches and smaller events are removed. Double events

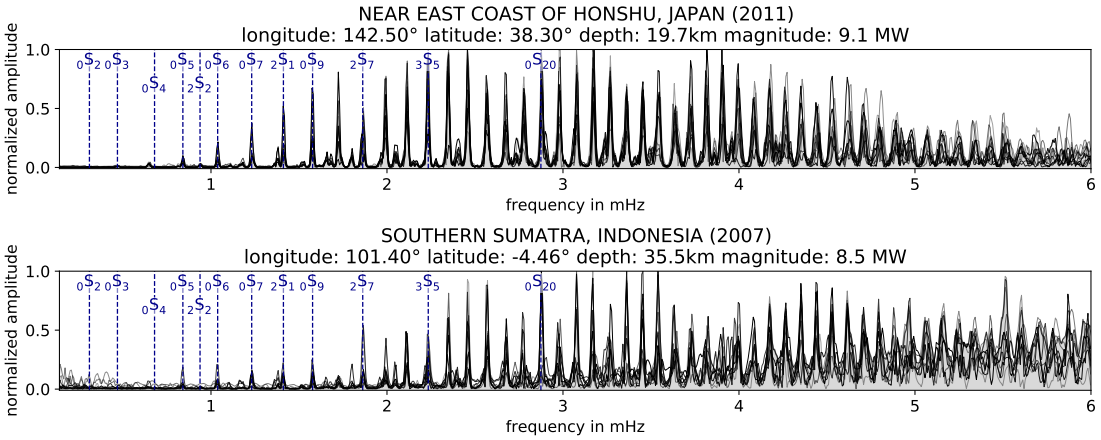

Figure 1.4: Spectra for two large events, Japan 9.1 MW and Sumatra 8.5 MW, in the IRIS database till 6 mHz for vertical components of several receivers over the globe. Some synthetic mode center frequencies calculated with `specnm` (*Kemper et al.*, 2021) (see chapter 2) for anisotropic PREM (*Dziewonski and Anderson*, 1981) are indicated in dark blue.

with roughly the same magnitude in close succession are removed. Station response functions are deconvolved and the signal is reconvolved with standard responses. The time series is zero padded, tapered and then Fourier transformed to get the spectrum (see Figure 1.4 for two example spectra). In past studies, such as *Masters and Widmer* (1995), for the measurement of the central frequency of singlets, a histogram analysis of peak-frequency from single recordings was made which then had to be corrected for 3D structure. For strongly coupled modes a multiple-record analysis to isolate the individual singlets of a multiplet was performed to reliably estimate the mean frequency, in which 3D perturbations on the spherical symmetry, such as ellipticity, were included. The measurement of quality factors depend on the spectral amplitude that is strongly influenced by noise which makes it potentially harder than the measurements of central frequencies. The traditional way to detect quality factors is to perform a time lapse analysis where the amplitude of a mode is measured from the spectra of successive time windows and the damping is estimated from the amplitude decay (*Smith*, 1972; *Masters and Gilbert*, 1983). *Buland and Gilbert* (1978) employed the minimum width technique for measuring Q, which detects the decay factor by multiplying the record by a trial growing exponential function $e^{\gamma t}$, in which the decay factor is varied until the trial function matches the width of the spectral peak of the mode. These methods only work for single modes and it is hard to perform a formal error analysis to properly estimate uncertainties for the measured parameters. In contrast, the quality factors measured in *Masters and Widmer* (1995) are produced by an autoregressive, nonlinear least square method, which was first introduced for mode measurements by *Masters and Gilbert* (1983) building on the work of *Bolt and Brillinger* (1979), which allows for the simultaneous fitting of multiple splitting coefficients and multi-mode estimation. A major advantage of this method is that extensive error analysis exists which allows

for the determination of formally proper uncertainties (*Dahlen*, 1982). In addition, it allows for the easy incorporation of tapering of the signals that is essential to isolate modes in the spectrum (*Dahlen*, 1982). One disadvantage of these early estimations is the assumption that the mean width of a mode multiplet is directly related to the attenuation rate of the singlet associated to the multiplet (*Masters and Widmer*, 1995).

By incorporating the effects of group coupling through aspherical structure and the Coriolis force, general spectral fitting (GSF) surpasses the aforementioned spectral fitting approaches in accuracy and precision by improving the internal consistency of structure coefficient estimates and hence yielding better fits to normal modes of intermultiplet coupled modes (*Resovsky and Ritzwoller*, 1998). Interestingly, toroidal and spheroidal modes can couple together in this approach, as happens to be the case for example between ${}_0\mathrm{T}_{18}$ and ${}_0\mathrm{S}_{17}$ (*Resovsky and Ritzwoller*, 1998). The uncertainties produced by this method can be described as numerical errors in the synthetic formulations, covariance errors of the regression matrices, and truncation errors by using the first order approximation.

All the measured normal mode parameters in chapter 3 are inferred from modal spectra up to 10 mHz and include either self-coupling or group-coupling in the measured splitting functions. Splitting of the gravest modes is primarily due to rotation and ellipticity of the Earth, while splitting of short-period modes results from heterogeneity and anisotropy as they are more sensitive to small-scale structure (*Deuss et al.*, 2013).

In modern catalogues, such as *Deuss et al.* (2013), the data is collected by comparing synthetic seismograms produced by normal mode summation to observed seismograms. Since the seismograms depend non-linearly on the splitting function coefficients c_{st}, the used inversion algorithm is the iterated damped least squares inversion (*Tarantola and Valette*, 1982). The normal mode parameters most relevant to us, i.e. the central frequency f_c and quality factor Q, are the most robust parameters in this type of inversion since they are not damped (*Deuss et al.*, 2013) and hence they do not depend on the choice of the dampening factor. They are generally measured in relation to the 1D reference model PREM (*Dziewonski and Anderson*, 1981) by:

$$f_c = f_0 + (4\pi)^{-1/2}\mathrm{Re}(c_{00}), \tag{1.1}$$

$$Q = \frac{f_c}{2\left(\frac{f_0}{2Q_0} + (4\pi)^{-1/2}\mathrm{Im}(c_{00})\right)}, \tag{1.2}$$

where the frequency f_0 and the quality factor Q_0 refer to the reference model. The c_{st} coefficients are following the same definition as in *Resovsky and Ritzwoller* (1998)

and have units of frequency. Specifically, the c_{00} coefficient is directly related to the shift in center frequency and the global quality factor by its real and imaginary parts respectively.

The main challenge encountered with measurements of toroidal normal mode parameters is that high quality horizontal component seismic traces are required and they are harder to collect than the radial traces needed for spheroidal mode measurements due to increased noise levels (*Tromp and Zanzerkia*, 1995). For the estimation of uncertainties, *Deuss et al.* (2013) do not use the algorithmically-determined uncertainties, but perform a cross-validation of the results. The method leaves out individual events in the inversions and thus estimates the importance of the large earthquakes on the final results. The maximum spread in the results given by this procedure for each measured splitting function coefficient gives its uncertainty. This cross-validation method yields a conservative estimate of the error in the measurements (*Deuss et al.*, 2013). It should be noted that the uncertainties in these studies are generally understandable as relative uncertainties between the simultaneously measured modes (A. Deuss, pers. comm., 2021). This allows for accounting of other error sources, such as numerical errors, in the uncertainties of the central frequencies by introducing a multiplicative factor and thus reweighting them in relation to other catalogues.

1.5 Inverse Problems

Inverse problems are a cornerstone in scientific modelling and especially in the geosciences. The solving of geophysical inverse problem is used to directly infer models or their structure parameters from observed data. The general inverse problem is typically characterised by a highly nonlinear dependence of the data on the model parameters that can be expressed by means of a numerical algorithm (forward). The forward problem has a general, unique solution for deterministic physical problems, while the inverse problem does not (*Tarantola*, 2005). As a consequence, it is important to consider the a priori information on the model parameters and the data uncertainties. The most general theory for this inverse problem is obtained from a probabilistic viewpoint and is based on Bayes's theorem. A common way to describe these inverse problems with negligible modelling uncertainties is:

$$\sigma(\mathbf{d}, \mathbf{m}) \propto \rho(\mathbf{m}) L(\mathbf{d}, \mathbf{m}). \tag{1.3}$$

In this, $\rho(\mathbf{m})$ is the prior probability distribution that is multiplied by the likelihood function $L(\mathbf{d}, \mathbf{m})$ to give the posterior probability density $\sigma(\mathbf{d}, \mathbf{m})$ that depends on the data (including uncertainties) $\mathbf{d}$ and model parameters $\mathbf{m}$. The prior probability distribution $\rho(\mathbf{m})$ represents all the a priori information on the model parameters.

Here, the likelihood function measures how well a model **m** is fitting the data by employing a misfit function. In our model inversion (see chapter 3), we rely on a stochastic-based sampling algorithm, called Metropolis-Hastings, to sample the posterior probability space. The algorithm works in an iterative fashion by randomly perturbing the parameters of an initial model and then accepting the new model based on the likelihood and hence data misfit of the initial to the perturbed model with higher probability given to better fitting models (*Metropolis et al.*, 1953; *Hastings*, 1970). The main advantage of this algorithm is its ability to step within the model space without excessively sampling areas that are inconsistent with data and prior information. This probabilistic approach allows for nonlinear inverse modelling bringing forth the possibility to obtain uncertainties for the modelling parameters which in turn allow for interpretation of the data sensitivities. Since its beginning, the development of geophysical inverse theory was predominantly driven by long period seismologists engaged in the study of free oscillations to map the radial structure of the Earth (*Dahlen and Tromp*, 1998).

1.6 Earth radial reference models

Seismological observations are summarised through one-dimensional radial reference models specifying density, compression & shear wave velocities, and their respective attenuation parameters, i.e. quality factors. All the models described here agree on the general structure of Earth given by: Crust (≈0–35 km, upper mantle (≈35–670 km depth), lower mantle (≈670–2,890 km depth), liquid outer core (≈2,890–5,150 km), and inner core ≈5,150–6,371 km.

Reference models are utilized regularly for location and characterization of seismic sources. Material scientists who are interested in the internal constitution of the Earth, use the models for reconciliation of their results derived from laboratory experiments and mechanical modelling. As has been identified by *Kennett* (2020), the structure modelling methods can be divided into three distinct categories: normal mode, body wave, and equation-of-state studies. All these models have significant limitations that, although in some cases are blatantly obvious, are often disregarded or not even recognized by scientists looking for a radial Earth structure reference.

First reference models for the structure of Earth were derived based on travel-time tables (*Jeffreys and Bullen*, 1940) and emerged in the context of interpreting arrival times of seismic phases. Significant progress was made once a larger number of free oscillations of the Earth were observed, which not only provided more insight into the density structure, but also improved the core structure. This led to the development of the 1066A and 1066B models by *Gilbert and Dziewonski* (1975) that differ mostly in the upper mantle structure due to the insensitivity of the employed

normal modes in that region. This type of modelling culminated in the release of the classical radial Earth model of *Dziewonski et al.* (1981), called Preliminary Reference Earth Model (PREM), which was the most important result of the Standard Earth Model project sponsored by the International Association of Seismology and Physics of the Earth's interior (IASPEI). Even though the model is 40 years old at the time this thesis is written, it is still widely employed and takes a dominant role as reference for a wide range of diverse scientific studies. Although the data used in the study consists of free oscillations (normal modes and surface waves), geodetic observables, and travel-times it is mostly recognized to be a long period study mainly due to the large number of modes (>1000) used in its inversion. In addition to providing a basic (shear wave) attenuation structure, which makes the model inherently frequency dependent, PREM also includes transverse anisotropy in the upper mantle to reconcile the central frequencies of Love and Rayleigh surface wave modes. The normal modes control the global radial seismic structure in PREM, while the high frequency body wave travel times were used to obtain fine-scale perturbations in the wave speeds (*Dziewonski et al.*, 1981). PREM is rarely used for high frequency body wave studies, since particularly for core phases there are offsets in the travel time predictions (*Kennett*, 2020). In addition, the employed parametrization of density and velocities in radius with low order polynomials is not accurate enough to model the complexity needed to describe travel times of all high frequency phases (*Kennett*, 2006).

To update the outdated, and in part incorrect, travel time tables of *Jeffreys and Bullen* (1940), the IASPEI established a working group to work on the creation of a new radial Earth model to match the behaviour of the empirical travel times. For that, *Kennett and Engdahl* (1991) used a parametric representation similar to PREM to directly represent high-frequency (1 Hz) mantle phase travel times together with the core structure from PEM (*Dziewonski et al.*, 1975), which resulted in the IASP91 model. The IASP91 model improved on the estimation of depth of events in the source location process mainly due to the use of updated compression, P phase arrival times, specifically of their associated surface reflections (pP, sP) (*Kennett*, 2006). Due to the addition of the core structure from a different model, IASP91 is not consistent in fitting core phases and manifests the same problems as PREM with the restrictiveness of large scale polynomial representation of the velocities. Based on the relocation of events with wide geographic coverage using IASP91, another update to the travel time tables resulted in an inversion that in turn produced the AK135 model (*Kennett et al.*, 1995). In contrast to the slightly higher order polynomial parameterisation of PREM (*Dziewonski et al.*, 1981) and IASP91 (*Kennett and Engdahl*, 1991), the AK135 model is represented as a sequence of linear gradients in radius. In comparison to IASP91, AK135 exhibits only slight differences in velocity structure except in the core and specifically at the inner core

boundary, hence it mainly improves the representation of core phases. Like IASP91, the model suffers from the nonuniform distribution of seismic events and stations on Earth resulting in a northern hemisphere bias due to oversampling (*Kennett*, 2020). Both models do not provide any attenuation information, are transversely isotropic and either do not provide any or have high uncertainties on their density structure. In an attempt to construct a travel time model that also represents geodetic and normal mode constraints, *Kennett* (2020) included results from different normal mode and equation of state studies and perturbed the AK135 structure accordingly. The main change is that the model shows higher compressional wave speeds in the upper part of the outer core with respect to AK135 to improve the misfit to core transitioning SmKS phases that are for the most part sensitive to the gradient in compressional velocity in the uppermost outer core. The subtle differences in core structure also produce a decrease of 2.5 per cent in shear wave speed in the inner core with respect to PREM. Although the model was created with restrains from models derived from normal mode and geodetic constrains the required features by normal modes and travel times do not consistently converge and the EK137 model likewise does not provide an equally satisfactory fit to both classes of observations. Due to the use of AK135 (*Kennett et al.*, 1995) as a reference model, and since density is not constrained by travel times, it is still the least defined aspect of the radial Earth structure in EK137 (*Kennett*, 2020). Starting from the PREM radial structure, *Stacey and Davis* (2004) used equations of state to develop radial models of elastic moduli and density. The idea of a well mixed (isentropic) outer core together with newly available normal mode databases led *Irving et al.* (2018) to select normal modes sensitive to the outer core structure, including ones that were not present at the time PREM was build, to invert the density and compression wave structure based on a Vinet equation-of-state. It is important to note that the use of an equation of state naturally maintains an adiabatic state (Adams-Williamson condition) in the core resulting in a Bullen parameter that is indistinguishable from unity. The main finding is that with respect to PREM the outer core is denser and shows a slightly higher gradient in compression wave velocity at the top of the outer core, which is depicted as a green line in Figure 1.5. Though the pressure is self-consistent, the primary geodetic constraints on mass and moment of inertia cannot be fulfilled by the model as the remaining Earth structure is fixed to PREM. In any case, all the models are shown in relation to the PREM values in Figure 1.5. The most striking differences of the newer models with respect to PREM are situated in the upper mantle, the D" region and the outer core.

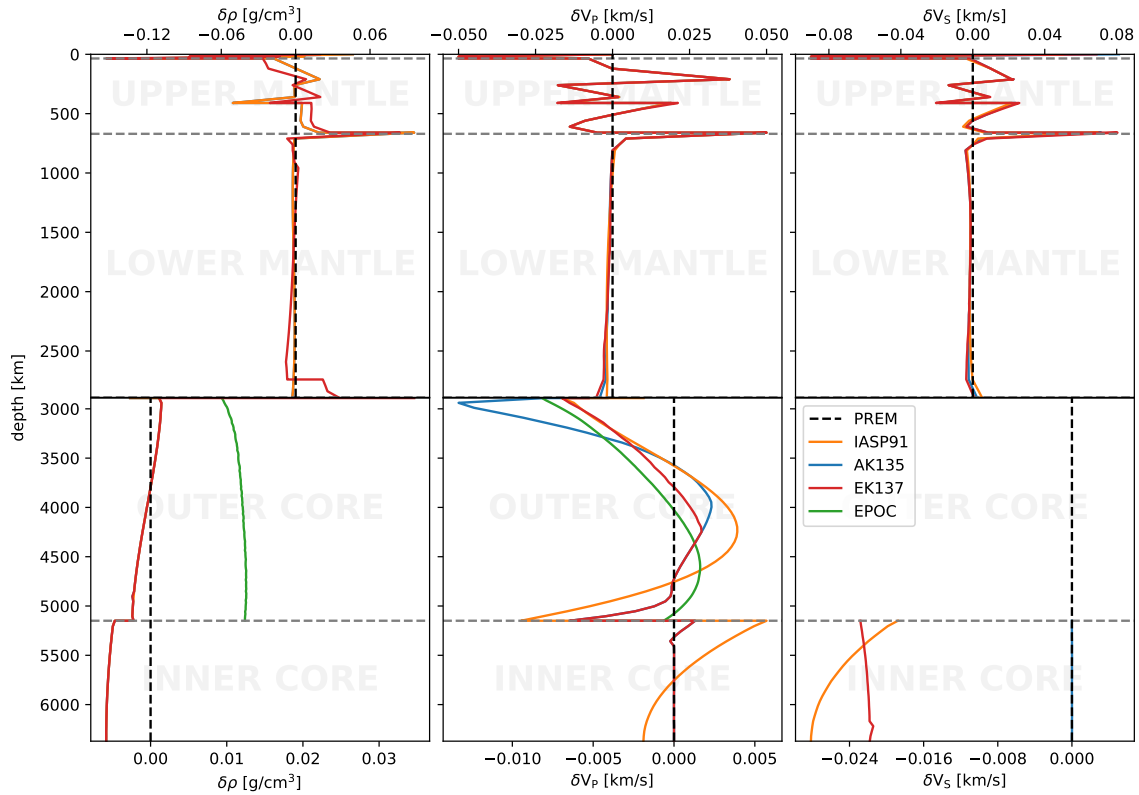

Figure 1.5: Historic models for isotropic radial Earth structure. All models are shown relative to the PREM (*Dziewonski and Anderson*, 1981) (black dashed line) values due to the fact that PREM is afaic the reference model for most studies. Shown here are as line plots in order (omitting PREM): IASP91 (*Kennett and Engdahl*, 1991) in orange, AK135 (*Kennett et al.*, 1995) in blue, EK137 (*Kennett*, 2020) in red, and EPOC (*Irving et al.*, 2018) in green.

1.7 Thesis outline

The chapters in this thesis are based either on peer reviewed publications in international scientific journals or in the case of chapter 3 on a submitted publication to Geophysics Journal International. Any changes to the peer reviewed papers are indicated by footnotes in their respective chapters. Redundancies, especially in the introductions of the following chapters and this introduction chapter can be expected.

Chapter 2 describes the use of spectral elements for the computation of normal modes of general spherical bodies. We derive the weak form of the associated ordinary differential equations for radial, spheroidal and toroidal modes and the discretization of the integrals. Furthermore, we describe the challenges we faced in computing normal modes in non regularly stratified liquids concerning undertones, as well as the occurrence of numerical spurious modes. We end the chapter by showing applications of the normal mode code and to this end show Earth, Europa and Mars spectra with respective distinctive mode types.

The next two chapters can be considered applications of the spectral element

normal mode code (`specnm`) developed in chapter 2.

In chapter 3, we invert one-dimensional, average isotropic radial Earth structure models using probabilistic inversion based on Bayesian posterior sampling. An advantage of our modelling approach to former studies is a consistent utilization of highly accurate spectral element synthetics for the description of the long period signals (forward), i.e. tides and normal modes, which in turn improves density resolution. In addition to that, we use a thermodynamically self-consistent formulation of the planet by employing Gibbs minimization in the mantle and equation of state modelling in the outer and inner core. One important difference to former models is that we base our one-dimensional mantle attenuation profile on the viscoelastic extended Burgers model allowing us to gain further insight into the Earth anelastic behaviour.

Chapter 4 presents a simplification approach to the self-gravitation problem in the three-dimensional description of long period seismic signals. One important challenge in the case of wave propagation affected by gravity is that associated the gravity potential, as described by a Poisson equation coupled into the wave equation, extends outside of the planet. The crucial realization regarding gravity is that the potential falls off with $1/r$ to infinity. We show that a combination of adaptive mesh refinement, higher order shape-mapping and multipole expansion of the boundary condition of this external gravity potential improves efficiency of the solving of the Poisson equation to the order of the solving of the elastic time stepping problem in the global three-dimensional wave equation.

We summarize, discuss and give an outlook to this thesis in chapter 5.

Chapter 2

A spectral element approach to computing normal modes

This chapter is published in Geophysical Journal International, as *A spectral element approach to computing normal modes*, J. Kemper, M. van Driel, F. Munch, A. Khan, D. Giardini (2021).

2.1 Introduction

The analysis of the global seismic displacement wavefield in terms of discrete frequencies termed normal modes or free oscillations is a classical approach in long-period seismology that dates back to the work of *Poisson* (1829); *Thomson* (1863); *Lamb* (1881). Mathematically, the modes are described as eigenfunctions and eigenvalues of a linear operator that incorporates the elastic and gravitational forces as well as the full coupling between mass displacement and changes of the gravitational potential (*Woodhouse and Deuss*, 2015).

Normal mode seismology has proved versatile by being able to provide information on the radial and lateral seismic structure of the Earth (e.g. *Dziewonski and Anderson*, 1981; *Woodhouse and Dziewonski*, 1984; *Giardini et al.*, 1987; *Lognonné*, 1991; *Resovsky and Ritzwoller*, 1999; *Al-Attar et al.*, 2012; *Irving et al.*, 2018). While Earth's seismic velocity structure continues to be imaged at ever increasing resolution (e.g. *French and Romanowicz*, 2014; *Lei et al.*, 2020; *Simmons et al.*, 2021), normal modes nevertheless remain the most promising means to constrain Earth's global-scale density structure (e.g. *Ishii and Tromp*, 1999; *Trampert et al.*, 2004). Yet, despite its importance in governing the dynamical evolution, Earth's density structure remains relatively poorly resolved. The numerical calculation of the free oscillations of Earth originated with the work of (*Alterman et al.*, 1959), who determined the periods of spheroidal oscillations of a spherically symmetric non-rotating Earth. Today, one of the most commonly used, "battle-tested" (p. 163 *Nolet*, 2008), and openly available programs to compute the free oscillations of a planet is `MINEOS`

Masters et al. (2011). The main challenge in the numerical computation of normal modes stems from the free surface boundary condition as this takes the form of a determinant of a matrix that should vanish. As all entries of this matrix are only known to finite accuracy and the determinant is computed as the difference of large numbers, its computation becomes numerically unstable. This complicates the detection of eigenfrequencies, where the boundary condition is fulfilled. Moreover, the algorithm has to find the complete spectrum of eigenfrequencies below a certain cutoff frequency and these can be arbitrarily close to each other, in particular for spheroidal modes, such that bracketing individual modes is difficult.

The reformulation of the underlying operator into minors and the introduction of mode counters by *Woodhouse* (1988) largely addressed the aforementioned issues. However, as mode counting is based on detection of the zero crossings of the characteristic function that is only known to finite accuracy, finding all modes in a reliable way remains a challenge, particularly at high frequencies. Additionally, the identification of Stoneley (*Stoneley*, 1924) and Slichter (*Slichter*, 1961) modes to high accuracy remains problematic, as the eigenfunctions are vanishingly small at the surface, where the boundary condition needs to be imposed by correct summation of the fundamental solutions. Possibly the first work to employ spectral elements for the calculation of normal modes (in the time domain) is that of *Chaljub and Valette* (2004). Here, we apply the spectral element method to discretize the weak form of the second-order ordinary differential equations (ODEs) of motion and formulate a generalized matrix eigenvalue problem in the spectral domain. We apply an iterative solver to this problem, whereby we circumvent all aforementioned issues related to the integration methods. In particular, all boundary conditions at the free surface, internal discontinuities, and the center of the planet are readily implicitly fulfilled in the weak form, such that Stoneley and Slichter modes pose no particular challenge. Modern Krylov-subspace solvers reliably find all eigenvalues (*Hernandez et al.*, 2005), including degenerate eigenvalues, such that finding the complete spectrum is straightforward without the need for a mode counter.

Matrix-based approaches have previously been proposed by *Wiggins* (1976) and *Buland and Gilbert* (1984), but both the theory of (higher-order) finite element methods and available numerical software for solving eigenvalue problems have seen a lot progress since. More recently, *Zábranová et al.* (2017) employed Chebychev polynomials to discretize the strong form of the equations to derive a matrix formulation of the eigenvalue problem. In their approach, the matrices are non-sparse and non-symmetric and the boundary conditions need to be treated explicitly. A direct eigenvalue problem solver that always computes the full spectrum is used, leading to computation times that are substantially longer than `MINEOS`. In an effort to improve computational efficiency, we derive sparse and symmetric matrices and only solve for the eigenpairs of interest through an iterative solver.

In the following, we briefly describe the underlying theory (detailed treatments can be found in *Takeuchi and Saito*, 1972; *Dahlen and Tromp*, 1998; *Woodhouse and Deuss*, 2015), adhering to the notation of *Dahlen and Tromp* (1998) (section 2.2). Following this, we detail the methodology behind the use of spectral elements for the discretization of the weak form of the ODEs and the computation of normal modes in general (section 2.3). Next, we apply our method to the computation of toroidal and spheroidal normal mode spectra for several planetary bodies, including Earth, Mars, and the Galilean moon Europa, and compare results with those obtained using other numerical schemes (section 2.4). Finally, the python-based implementation of the normal mode spectral element method presented herein (spectral element normal mode code; `specnm`) is available open source (see data availability section).

2.2 Theory

2.2.1 Radial Scalar Equations

For spherically symmetric, non-rotating, elastic (SNRE) planets, the wave equation can be simplified by a separation of variables in spherical coordinates, e.g. by using vector spherical harmonics (*Dahlen and Tromp*, 1998) as an Ansatz for the displacement eigenfunctions. This leads to a set of ordinary differential equations with the radius of the planet as the only coordinate and where the dependence of the solution on latitudinal and longitudinal coordinates is readily incorporated via spherical harmonics (see Appendix A.2.1 and *Dahlen and Tromp* (1998)). Normal modes are classified in two types as toroidal T (SH or Love wave interference) or spheroidal S (P-SV or Rayleigh wave interference) modes. Hereinafter, we denote $n \in [0, \infty)$ as the radial order or overtone number, $l \in [0, \infty)$ as the angular degree and m as the azimuthal order in the range $-l \leq m \leq l$. The asymptotic angular wavenumber that is associated with each mode is defined as $k = \sqrt{l(l+1)}$. We further denote the toroidal displacement eigenfunctions as $W(r)$ and the spheroidal displacement eigenfunctions as $U(r)$ and $V(r)$. Since spheroidal oscillations also involve changes in density, and therefore perturbations in the gravitational potential, we define the associated function $P(r)$ through an additional coupled ODE. The spheroidal modes with angular degree $l = 0$ are a special case and are called radial modes, as the horizontal displacement vanishes and the system of ODEs is simplified to a single second-order ODE. Toroidal modes only exist for angular degrees $l \geq 1$. The toroidal mode ${}_0\mathrm{T}_1$ and the spheroidal mode ${}_0\mathrm{S}_1$ correspond to solid body rotation and translation, respectively, with a zero eigenfrequency and are thus discarded in the computation of synthetic seismograms. It should be noted here, that for spherically symmetric non-rotating bodies, the azimuthal order m does not appear in the equations and the eigenfrequencies are thus degenerate with multiplicity

Table 2.1: Boundary conditions for the second-order radial equations for the eigenfunctions U, V, W, P and corresponding tractions T_U, T_V, T_W, T_P. Zero radius (center of planet) boundary conditions are based on *Zábranová et al.* (2017).

toroidal	$W(r)$
free surface and solid-fluid boundary	$T_W = 0$
zero radius	$W = 0$
radial	$U(r)$
free surface	$T_U = 0$
zero radius	$U = 0$
spheroidal	$U(r), V(r), P(r)$
free surface	$T_U = T_V = T_P = 0$
solid side of solid-fluid boundary	$T_V = 0$
zero radius	$\partial_r U = \partial_r V = P = 0, \quad (l = 1)$ $U = V = P = 0, \quad (l \geq 2)$

$2l+1$. The eigenfrequencies and radial eigenfunctions are then uniquely determined by their angular degree l and overtone number n so that the modes of both types are identified as ${}_n\mathrm{T}_l$ and ${}_n\mathrm{S}_l$. To achieve symmetry, the weak form is usually derived from the second-order form of the ODE in wave propagation problems. Here, we derive the second-order ODEs for all three mode types and for transversely isotropic media (parametrized by the Love parameters A, C, L, N, F and density ρ) from the more commonly-used first-order form (Appendix A.2.1). For toroidal oscillations, we obtain a second-order ordinary differential equation by taking the radial derivative of the toroidal first-order equation (Eq. A.2) and inserting the expression for the radial derivative of the traction (Eq. A.3):

$$\rho\omega^2 W = -\partial_r T_W + (k^2 - 2)Nr^{-2}W - 3r^{-1}T_W, \tag{2.1}$$

where the traction $T_W(r)$ is given by (*Dahlen and Tromp*, 1998, Eq. 8.193)

$$T_W = L(\partial_r W - r^{-1}W). \tag{2.2}$$

The boundary conditions are given in table 2.1, which together with the jump condition at the internal discontinuities that follows from the continuity of the eigenfunctions and tractions, define the solution space. For spheroidal oscillations there are three coupled second-order ODEs corresponding to the eigenfunctions $U(r)$, $V(r)$, and $P(r)$. As for the toroidal case, the equations for the spheroidal case are obtained by taking the radial derivative of the spheroidal first-order equations (Eqs. A.4–A.6)

and inserting the tractions (Eqs. A.7–A.9):

$$
\begin{aligned}
\rho\omega^2 U = &- \partial_r T_U \\
&- [4\rho g r^{-1} - 4(A - N - C^{-1}F^2)r^{-2}]U \\
&+ [k\rho g r^{-1} - 2k(A - N - C^{-1}F^2)r^{-2}]V \\
&- (l+1)\rho r^{-1} P \\
&- 2(1 - C^{-1}F)r^{-1}T_U + k r^{-1} T_V + \rho T_P, \\
\rho\omega^2 V = &- \partial_r T_V \\
&+ [k\rho g r^{-1} - 2k(A - N - C^{-1}F^2)r^{-2}]U \\
&- [2N r^{-2} - k^2(A - C^{-1}F^2)r^{-2}]V \\
&+ k\rho r^{-1} P \\
&- kC^{-1}F r^{-1} T_U - 3 r^{-1} T_V, \\
0 = &- \partial_r T_P \\
&- 4\pi G(l+1)\rho r^{-1} U \\
&+ 4\pi G k \rho r^{-1} V \\
&+ (l-1) r^{-1} T_P.
\end{aligned}
\tag{2.3}
$$

Here the tractions $T_U(r)$, $T_V(r)$ and $T_P(r)$ are defined as:

$$
\begin{aligned}
T_U &= C\partial_r U + F r^{-1}(2U - kV), \\
T_V &= L(\partial_r V - r^{-1}V + k r^{-1} U), \\
T_P &= \partial_r P + 4\pi G \rho U + (l+1) r^{-1} P,
\end{aligned}
$$

where G denotes the gravitational constant and $g(r)$ the gravitational acceleration in the undeformed planet, which is uniquely determined from the density profile $\rho(r)$. The boundary conditions can be found in table 2.1 and continuity of eigenfunctions and tractions holds as in the toroidal case.

For short-period oscillations, self-gravity plays a negligible role as a restoring force compared to the elastic forces (*Dahlen and Tromp*, 1998) and the change in the gravitational potential due to the mass redistribution caused by the seismic disturbance can be omitted (for a quantitative error estimate see Fig. 4.1). This approximation is known as the Cowling approximation (*Cowling*, 1941; *Dahlen and Tromp*, 1998). In the Cowling approximation, the system of governing equations reduces to two coupled second-order ODEs for $U(r)$ and $V(r)$, since the perturbation in the gravity potential and its related eigenfunction $P(r)$ can be excluded.

Consequently, the approximated system of ODEs is given by:

$$\begin{aligned}
\rho\omega^2 U =& -\partial_r T_U \\
&- [4\rho g r^{-1} - 4(A - N - C^{-1}F^2)r^{-2}]U \\
&+ [k\rho g r^{-1} - 2k(A - N - C^{-1}F^2)r^{-2}]V \\
&- 2(1 - C^{-1}F)r^{-1}T_U + kr^{-1}T_V, \\
\rho\omega^2 V =& -\partial_r T_V \\
&+ [k\rho g r^{-1} - 2k(A - N - C^{-1}F^2)r^{-2}]U \\
&- [2Nr^{-2} - k^2(A - C^{-1}F^2)r^{-2}]V \\
&- kC^{-1}Fr^{-1}T_U - 3r^{-1}T_V.
\end{aligned} \tag{2.4}$$

The tractions $T_U(r)$ and $T_V(r)$ are the same as in the case with full gravity, and the same boundary conditions apply.

The ODE for spheroidal modes with zero angular degree $l = 0$ (radial modes) consists of a single second-order equation involving the radial displacement eigenfunction $U(r)$ only and is given by:

$$\begin{aligned}
\rho\omega^2 U =& -\partial_r T_U \\
&- [4\rho g r^{-1} - 4(A - N - C^{-1}F^2)r^{-2}]U \\
&- 2(1 - C^{-1}F)r^{-1}T_U.
\end{aligned} \tag{2.5}$$

The traction $T_U(r)$ is identical to the one for spheroidal modes with $V(r)$ set to zero. The boundary conditions are again given in table 2.1.

To ignore gravity completely, it is sufficient to set all terms related to gravity to zero in the Cowling approximation. This includes terms involving either the gravity constant G or the gravitational acceleration $g(r)$. This is particularly useful as a means of benchmarking with time-domain methods that do not incorporate the effects of gravity such as *AxiSem* (*Nissen-Meyer et al.*, 2014).

2.2.2 Weak Form

To enable a spectral element formulation, the set of ODEs together with their respective boundary conditions can be transformed from the strong to the weak form. Alternatively, it is also possible to start from the variational principle and vary the action of the respective mode type as shown in *Dahlen and Tromp* (1998, sec. 8.6.4). Interpreting the variation of the eigenfunctions as the test function leads to the weak form. Another possibility is to start from the general three-dimensional (3-D) weak form and use spherical harmonics as Ansatz to derive the radial ODEs as shown by *Al-Attar and Tromp* (2013). Here, we start from the strong form and illustrate the

derivation for the toroidal modes (the weak forms for spheroidal and radial modes can be found in appendix A.2.2).

To derive the weak form, we multiply the strong form with a test function $\tilde{W}$ and integrate over the radial domain, Ω, of the planet. An additional geometric integral kernel r^2 that stems from the volume element is introduced for consistency with the physical normalization and partial integration is applied to achieve a symmetric form. Note that the weak form is equivalent to the strong form if the equation for the weak form is fulfilled for all test functions from an appropriately chosen set.

Writing this step explicitly for the toroidal equation (2.1) gives us:

$$\begin{aligned}
\omega^2 \int_\Omega \rho W \tilde{W} r^2 \,\mathrm{d}r = &- \int_\Omega \partial_r T_W \tilde{W} r^2 \,\mathrm{d}r \\
&+ \int_\Omega N(k^2-2) W \tilde{W} \,\mathrm{d}r \\
&- \int_\Omega 3 r T_W \tilde{W} \,\mathrm{d}r \\
= &- \left[T_W \tilde{W} r^2 \right]_{r_0}^{r_\mathrm{surf}} + \sum_{r \in d} \left[T_W \tilde{W} r^2 \right]_-^+ \\
&+ \int_\Omega T_W (r^2 \partial_r \tilde{W} + 2 r \tilde{W}) \,\mathrm{d}r \\
&+ \int_\Omega N(k^2-2) W \tilde{W} \,\mathrm{d}r \\
&- \int_\Omega 3 r T_W \tilde{W} \,\mathrm{d}r
\end{aligned} \tag{2.6}$$

Boundary terms from integration by parts need to be considered for all internal discontinuities d, at the free surface r_surf and at the core-mantle-boundary or at the center of planets without a liquid core r_0. However, these terms vanish at the center because both $\tilde{W}$ and r are zero here (the same boundary conditions apply to the test function as for the eigenfunctions) and at the free surface or solid fluid boundary, where T_W is zero. At internal discontinuities, the continuity of the eigenfunction W and its related traction T_W ensures that each term appears twice with opposite sign. As a consequence, all boundary conditions are readily implicitly fulfilled. Finally, from the definition of the traction T_W (Eq. 2.2), we arrive at the symmetric weak form:

$$\begin{aligned}
\omega^2 \int_\Omega \rho W \tilde{W} r^2 \,\mathrm{d}r = &\int_\Omega L (r \partial_r W - W)(r \partial_r \tilde{W} - \tilde{W}) \,\mathrm{d}r \\
&+ \int_\Omega N(k^2-2) W \tilde{W} \,\mathrm{d}r.
\end{aligned} \tag{2.7}$$

2.2.3 Discretization

Using the Galerkin method, we approximate the solution for the eigenfunction $W(r)$ by a finite set of basis functions $\psi(r)$:

$$W(r) \approx \sum_i w_i \psi_i(r), \tag{2.8}$$

where w_i are the toroidal expansion coefficients (degrees of freedom). The same basis functions ψ_i are used as test functions in the weak form. Consequently, we end up with the following discrete approximation for the toroidal modes (Eq. 2.7):

$$\begin{aligned}\omega^2 w_j \int_\Omega \rho \psi_i \psi_j \,\mathrm{d}r = w_j \int_\Omega \big[& L(r\partial_r \psi_i - \psi_i)(r\partial_r \psi_j - \psi_j) \\ & + N(k^2 - 2)\psi_i \psi_j \big] \,\mathrm{d}r,\end{aligned} \tag{2.9}$$

where w_j are again the basis coefficients from the expansion of W as in (Eq. 2.8) and summation over repeated indices is implied. Given the basis function, the integrals can be evaluated and the equation can equivalently be written in matrix form. Identifying the terms for the mass matrix $\mathbf{M}$ and stiffness matrix $\mathbf{K}$ for toroidal modes and denoting $\mathbf{w}$ as a vector containing the coefficients w_i, this reads

$$\omega^2 \mathbf{M}\mathbf{w} = \mathbf{K}(l)\mathbf{w}. \tag{2.10}$$

For the spheroidal case, there is the additional complexity that multiple eigenfunctions need to be included in the eigenvector with a well-defined order. We group the three degrees of freedom for each basis function together, such that in the case of full gravity with eigenfunctions $U(r)$, $V(r)$ and $P(r)$, the vector reads $(u_0, v_0, p_0, u_1, v_1, p_1, \ldots)$, where u_i, v_i, and p_i are the spheroidal basis coefficients from the expansion of U, V, and P, respectively.

2.2.4 Spectral Elements

The spectral element method consists of a particular choice of test functions together with a quadrature rule to approximate the integrals of the weak form. The challenge in finding an appropriate set of test functions is to come up with functions that fulfill the boundary conditions at all internal discontinuities, while guaranteeing higher-order convergence of the method to efficiently achieve a high level of accuracy. The first condition is solved by subdividing the domain into N_e subdomains Ω_e called elements, such that the internal discontinuities of the model align with element boundaries. To address the second condition, the solution within each element is expanded in terms of $p+1$ Lagrange polynomials ψ_i^e $(i = 1, ..., p+1)$ of degree p

on the Gauss-Lobatto-Legendre (GLL) points. These points represent the optimal choice for Lagrange interpolation with the first and last point located on the element boundary (e.g. *Igel*, 2017, eq. 7.33). This particular choice coincides with the optimal points for Gauss quadrature that integrate polynomials of degree $2p-1$ exactly. At element boundaries, continuity of the test functions is enforced explicitly as discussed in the following and continuity of traction is implied by the weak form as discussed in the previous section. Given the subdivision of the domain, the integrals over the whole domain in the weak form can be split up into a sum of integrals over all elements. While the integrals could in principal be solved analytically given the test functions, it is common practice to apply a quadrature rule instead. The Gauss quadrature on the GLL points is accurate for polynomials up to degree $2n-1$, while the equations contain terms up to order $2n$. While this implies that the integrals are computed approximately, it is sufficiently accurate to maintain the convergence order of the method (e.g. *Cohen and Pernet*, 2017, p.208). The main benefit of this quadrature is that the mass matrix $\mathbf{M}$ becomes diagonal as the quadrature points are identical to the interpolation points, i.e., the Lagrange basis on the GLL point is orthogonal with respect to the GLL quadrature. The mass matrix induces an inner product in the discrete space equivalent to the integrals in the continuous variational principle, such that the discrete weak form of the equation corresponds to a discrete variational principle. If the mass matrix is diagonal this inner product is particularly simple and all integral quantities derived from perturbation theory in the continuous problem (such as attenuation factors, group velocity) hold exactly in the discrete case if the same quadrature is used to approximate the integral.

To evaluate the integral, each element Ω_e needs to be mapped onto a reference element, which, in the one-dimensional case considered here, is just the interval $[-1, 1]$. This mapping is defined as

$$F_e : [-1, 1] \to \Omega_e, \qquad r = F_e(\xi), \qquad e \in [1, \ldots, N_e]. \tag{2.11}$$

We define the Lagrange polynomials of order p within an element by

$$\ell_i^p(\xi) := \prod_{j \neq i}^{p+1} \frac{\xi - \xi_j}{\xi_i - \xi_j}. \tag{2.12}$$

The element-wise integrals can then be expressed in the reference coordinates ξ and approximated by Gauss quadrature as

$$\int_{\Omega_e} f(r)\,\mathrm{d}r = \int_{-1}^{1} f(\xi) J(\xi)\,\mathrm{d}\xi \approx \sum_{i=1}^{p+1} \sigma_i f(\xi_i) J(\xi). \tag{2.13}$$

where $J(\xi)$ is the Jacobian given by $J(\xi) = \frac{\mathrm{d}r}{\mathrm{d}\xi}$ and the GLL integration weights

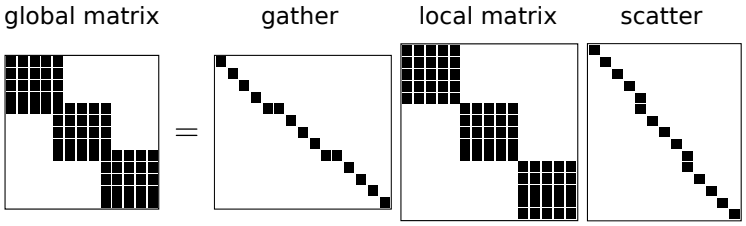

Figure 2.1: Illustration of the local-to-global transformation for DOFs on the boundary of the elements using gather and scatter operators according to (eq. (2.14)). The simplest case is for toroidal modes, where the solution is scalar. For spheroidal modes the solution has multiple DOFs per Gauss-Lobatto-Legendre point, which needs to be reflected in the gather/scatter operators.

are $\sigma_i = \int_{-1}^{1} \ell_i^p(\xi)\,\mathrm{d}\xi$. The derivative of the Lagrange polynomials needed in the discretization of the full equations can readily be derived from the polynomial basis functions.

Requiring continuity of the solution at the element boundaries is simplified by the fact that the GLL points include the boundary. The two DOFs on the boundary of two neighbouring elements correspond to a single global DOF, so no linear system needs to be solved but the mass and stiffness matrices need to be assembled. This can be done in terms of gather and scatter matrices $\mathbf{Q^T}$ and $\mathbf{Q}$ (e.g. *Nissen-Meyer et al.*, 2007): The scatter operator copies elements from global-to-local degrees of freedom, while its transpose, the gather operator, sums up element boundary contributions into the single global DOF.

A global operator $\mathbf{A}$ corresponding to an ODE on the full domain can then be assembled from the element-wise operator $\mathbf{A}_L$ as:

$$\mathbf{A} = \mathbf{Q}^{\mathrm{T}}\mathbf{A}_L\mathbf{Q}. \tag{2.14}$$

In the 1D case, where each element has exactly two neighbours and the DOFs can trivially be indexed by sorting along the radius, the gather and scatter operators take a very simple form. The resulting matrix then is a band matrix where the bandwidth is equal to the size of the blocks in the local operator, i.e., the number of degrees of freedom per element (Fig. 2.1).

Finally, we can write the ODE in terms of a generalized weakly non-linear matrix eigenvalue problem

$$\omega^2\mathbf{M}\mathbf{s} = \mathbf{K}(l,\omega)\mathbf{s}, \tag{2.15}$$

where $\mathbf{K}(l,\omega)$ is the positive definite stiffness matrix that is a function of angular degree l and frequency ω. This is the case when attenuation is taken into account, in which case the material parameters become frequency-dependent (see section 2.3.4 for details). $\mathbf{M}$ is the mass matrix, which is positive semi-definite for the spheroidal equation with full gravity and positive-definite otherwise. The system can be solved numerically for the $\mathbf{M}$-orthonormalized eigenvectors ${}_n\mathbf{s}_l$, where n is the overtone

number and to each of these eigenvectors there exists a corresponding eigenfrequency ${}_n\omega_l$.

2.2.5 Fluid Layers

In fluid layers ($L = N = 0$), the shear traction T_V vanishes and the horizontal displacement V can be computed from the other two degrees of freedom (*Dahlen and Tromp*, 1998, eq. 8.143). However, due to the occurrence of ω^2 in this relation, this replacement would render the eigenvalue problem quadratic. Typically, quadratic eigenvalue problems are transformed to linear problems, doubling the size of the matrices in the process. To avoid this complication, we follow the same approach as *Wiggins* (1976), *Buland and Gilbert* (1984), and *Zábranová et al.* (2017) and keep the same representation of the solution in the fluid as in the elastic part of the domain. If the boundary condition on the solid side of the solid-fluid boundary is correctly set (no horizontal traction, $T_V = 0$) then the eigenvectors are computed correctly both in the fluid and the solid. This boundary condition again corresponds to the natural boundary condition of the weak form of the equations. As a result, it is easily implemented by dropping the explicit condition of continuity of V at the solid-fluid boundary in the gather and scatter operators. The additional degrees of freedom in the fluid are not constrained by the physics and lead to spurious, i.e., unphysical, additional solutions of the discrete system (*Wiggins*, 1976). The spurious modes, how they differ from the undertones discussed by *Buland and Gilbert* (1984) and our filtering technique to remove them from the spectrum will be further discussed in section 2.3.3.

2.3 Numerical Implementation

2.3.1 Overview of the workflow

The schematic workflow for computing complete catalogues of normal modes as implemented in our software `specnm` is shown in Fig. 2.2. In the following, we provide an overview after which we detail the most important steps. The workflow is divided into three main parts:

Firstly, a `set-up stage` generates the mesh based on the `input` 1D model and frequency range, such that each discontinuity in the model aligns with an element boundary and the element size is smaller than a given fraction of the S-wavelength (P-wavelength in the fluid). In the examples shown below, we find that two elements per wavelength with a polynomial order $p = 5$ provides sufficient accuracy. The model parameters are subsequently converted to the transverse isotropic parameters

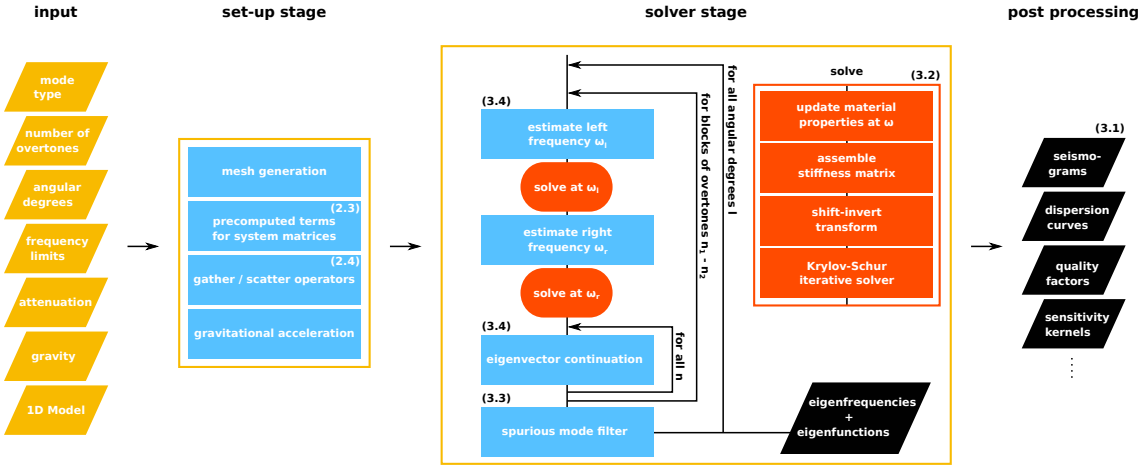

Figure 2.2: Logical flow chart of the `specnm` software as summarized in section 2.3.1. Numbers in parenthesis indicate sections where details of the respective step can be found.

$(A, C, L, N, F$, see e.g. *Dziewonski and Anderson*, 1981), the most general elastic medium with spherical symmetry, and the gravitational acceleration as a function of the radius $g(r)$ is computed from the density profile by numerical integration. Given the discretization and model parameters, the gather and scatter operators, mass matrix, and all terms needed to build the stiffness matrices can be precomputed. As the stiffness matrix is a function of the angular degree and frequency through the material parameters, it is split into terms independent of the angular degree l and the material properties (see Eq. 2.15). Assembly of the full stiffness matrix is then efficiently implemented as a series of sparse matrix operations.

Secondly, a `solver stage` computes the normal mode catalogue by iterating over all angular degrees l and computing all overtones n up to a user-defined frequency $f_{\max}$. If the frequency dependence of the material parameters due to attenuation is ignored, the eigenvalue problem is linear and the eigenpairs can be directly computed (see section 2.3.2). If this is not the case, the stiffness matrix needs to be updated as a function of frequency and we solve the nonlinear problem using eigenvector continuation in an inner loop over overtones (see section 2.3.4). In the spheroidal case with fluid layers, the spurious modes need to be filtered from the mode spectrum (section 2.3.3).

Thirdly, once the eigenfrequencies and eigenfunctions are known, the decay factors $\gamma = \frac{\omega}{2Q}$ (from first order perturbation theory), dispersion curves, sensitivities as well as the displacement $\mathbf{s}(\mathbf{x}, \omega)$ at any location within the planet can be calculated by summation over all angular degrees l and overtones n (*Dahlen and Tromp*, 1998, eq. 10.61) in a `post processing` stage:

$$\mathbf{s}(\mathbf{x}, t) = \sum_{n=0}^{\infty} \sum_{l=0}^{\infty} {}_n\mathbf{A}_l(\mathbf{x})\, {}_n\omega_l^{-2} [1 - \cos({}_n\omega_l t) \exp(-{}_n\gamma_l t)]. \tag{2.16}$$

Here, the amplitude factor ${}_n\mathbf{A}_l$ is computed from the eigenfunctions and a given source location, depth and, moment tensor. For comparison to `MINEOS`, the corrections of the eigenfunctions for the response of a seismometer on Earth's surface need to be included (*Dahlen and Tromp*, 1998, eq. 10.71-72).

2.3.2 Numerical solution of the eigenvalue problem

While small eigenvalue problems can be solved directly via matrix decomposition, it is more efficient to use iterative methods, such as the Lanczos or Arnoldi methods, for large matrices (*Lehoucq et al.*, 1998). This is particularly true for sparse matrices and in case that only a fraction of the eigenvalue spectrum needs to be computed. For the particular matrices in the problem we consider here, we found a modern variation of the Arnoldi method called implicitly restarted Krylov-Schur (*Hernandez et al.*, 2005) to be efficient and reliable.

Iterative eigenvalue solvers converge to eigenvalues successively, starting from the largest. In the normal mode problem, we are interested in small eigenvalues, but not necessarily the smallest because of the presence of undertones (*Buland and Gilbert*, 1984). The undertones for a fixed angular degree l have eigenfrequencies that accumulate at zero with an infinite number of modes below any finite frequency. To select the range of eigenvalues of interest, we apply a shift-invert method and solve the corresponding auxiliary problem in which the eigenvalues of interest are in fact the largest (*Scott*, 1982). Importantly, this method can be applied to the generalized eigenvalue problem with a semi-definite mass matrix, as in the case of spheroidal modes with full gravity.

The auxiliary problem of the shift-invert method is defined as

$$(\mathbf{K} - \sigma\mathbf{M})^{-1}\mathbf{M}\mathbf{s} = \mathbf{C}\mathbf{s} = \mu\mathbf{s}, \tag{2.17}$$

where σ is the shift-value around which the eigenvalues are sought, μ is the eigenvalue of the auxiliary problem and related to the eigenvalue ω^2 of the original problem by

$$\mu = \frac{1}{\omega^2 - \sigma}. \tag{2.18}$$

The eigenvectors remain identical under this transformation.

As $\mathbf{K}$ is banded (see fig.2.1) and $\mathbf{M}$ is diagonal, the inverse can be computed via sparse LU decomposition (*Amestoy et al.*, 2001) and the fill-in is limited to the bandwidth of $\mathbf{K}$. The iterative solution for the eigenvalues hence remains highly efficient under this transformation.

The convergence criterion to accept the eigenvalues from the iterative method is

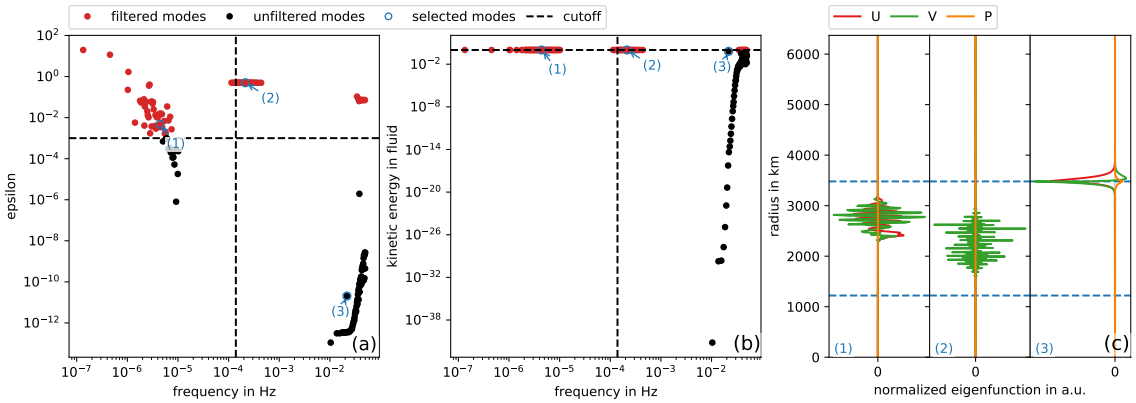

Figure 2.3: Detection of three classes of modes for anisotropic PREM and spheroidal modes with full gravity. In both (a) and (b), the horizontal dashed lines indicate the cutoff Rayleigh quotient epsilon and cutoff kinetic energy in fluid, while the vertical dashed lines show the frequency cutoff used for the filtering of the modes. (a) The Rayleigh quotient filter identifies well-resolved solutions, corresponding to the physical modes of interest and long-wavelength undertones. (b) The normalized fluid kinetic energy is used to separate the modes of interest from undertones and spurious modes. (c) Eigenfunctions of three modes representative of the different classes are labelled (1), (2), and (3) in panels a) and b).

based on the L_2-norm of the residuum vector of the generalized eigenvalue problem

$$\mathbf{r} = (\mathbf{K} - \omega^2\mathbf{M})\mathbf{s} \tag{2.19}$$

scaled by the matrix norms of the mass and stiffness matrices:

$$\epsilon > \|\mathbf{r}\|_2 / \left(\|\mathbf{K}\|_2 + \omega^2\|\mathbf{M}\|_2\right). \tag{2.20}$$

This scaling is crucial as the matrix norms can vary significantly and this choice guarantees consistently small relative errors on the eigenvalues. By default, we conservatively choose $\epsilon = 10^{-12}$, as potential performance gains for larger residuals appear marginal in the cases we consider below. Importantly, this criterion only refers to the discrete problem. An estimation of the error of the eigenvalue for the continuous problem is discussed in the next section.

2.3.3 Spurious modes and undertone filter

Spurious modes have previously been reported in matrix-based approaches in the spheroidal case for planets with fluid layers (*Wiggins*, 1976; *Buland and Gilbert*, 1984; *Zábranová et al.*, 2017). While *Wiggins* (1976) attributed their presence to the overparametrization in the fluid, where only two of the three eigenfunctions are linearly independent, *Buland and Gilbert* (1984) attributed them to under-resolved undertones that can be mapped to higher frequency in the discrete system. Here we will argue that both interpretations are partially valid and that two corresponding distinct additional mode types can be identified.

Undertones occur in fluid layers that are not neutrally stratified, as a consequence of which the Brunt-Väisälä frequency is non-zero (*Dahlen and Tromp*, 1998, section 8.8.11). The dominant forcing for these modes is gravitational and derives from density and buoyancy changes as the material experiences a difference in pressure when displaced vertically. In contrast to modes dominated by elastic forces, these modes have very low eigenfrequencies despite having highly complex eigenfunctions. The maximum frequency of the undertones is bound by the maximum of the Brunt-Väisälä frequency as a function of depth. As a consequence, the undertones violate the typical meshing criterion based on the seismic velocities and may have arbitrarily high errors relative to the corresponding solution of the continuous equation. Importantly, we do not observe this class of solutions in the discrete system when the Cowling approximation is used and $P = 0$, although undertones may in principle still exist. In any case, we do not observe a mapping of the discrete eigenfrequencies of the undertones into the elastic eigenfrequency range, in contrast to earlier suggestions by *Buland and Gilbert* (1984).

A second class of spurious modes can be observed independently of gravity and as there is no correspondence in the continuous solution, the Rayleigh quotient error ϵ (*Takeuchi and Saito*, 1972) is consistently high. These modes overlap with the elastic modes of interest in the spectrum and we identify the modes through the interpretation of *Wiggins* (1976).

Buland and Gilbert (1984) use the fraction of kinetic energy in the fluid as a discriminant for these additional modes $E_{\text{kin}}(\Omega_{\text{fluid}})/E_{\text{kin}}(\Omega)$, where the kinetic energy is given by (*Dahlen and Tromp*, 1998)

$$E_{\text{kin}}(\Omega) = \int_{\Omega} \rho(U^2 + V^2) r^2 \, \mathrm{d}r. \tag{2.21}$$

While this seems appropriate for almost all modes, we nevertheless find that some of the modes belonging to the second class may also include non-zero energy in the elastic part, rendering this criterion by itself unreliable. Instead, we use a combined criterion of Rayleigh quotient error ϵ_{RQ} and fluid kinetic energy together with a minimum frequency (for an early discussion on this see *Valette* (1987)) to separate the three mode types. Thus, if any mode in the frequency range of interest has a high Rayleigh quotient error but a low fluid kinetic energy, the separation fails and mesh refinement or higher a polynomial order is required to ensure that this mode is either well-resolved or correctly identified as spurious.

Importantly, the discrete Rayleigh quotient is exactly what the eigenvalue solver minimizes, so we cannot compute it directly using the mass and stiffness matrices in the same discretization. Instead, we interpolate the eigenfunctions to the next higher polynomial degree and use GLL quadrature to approximate the integrals in

the analytical expressions of the Rayleigh quotient for the anisotropic case (*Dahlen and Tromp*, 1998, eqs. 8.126-130, 8.208). This ensures exactness of quadrature and provides a reliable and efficient estimator for the relative error of the eigenfrequency of the continuous problem as suggested by *Takeuchi and Saito* (1972), which is given by

$$\epsilon_{\mathrm{RQ}} = \frac{1}{2}\left(\frac{E_{\mathrm{pot}}}{\omega^2 E_{\mathrm{kin}}} - 1\right), \tag{2.22}$$

where E_{pot} is the total potential energy and the additional factor $\frac{1}{2}$ is needed to propagate the error from the eigenvalue to the eigenfrequency.

Figure 2.3 shows a comparison of the three mode types and their Rayleigh quotient error ϵ_{RQ} as well as their fluid energy. While the Stoneley mode has a high fluid kinetic energy, it is nonzero also in the elastic part and has a low Rayleigh quotient error. Both the spurious modes and the undertones are concentrated in the fluid and have a high Rayleigh quotient error. The spurious mode, however, has oscillations at the resolution limit, while the physical undertone is significantly smoother.

2.3.4 Attenuation

As a consequence of the Kramers-Kronig relations and causality, attenuation of the elastic waves is directly related to the frequency dependence of the elastic moduli, that is, physical dispersion. This results in a weakly frequency-dependent stiffness matrix and consequently a weakly non-linear eigenvalue problem. Instead of using perturbation theory to only correct the eigenfrequencies and not the eigenfunctions for the frequency-dependence, we follow the same approach as established in `MINEOS` and other codes and include the physical dispersion by evaluating the model parameters at the frequency of the mode. The amplitude decay due to attenuation (i.e., the imaginary part of the eigenfrequency) is thus incorporated in the computation of the seismograms. Although exact methods are available (*Tromp and Dahlen*, 1990), this approximation has proven accurate enough for most applications (e.g. *Dahlen and Tromp*, 1998; *Al-Attar*, 2007, and references therein).

Assuming the quality factors Q to be independent of frequency ω and that the five elastic parameters $\alpha \in \{C, F, N, L, A\}$ are specified at a given frequency ω_0 in the 1D model of interest, the elastic parameters can be evaluated at any frequency ω using the logarithmic relation (*Dahlen and Tromp*, 1998)

$$\alpha(r, \omega) \propto \alpha(r, \omega_0) \ln\left(\frac{\omega}{\omega_0}\right). \tag{2.23}$$

As solvers for non-linear eigenvalue problems are much less developed than for

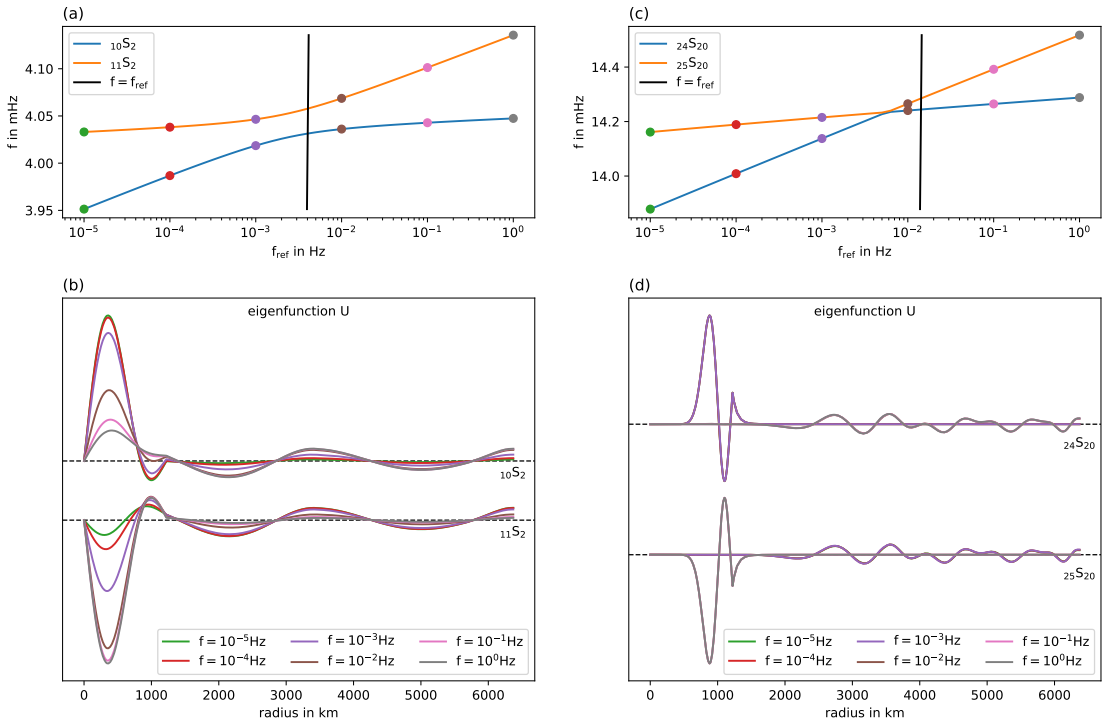

Figure 2.4: Illustration of avoided (subfigures (a) & (b)) and true mode crossings (subfigures (c) & (d)). (a) Avoided crossing of ${}_{10}S_2$ with ${}_{11}S_2$ and (c) true crossing of ${}_{24}S_{20}$ with ${}_{25}S_{20}$ as a function of the reference frequency at which the material properties are evaluated. In the vicinity of an avoided crossing, the radial eigenfunctions U of these spheroidal modes exchange character (b), rendering the perturbation of the eigenfrequencies nonlinear. This is not the case for a true crossing (d).

linear problems and the solutions of the normal mode problem are only weakly non-linear, we adopt a strategy based on linear solvers. This is as an extension of the approach by *Zábranová et al.* (2017), who proposed to solve the full eigenvalue problem at a series of fiducial frequencies and then used interpolation to obtain the eigenfrequencies, eigenfunctions, and attenuation factors of the non-linear problem. As mentioned by *Zábranová et al.* (2017), one problem that arises is the association of the modes between the eigenvalues computed at different reference frequencies for spheroidal modes, related to the observation that some eigenfunctions exhibited a strong dependence on the reference frequency.

We confirm this observation and provide an interpretation in Fig. 2.4. As eigenvalue branches may cross as a function of reference frequency, there are two distinct types of crossings: avoided and true crossings. Avoided crossings or level repulsions are well known for overtone branches as a function of angular degree (*Dahlen and Tromp*, 1998) and have been observed in several studies of normal mode coupling (*Park*, 1986; *Snieder and Sens-Schönfelder*, 2021). In the particular case illustrated in Fig. 2.4, we observe that the eigenvalues of ${}_{10}S_2$ and ${}_{11}S_2$ avoid a crossing close to their eigenfrequencies in PREM. The eigenfunctions overlap and exchange character in the avoided crossing, that is, the eigenfunctions of the two modes are rotated

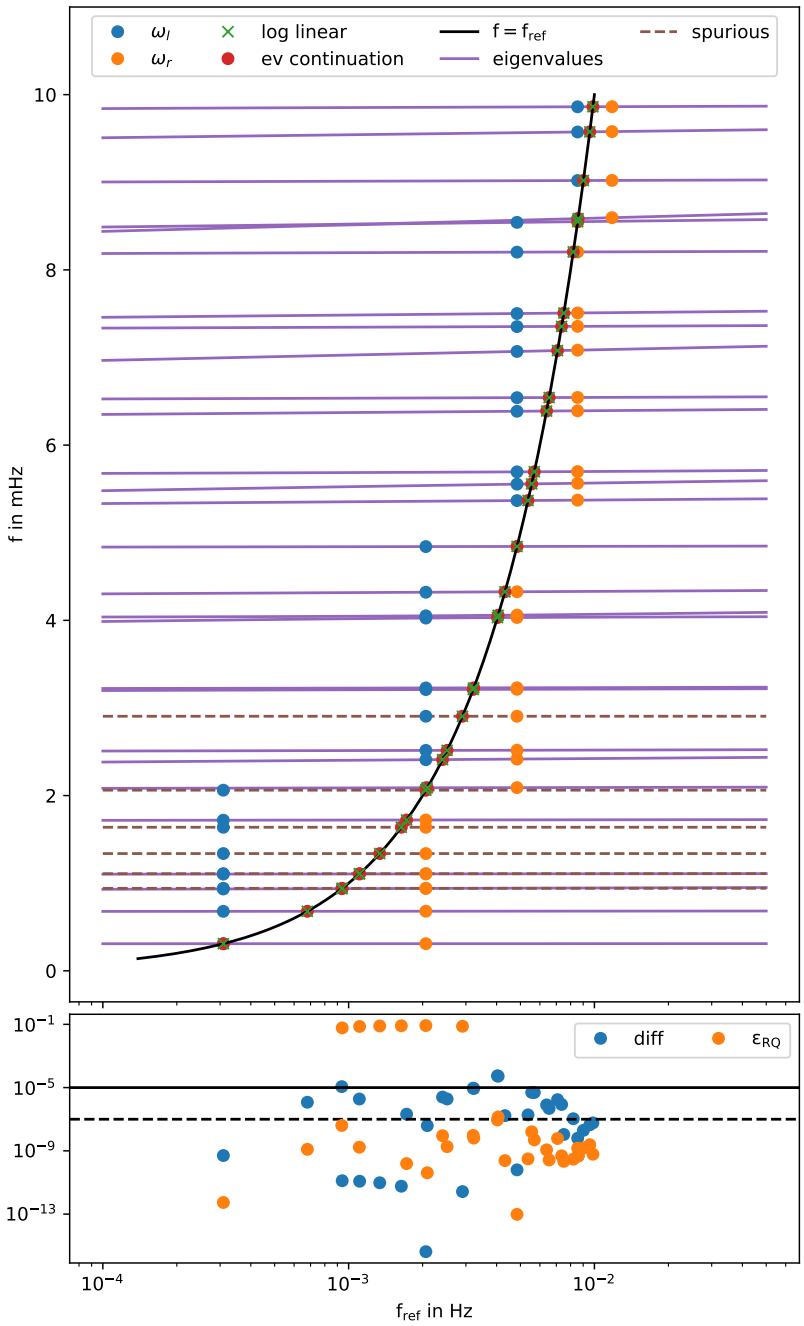

Figure 2.5: Iterative strategy to find the solutions of the non-linear eigenvalue problem for spheroidal modes at angular degree $l = 2$. Firstly, two fiducial frequencies ω_l and ω_r are used to bracket blocks of eigenfrequencies that are shown here in blue and orange. Secondly, log-linear interpolation is applied to update the stiffness matrix that results in the solutions depicted by the green crosses. Lastly, eigenvector continuation improves the accuracy of eigenpairs giving the solution for the modes depicted by the red circles. This solution has a much higher accuracy than the simple solution we get by applying the log-linear interpolation as shown in the bottom panel, which indicates the relative difference between the log-linear interpolation and the final solution in blue and the estimate of the final relative error ϵ_{RQ} of the eigenvalue based on the Rayleigh quotient.

in a two-dimensional subspace. In contrast, the eigenfunctions of ${}_{24}S_{20}$ and ${}_{25}S_{20}$ do not overlap and the eigenvalue branches cross without any interaction. The eigenfunctions switch character from one overtone to the other and the eigenvalues

are log-linear in the reference frequency. In order to achieve a reliable association of branches across discretely sampled reference frequencies as required for interpolation of the eigenfrequencies, a dense sampling is required.

Using the iterative solver with the shift-invert method as described in section 2.3.2 is most efficient if a small number (between 5 and 20) of eigenvalues are computed at once for a fixed reference frequency due to the overhead related to updating the stiffness matrix and computing the inverse for the auxiliary problem. We thus follow the approach illustrated in Fig. 2.5: we first solve the linear problem for a block of eigenfrequencies which is bounded by two fiducial reference frequencies. Importantly, the difference between the two reference frequencies is small, as a result of which the eigenfunctions only change slightly and the aforementioned association problem does not occur. In the next step, we estimate the eigenfrequency of the mode by log-linear interpolation between the fiducial frequencies. As the interpolation has no closed-form solution, we employ numerical root-finding instead of the ad hoc relation proposed by *Zábranová et al.* (2017, eq. 68). Using the resulting approximate eigenfrequency, we update the stiffness matrix and use the eigenfunctions computed at the two fiducial frequencies as a basis in a Rayleigh-Ritz approach (*Dahlen and Tromp*, 1998) to account for the potential non-linearity close to avoided crossings. This idea is also called 'eigenvector continuation' in other fields (e.g. *Frame et al.*, 2018) and we summarize the main steps in the following.

First, the mass and stiffness matrix are projected into the subspace spanned by the two eigenfunctions $\mathbf{s}_l, \mathbf{s}_r$ computed at the fiducial reference frequencies ω_l, ω_r:

$$\mathbf{N} = \begin{pmatrix} \mathbf{s}_l^T \mathbf{M} \mathbf{s}_l & \mathbf{s}_r^T \mathbf{M} \mathbf{s}_l \\ \mathbf{s}_l^T \mathbf{M} \mathbf{s}_r & \mathbf{s}_r^T \mathbf{M} \mathbf{s}_r \end{pmatrix} \tag{2.24}$$

$$\mathbf{H} = \begin{pmatrix} \mathbf{s}_l^T \mathbf{K} \mathbf{s}_l & \mathbf{s}_r^T \mathbf{K} \mathbf{s}_l \\ \mathbf{s}_l^T \mathbf{K} \mathbf{s}_r & \mathbf{s}_r^T \mathbf{K} \mathbf{s}_r \end{pmatrix}, \tag{2.25}$$

The solution of the two-dimensional generalized eigenvalue problem

$$\omega^2 \mathbf{N} \mathbf{v} = \mathbf{H} \mathbf{v} \tag{2.26}$$

then provides the eigenvalue ω^2 and basis coefficients as eigenvector $\mathbf{v}$ to reconstruct the eigenfunction in the original solution space of the spectral elements.

As this method only requires a few sparse matrix-vector products and the solution of a two-dimensional eigenvalue problem, it is computationally cheap. Yet, it improves the accuracy relative to the log-linear interpolation by approximately two orders of magnitude (cf. lower panel in Fig. 2.5). Note that although the spurious modes are well-behaved throughout this process, we include them in the figure here for the purpose of illustration, but always filter them out in a final step.

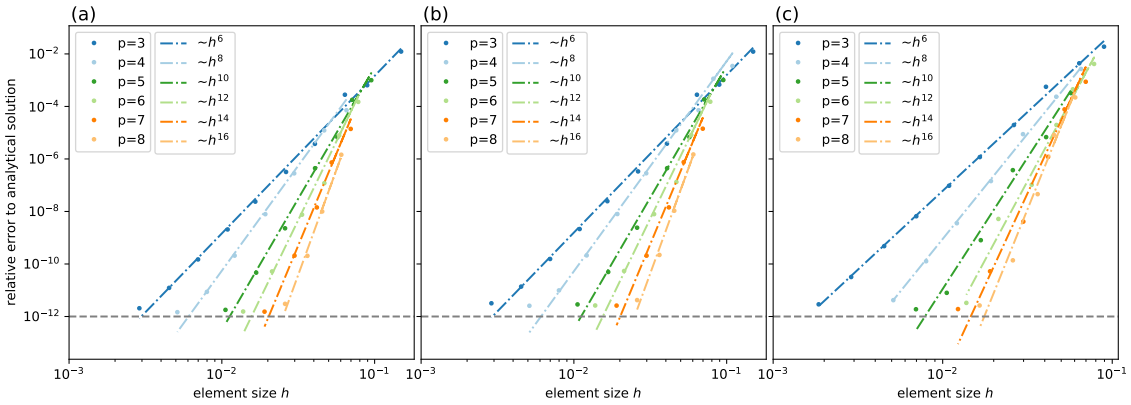

Figure 2.6: Relative error of eigenvalues compared to the analytical solution for the homogeneous sphere for spheroidal modes with (a) full gravity, (b) without gravity, and (c) for toroidal modes. The error is calculated for angular degree $l = 5$, and we show the mean relative error of the first ten overtones $n < 10$ as a function of the element size h. As expected based on theoretical consideration, the eigenvalues converge with order h^{2p}.

2.3.5 Accuracy of the method

One major advantage of the spectral element method is the flexibility in choosing the polynomial degree of the Lagrange basis functions. Higher orders typically result in higher efficiency, particularly if high accuracy of the solution is required. Here, we demonstrate that the theoretically expected convergence rates can also be observed in the numerical solution in comparison to analytical solutions on a homogeneous sphere (*Takeuchi and Saito*, 1972; *Dahlen and Tromp*, 1998).

According to *Babuška and Osborn* (1991), the absolute error in the eigenvalue λ_h calculated on a mesh with element size h is bounded by

$$C_1\|\mathbf{r}\|_2^2 \leq |\lambda_h - \lambda| \leq C_2\|\mathbf{r}\|_2^2, \tag{2.27}$$

where C_1 and C_2 are constants and $\mathbf{r}$ is the residuum of the eigenfunction. $\|\mathbf{r}\|_2$, however, is proportional to h^p, where p is the polynomial degree of the test function (*Cohen and Pernet*, 2017). As a consequence, the eigenvalues λ_h converge with $\mathcal{O}(h^{2p})$ and the same order is expected for the eigenfrequencies $\omega_h = \sqrt{\lambda_h}$, with the relative error offset by a constant factor (0.5). This result is numerically confirmed for spheroidal modes with full gravity, spheroidal modes without gravity and toroidal modes for a homogeneous elastic sphere in Fig. 2.6.

2.4 Benchmark and applications

In the following, we benchmark `specnm` against mode catalogues and seismograms calculated for Earth (PREM *Dziewonski and Anderson*, 1981) using `MINEOS` (*Woodhouse*, 1988; *Masters et al.*, 2011). To further demonstrate the versatility of `specnm`,

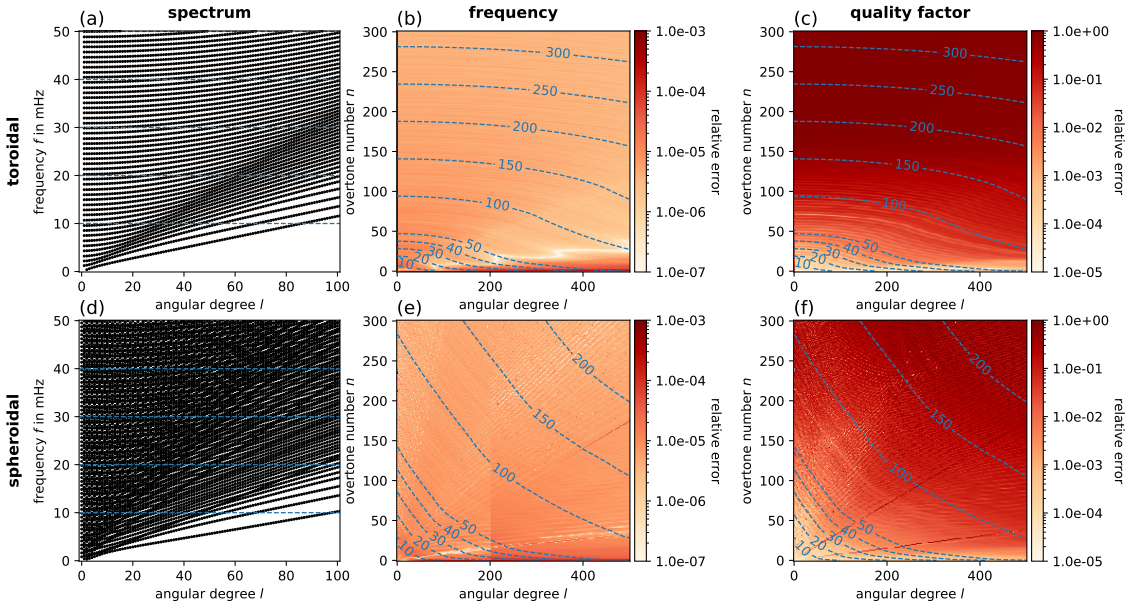

Figure 2.7: Dispersion diagram and comparison of eigenfrequencies and quality factors for toroidal (a–c) and spheroidal (d–f) modes with full gravity computed with `specnm` and `MINEOS`. For the spheroidal case, the Cowling approximation was employed in both codes for $l > 200$ due to stability issues with `MINEOS`. Since we were unable to produce the complete spectrum needed for this comparison with `MINEOS`, we had to bi-linearly interpolate the relative error for a small number of modes (13) in the spectrum. Due to the use of the approximation, the subfigures (e) and (f) show a visible discontinuity at angular degree $l = 200$. The dashed light blue curves indicate isofrequency levels in which the labels are given in mHz.

we apply the method to models of Mars and Jupiter's moon Europa, two planetary objects that differ in structure from the Earth: the former has a purely liquid core (*Stähler et al.*, 2021), whereas the latter consists of a global ice layer that overlies a liquid ocean (*Stähler et al.*, 2018), giving rise to a plethora of interesting seismic phases.

2.4.1 Earth

Mode comparison

Figure 2.7 shows a comparison between the results obtained with `specnm` and `MINEOS` in terms of the eigenfrequencies and quality factors Q for both toroidal and spheroidal modes up to a maximum angular degree $l = 500$ and overtone number $n = 300$, corresponding approximately to eigenfrequencies up to 320 mHz and 230 mHz, respectively.

For the majority of the modes, the relative difference of the eigenfrequencies is below 10^{-4}. Somewhat surprisingly, the relative error is largest for the lowest modes, where the spatial resolution of the spectral element mesh is the highest relative to the complexity of the eigenfunctions. This is most clearly observed for toroidal modes, but is also the case for spheroidal modes. A similar pattern was also observed by

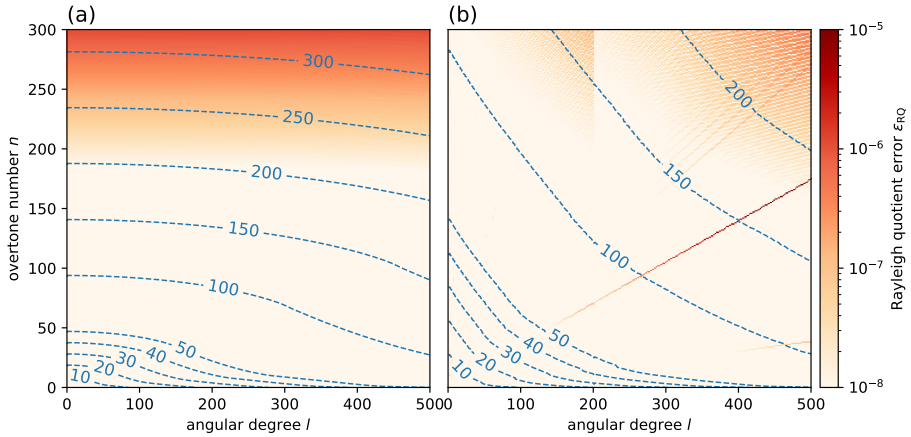

Figure 2.8: Estimate of the eigenfrequency error from the Rayleigh quotient ϵ_{RQ} for (a) toroidal and (b) spheroidal modes in PREM. The calculations were performed with polynomial order 5 and a mesh with two elements per wavelength at the maximum frequency. Due to the use of the Cowling approximation for angular degree of $l > 200$, the subfigure (b) shows a visible discontinuity in the Rayleigh quotient ϵ_{RQ} at angular degree $l = 200$. The dashed light blue curves indicate isofrequency levels in which the labels are given in mHz.

Zábranová et al. (2017) in the comparison of their method to `MINEOS`, and therefore this is unlikely an issue with `specnm`.

The relative difference of the quality factors is approximately below 1% for most modes with eigenfrequencies smaller than 50 mHz, but becomes unacceptably large at higher frequencies, in particular for Stoneley modes at the core-mantle-boundary and the outer-inner core boundary. Again, this was also observed by *Zábranová et al.* (2017). Stoneley modes are known to be particularly challenging for integration methods because of the explicit boundary condition on the free surface, where the eigenfunctions are very close to zero (*Dahlen and Tromp*, 1998). For a verification of our calculation of the attenuation factors independent of other software, we use the linear approximation of the dispersion correction (*Dahlen and Tromp*, 1998, eq. 9.55) and find very good agreement with the non-linear solution if the reference frequency is chosen close to the mode of interest, that is where the linearization is a good approximation (not shown).

An alternative error quantification for the eigenfrequencies is provided by the Rayleigh quotient error $\epsilon_{\mathrm{RQ}}$and shown in Fig. 2.8. Using a polynomial order $p = 5$ and a mesh resolution of two elements per wavelength at the highest frequency, we reliably achieve an error $\epsilon_{\mathrm{RQ}} < 10^{-5}$, which we consider acceptable for most applications. As previously observed by *Zábranová et al.* (2017), the error is largest for the inner-core Stoneley modes, but is more than two orders of magnitude smaller in our work. If higher accuracy is needed for these modes, a mesh refinement around the solid-fluid boundary would be a simple and efficient solution.

In summary, we consider the comparison to `MINEOS` together with the low Rayleigh quotient error and the convergence test in the previous section as a confirmation of

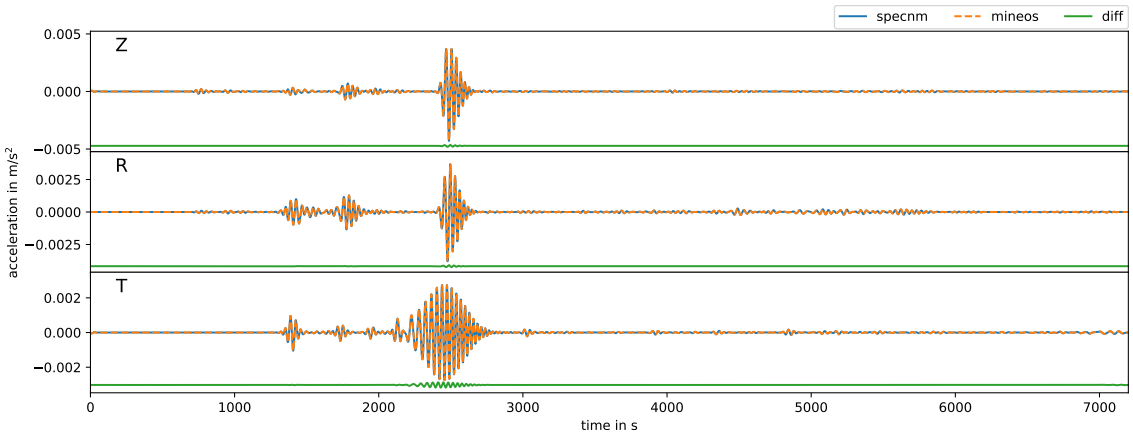

Figure 2.9: Synthetic acceleration seismograms computed for the Tohoku Oki earthquake at the Black Forrest Observatory (BFO) seismic station. Z, R, and T refer to vertical, radial, and transverse component, respectively. The green line indicates the difference between `MINEOS` and `specnm`. All modes up to 40 mHz are included in both `MINEOS` and `specnm`. A low-pass filter was applied at 33.3 mHz.

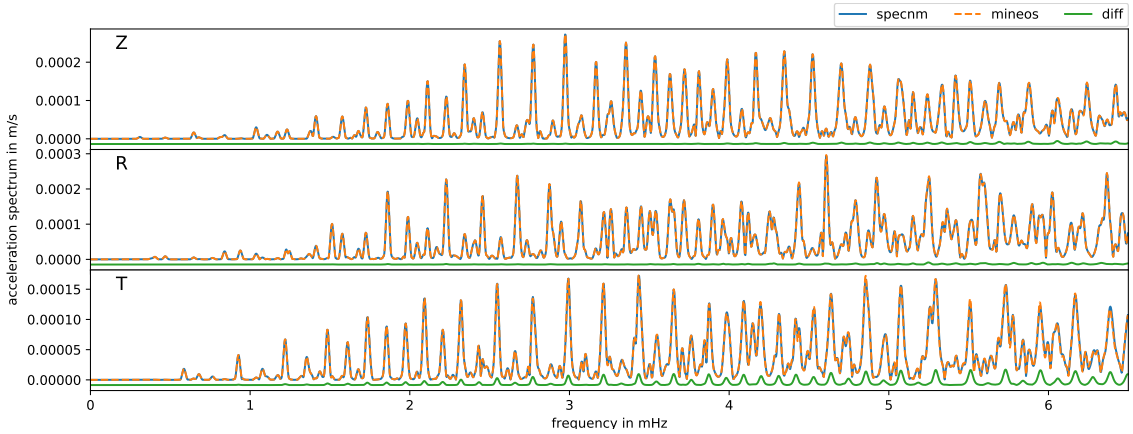

Figure 2.10: Three-component amplitude spectra of the seismic traces shown in Fig. 2.9 computed from a 24-hr time window. Z, R, and T refer to vertical, radial, and transverse component, respectively. The difference (green line) is computed as the absolute value of the difference of the complex spectra and therefore mostly shows phase shifts due to the slight difference in the eigenfrequencies of the fundamental mode and first overtones.

the correctness of our implementation.

Seismogram comparison

Figure 2.9 shows a comparison between seismograms computed with `specnm` and `MINEOS`. We computed all modes up to a maximum frequency of 40 mHz as eigenfrequencies and attenuation factors computed with `specnm` and `MINEOS` agree reasonably well in this range, and `MINEOS` reliably computes all modes with full gravity (which is not the case for higher frequencies). For the computation, we use the centroid solution of the 2011 Tohoku Oki earthquake as source and the black forest observatory (BFO) as representative station. Free air, potential, and tilt corrections to the eigenfunctions are applied before calculating the excitation coefficients for

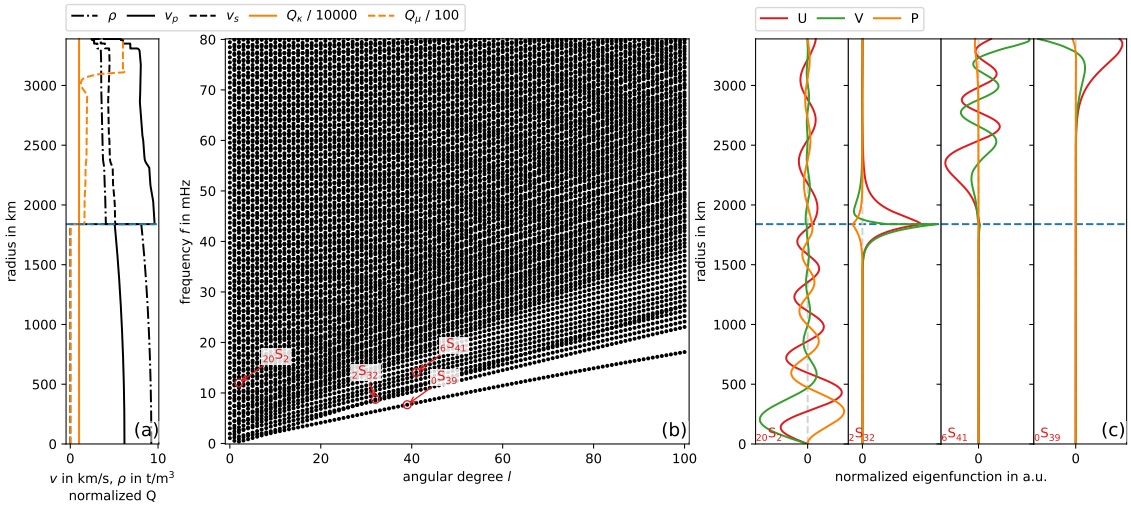

Figure 2.11: Normal mode seismology on Mars. (a) Radially symmetric Mars model. (b) Spheroidal spectrum of modes for Mars using full gravity with fluid core and attenuation. (c) Spheroidal mode eigenfunctions for the modes indicated in (b): ${}_{20}S_2$, ${}_2S_{32}$, ${}_6S_{41}$, ${}_0S_{39}$. See main text for details.

each mode.

The resultant three-component acceleration seismogram for a duration of 2 hr (after the event) is shown in Figure 2.9. The seismograms are low-pass filtered at 33.3 mHz to avoid ringing at the cut-off frequency of the mode catalogues. The difference between `specnm` and `MINEOS` is only a few percent in amplitude relative to the signal, with the largest discrepancy caused by slight phase shifts of the fundamental mode surface waves, as expected from the difference in eigenfrequencies discussed above. We also computed and compared spectra from the seismograms, which are illustrated in Fig. 2.10. The spectra are computed over a time window of 24 hr. The spectra are seen to be commensurate, with the largest difference again occurring on the transverse component, which is dominated by toroidal modes. This provides further evidence for the proper calculation of long-period seismograms.

2.4.2 Mars

Normal mode seismology on Mars has been considered in the context of theoretical and pre-mission (e.g., Viking 1 and 2, Mars 96, InSight) science studies on Mars (e.g. *Bolt and Derr*, 1969; *Okal and Anderson*, 1978; *Gudkova et al.*, 1993; *Lognonné et al.*, 1996; *Zheng et al.*, 2015; *Bissig et al.*, 2018). Presently, Mars' internal structure is informed by recent observations of seismic body wave phases from marsquakes recorded by the InSight lander (*Banerdt et al.*, 2020). The data indicate that Mars consists of a volatile-rich liquid Fe core, an iron-enriched silicate mantle (relative to Earth), and a crust with a thickness in the range 25–45 km (*Knapmeyer-Endrun et al.*, 2021; *Khan et al.*, 2021a; *Stähler et al.*, 2021). In anticipation of the detec-

Table 2.2: Selected fundamental mode periods, phase velocities and group velocities for toroidal and spheroidal modes with full gravity for the Mars model shown in Figure 2.11.

mode	period in s	phase velocity in km/s	group velocity in km/s
${}_0T_2$	1976.3	4.399	6.479
${}_0T_3$	1266.1	4.856	5.594
${}_0T_4$	957.3	4.974	5.205
${}_0T_5$	778.6	4.994	4.974
${}_0T_6$	660.1	4.979	4.827
${}_0T_7$	574.8	4.951	4.730
${}_0T_8$	510.0	4.921	4.665
${}_0T_9$	458.9	4.892	4.618
${}_0T_{10}$	417.5	4.864	4.583
${}_0S_2$	2742.1	3.171	4.348
${}_0S_3$	1721.9	3.570	4.829
${}_0S_4$	1217.4	3.912	5.289
${}_0S_5$	929.2	4.185	5.469
${}_0S_6$	749.6	4.384	5.440
${}_0S_7$	630.6	4.513	5.225
${}_0S_8$	548.5	4.576	4.845
${}_0S_9$	489.9	4.582	4.434
${}_0S_{10}$	446.0	4.553	4.149

tion of normal modes on Mars by InSight, we consider the elastic model shown in Figure 2.11a from (*Stähler et al.*, 2021), augmented with anelastic information from (*Khan et al.*, 2018).

The spheroidal mode spectrum with full gravity is shown in Figure 2.11b and, because of the absence of an inner core and associated inner-core-boundary modes appears less complex relative to Earth's spectrum (Figure 2.7d). However, as the boundary conditions are all implicitly included in the weak form, this poses no additional challenge to `specnm`. For the four modes marked with red circles in Figure 2.11b, we show the corresponding eigenfunctions in Figure 2.11c: ${}_{20}S_2$ is representative of a core-sensitive mode; ${}_2S_{32}$ is a core-mantle boundary (CMB)-sensitive Stoneley mode; ${}_6S_{41}$ is exemplary of a mode that has sensitivity throughout the entire mantle; and ${}_0S_{39}$ is depictive of an upper mantle-sensitive fundamental mode. Finally, we have tabulated the periods of the first ten fundamental spheroidal and toroidal modes, including their group and phase velocities, for the Mars model considered here in Table 2.2.

2.4.3 Europa

Europa is the smallest of the four Galilean moons of Jupiter and of intense interest because of its astrobiological potential (*Vance et al.*, 2018). Direct, spectroscopic, gravity (*Anderson et al.*, 1998), and magnetic field measurements (*Khurana et al.*,

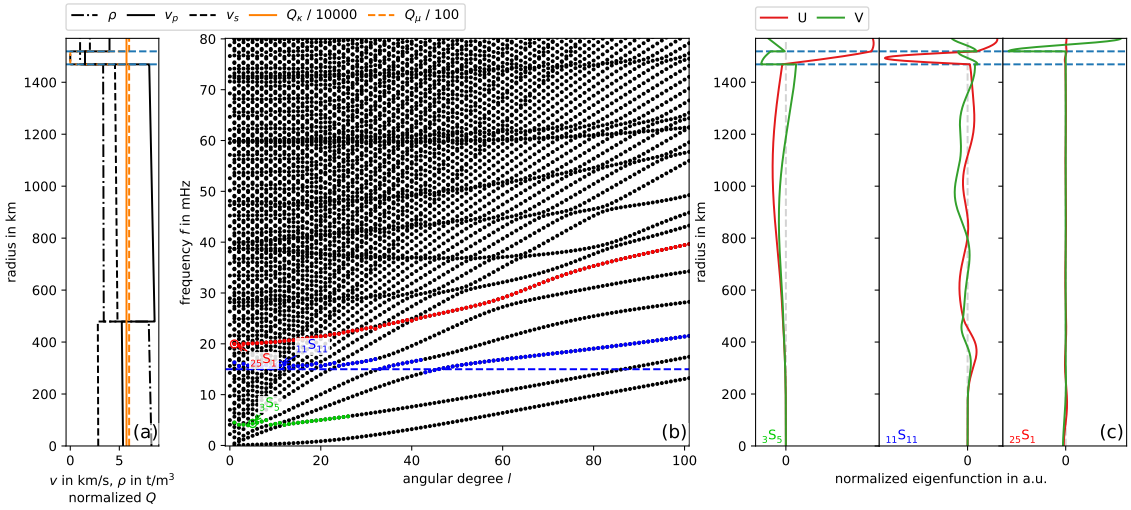

Figure 2.12: Normal mode seismology on Europa. (a) Radially symmetric model of the Jovian moon Europa with 50 km ice thickness over a fluid ocean. (b) Spheroidal mode spectrum based on the Cowling approximation, since the size of the moon is small this is appropriate as gravity forces are small, and using attenuation. The horizontal dotted green, blue, and red points indicate the flexural, ocean resonance, and Crary model pseudo branches, respectively. The blue dashed line indicates the frequency of the vertical fluid resonance branch when approximated as a simple vertical cavity resonator according to Eq. (2.28). (c) Spheroidal mode eigenfunctions for the modes indicated in the (b): $_3S_5$ (flexural mode), $_{11}S_{11}$ (ocean resonance mode), $_{25}S_1$ (Crary mode). See main text for details.

1998) suggest that Europa is covered by a global layer of ice lying over an ocean of liquid water. There is evidence, based on an approximate surface age of 10 Myr (*Zahnle et al.*, 1998), that geothermal sources and tidal heating is keeping the ocean from freezing. For the calculations performed here, we rely on a modified version of the interior structure model of (*Panning et al.*, 2017). The model, which is shown in Figure 2.12a, consists of a 50 km thick ice layer atop a 50 km thick water layer. The mantle consists of rocky silicate material, whereas the core is considered to be Fe-rich and solid.

A planetary body with a decoupled ice-covered surface is, from a seismic perspective, an interesting object because it gives rise to evanescent seismic phases that predominantly excite the ice sheet. These seismic phases are called Crary and flexural waves (*Crary*, 1954). Crary waves are resonant SV-waves in the ice sheet produced by multiple reflections at the boundaries. Hence, their resonance frequency depends strongly on the thickness of the ice sheet. Flexural waves are a predominantly vertical motion of the ice as a whole. Consequently, studying the interior of Europa is probably best undertaken through detection and analysis of seismic surface waves (*Kovach and Chyba*, 2001; *Panning et al.*, 2006).

Because of the small mass of the moon, there is little difference in normal mode spectra between full gravity and Cowling. Hence, we employ the Cowling approximation for the computations performed here. Resultant low-frequency spheroidal modes for Europa are shown in Figure 2.12b, up to a frequency of 80 mHz and an

angular degree of 100.

In contrast to the terrestrial and Martian spectra shown earlier, Europa modes also include flexural and Crary modes that are exemplary of modes that are trapped in the ice sheet. For the three modes marked in green, blue, and red in Figure 2.12b, we show the corresponding eigenfunctions in Figure 2.12c: ${}_3\mathrm{S}_5$ represents a flexural mode; ${}_{11}\mathrm{S}_{11}$ illustrates an ocean resonance mode; while ${}_{25}\mathrm{S}_1$ indicates a Crary mode. We further identify flexural (green dotted lines), water resonance (blue dotted lines), and Crary (red dotted line) pseudo-branches.

The fundamental flexural pseudo-branch (green dotted line) in the spectrum shows a similar structure as the Crary pseudo-branch. We also identify a vertical fluid resonance branch (blue dotted line). The frequency f of this vertical fluid resonance branch can, assuming a simple vertical cavity resonator, be approximately estimated from

$$f(\tilde{n}) = \frac{(\tilde{n}+1)\mathrm{V_P}}{2d}, \tag{2.28}$$

where $\tilde{n}$ is the mode number and d is ocean thickness. For the case of a 50-km thick fluid layer and a P-wave velocity of $\mathrm{V_P}$=1.5 km/s, a frequency $f = 15.0$ mHz is obtained for $\tilde{n}$=0, which is indicated by the horizontal blue dashed line in Figure 2.12b. This value is seen to be in good agreement with the value obtained from superposition of the vertical fluid resonance branch (blue dotted line). Generally, the various branches do not follow the overtone branches strictly, but at times instead consist of multiple overtones, which in superposition will give rise to flexural, vertical fluid resonance, and Crary phases in a seismogram.

2.5 Discussion & Conclusion

In this work we have employed the spectral element method to build the software package `specnm` for the generation of normal mode spectra of spherically symmetric bodies. One of the main motivations for this approach was to avoid the potentially unstable mode counting based on zero crossings of the characteristic function (*Woodhouse*, 1988) that is required in classical methods to ensure all eigenfrequencies are found. While we succeeded in this goal, the eigenfunctions are computed directly in the matrix-based approach and not as a linear combination of fundamental solutions. The characteristic function, computed from the fundamental solutions and used for mode counting, is therefore not accessible. As a potential drawback, the overtone number of a given mode can thus not be obtained from the mode itself, but only indirectly from its location in the spectrum.

Nevertheless, we are confident that the versatility, simplicity, and accuracy of `specnm`, it is of benefit to the community and we publish it alongside this study in

open source format.

Future developments in normal mode seismology will include the development of 3-D long-period numerical time simulations, in which `specnm` may be used as a tool for setting limits on the frequency range for which a full gravity implementation will be needed (*van Driel et al.*, 2021).

Chapter 3

Self-consistent models of Earth's mantle and core from long-period seismic and tidal constraints

This chapter is submitted to Geophysical Journal International, as *Self-consistent models of Earth's mantle and core from long-period seismic and tidal constraints*, J. Kemper, A. Khan, G. Helffrich, M. van Driel, D. Giardini.

3.1 Introduction

The structure of Earth's crust, mantle, and core holds clues to its thermal state and chemical composition, and, in turn, its origin and evolution (e.g., *Drake and Righter*, 2002; *Khan et al.*, 2008; *Javoy et al.*, 2010). While the radial and lateral seismic structure of the Earth continues to be imaged at increasing resolution (e.g., *Ritsema et al.*, 2004; *French and Romanowicz*, 2014; *Moulik and Ekström*, 2016), applying the information provided by seismic tomography images in a geodynamical sense has proved complicated due to lack of direct sensitivity of seismic data to the density contrasts that drive mantle flow (e.g., *Hager et al.*, 1985; *Ishii and Tromp*, 1999; *van Gerven et al.*, 2004; *Tapley et al.*, 2005; *Moucha et al.*, 2007; *Khan et al.*, 2013; *Moulik and Ekström*, 2016). In this context, the density distribution of Earth's core plays a prominent role for understanding the generation of Earth's magnetic field, through its impact on the density contrast at the inner-core boundary that governs and maintains the geodynamo (e.g., *Loper*, 1978; *Gubbins et al.*, 1979).

The radial density structure of the Earth has principally been determined using normal mode, body wave, and geodetic constraints in the form of mass and moment of inertia (*Dziewonski and Anderson*, 1981; *Montagner and Kennett*, 1996) that were connected in the core and lower mantle through application of the Adams-Williamson equation-of-state (*Williamson and Adams*, 1923). The equations of Adams-Williamson, which assume stable stratification within mantle and core, provided the basis for establishing Earth's density profile through the nature of the temperature gradients in the mantle which influence the balance between the pres-

sure derivative of density and bulk sound speed.

While the preliminary reference Earth model (PREM) of *Dziewonski and Anderson* (1981) is still widely employed as reference for the average P- and S-wave velocity and density of Earth's mantle and core, a number of normal-mode studies have noted differences in the radial velocity and density distribution of the Earth relative to PREM (e.g., *Kennett*, 1998; *Resovsky and Trampert*, 2002, 2003; *Masters and Gubbins*, 2003; *Deuss*, 2008; *de Wit et al.*, 2014; *Irving et al.*, 2018; *Robson and Romanowicz*, 2019; *van Tent et al.*, 2020). These differences principally emanate from the increase in quantity and quality of normal-mode observations since the development of PREM as illustrated with the modern-day catalogue of *Deuss et al.* (2013). To the observational advances should be added theoretically- and numerically-driven improvements that have allowed for more accurate modeling of e.g., mode-splitting and -coupling resulting from lateral variations in structure (*Al-Attar et al.*, 2012; *Akbarashrafi et al.*, 2018) and through the use of novel spectral element-based modeling methods (*Afanasiev et al.*, 2019; *Kemper et al.*, 2021).

Relying on a larger normal-mode data set, *Irving et al.* (2018), for example, found a denser profile and a steeper velocity gradient in the outer core relative to PREM. Like PREM, the Bullen parameter (η) for the outer core model of *Irving et al.* (2018) is approximately 1, i.e., near-homogeneous and adiabatic, and is described by a set of physical parameters that provides a natural link between P-wave velocity and density without recourse to specific mixtures of elements. While the observation of *Irving et al.* (2018) of an overall denser outer core is potentially important inasmuch as it would point to a core composition with a different light element budget than currently predicted based on PREM (e.g., *Hirose et al.*, 2021), it was predicated on mantle and inner core being fixed to PREM and therefore *sensu stricto* incompatible with Earth's observed mass and moment of inertia. Similarly, *Robson and Romanowicz* (2019), using core sensitive modes, found variations in bulk S-wave velocity ($<$1%) and density ($\sim$1–2%) of the inner core relative to PREM, but did not study the impact on mass and moment of inertia because of the negligible influence of the inner core on these parameters.

As shown by the attenuation of seismic body waves, normal modes, and body tides, the Earth responds anelastically to excitations from earthquakes or the periodic forcing resulting from lunar and solar attraction. The anelastic behaviour of the materials that make up the planets is in turn governed by microscopic-scale dissipation processes that result in dissipation occurring almost entirely in shear, while dissipation associated with volume changes, i.e., in bulk, appears, for most purposes, to be negligible. To account for the attenuation behaviour of Earth, different mechanisms have been proposed that are based on observational, theoretical, and laboratory studies (e.g., *Liu et al.*, 1976; *Anderson and Minster*, 1979; *Karato*

and Spetzler, 1990; *Jackson and Faul*, 2010; *Takei et al.*, 2014; *Romanowicz and Mitchell*, 2015; *Ivins et al.*, 2021).

Conceptually, attenuation is represented by the quality factor Q, whose frequency (ω) dependence is expressed as $1/Q(\omega) \propto \omega^{-\alpha}$, where α is the frequency exponent. This relationship indicates that dissipation $1/Q$ increases (Q becomes smaller) with decreasing frequency as observed in going from high-frequency body waves ($\sim$1 s) over surface waves ($\sim$100 s) to normal modes ($\sim$1 hr), which formed the basis for the absorption band model of e.g., *Anderson and Minster* (1979) and *Anderson and Given* (1982). The value of α is less well-resolved, but, based on seismic, geodetic, and laboratory measurements, is constrained to range between 0.1 and 0.4 (*Anderson and Minster*, 1979; *Jackson and Faul*, 2010; *Bagheri et al.*, 2019; *Lau and Faul*, 2019).

To describe the attenuation behavior of planetary materials, several rheological models are available (e.g., Andrade, Burgers, Sundberg-Cooper, and the power-law approximation scheme) that have been studied experimentally using torsional forced-oscillations of anhydrous melt-free grains at pressure-temperature conditions equivalent of the upper mantle (e.g., *Gribb and Cooper*, 1998; *Jackson et al.*, 2002; *Sundberg and Cooper*, 2010; *Jackson and Faul*, 2010; *Takei et al.*, 2014; *Qu et al.*, 2021). These rheological models are able to describe the transition from (anharmonic) elasticity to grain size-sensitive visco-elastic behavior and because of their greater flexibility have resulted in considerable improvement in matching the observed frequency dependence of dissipation (*Havlin et al.*, 2021), in addition to simultaneously fitting attenuation-related data that span a frequency-range from 1 s to $\sim$10 yrs (*Lau and Faul*, 2019; *Bagheri et al.*, 2019) and beyond (*Lau et al.*, 2021).

Here we build upon our previous work that relies on a general-purpose geophysical inverse framework to infer anelastic properties of planets across different timescales (e.g., *Khan et al.*, 2018; *Bagheri et al.*, 2019) from geophysical data. For this purpose, we combine an experimentally constrained grain size-, temperature-, and frequency-dependent visco-elastic model with a geophysical parameterization for the mantle that relies on a unified description of phase equilibria, seismic properties, and thermochemical parameters (e.g., *Connolly*, 2009), whereas the core is parameterised using a physical equation-of-state following the work of *Irving et al.* (2018) for the outer core and *Davies and Dziewonski* (1975) for the inner core. This set-up ensures self-consistently-built models and computation of geophysical responses for quantitative comparison to observations. Moreover, the approach anchors internal structure parameters that are in laboratory-based models, while geophysical inverse methods are simultaneously employed to optimize profiles of seismic wave speeds, attenuation, and density to match a set of geophysical observations.

From an observational point of view, we rely on the larger modern catalog of nor-

mal mode centre-frequency and attenuation measurements of radial, toroidal, and spheroidal modes that have become available over the last two decades (e.g., *Masters and Widmer*, 1995; *Resovsky and Ritzwoller*, 1998; *Deuss et al.*, 2013; *Koelemeijer et al.*, 2013; *Schneider and Deuss*, 2020; *Talavera-Soza and Deuss*, 2020), but also include the higher-frequency fundamental spheroidal modes of (*Dziewonski and Anderson*, 1981). To avoid stepping beyond the self-consistent parameterisation, however, we obviate a joint consideration of higher-frequency fundamental spheroidal and toroidal normal-mode data that are strongly sensitive to lithospheric structure, which would otherwise require introduction of anisotropy-related parameters (see e.g., *Khan et al.*, 2011). In addition to the normal-mode data, we also consider the tidal response in the form of the Love numbers and phase lags, including the prediction of the tidal response of the Earth at very long periods, as well as mean mass and moment of inertia, to construct radial models of Earth's anelastic and density structure. This represents an extension of previous work that was tied to radial Earth models (e.g., *Irving et al.*, 2018; *Lau and Faul*, 2019) and the consideration of geophysical data at either seismic (e.g., *Lekić et al.*, 2009; *Bellis and Holtzman*, 2014; *Abers et al.*, 2014) or tidal periods (e.g., *Benjamin et al.*, 2006) that appeared to result in a discrepant view of the attenuation behaviour of the mantle.

In what follows, we briefly describe the normal mode, tidal, and geophysical constraints that are employed to infer the elastic and anelastic properties of the Earth (section 2); section 3 describes the computation of crust, mantle, and core properties; section 4 considers the inverse problem posited here; and, finally, in section 5, we present and discuss results.

3.2 Data

3.2.1 Normal mode catalogue

We consider spheroidal and toroidal normal-mode centre frequencies and quality factors up to 10 mHz. The advantage of employing normal-mode centre frequencies over body waves are twofold: 1) the former are less prone to be biased by the limitations imposed by the geographical source-station distribution, on account of their sensitivity to the average structure and close-to-uniform sampling of the globe (e.g., *Giardini et al.*, 1988; *Dziewonski and Romanowicz*, 2015), and 2) normal-mode centre frequencies are, unlike high-frequency body waves, sensitive to density (e.g., *Ishii and Tromp*, 1999; *Masters and Gubbins*, 2003; *Irving et al.*, 2018).

We employ a total of 403 spheroidal central frequencies, 201 spheroidal quality factors, 145 toroidal central frequencies, and 37 toroidal quality factors based on the observations of *Dziewonski and Anderson* (1981); *Masters and Widmer* (1995);

Resovsky and Ritzwoller (1998); *Deuss et al.* (2013); *Mäkinen and Deuss* (2013); *Talavera-Soza and Deuss* (2020); *Schneider and Deuss* (2020). Depending on the sensitivity, the spheroidal data can be further sub-divided (see section 3.2.1).

The normal-mode center-frequency data sets have been considered in a number of recent studies of Earth's lower mantle and outer- and inner-core structure (e.g., *Irving et al.*, 2018; *Robson and Romanowicz*, 2019; *van Tent et al.*, 2020). As discussed in *van Tent et al.* (2020), the centre-frequencies account for the effect of either self- or group-coupling, i.e., the normal-mode data have been corrected for the effect of three-dimensional structure, which allows for a spherically-symmetric treatment. While we include higher-frequency fundamental spheroidal modes (up to ∼10 mHz) from the PREM catalog to better constrain crust and lithospheric structure, we abstained from using higher-frequency fundamental toroidal modes to enable an isotropic treatment throughout (see section 3.5.2 and Appendix A.4). Finally, we eliminated CMB Stoneley modes from our data set as a full-coupling approach is required for proper treatment (*Robson et al.*, 2022).

Normal-mode clustering

To better identify which parts of the elastic model are sensed by the various modes, we computed synthetic normal modes using `specnm` (*Kemper et al.*, 2021) for isotropic PREM (*Dziewonski and Anderson*, 1981) up to 10 mHz and calculate the kinetic energy of each individual mode (*Dahlen and Tromp*, 1998):

$$E_{\text{kin}}(\Omega) = \int_{\Omega} \rho(U^2 + V^2) r^2 \, \mathrm{d}r. \tag{3.1}$$

We colour-coded the modes according to the region where most of the kinetic energy is concentrated. This is illustrated for a set of spheroidal mode eigenfunctions in Figure 3.1a. To cluster all synthetic modes (coloured circles in Figure 3.1b), we employ the KMeans algorithm as implemented in `scikit-learn` (*Pedregosa et al.*, 2011). Following the elbow method to select the number of clusters based on the sum of the squared errors for different cluster sizes, we chose six clusters to group the observed spheroidal normal modes (open circles in Figure 3.1b) (See supplementary section S5). This clustering scheme is used to label all of the observed spheroidal modes with the exception of the full-planet and inner-core modes that are combined into a single cluster. The normal-mode data sets are compiled in Table 3.1.

3.2.2 Tidal and astronomic-geodetic constraints

To constrain Earth's anelastic structure at frequencies beyond the normal modes, we employ body tide observations in the form of the degree-2 Love numbers k_2 and h_2

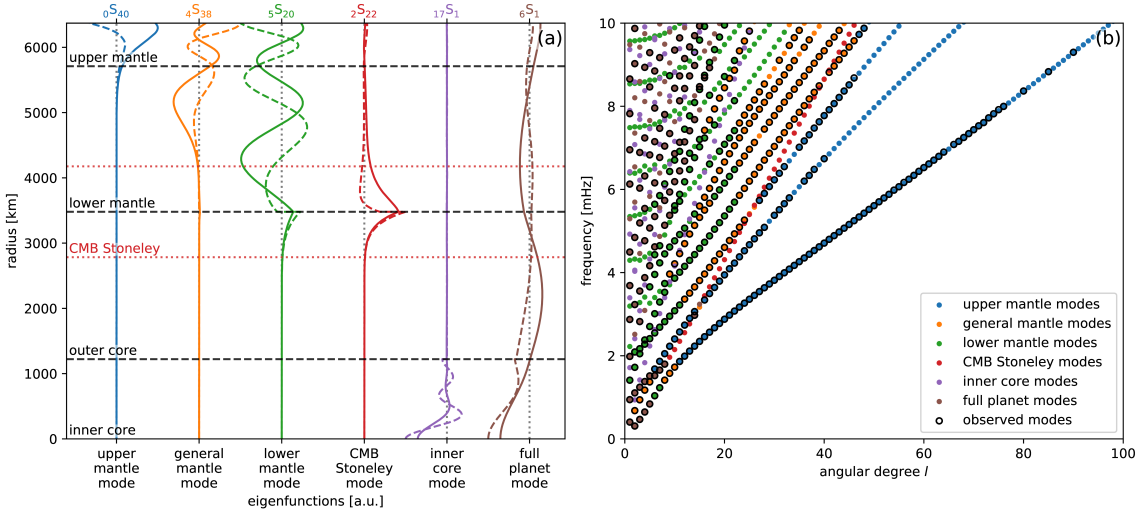

Figure 3.1: Spheroidal mode eigenfunctions and spectrum. (a) Examples of radial eigenfunctions U (solid lines) and V (dashed lines) for the six mode clusters that are defined by the radial location of the main part of the kinetic energy. (b) Spheroidal spectrum (angular order–frequency plot) depicting the clusters of synthetic modes computed using PREM (coloured circles) and the collection of observed spheroidal modes employed in this study (compiled in Tables S1–S15). Note that core-mantle-boundary (CMB) Stoneley modes, while shown here, are not considered in the inversion.

Table 3.1: Compilation of normal mode data, clustering, and sources: [MW] *Masters and Widmer* (1995); [RS] *Resovsky and Ritzwoller* (1998); [DE] *Deuss et al.* (2013); [MAE] *Mäkinen and Deuss* (2013); [TA] *Talavera-Soza and Deuss* (2020); [SND] *Schneider and Deuss* (2020); [PREM] *Dziewonski and Anderson* (1981). Tables A.2–A.15 are provided in the supplementary material.

Type	Center frequencies	Quality factors	Tables	Source
Spheroidal modes:				
upper mantle	118	55	A.2–A.4	[MW,RS,DE,PREM]
general mantle	114	25	A.5–A.7	[MW,RS,DE]
lower mantle	92	50	A.8–A.9	[MW,DE]
full planet and inner core	79	71	A.10–A.11	[MW,DE,MAE,TA]
Toroidal modes:				
mantle	145	37	A.13–A.15	[MW,RS,SND]

Table 3.2: Tidal and astronomic-geodetic observations, and sources: [A] *Jagoda et al.* (2018); [B] *Špičáková et al.* (2009); [C] *Ray et al.* (2001); [D] *Benjamin et al.* (2006); [E] *Dziewonski and Anderson* (1981); [F] *Chambat and Valette* (2001); [G] *Marchenko and Schwintzer* (2003). MoI refers to moment of inertia.

Parameter	Period	Observation$\pm\sigma$	Source
Tidal response k_2	12 h	0.3013 ± 0.0001	[A]
Tidal response h_2	12 h	0.6184 ± 0.007	[B]
Tidal attenuation Q_2^{M2}	12 h	295 ± 65	[C]
Tidal attenuation $Q_2^{18.6\mathrm{yr}}$	18.6 yr	37 ± 23	[D]
Radius R (km)	–	6371	[E]
Mean mass M ($\times 10^{24}$ kg)	–	5.9733 ± 0.009	[F]
Mean normalised MoI I/MR^2	–	0.32997884 ± 0.00000032	[G]

corresponding to the "M2" harmonic with a period of ∼12 h that are measured by the LAGEOS satellite laser ranging system (*Jagoda and Rutkowska*, 2013; *Jagoda et al.*, 2018). As concerns the associated tidal quality factor, labelled Q_2^{M2}, we employ measurements of Earth's body tide energy dissipation from satellite tracking and altimetry as described in *Ray et al.* (2001). To constrain the dissipation behaviour at very long periods, we consider the 18.6 yr tidal harmonic of *Benjamin et al.* (2006) ($Q_2^{18.6\mathrm{yr}}$). Finally, as a further means of constraining Earth's density profile, we also invert mean mass and normalized moment of inertia (*Chambat and Valette*, 2001; *Marchenko and Schwintzer*, 2003). The tidal and astronomic-geodetic data are compiled in Table 3.2.

3.3 Methods

3.3.1 Crust and mantle model

We model the crust as a stack of two layers of variable thickness and seismic parameters (V_P, V_S, and ρ) but exclude a global ocean layer. P-wave velocities and density are obtained by variable, but depth-independent scaling factors to S-wave velocity.

Mantle composition is characterized by a single variable that represents the weight fraction of basalt in a basalt-harzburgite mixture. For a given basalt fraction f the mantle composition $\mathbf{X}$ within the model chemical system Na_2O-CaO-FeO-MgO-Al_2O_3-SiO_2 (NaCFMAS) is computed from

$$\mathbf{X} = f\mathbf{X}_{\mathrm{B}} + (1-f)\mathbf{X}_{\mathrm{H}}, \tag{3.2}$$

where $\mathbf{X}_{\mathrm{B}}$ and $\mathbf{X}_{\mathrm{H}}$ are NaCFMAS basalt and harzburgite end-member model compositions, respectively (Table 3.3). This model is based on the observation that basaltic

Table 3.3: Model End-Member Bulk Compositions (in wt%). From *Khan et al.* (2009).

Component	MORB $\mathbf{X}_\mathrm{B}$	Harzburgite $\mathbf{X}_\mathrm{H}$
CaO	13.05	0.5
FeO	7.68	7.83
MgO	10.49	46.36
Al_2O_3	16.08	0.65
SiO_2	50.39	43.64
Na_2O	1.87	0.01

crust is generated at oceanic ridges through partial melting (e.g., *Ringwood*, 1975), leaving behind its depleted complement harzburgite, while at subduction zones, the physically and chemically stratified lithosphere is continuously being recycled back into the mantle, where it is continuously being remixed. This model accounts for more than 98% of the mass of Earth's mantle (e.g., *Irifune* (1994)) and a plethora of geophysical observations (e.g., *Xu et al.*, 2008; *Khan et al.*, 2009; *Ritsema et al.*, 2009; *Munch et al.*, 2020; *Bissig et al.*, 2021). In the present work, we parameterise the composition of the mantle as consisting of two entities, i.e., upper and lower mantle, corresponding to two variable basalt fractions. This choice reflects a certain parsimony in that we seek the parameterisation with the least number of parameters capable of matching data. The equilibrium mineralogy for this compositional model is computed as a function of pressure (P), temperature (T), and composition (X) by free energy minimization (*Connolly*, 2009) using the thermodynamic formulation of *Stixrude and Lithgow-Bertelloni* (2005a) with parameters as in *Stixrude and Lithgow-Bertelloni* (2011). We adopt the equilibrium assumption in this work on account of the averaging properties of the normal-mode centre frequencies. Isotropic bulk elastic moduli and densities are computed by Voigt-Reuss-Hill averaging from the individual minerals obtained by the free energy minimization procedure. This procedure allows for self-consistent computation of all seismic discontinuities, including the '410', '660', and the post-perovskite transition around 2700 km depth, as a function of X, P, and T.

Within the crust and lithosphere, temperature is computed by assuming a conductive geothermal gradient, which is anchored at the surface by a fixed temperature (0 °C) and at the bottom of the lithosphere (of variable thickness $\mathrm{Z_{lit}}$) by a variable temperature ($\mathrm{T_{lit}}$), while the sub-lithospheric mantle adiabat is defined by the entropy of the lithology at the base of the lithosphere as illustrated in Figure 3.2. The exact nature of the conductive geotherm is less important, since crustal structure is parameterised using variable seismic parameters. To obtain the mantle pressure profile, we integrate the vertical load from the surface pressure boundary condition.

Density and elastic moduli in this approach are found to be accurate to within ∼0.5% and ∼1–2%, respectively, relative to a radial reference model based on a

homogeneous mantle made of pyrolite and a sublithospheric mantle adiabat defined by the entropy of the lithology at the base of lithosphere corresponding to a temperature of 1300 °C at 100 km depth (*Connolly and Khan*, 2016). Finally, to allow for an improved fit to the higher-frequency fundamental spheroidal modes, we scaled S-wave velocity to PREM in the upper 120 km of the lithosphere through $|V_S - V_S^{\mathrm{PREM}}| \times 0.9 + V_S^{\mathrm{PREM}}$, where V_S and V_S^{PREM} are the thermodynamically-computed and isotropic PREM S-wave velocities, respectively. All parameters required to define the crust and mantle model are listed in Table 3.4.

3.3.2 Mantle attenuation

The response of a material to forcing consists of an instantaneous elastic response followed by a semi-recoverable transient regime that finally yields to steady-state creep. The general form of the time-dependent creep function, $J(t)$ from the start of the forcing, for a visco-elastic solid consists of three terms (e.g., *Nowick and Berry*, 1972)

$$J(t) = J_U + h(t) + t/\eta, \tag{3.3}$$

where J_U is the un-relaxed, i.e., infinite-frequency, compliance that describes the elastic response, $h(t)$ is the time-dependent strain-rate describing the transient response, and η is the Newtonian steady-state viscosity that delineates the viscous response. The elastic shear modulus (G_R) and the associated dissipation (Q_μ^{-1}) are obtained from

$$G_R(\omega) = [Re\{\hat{J}(\omega)\}^2 + Im\{\hat{J}(\omega)\}^2]^{-1/2} \tag{3.4}$$

$$Q_\mu^{-1}(\omega) = |Im\{\hat{J}(\omega)\}/Re\{\hat{J}(\omega)\}|, \tag{3.5}$$

where $\hat{J}(\omega)$ is the complex compliance.

To compute mantle shear attenuation profiles, we employ the laboratory-based visco-elastic dissipation model (extended Burgers) model of *Jackson and Faul* (2010). This temperature-, frequency-, and grain-size-dependent rheological model is based on the observed dissipation in melt-free polycrystalline olivine and orthopyroxene mixtures (*Jackson and Faul*, 2010; *Qu et al.*, 2021).

The main advantage of this model is the direct link with the petrological model, since the latter provides the unrelaxed (infinite-frequency) shear modulus, in addition to pressure and temperature, from which the relaxed shear modulus is computed using the extended Burgers model (e.g., *Khan et al.*, 2018; *Bagheri et al.*, 2019). This allows for self-consistent computation of relaxed shear modulus and shear-wave attenuation profiles through the use of the appropriate creep function (see Appendix A.5). Since the rheological model of *Jackson and Faul* (2010) is

calibrated at the conditions representative of the upper mantle, extrapolation is required for application to the transition zone and lower mantle. For this purpose, we vary attenuation-related parameters in the upper and lower mantle. Rheological parameters are listed in Table 3.4 and Table A.1.

3.3.3 Core model

To explain both seismic and geophysical observations, Earth's Fe-Ni core must have light elements dissolved into it (e.g., *Birch*, 1964; *Poirier*, 1994). The nature of the light elements, which is directly related to Earth's bulk composition, core-formation conditions, and core thermal state, is, however, the subject of considerable speculation (e.g., *Hirose et al.*, 2021). To circumvent the problems associated with the uncertain core composition, we assess the elastic properties of the core using physically-consistent parameterizations for both the outer and inner core by relying on equation-of-state (EoS) approaches. All EoS parameters are compiled in Table 3.4.

Outer core

For the outer core, we follow the work of *Irving et al.* (2018), who implemented an isentropic Vinet EoS to compute seismic properties (density and P-wave velocity), which involves the following parameters that we need to determine: bulk modulus at ambient conditions ($K_{0\mathrm{S}}$), the pressure derivative of the bulk modulus ($K'_{0\mathrm{S}}$), and molar density ϱ (through $\varrho = \frac{m}{V_0}$, where m is the molar mass and V_0 the molar volume at the CMB). In this EoS, the temperature dependence is implicit in the reference condition and the assumption of an adiabat, notwithstanding the EoS being isothermal (*Vinet et al.*, 1987).

The Vinet EoS provides a means for solving for volume given pressure (numerical details are provided in supplementary section S4)

$$P(V) = 3K_{0\mathrm{S}}\hat{V}^{-2/3}\left(1-\hat{V}^{1/3}\right)\exp\left[\eta\left(1-\hat{V}^{1/3}\right)\right], \tag{3.6}$$

where $\hat{V} = V/V_0$ and η is given by

$$\eta = \frac{3}{2}(K'_{0\mathrm{S}} - 1). \tag{3.7}$$

From this we compute density using $\rho = m/V$ with $m = 0.05$ kg/mol, which implies outer-core material that is 10 % less dense than pure Fe (*Irving et al.*, 2018). To continue the construction of the self-consistent model, the pressure at the CMB coming from the mantle model (section 3.3.1) acts as anchoring point for the computation

in the outer core. Having determined the volume V (Eqs. 3.6 and 3.7), we then proceed to infer outer-core P-wave velocity (V_{P}) using

$$V_{\mathrm{P}} = \sqrt{\frac{K_{\mathrm{S}}(V)}{\rho}}. \tag{3.8}$$

with $K_{\mathrm{S}}(V)$ determined from

$$K_{\mathrm{S}}(V) = K_{0\mathrm{S}}\hat{V}^{-2/3}\left[1 + \left(\eta\hat{V}^{1/3} + 1\right)\left(1 - \hat{V}^{1/3}\right)\right]\exp\left[\eta\left(1 - \hat{V}^{1/3}\right)\right]. \tag{3.9}$$

Using the new density, we update the pressure at the current depth node and solve the Vinet EoS again for the following node. In this manner, we iteratively build up the seismic parameter profile for the outer core and provide another anchoring point when propagating the calculation to the inner core (see next section) through the pressure at the inner-core-boundary.

As discussed by *Irving et al.* (2018), an immediate advantage of this parameterisation is that the Bullen (inhomogeneity) parameter for this model of the outer core is ≈1, i.e., homogeneous and adiabatic, and the Brunt-Väisälä frequency is ≈0, i.e., neutrally stratified, as expected for a well-mixed outer core. While we rely on the Vinet EoS in this work, other EoSs, such as Birch-Murnaghan, could equally have been considered. However, since *Irving et al.* (2018) showed that there is little difference between the two EoSs in terms of modeling results, we focus on the Vinet EoS here.

Inner core

We model the inner core using a fourth-order Birch–Murnaghan strain EoS, assuming near-adiabatic conditions (*Birch*, 1952; *Davies and Dziewonski*, 1975). To compute the seismic properties of the inner core (P- and S-wave velocities and density ρ), we relate these to strain (ϵ) through the following relations (numerical details are provided in supplementary section S4)

$$P = -(1-2\epsilon)^{5/2}\left[C_1\epsilon + \frac{1}{2}C_2\epsilon^2 + \frac{1}{6}C_3\epsilon^3\right], \tag{3.10}$$

$$\rho = \rho_0\left[1-2\epsilon\right]^{3/2},$$

$$\rho V_{\mathrm{P}}^2 = (1-2\epsilon)^{5/2}\left[L_1 + L_2\epsilon + \frac{1}{2}L_3\epsilon^2\right], \tag{3.11}$$

$$\rho V_{\mathrm{S}}^2 = (1-2\epsilon)^{5/2}\left[M_1 + M_2\epsilon + \frac{1}{2}M_3\epsilon^2\right].$$

The subscript 0 corresponds to zero-strain or -pressure values at the foot of some adiabat, while the expansion coefficients L and M are given by (*Davies and Dziewonski*, 1975)

$$\begin{aligned}
L_1 &= K_0 + 4/3\mu_0, \\
L_2 &= 5L_1 - 3\left(K_0' + 4/3\mu_0'\right) K_0, \\
L_3 &= 9L_1\left(K_0'' + 4/3\mu_0''\right) K_0^2 + 5(3K_0' - 5)L_1 - 3(K_0' - 4)L_2, \\
M_1 &= \mu_0, \\
M_2 &= 5M_1 - 3K_0\mu_0', \\
M_3 &= 9K_0^2\mu_0'' + 5(3K_0' - 5)M_1 - 3(K_0' - 4)M_2,
\end{aligned} \tag{3.12}$$

whereas the expansion coefficients C are related to L and M through the relations

$$\begin{aligned}
C_1 &= 3L_1 - 4M_1, \\
C_2 &= 3L_2 - 4M_2 + 7C_1, \\
C_3 &= 3L_3 - 4M_3 + 9C_2.
\end{aligned} \tag{3.13}$$

In summary, this results in 7 parameters that need to be determined in the inversion: K_0, K_0', K_0'', μ_0, μ_0', μ_0'', and ρ_0. In addition to these parameters, we also invert for the shear and bulk attenuation properties of the inner core, but neglect anisotropy. Integration of the pressure profile is performed through the use of hydrostatic equilibrium and Poisson's equation as in *Rivoldini et al.* (2011).

3.4 Solving the inverse problem

To solve the inverse problem $\mathbf{d} = \mathrm{g}(\mathbf{m})$, where $\mathbf{d}$ and $\mathbf{m}$ are data and model parameter vectors consisting of observations (normal mode and tidal response data) and anelastic mantle and core parameters, and g is an operator that maps from the model space into the data space, we employ a Bayesian approach as outlined in *Mosegaard and Tarantola* (1995)

$$\sigma(\mathbf{m}) = k\, h(\mathbf{m}) L(\mathbf{m}), \tag{3.14}$$

where $h(\mathbf{m})$ represents prior information on model parameters (described in section 3.4.1), $L(\mathbf{m})$ is the likelihood function, which measures the misfit between observed and predicted data, k is a normalization constant, and $\sigma(\mathbf{m})$ symbolises the posterior model parameter distribution that represents the solution to the inverse problem. $L(\mathbf{m})$ is determined from the observed data, the data uncertainties,

and the way in which data noise is modeled (L_1-norm) and is given by:

$$L(\mathbf{m}) = \sum_j \frac{1}{N_j} \sum_{i=1}^{N} \frac{|\mathrm{d}^i_{\mathrm{obs}}(\mathbf{m}) - \mathrm{d}^i_{\mathrm{calc}}|}{\sigma^i}, \tag{3.15}$$

where N_j is the number of observed data samples for each type of data parameter j: spheroidal and toroidal central frequencies and quality factors, respectively, tidal response, and mean mass and moment of inertia.

To compute model predictions, i.e., normal-mode centre frequencies and quality factors and tidal responses, we employ a spectral element discretization of the underlying differential equations (see appendix A.4 for more details). The body tide response (Love numbers and global tidal quality factors) is computed using the spectral-element-based tidal code of *Bagheri et al.* (2019) that solves the quasi-static momentum equation (Eq. A.12). To compute normal-mode centre frequencies and global quality factors, we use the spectral-element code `specnm` with full gravity as described in *Kemper et al.* (2021).

3.4.1 Parametrization and prior information

The thermo-chemical parameters defining the structure of the mantle are illustrated in Figure 3.2, while model parameters and prior model parameter ranges are summarized in Table 3.4. The prior ranges represent the information acquired from data and results from experimental and numerical studies as described in the foregoing sections and cover wide model parameter ranges.

3.4.2 Stochastic sampling

We employ the Metropolis algorithm to sample the posterior model parameter distribution (Eq. 3.14) (*Mosegaard and Tarantola*, 1995). The Metropolis algorithm, which samples the model space randomly, is an importance sampling algorithm and ensures that models that fit data well and are simultaneously consistent with prior information are sampled more frequently. The Metropolis algorithm samples the model space with a sampling density that is proportional to the (target) posterior probability density and thus ensures that low-probability areas are sampled less excessively. This is an important feature of any algorithm that wishes to randomly sample high-dimensional model spaces where the probability density over large proportions of the volume are near zero. We sampled 10^5 models in total. We downsampled the original set of models to ensure statistically uncorrelated models, as a result of which $\sim 10^4$ models were retained for analysis here.

Table 3.4: Overview of model parameters, prior model ranges, and distributions. Mantle attenuation parameters relate to the lower mantle (parameters related to upper mantle and transition zone attenuation are listed in Table A.1). Outer-core parameters relate to the Vinet equation-of-state (EoS), whereas the inner-core is based on a Birch-Murnaghan finite-strain EoS. Primes on parameters refer to pressure derivatives.

Description	Parameter	Quantity	Value/Range	Distribution
Crustal parameters				
Depths	z_1 & z_2	2	10–50 & 20–80 km	uniform
S-Wave velocities	V_{S1} & V_{S2}	2	3.1–3.3 & 3.7–4.0 km/s	uniform
Ratio V_P/V_S	δ	1	1.6–1.9	uniform
Ratio ρ/V_S	β	1	0.7–0.9	uniform
Mantle parameters				
Lithospheric temperature	T_{lit}	1	1200–2000 K	uniform
Lithospheric thickness	Z_{lit}	1	50–300 km	uniform
Basalt fraction	f	2		
upper mantle			0–0.5	uniform
lower mantle			0–0.5	uniform
Attenuation (Q_μ)		3	$Q_\mu \leq 600$	
Grainsize	d_g	2		
upper mantle			10^{-4}–10^{-1} m	uniform
lower mantle			10^{-4}–10^{-1} m	uniform
Activation volume	V_a	1	10^{-7}–10^{-5} m^3/mol	uniform
Scaling exponent	α	1	0.1–0.4	uniform
Outer core parameters				
Isentropic bulk modulus	K_{0S}	1	60–80 GPa	uniform
	K'_{0S}	1	5–7	uniform
Molar volume	V_0	1	10^{-8}–10^{-5} m^{-3}	uniform
Attenuation		2		
Shear quality factor	Q_μ		0	fixed
Compressional quality factor	Q_κ		57827	fixed
Inner core parameters				
Bulk modulus	K_{ic}	1	350–500 GPa	uniform
	K'_{ic}	1	2.5–4	uniform
	K''_{ic}	1	-10^{-2}– -10^{-4} GPa^{-1}	uniform
Shear modulus	μ_{ic}	1	15–22 GPa	uniform
	μ'_{ic}	1	0.2–0.35	uniform
	μ''_{ic}	1	10^{-4}–10^{-2} GPa^{-1}	uniform
Density (reference state)	ρ_0	1	5–15 kg/m^3	uniform
Attenuation		2		
Shear quality factor	Q_μ		50–600	uniform
Compressional quality factor	Q_κ		50–57827	uniform

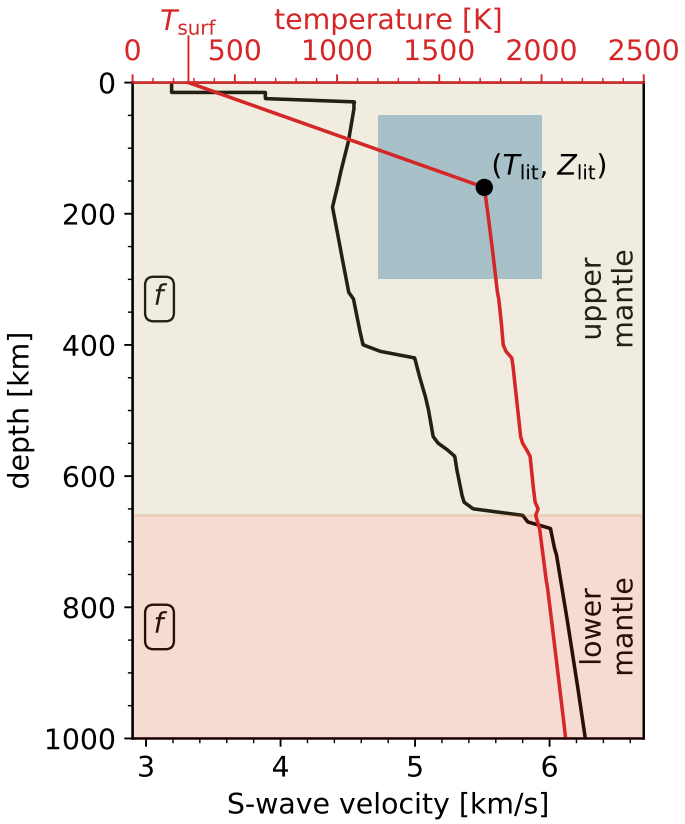

Figure 3.2: Thermo-chemical model parameterisation. An example geotherm is shown in red and defined using the parameters surface temperature T_{surf} (fixed T_{surf}=273.15 K), temperature at the base of the lithosphere T_{lit}, and lithospheric thickness Z_{lit} and composition (upper- and lower-mantle basalt fraction, f). Prior ranges on T_{lit} and Z_{lit} are indicated by the blue box. Temperatures below the lithosphere are computed from the entropy of the lithology at the base of the lithosphere. Mantle composition is described by upper and lower mantle basalt fraction, indicated by the two coloured regions above and below 660 km depth. All model parameters and prior ranges are defined in Table 3.4. For illustration, a self-consistently-computed isotropic shear-wave velocity profile for the geotherm is shown in black (for a uniform mantle basalt fraction of 0.2). As part of the parameterisation, we employ depth nodes at 5-, 10-, and 5-km intervals in the upper mantle, between lower mantle and D″, and throughout D″, respectively.

3.5 Results

3.5.1 Data fit

Data fits for all observed spheroidal centre frequencies are summarised in Figure 3.3, while fits to the astronomic-geodetic data (tidal Love numbers and mean mass and moment of inertia) are shown in Figure 3.4. Data fits to toroidal and radial centre frequencies and spheroidal, toroidal, and radial quality factors are shown in Figures A.1–A.5, respectively. Data fits are summarised using violin plots that show the probability density distribution of the sampled model predictions (synthetic data) smoothed by a vertically-mirrored kernel density estimator (*Wilke*, 2019). We have centered individual violins in all our plots of data fit so that the observed value is at zero and the observational uncertainties indicated by error bars are centered vertically around the observation. To quantify the data fit, we color-coded the violins by the distance of the mean of their probability density functions to the observed value in multiples of the observational uncertainty. A red color-coded violin therefore does not necessarily imply that the models do not fit the data, but merely that the mean is outside of the measured uncertainty interval.

In general, all spheroidal normal mode centre frequencies are fit within observational uncertainties. For comparison, we are also showing the predicted data fits for PREM and EPOC-Vinet, which indicate an overall similar level of data fit as our models. The fit of PREM to most of the spheroidal, toroidal, and radial normal-mode centre frequencies considered here is notable. The fit of PREM to most of the spheroidal, toroidal, and radial normal-mode quality factors that were mostly unavailable at the time PREM was built is, not suprisingly, of lower quality in comparison to that based on our models (Figures A.3–A.5).

The astronomic-geodetic data are also seen to be fit within observational uncertainties (Figure 3.4). In comparison, PREM and EPOC-Vinet do not fit the present-day mean normalised moment of inertia (MoI) and EPOC-Vinet is too heavy. In addition, PREM and EPOC-Vinet have difficulties in matching the modern-day tidal response values for k_2 and h_2. These discrepancies arise because 1) PREM was constructed using a value of MoI available at the time, whereas 2) EPOC-Vinet (*Irving et al.*, 2018) did not consider MoI and M in their inversion, and 3) neither model included the tidal response data.

3.5.2 Mantle thermo-chemical and seismic structure

Inverted models in the form of radial density, isotropic P- and S-wave velocity, shear attenuation, and thermal profiles, including upper and lower mantle composition,

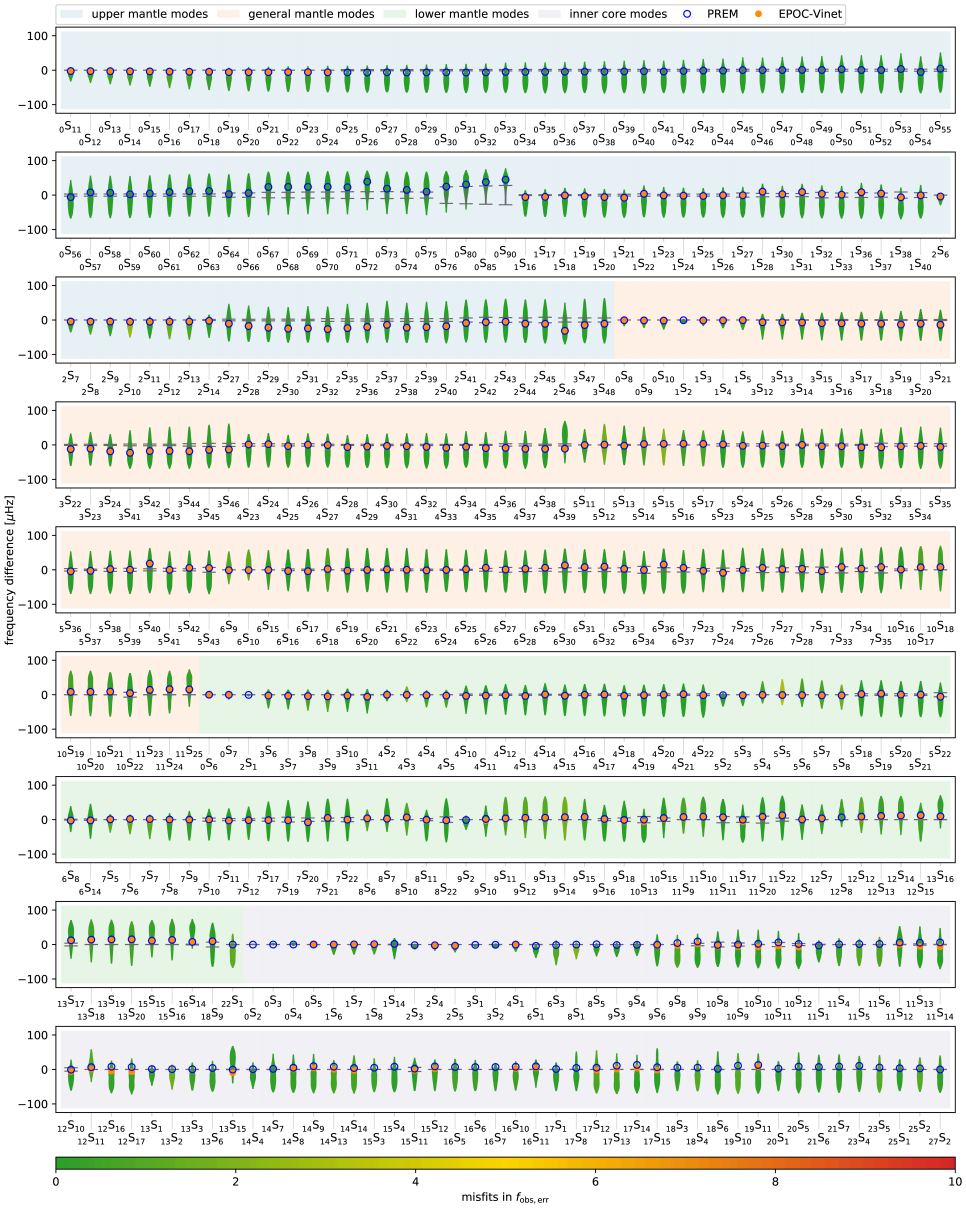

Figure 3.3: Spheroidal centre-frequency data fit. The observed centre frequency is located at zero of each violin. Color coding indicates the distance of the mean of the probability density function to the observed centre frequency in multiples of the observational uncertainties. Observed spheroidal centre frequencies are compiled in Tables (S1–S11) and observational uncertainties span the breadth of the black horizontal bars. A violin plot represents a density estimate of the sampled centre frequencies that has been rotated by 90° and mirrored, wherefrom it obtains its vertical symmetric form. The end points of a violin indicate minimum and maximum sampled centre frequency values, while the thickest part of the violin corresponds to the highest density point of sampled centre frequencies. For comparison, predictions based on the radial seismic reference model PREM and “outer-core-only" model EPOC-Vinet are also shown. Note that in the case of EPOC-Vinet, only the modes considered in their study are indicated. Background panel colour indicates the part of the planet to which a given mode is mainly sensitive. See main text for details. Data fits to toroidal and radial normal-mode centre frequencies are shown in Figures A.1–A.2, respectively.

Table 3.5: Summary of posterior results based on inversion of normal modes and astronomic-geodetic and tidal constraints. Model parameter ranges are represented using the 75% credible intervals. Mantle attenuation parameter activation volume refers to the lower mantle. Primes indicate pressure derivatives.

Description	Parameter	Range
Mantle parameters		
Lithospheric temperature	T_{lit}	1570–1722 K
Lithospheric depth	Z_{lit}	141–170 km
Basalt fraction	f	
upper mantle		0.11–0.25
lower mantle		0–0.05
Attenuation (Q_μ)		
Grainsize	d_g	
upper mantle		0.8–1.3 cm
lower mantle		2.9–5.3 cm
Activation volume	V_a	2.9–5.4$\times 10^{-6}$ m^{3}mol^{-1}
Scaling exponent	α	0.26–0.28
Outer core parameters		
Isentropic bulk modulus	K_{0S}	64–78 GPa
	K'_{0S}	5.7–6.3
Molar volume	V_0	7.9–8.4$\times 10^{-6}$ m^3
Molar density	ρ_0	5985–6312 kg m^{-3}
Inner core parameters		
Bulk modulus	K_{ic}	438–453 GPa
	K'_{ic}	3.3–3.5
	K''_{ic}	-8.0– -7.6$\times 10^{-3}$ GPa^{-1}
Shear modulus	μ_{ic}	15–20 GPa
	μ'_{ic}	0.26–0.29
	μ''_{ic}	1.0–1.2$\times 10^{-3}$ GPa^{-1}
Density (reference state)	ρ_0	8142–8773 kg m^{-3}
Attenuation		
Shear quality factor	Q_μ	77–190
Compression quality factor	Q_κ	51–33511

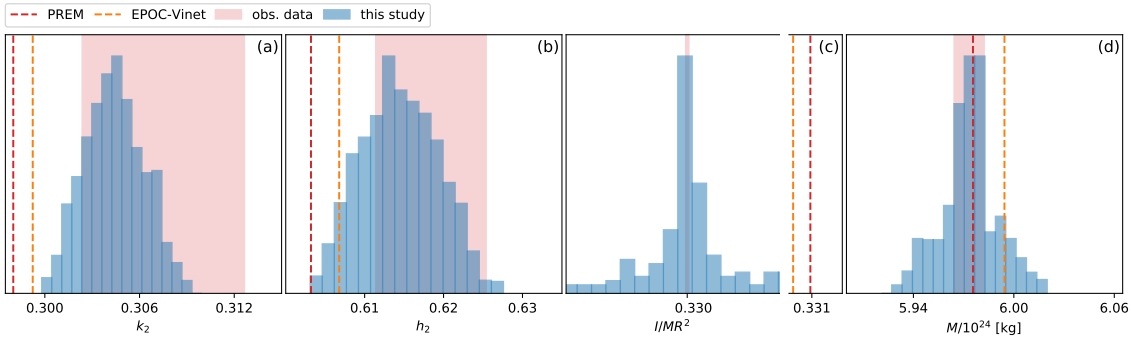

Figure 3.4: Astronomic-geodetic data fit. Tidal response in the form of the degree-2 Love numbers (a) k_2 and (b) h_2, mean normalized moment of inertia I/MR^2 (c), where R is Earth's radius, and mean mass M (d). The present-day astronomic-geodetic data are summarised in Table 3.2. For comparison, astronomic-geodetic data fits for the radial seismic reference model PREM and "outer-core-only" model EPOC-Vinet are also shown. See main text for details.

are shown in Figure 3.5 and the main results are summarised in Table 3.5. The seismic models are compared to isotropic PREM and the normal-mode-outer-core-only model EPOC-Vinet of *Irving et al.* (2018), while the thermal profiles are compared to the laboratory-based adiabat of *Katsura* (2022). We may note that our resultant uppermost mantle seismic velocity models may be biased toward their vertically-polarised counterpart, because only higher-frequency fundamental spheroidal modes are inverted. Results are generally displayed using credible intervals, which provide a quantitative means of describing the information contained in the posterior distribution. The credible interval is defined as the shortest possible interval containing a given probability, and in the following figures, we depict credible intervals containing 25%, 50%, and 75% of the marginal probability.

Mantle composition and thermal state

Here we briefly describe the inverted mantle thermo-chemical structure. Sampled geothermal mantle profiles are shown in Figure 3.5e. For comparison, the temperatures at which the mineral phase transformations in the system $(Mg,Fe)_2SiO_4$ have been observed in the laboratory are also indicated (vertical red bars) based on the measurements of *Katsura* (2022), including their adiabatic temperature profile (red line). There appears to be excellent agreement in the upper mantle between the normal-mode-based and the experimentally-determined temperatures for the reactions olivine$\longrightarrow$wadsleyite and ringwoodite$\longrightarrow$ferroperoclase+bridgmanite that are representative of the "410-km" and the "660-km" seismic discontinuities, respectively. Consistency is also observed between the inverted potential temperatures and the predictions of the adiabat of *Katsura* (2022) (cf. solid vertical line in inset in Figure 3.5e). While the laboratory-based adiabatic temperature profile of *Katsura* (2022) and our geophysically-determined mantle *isentropes* are overall in agreement, discrepancies are nevertheless present. Firstly, *Katsura* (2022) consid-

ers a single composition (peridotite), whereas we investigate a range of compositions; secondly, mantle temperatures below 660 km depth in the profile of *Katsura* (2022) are obtained by extrapolation employing PREM values for density, pressure, and gravitational acceleration, which results in a temperature profile that is, *sensu stricto*, not self-consistent; thirdly, the extrapolation explains the absence of a thermal boundary layer across D″ at the bottom (∼2700 km depth) of their model.

Mantle composition in the form of basalt fraction is shown in the second inset of Figure 3.5e and indicates upper and lower mantle basalt fractions of ∼0.15–0.25 and ∼0–0.2, respectively, corresponding to a pyrolite-dominated upper mantle, for which f∼0.2, and a lower mantle that is compositionally distinct to the upper mantle. The pyrolite model of *Ringwood* (1975) is widely considered representative of the Earth's average upper mantle composition (see also *Taylor*, 1980), on account of its ability to satisfy a large range of geochemical and geophysical data, including the radial mantle seismic velocity (e.g., *Weidner*, 1985; *Jackson and Rigden*, 1998; *Drake and Righter*, 2002) and electrical conductivity structure (e.g., *Xu et al.*, 2000; *Grayver et al.*, 2017), although more chondritic (silica-enriched) lower mantle compositions cannot be ruled out (e.g., *Khan et al.*, 2006; *Matas et al.*, 2007; *Murakami et al.*, 2012).

In spite of the fact that a compositionally-layered mantle provides a good match to global data, deviations are nevertheless required to account for the seismic properties of the mantle at a more detailed level (see section 3.5.2). However, given the averaging properties of the normal-mode centre frequencies and tidal observations, the assumption of a compositionally-layered mantle as envisaged here is justifiable, with the exception of maybe D″ – a highly heterogeneous layer that likely represents a thermal boundary layer and comprises the large low shear wave velocity provinces (e.g., *Lay*, 2015), sitting atop the CMB. While this layer would mostly affect the modes that sample the lower mantle and outermost core, *van Tent et al.* (2020) showed that the variations in centre frequencies (∼1–5 μHz) induced by different D″ structure are well within the uncertainties of the normal-mode measurements. Similarly, sensitivity tests performed by *Lau and Faul* (2019) also showed that the effects of varying structure associated with D″ on global tidal dissipation were small relative to the observational uncertainties.

Seismic wave velocity structure

The crust (shown in the inset in Figure 3.5c) and lithospheric structure obtained here is in good agreement with PREM and thus representative of a global average crust. This is to be expected in view of the fact that we consider a large portion of the fundamental (spheroidal) normal-mode data set considered in the construction of

PREM. Generally, we observe that throughout most of the upper mantle and transition zone (TZ) our seismic profiles match those of PREM, although shallower P-wave and steeper S-wave velocity gradients in the upper mantle and TZ, respectively, are apparent. Differences in velocity gradients relative to PREM have been reported earlier (*Cobden et al.*, 2008) and were identified as originating from variations in mantle mixing state (*Xu et al.*, 2008) and thermo-chemical changes (*Cammarano et al.*, 2009; *Ritsema et al.*, 2009; *Khan et al.*, 2013; *Bissig et al.*, 2021). The latter also explains the changes in mantle TZ discontinuity depths observed here relative to PREM.

While we presently lack the resolution to investigate this in more detail, there is accumulating evidence for a mantle that consists of a composite of equilibrated and mechanically-mixed portions from both geodynamics (*Nakagawa et al.*, 2009; *Yan et al.*, 2020) and seismology (*Munch et al.*, 2020; *Tian et al.*, 2020; *Waszek et al.*, 2021; *Tauzin et al.*, 2022; *Bissig et al.*, 2022a,b). Using global converted, triplicated, and reflected P- and S-waveforms, *Munch et al.* (2020) and *Bissig et al.* (2022a,b), for example, showed that sub-cratonic mantle is better matched by a mechanically-mixed mantle, whereas subduction zones are better fit by a thermodynamically-equilibrated assemblage. Several studies also showed that to further increase upper mantle and TZ velocity gradients, radial chemical variations and/or deviations from an adiabatic geotherm are necessary (e.g., *Irifune et al.*, 2008; *Khan et al.*, 2009; *Cammarano et al.*, 2009; *Munch et al.*, 2020; *Bissig et al.*, 2022b).

Significant differences are apparent in the lower mantle as shown in the insets of Figure 3.5a and c. Our profiles indicate that the lower mantle is overall less dense, slower (S-wave velocity), and faster (P-wave velocity) than PREM. The discontinuity in seismic properties toward the lowermost mantle (at a depth of around 2700 km) coincides with the mineral transformation bridgmanite$\longrightarrow$post-perovskite that signals the onset of D$''$. The off-set in mantle properties seen in our models is compensated by a higher density and a lower P-wave velocity in the outer core relative to PREM (this will be discussed in more detail in section 3.5.3), whereas the seismic properties of the inner core are in accord with PREM, and reflects the very limited increase in the number of new inner-core-sensitive modes.

To verify the robustness of the observed decrease/increase in mantle/outer-core density, we performed an inversion of the normal-mode catalog only, i.e., without the astronomic-geodetic data. The results (SM Figure A.10) confirm the mantle/outer-core density structure shown in Figure 3.5, which is thus partly driven by the outer-core sensitive modes.

To study the impact of the inverted mantle properties, we randomly selected a subset of models from the entire set of sampled models and computed P- and S-wave travel times that we compare to the globally-averaged P- and S-wave travel times

from the reprocessed ISC catalog (*Engdahl et al.*, 1998). The catalog contains more P-wave ($\sim 10^6$) than S-wave ($\sim 10^4$) arrivals and the quality of the P-wave arrivals is better. The ISC catalog covers epicentral distances (Δ) in the range 18.5°–90° for P-waves and 19.5°–80° for S-waves. This corresponds to rays turning between 300 km and ∼2500 km depth, reaching well into the lower mantle. The comparison is shown in Figure 3.6 and indicates that the most probable P- and S-wave travel time differences (between the observations and the predictions) are generally well within observational uncertainties. Also shown are the predicted travel times based on PREM and the body-wave model AK135 (*Kennett et al.*, 1995). While AK135 is, as expected, seen to provide the best overall fit to the ISC data, our most probable predictions in the form of the 25% credible intervals (ci.), encompass both PREM and AK135. Overall, the travel time difference plots show little structure, except for Δ<25°, which is attributed to the fewer constraints provided by the travel time data at shorter Δ, covering the upper 300 km of crust, lithosphere, and mantle, in addition to the presence of upper mantle discontinuities and lateral heterogeneity in the first ∼250 km. Thus we may conclude that, like AK135, our mantle seismic models are not observed to result in systematic differences in comparison to global travel time observations. Yet, given the greater number of stations over continents, a continental bias is to be expected in the ISC travel time data set.

With regard to the inner core, several studies have suggested discrepant inner-core seismic properties relative to PREM. Inner-core S-wave velocity is mostly constrained through detection of PKJKP body wave phases or their equivalent normal-mode representation. Using pPKJKP and SKJKP body waves, *Deuss et al.* (2000), for example, found inner-core S-wave velocities in agreement with PREM. Relying on normal modes, *Deuss* (2008) further showed that moving beyond ∼1.5% of PREM is incompatible with the seismic data. *Cao et al.* (2005) required a 1.5 % increase in inner-core S-wave velocity with respect to PREM to fit their intermediate-period PKJKP observations, while *Wookey and Helffrich* (2008), who focused on high-frequency PKJKP body waves, obtained inner-core S-wave velocities not much different from PREM. In contrast, *Tkalčić and Pham* (2018), also relying on PKJKP waves, detected inner-core S-wave velocities 2.5% lower than PREM, while *Robson et al.* (2022), relying on core modes, suggested a decrease in inner-core S-wave velocity of ∼1 % with the caveat that structure above the inner core is fixed to either PREM or the NREM model of *Moulik and Ekström* (2016). Apart from *Tkalčić and Pham* (2018), the aforementioned observations are within the uncertainties of our results.

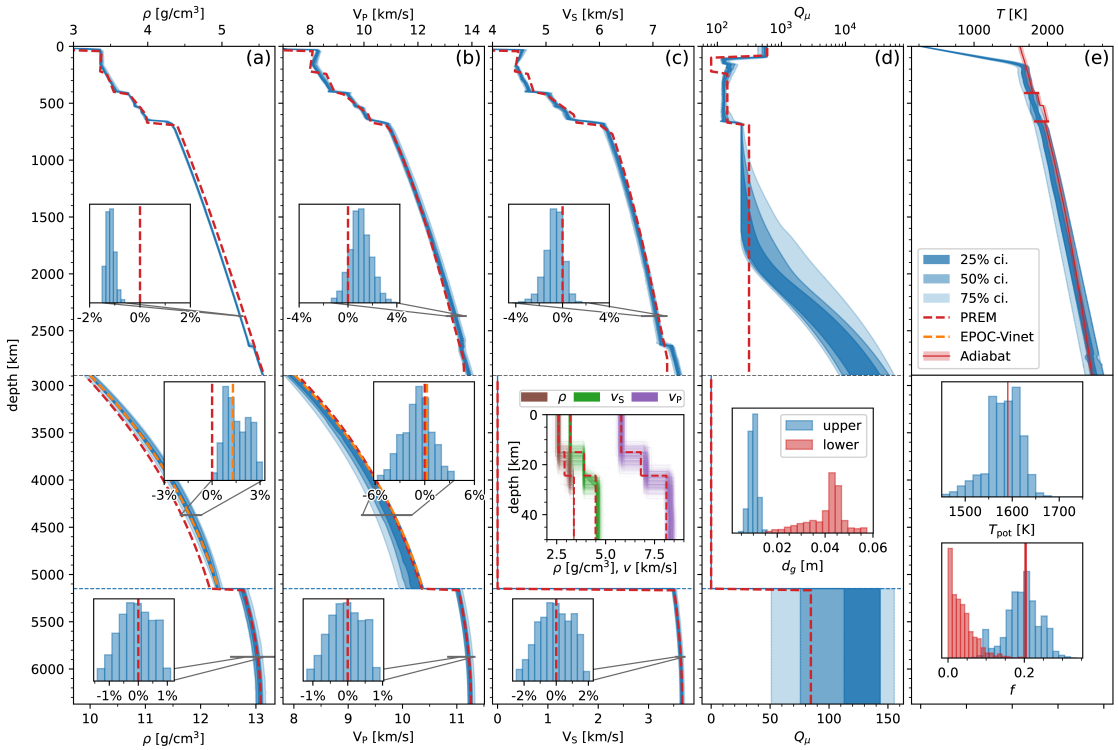

Figure 3.5: Inverted radial seismic models of the Earth. The blue areas indicate the range of sampled profiles of (a) density ρ, (b) P-wave velocity V_P, (c) S-wave velocity V_S, (d) shear-wave quality factor Q_μ, and (e) temperature T. Histograms of sampled seismic properties at selected depth nodes (2400 km, 4400 km, and 5700 km), are shown in the insets in (a), (b), and (c). Insets in (c), (d), and (e) show sampled crustal velocity structure, mantle grain size distribution, mantle potential temperature T_{pot}, and mantle composition (basalt fraction f), respectively. "upper" and "lower" in the insets in panels (d) and (e) refer to upper and lower mantle, respectively. The sampled models are color-coded using the 25 %, 50 %, and 75 % credible intervals (ci.). Profiles of credible intervals, indicating sampled uncertainty ranges, are shown separately in supplementary material Figures S9–S12. Models are compared to the isotropic preliminary reference Earth model (PREM) (*Dziewonski and Anderson*, 1981) (a–d), "outer-core-only" model EPOC-Vinet (*Irving et al.*, 2018) (a–c), and the peridotitic laboratory-based mantle adiabat of *Katsura* (2022) (e and solid vertical red line in top inset in e). The vertical red line in the bottom inset in (e) indicates the value of f corresponding to pyrolite. All models refer to a reference period of 1 s.

Shear-wave attenuation structure

The laboratory-based visco-elastic shear attenuation models obtained here are shown in Figure 3.5d. We display sampled mantle grain sizes in the inset in Figure 3.5d that indicate upper and lower mantle grain sizes in the cm-range, in general agreement with the seismic and tidal attenuation study of *Lau and Faul* (2019), who found lower mantle grain sizes in the range 0.1–10 cm.

As for the attenuation structure, we find that Q_μ is high (∼600) in the crust and lithosphere, while it is low (100–200) in and around the asthenosphere, but increases (∼250) across the mantle transition zone (MTZ) and remains roughly constant in the first 800 km of the lower mantle, after which Q_μ increases almost linearly until the core-mantle-boundary (CMB), where Q_μ reaches values in excess of 1000. Comparison with PREM reveals similar behaviour to a depth of about 1800 km. Differences exist in the lowermost mantle, where PREM suggests a constant Q_μ (∼300) down to the CMB.

As reviewed by *Romanowicz and Mitchell* (2015), studies based on normal-mode and surface-wave data (*Anderson and Hart*, 1978; *Widmer et al.*, 1991; *Durek and Ekström*, 1996; *Resovsky et al.*, 2005) showed the largest scatter in lower mantle Q_μ, but generally accorded with the observation made here that the average Q_μ is higher in the lower than in the upper mantle. A similar observation was also made by *Zhu et al.* (2022) using 20-s direct and surface-reflected S-waves (SS, SSS, and SSSS).

Our inner-core Q_μ is less well constrained, but largely consistent with PREM, which in part results from the simplified parameterisation (homogeneous structure) and the fact that mode-sensitivity diminishes to zero at the center of the Earth. This implies that our Q_μ results, because of the greater sensitivity of normal modes at shallower depths of the inner core, are more representative of the uppermost inner core. Independent determinations of inner-core Q_μ come from the aforementioned studies of PKJKP waves, where Q_μ is found to lie in the range 100–600 (*Deuss et al.*, 2000; *Cao and Romanowicz*, 2009; *Wookey and Helffrich*, 2008). A relatively large inner core Q_μ was also observed by *Tkalčić and Pham* (2018) in their detection of PKJKP waves through correlation of the earthquake coda wavefield, although the latter study only explored Q_μ variations while keeping other parameters fixed, leaving potential trade-offs unexplored.

3.5.3 Implications for outer-core seismic structure

A characteristic feature of many P-wave velocity models that derive from analyses of SKS waves that are multiply reflected from the underside of the CMB (e.g., *Tanaka*,

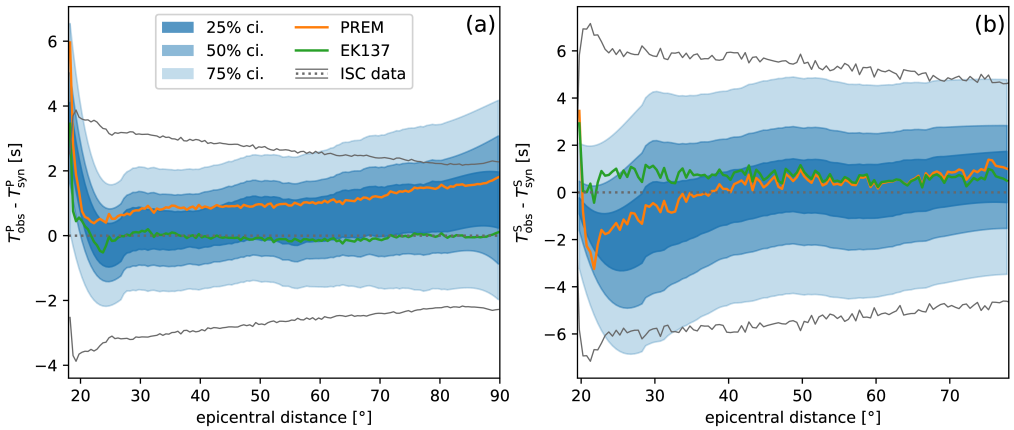

Figure 3.6: Comparison of observed and computed globally-averaged ISC P-wave (a) and S-wave (b) travel time differences (T_{obs}–T_{syn}). ISC refer to the globally-averaged P- and S-wave travel times from the reprocessed ISC catalog of *Engdahl et al.* (1998) with dotted and solid black lines indicating observations and uncertainties, respectively. For comparison, we also show travel time differences based on the radial seismic reference models PREM and EK137 (*Kennett*, 2020). Sampled models are shown using probability contours in the form of credible intervals (ci.). Differential travel times were computed at a reference period of 1 s.

2007; *Alexandrakis and Eaton*, 2010; *Helffrich and Kaneshima*, 2010; *Kaneshima and Matsuzawa*, 2015; *Tang et al.*, 2015; *Kaneshima*, 2018; *Wu and Irving*, 2020) is that they are generally slower than PREM throughout the outer core with the largest deviations in P-wave velocity gradient concentrated in the upper ∼400 km beneath the CMB. Deviations from PREM in the topmost outer core have been employed to suggest the presence of stratification that is expected to result from inner-core crystallization. Light elements are excluded from the solid near the inner-core boundary, as the outer core crystallises, and rise to the top of the core where they accumulate producing a chemically- and possibly thermally-stratified layer, the E′ layer (*Fearn et al.*, 1981; *Loper*, 2000; *Helffrich*, 2014; *Buffett*, 2014; *Gubbins and Davies*, 2013; *Landeau et al.*, 2016; *Nakagawa*, 2018; *Bouffard et al.*, 2019). Possible mechanisms for the formation of a stably stratified layer could be immiscibility in molten iron alloy systems such as Fe-O-S (*Helffrich and Kaneshima*, 2004), Fe-Si-O (*Arveson et al.*, 2019), and Fe-S-H (*Yokoo et al.*, 2022), or diffusion of light elements in Fe-metal liquids (*Buffett and Seagle*, 2010; *Gubbins and Davies*, 2013; *Li et al.*, 2023); other possibilities are discussed by *Brodholt and Badro* (2017).

As a means of further testing our models, we computed differential travel times between SmKS phases, where m ranges between 2 and 5 and m–1 refers to the number of CMB underside reflections, and compare these in Figure 3.7 to the observations of *Kaneshima* (2018) and predictions based on PREM, the radial seismic body wave model EK137 (outer-core update of AK135) (*Kennett*, 2020), EPOC-Vinet (*Irving et al.*, 2018), and the CCMOC model obtained from correlation of the earthquake coda wavefield (*Ma and Tkalčić*, 2022).

Although normal modes are not expected to fit this level of detail because the

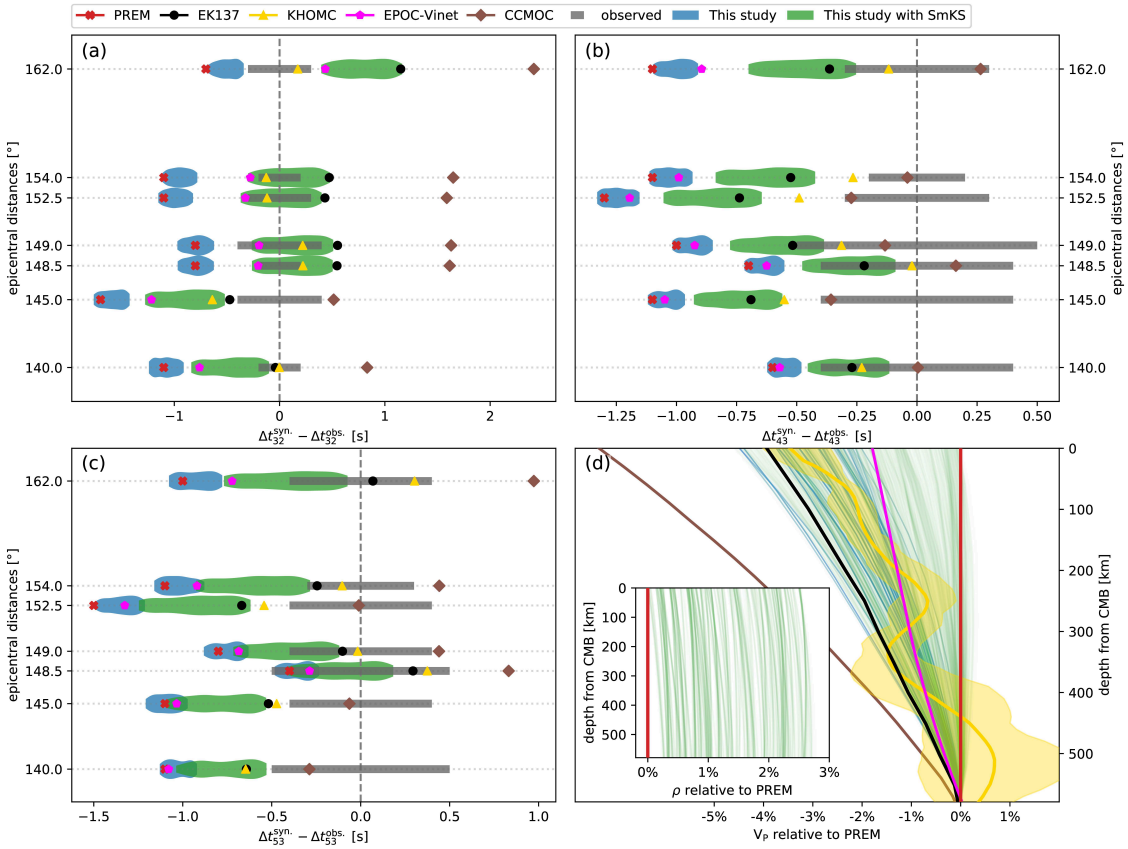

Figure 3.7: Differential travel time predictions $\Delta t_{nm}^{\text{syn.}}$ for underside core-mantle-boundary reflected body waves phases (SmKS) for the best-fitting models (25% credible interval) (a–c) based on inversion of normal modes and astronomic-geodetic data (blue violins) and inversion of normal modes, astronomic-geodetic data, and SmKS differential travel times (green violins). Differential travel time predictions for the radial reference models PREM and EK137 are also shown, in addition to the normal-mode model EPOC-Vinet, the "coda-correlation" model CCMOC, and the outer-core model KHOMC. Synthetics are relative to the observed SmKS differential travel times $\Delta t_{nm}^{\text{obs.}}$ of *Kaneshima* (2018), which are shown for three phase pairs (nm= (a) 32, (b) 43 and (c) 53) and seven epicentral distances (events). Observational uncertainties are given by the width of the dark gray horizontal bars. (d) Comparison of a subset of our best-fitting outer-core models with PREM and radial seismic models. To better compare P-wave velocity gradients, all models were shifted so that these coincide at the lower bound in (d). The inset shows predicted outer-core density profiles. All models refer to a reference period of 1 s.

sensitivity kernels are too broad to separate the S2KS–S3KS bottoming points, where most of the travel time signal lies, we can nevertheless make a number of observations from the comparison: 1) all models with the exception of KHOMC, i.e., the model obtained from inversion of the SmKS observations (*Kaneshima*, 2018), imply a well-mixed and homogeneous core; 2) the differential SmKS predictions based on our models (blue violins) generally match the observations similar to or better than PREM and CCMOC at all distances (panels a–c); and 3) none of the models are capable of reproducing the change in P-wave velocity gradient of KHOMC in the outermost core.

In an attempt to improve the match to outer-core body waves, we re-inverted our entire data set and included the observed differential SmKS travel times of *Kaneshima* (2018). The resultant fit to the observations and models are shown in Figure 3.7a–c (green violins) and Figure 3.7d (green lines), respectively. The fit has clearly improved relative to our normal-mode and astronomic-geodetic-data-only predictions, yet deviations remain. Our new outer-core P-wave velocity models have steeper gradients than our previous predictions (blue lines in Figure 3.7d), but are, because of the nature of our outer-core parameterisation, unable to reproduce the change in P-wave velocity gradient characteristic of models such as KHOMC (*Kaneshima*, 2018) with the caveat that only $\sim 2/3$ of the SmKS observations are fit by KHOMC. We may summarise the situation thus: while our well-mixed homogeneous and adiabatic outer-core models provide a reasonable match to the SmKS observations, discrepancies nevertheless persist that point to a more complicated outer-core structure than is attainable within the context of the current parameterisation, including that of KHOMC.

Future attention to modes with significant energy in the top of the outer core will yield density information to improve the constraints beyond the SmKS data. In this context, Figure 3.7d (inset) also shows our predicted density profiles that indicate a 1-3% denser outermost core relative to PREM.

Finally, although *Garnero* (2000) and *Wu and Irving* (2020) conjectured that lateral variations in mantle structure can possibly affect differential SmKS travel times, *Ji and Zhao* (2022) showed, based on waveform modeling experiments, that neither finite-frequency effects nor large-scale mantle heterogeneities are large enough to explain the observed travel time differences.

3.5.4 Inner-outer-core density contrast and core composition

From a seismological point of view, one or more light elements need to be dissolved into the Fe-Ni alloy forming the Earth's core in order to explain the seismic observations in the form of e.g., the density jump across the inner core boundary (ICB)

(*Anderson et al.*, 2003). The density jump between the solid inner core and liquid outer core has been constrained seismically from relative amplitude measurements of PKiKP/PcP and PKiKP/P (*Shearer and Masters*, 1990; *Cao and Romanowicz*, 2004; *Koper and Pyle*, 2004; *Koper and Dombrovskaya*, 2005; *Tkalčić et al.*, 2009; *Waszek and Deuss*, 2015; *Shen et al.*, 2016) to be <1.2 g/cm^3. The density contrast from core-sensitive normal-mode studies is similar ($\leq$1.0 g/cm^3) (*Dziewonski and Anderson*, 1981; *Shearer and Masters*, 1990; *Robson and Romanowicz*, 2019; *Masters and Gubbins*, 2003). The lower value of *Koper and Pyle* (2004) relative to the other body wave studies could be due to either an observational bias in that PKiKP is only observed when it has a larger-than-average amplitude (*Shearer and Masters*, 1990; *Waszek and Deuss*, 2015) or through the neglect of the effect of anisotropy on inner core reflection amplitudes (*Helffrich and Mainprice*, 2019). Moreover, trade-offs between density and velocity at the top of the inner core and bottom of the outer core will add additional uncertainty. It should also be noted that whereas reflected body wave data generally provide localised estimates and are affected by lateral heterogeneities, normal-mode data yield depth-averaged estimates that are representative of the global mean. In any case, the density difference exceeds that of the solid–liquid phase transition and is compatible with an inner-outer-core relative light element enrichment of ∼5–10 % (*Hirose et al.*, 2021).

The nature of the light elements has been the subject of considerable speculation due to its fundamental importance on the bulk composition of the Earth, the conditions under which the core formed, the temperature regime in the core, and the continuing process of core-mantle reaction (*Poirier*, 1994; *Wood et al.*, 2008; *Lin et al.*, 2002; *Badro et al.*, 2007). Since Birch initially established the density deficit of Earth's outer core to be ∼10 % relative to pure Fe (*Birch*, 1964), candidate elements have ranged in both diversity and number. The primary candidates include Si, S, C, O, and H (*Alfè et al.*, 2002; *Belonoshko et al.*, 2007; *Vočadlo*, 2007; *Antonangeli et al.*, 2010; *Bazhanova et al.*, 2012; *Martorell et al.*, 2013; *Badro et al.*, 2014; *Caracas et al.*, 2015; *Sakamaki et al.*, 2016; *Tagawa et al.*, 2016; *Hirose et al.*, 2017). The problem has been compounded by the difficulty of both laboratory measurements and first-principles calculations to reconcile the various compositions with seismic observations, which is borne out in the difficulty of simultaneously matching density and seismic velocities (*Li et al.*, 2018; *Nakajima et al.*, 2020). A solution has been to consider multiple light elements, but core composition models are non-unique and allow for a mixture of several light elements, of which Si, O, C, and possibly H are currently considered the most likely candidates (*Lin et al.*, 2002; *Takafuji et al.*, 2005; *Wood*, 2008; *Wood et al.*, 2008; *Antonangeli et al.*, 2010; *Rubie et al.*, 2011; *Badro et al.*, 2014, 2015; *Brodholt and Badro*, 2017; *Huang et al.*, 2019; *Umemoto and Hirose*, 2020; *Tagawa et al.*, 2022; *Yang et al.*, 2022).

We plot the density contrast across the ICB based on our sampled models in

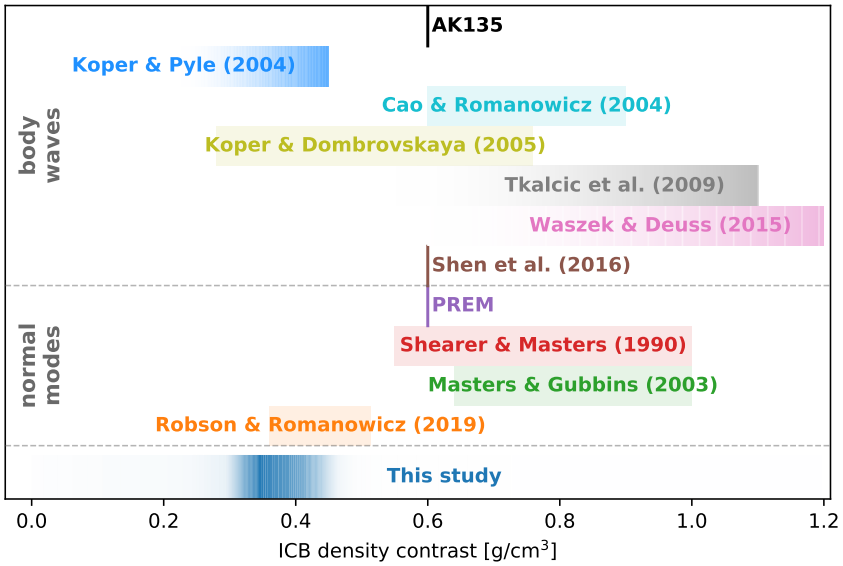

Figure 3.8: Density contrast across the inner-core-boundary (ICB). The probability distribution at the bottom (this study) shows the density difference across the ICB for all inverted models obtained here. For comparison, literature estimates of the density difference based on body wave analyses of core phases and normal-mode data are also shown for comparison. Fading colored horizontal lines indicate that only an upper bound on the density jump could be determined.

Figure 3.8, which shows that the most probable ICB density contrast ranges between 0.3 and 0.45 g/cm^3. For comparison, the results from the aforementioned body wave and normal mode observations are also included in Figure 3.8. Our result appears to be lower than previous body wave and normal mode estimates, with the exception of maybe *Koper and Pyle* (2004) and *Robson and Romanowicz* (2019). Bearing in mind that the magnitude of the density difference arising from solidification alone has been estimated at ∼0.2 g/cm^3 (*Alfe et al.*, 2000), our inferred reduction may be appreciable and may also significantly diminish the part of the density contrast associated with light element partitioning. Since the compositional heterogeneity associated with light element partitioning is considered the main driving force for the compositional convection that powers the geodynamo (*Nimmo*, 2015), the observed reduction in the density difference across the ICB could have important consequences for our understanding of the mechanism that sustains and operates the geodynamo. Apart from inner core crystallization, the dynamo can also be powered by exsolution of solids from the liquid outer core (*Hirose et al.*, 2017), which also solves the problem that a young inner core presents to paleomagnetic records of magnetic fields at >2 Ga (*Biggin et al.*, 2020).

3.5.5 Global dissipation and its frequency dependence

In a study of the attenuation behaviour of the mantle from long-period seismic to tidal time scales (∼500 s–18.6 yr), *Lau and Faul* (2019) previously applied the extended Burgers rheology and were able to explain dissipation across the studied

period range on the basis of a single frequency exponent. This helped harmonise apparently disparate observations of Earth's mantle attenuation based on surface-wave and normal-mode observations (∼100–3000 s) of *Lekić et al.* (2009) with the geodetically-determined body tide phase lags (12 hr–18.6 yr) of *Benjamin et al.* (2006). *Lekić et al.* (2009) had found that the frequency exponent α was positive toward the lower of period range studied but shifted to negative values at the upper end, while *Benjamin et al.* (2006) found $\alpha \sim 0$, i.e., near-frequency-independent dissipation across tidal time scales.

Thus, while the study of *Lau and Faul* (2019) indicated that a laboratory-based frequency-, temperature-, and grain-size-sensitive visco-elastic model appears to be capable of capturing the observed response behaviour of Earth's mantle from long-period seismic to tidal timescales, they limited consideration to a handful of spheroidal modes to ensure overlapping sensitivity (similar Fréchet kernels) between the mode and tidal $1/Q$ constraints. As a consequence of the restricted number and the particular nature of the normal modes studied (lower-mantle sensitive), the more general question of how well the extended Burgers model is capable of matching mode constraints with sensitivity distributed from surface to center was not addressed.

Here we extend the study of *Lau and Faul* (2019) by considering a much larger data and model parameter problem. To better represent the observed dissipation information, we clustered all spheroidal, toroidal, and radial modes considered here according to the depth sensitivity of the individual modes by computing their Fréchet kernels (see Appendix). The observed global dissipation ($1/Q$), spanning the period range from 100 s to 18.6 yr are shown in Figure 3.9 for a subset of modes and both tides (the entire data set is shown in Figure A.9). We find that the frequency-, temperature-, and grain-size-sensitive visco-elastic model implemented here is indeed capable of capturing a significant part of the observed response behaviour of the Earth. In particular, dissipation as predicted by the extended Burgers model is reasonably well-matched by a dissipation function with a slope given by the range of sampled frequency exponents (α) between 0.26–0.28 (see inset), upper and lower mantle grain sizes in the ranges ∼1 cm and 2–5 cm (inset Figure 3.5e), respectively, and a lower mantle activation volume between $\sim 3\text{–}5 \times 10^{-6}$ $\mathrm{m^3 mol^{-1}}$ (all inverted parameter values are listed in Table 3.5).

Despite the reasonable match, discrepancies are apparent in the fits to several modes that appear to be distributed in all clusters (see also Figure A.9) without any discernable trend. This may possibly signal an inherent limitation of the use of an experimental viscoelastic model that has been calibrated at upper mantle conditions (900–1200 °C), at oscillation periods in the range 1–1000 s, and μm grain sizes, although we have to note that there appear to be as many upper-mantle as

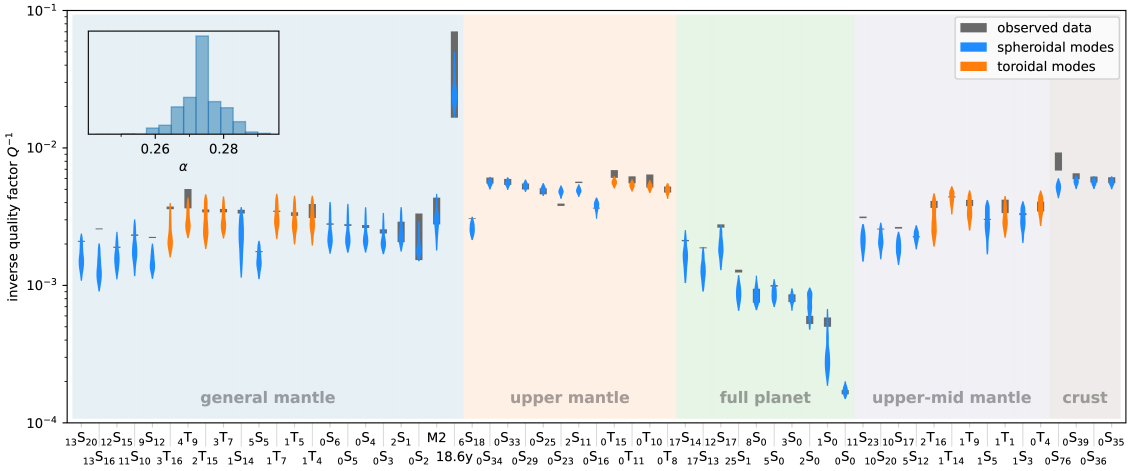

Figure 3.9: Comparison of observed and computed global dissipation ($1/Q$) across the normal-mode and tidal period bands. Modes and tides have been clustered according to their depth sensitivity (described in Appendix). Within each cluster, the modes and tides are ordered with increasing period from left to right. In order to avoid clutter, only a subset of the normal modes considered here are shown (the entire data set is shown in Figure A.9). Observed inverse global quality factors (dissipation) for normal modes and the M2 and 18.6-year tides are indicated by vertical dark grey lines whose vertical extent represents measurement uncertainty. The top inset shows the sampled distribution of frequency exponents (α) that determine Earth's dissipation behaviour with period. Predicted spheroidal and toroidal mode dissipation distributions are indicated by blue and orange violins, respectively. The violins represent 25% credible intervals.

full-planet and general-mantle modes that do not match the dissipation observations.

As mentioned, the extended Burgers models is not the only rheological model available to describe the attenuation behavior of planetary materials; several models are available, including Andrade, Sundberg-Cooper, and the power-law approximation scheme (see e.g., *Bagheri et al.*, 2019, for a geophysical comparison). Application of the other laboratory-based visco-elastic models may prove a better match to our data than the extended Burgers model. We leave it for a future study to consider this in more detail.

3.6 Discussion

In the following, we compare our study with PREM to draw parallels and point out differences from a range of perspectives.

From a data perspective, our study has features in common with PREM. We rely on the latest normal-mode catalogue that contains a significantly updated set of normal modes, both in terms of quantity and quality, that were unavailable at the time PREM was constructed. Uncertainty estimates on centre frequency and shear quality factors have also improved relative to what was available at the time of PREM, where uncertainties on Q measurements average more than 20% as opposed to <5% in *Deuss et al.* (2013). In spite of these improvements, the fit of PREM to

most of the modes considered here is remarkable.

The tidal response data (k_2 and h_2), which were not considered in the construction of PREM, and the modern-day astronomic-geodetic value for the normalised mean moment of inertia of the Earth, indicate a slight mismatch, demonstrating that changes to the PREM density and rigidity profiles are necessary. PREM made use of an extensive set of core-related body wave travel times (PKiKP-PcP, PcP-P, and ScS-S), not accounted for here, to determine outer- and inner-core radius. Since outer- and inner-core radii are fixed to PREM in this study, it can be argued that there is little loss of information in disregarding the aforementioned body waves. Like PREM, our radial seismic velocity models match global P- and S-wave travel times. Finally, we also inverted for an improved model of outer-core P-wave velocity structure by considering a set of differential travel times of multiple SKS reflections from the underside of the CMB (SmKS). While our outer-core P-wave velocity models provide a reasonably good fit to the observations that is better than most outer-core models, subtle differences remain that appear difficult to capture by a homogeneous and well-mixed outer core. Yet, the exact nature of the P-wave velocity gradients needed to fit all SmKS observations remains to be established.

From the point of view of normal modes, better understanding of the effects of normal-mode coupling (*Al-Attar et al.*, 2012; *Yang and Tromp*, 2015; *Akbarashrafi et al.*, 2018; *Robson et al.*, 2022) would allow for improved constraints on outer-core structure through the use of CMB Stoneley modes (*Koelemeijer et al.*, 2013). As for the inner core, the database of inner-core modes has not been considerably enlarged relative to what was available at the time of PREM. For improved models of inner-core structure, more observations of inner-core-sensitive modes are needed that are possibly inverted in combination with core-relevant body wave phases.

From a seismological perspective, the present models also have characteristics in common with PREM. Like PREM, we are only able to constrain the spherically-symmetric structure of the Earth, which represents a mathematical, yet useful, approximation as attested to through numerous seismic tomography models that rely on radial models for regularisation, which is to say that most of the non-linearity in inversion for Earth structure is captured in radial models. Unlike PREM we do not consider a global ocean layer in our model and unlike PREM, which included transverse anisotropy (TI) in the upper mantle to fit Rayleigh and Love surface-wave data simultaneously, we considered a purely isotropic model, since only high-frequency fundamental spheroidal modes, are considered here. In passing, we may note that our lithospheric S-wave velocity model is expected to be more representative of a vertically-polarised S-wave velocity model than a purely isotropic model and that the data fit for some of the higher-frequency fundamental modes may possibly be improved if anisotropy had been included (*Beghein et al.*, 2008). A future study will

have to consider the effect of anisotropy in more detail and allow for inversion of both high-frequency fundamental spheroidal and toroidal modes. Like PREM, we do not incorporate anisotropy in the inner core. The assumption that anisotropy arising from large-scale inner-core lateral thermo-chemical variations is negligible is supported by the observation that isotropically-averaged P-wave speeds are similar in the eastern and western hemispheres (e.g., *Creager*, 1999). The picture is likely more complicated in detail as both normal-mode and body-wave analyses appear to suggest (e.g., *Woodhouse et al.*, 1986; *Shearer*, 1994; *Song*, 1997; *Tromp*, 2001; *Wookey and Helffrich*, 2008), but will be left for a future study.

From a modelling perspective, our model set-up (model parameterisation) shares features in common with PREM, in that both rely on equation-of-state approaches and assume homogeneous, i.e., well-mixed, and adiabatic conditions in the mantle and core, with the exception of the upper mantle in PREM, which is modelled using a linear relationship between density and P-wave velocity (Birch's law), because the premises underlying the Adams-Williamson EoS are not satisfied in the upper mantle (*Butler and Anderson*, 1978). In contrast, we employ Gibbs energy minimization as a means of computing mantle mineralogy and its elastic (and other thermodynamic) properties, as a function of pressure, temperature, and bulk composition from thermodynamic data.

The application of such calculations for geophysical models of the Earth's mantle have become feasible, because of the availability of comprehensive thermodynamic data bases (e.g., *Fabrichnaya et al.*, 2004; *Khan et al.*, 2006; *Matas et al.*, 2007; *Piazzoni et al.*, 2007; *Stixrude and Lithgow-Bertelloni*, 2005a, 2011, 2021; *Khan et al.*, 2021b). A means of measuring the discrepancy between the two approaches is through the Bullen parameter (*Bullen*, 1963), which measures the deviation from the conditions of homogeneity and adiabaticity, i.e., from the conditions of validity of the Adams and Williamson equation, which underlies the computation of properties in the lower mantle and core of PREM. On account of the self-consistent nature of our models, the Bullen parameter equals 1 throughout (base of the lithosphere to the center), while for PREM it is greater than 1 in the upper mantle, below but close to 1 in the lower mantle, and $\sim$1 in the core.

Despite the indications for a thermo-chemically well-mixed mantle in the form of the globally-averaged structure seen by normal modes, there is ample seismic evidence that mantle structure is more complex in detail (see section 3.5.2). Geodynamical models, for example, indicate that the mantle convects in a mode between layered- and whole-mantle convection, wherein slabs penetrate intermittently in space and time (e.g., *Tackley et al.*, 2005; *Yan et al.*, 2020), resulting in heterogeneities at a range of scales below the resolution of the normal modes.

From an attenuation modelling perspective, we considered the anhydrous, melt-

free case that is representative of a low-dissipation end-member model. Addition of both melt and water would likely lead to reduction of the effective viscosity and enhanced dissipation (e.g., *Faul et al.*, 2004; *McCarthy and Takei*, 2011; *Yamauchi and Takei*, 2016; *Takei*, 2017; *Havlin et al.*, 2021). While partial melting has often been cited as a possible physical mechanism for the low-velocity, high-attenuation zone in the upper mantle (*Karato*, 2014), the latter can be explained by purely solid state mechanisms, such as anelastic relaxation (*Jackson et al.*, 2005), without the presence of melt or fluids (see also *Stixrude and Lithgow-Bertelloni*, 2005b). In this context, the laboratory-based visco-elastic model represents a limitation inasmuch as it has been calibrated at conditions relevant to the upper mantle. Application of this model to the lower mantle represents an extrapolation that will need to be verified by future experiments. Notwithstanding this caveat, the frequency-, temperature-, and grain-size-sensitive visco-elastic model implemented here nevertheless captures the response behaviour of the Earth across a frequency range that matches a large part of the observations from ∼100 s to ∼20 yr. Any remaining discrepancies that are present may require the incorporation of more physical details into the dissipation model.

One of the differences in comparison to PREM is that where the latter lacks model uncertainties, our inversion method provides statistical measures of model variability and resolution, with the caveat that the resolving power of the normal modes and tides has not been accounted for. This has been considered in more detail by *Masters and Gubbins* (2003), who showed that normal modes, because of their radial averaging properties, described by sensitivity kernels, only provide radially-averaged rather than point estimates of uncertainty at a specific depth. Thus, while the sampled models presented here do not reflect this additional source of uncertainty, it is nevertheless the case that the range spanned by our sampled models is sufficiently representative of the inherent model uncertainty. The linearised analysis of *Masters and Gubbins* (2003) will need to be extended to a full non-linear investigation in a future study. The uncertainties reported here also do not account for uncertainties associated with the thermodynamic parameters employed for modeling mantle seismic properties and are therefore likely to be underestimated (cf. *Connolly and Khan* (2016) for quantitative modelling of uncertainties associated with phase equilibrium computations). While the derived uncertainties invariably reflect the modelling assumptions that have gone into building our radial seismic model of the Earth (e.g., through choice of thermodynamic database of mantle minerals, mantle rheological model, thermo-chemical parameterisation, and core equation-of-state), we are nevertheless convinced that the models will prove valuable to the community. As a final note in this context, we would like to emphasise that the present models are not meant as a replacement for radial reference models like PREM, AK135, and EK137, but as complementary to these.

Finally, lacking a proper thermodynamic model for computing phase equilibria and physical properties of Fe-Ni-X alloys, where X is either of the possible light alloying elements Si, S, C, O, and H, we employed an EoS approach to modelling the seismic structure of the core. As an alternative, one could assemble a database of seismic properties based on first principles calculations for a set of appropriate core compositions and pressure-temperature conditions. Since the entire system here is solved for self-consistently and therefore allows for quantitative testing against seismic and geophysical observations, it is conceivable that this could lead to a potential improvement in our understanding of core composition over current mineral physics-based approaches that attempt to constrain core composition through qualitative comparison with radial reference models (e.g., *Badro et al.*, 2014, 2015; *Brodholt and Badro*, 2017; *Sakamaki et al.*, 2016; *Umemoto and Hirose*, 2020; *He et al.*, 2022). In any case, the implication of the new low-P-wave-velocity-high-density outer-core model for the composition and light element content of the core, clearly warrants re-examination.

3.7 Conclusion

In this study, we have investigated a set of mineral physics-based models and tested the underlying physical assumptions by inverting a large set of normal-mode centre frequencies and quality (attenuation) factors, including astronomic-geodetic and mantle- and core-sensitive seismic body wave data for the radial elastic and anelastic seismic structure of Earth's crust, mantle, and core. The emphasis here has been on self-consistency, which has ultimately allowed us to integrate different data sets that cover widely separated timescales.

Our new radial seismic model(s) of the Earth include a number of novel features as a result of an expanded set of normal-mode data, on the one hand, and modern-day large-scale geophysical data, on the other hand. Chief among these are density and P-wave velocity changes in the lower mantle and outer core relative to PREM with potential implications for the composition of the core.

With this study, we provide models of all relevant seismic properties and uncertainties, including density, P- and S-wave velocity, bulk and shear moduli, attenuation parameters, gravitational acceleration, pressure, and mantle temperature. Our new seismic model(s) should be of interest to the wider community and will stand to be further tested and refined with the addition of more geophysical data (sets), improved thermodynamic data for modelling mantle mineral phase equilibria, and equation-of-state parameters for modeling the composition of the core.

Chapter 4

On the modeling of self-gravitation for full 3D global seismic wave propagation

This chapter is published in Geophysical Journal International, as *On the modelling of self-gravitation for full 3-D global seismic wave propagation*, M. van Driel, J. Kemper, C. Boehm (2021).

4.1 Introduction

The last decade has witnessed an unprecedented increase in high quality long period seismic data. This is because of the occurrence of several very large Earthquakes that were recorded on an exponentially growing number of broad band seismic stations that are installed in very dense networks such as the USArray. These new data have led to an ever increasing resolution in tomography for seismic velocities. Density however, even though it is a key parameter in models of the geodynamical evolution of Earth's mantle as density differences drive mantle flow, remains poorly constrained.

While tomography based on full 3D simulations of the seismic wavefield has become a standard tool in local to continental scale seismology (e.g. *Tape et al.*, 2009; *Fichtner et al.*, 2009; *Zhu et al.*, 2012; *Virieux and Operto*, 2009; *Warner et al.*, 2013; *Virieux et al.*, 2017), this is not yet the case for whole planet models. Early attempts (*Lekić and Romanowicz*, 2011; *French and Romanowicz*, 2014) used approximations for the gradients and only recently the first global model fully based on the adjoint method became available (*Bozdağ et al.*, 2016; *Lei et al.*, 2020). To the best of our knowledge, no such study exists for the normal mode frequency range. However, it is the long period range in which density is more likely to be accessible than for other seismic observables (*Ishii and Tromp*, 1999; *Koelemeijer et al.*, 2017). The main reason for this discrepancy is the fact that there is no established method to model the full physics of long period seismology in 3D and compute gradients with respect to material properties at reasonable computational cost.

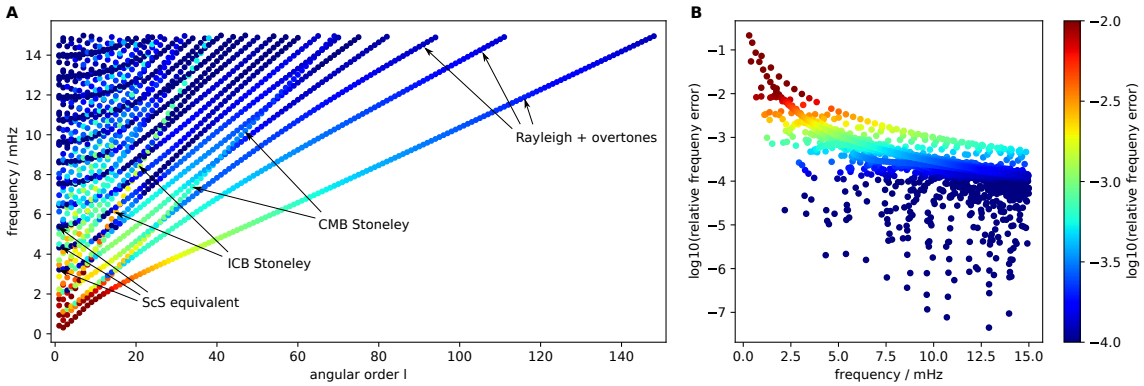

Figure 4.1: Relative error in eigenfrequency / phase velocity due to the cowling approximation for all spheroidal modes up to 15 mHz (equivalent to approximately 66 s period) computed in PREM. A) dispersion diagram, B) error as a function of frequency.

Because density information is contained in the normal mode spectra at relatively small amplitudes compared to the seismic velocity structure, an accurate implementation of the underlying physics is required. The widely used splitting functions are based on the self- or group-coupling approximation, which introduces an error on the same order of magnitude as the effect of density perturbations itself (*Akbarashrafi et al.*, 2018). Another difficulty in normal mode coupling theory arises from the linearization of the effects of boundary perturbations such as topography, ellipticity and crustal thickness, though recent work by *Al-Attar et al.* (2018) addresses this issue by means of a particle relabling transform. In related work, *Maitra and Al-Attar* (2019) apply the same spatial mapping to the Poisson equation to derive an efficient and numerically exact solution in aspherical planets.

In contrast, time domain methods such as the spectral element method, usually avoid the full implementation of gravity and use the Cowling approximation instead (e.g. *Komatitsch and Tromp*, 2002b). This approximation assumes that the gravitational potential is constant in time and ignores gravity perturbations caused by the seismic displacement itself. The theory describing the complete gravity physics is however well established and demonstrated to work with the spectral element method (*Chaljub and Valette*, 2004).

Fig. 4.1 shows the relative error caused by the Cowling approximation in eigenfrequency or, equivalently, phase velocity for all spheroidal modes up to 15 mHz in PREM (*Dziewonski and Anderson*, 1981) in a dispersion diagram (A) and as a function of frequency (B). As expected, a clear tendency of a decreased error with increased frequency is apparent and the error is largest for the lowest frequency modes. However, especially at higher frequencies the error also depends on the mode type: the lowest error is seen for the ScS equivalent modes with very low group velocity at low angular degree. A slightly higher error level is exposed by the fundamental mode Rayleigh waves and their overtones. Most sensitive are the CMB and ICB Stoneley modes as well as the core modes. This pattern can be explained by the

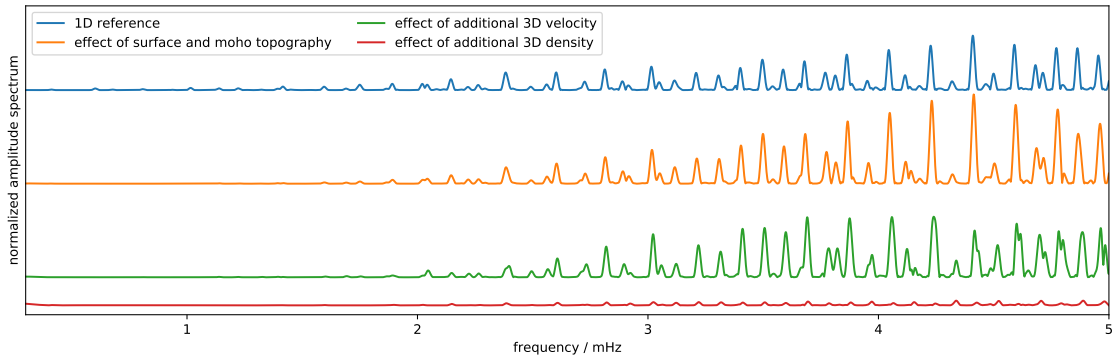

Figure 4.2: Long period amplitude spectra computed from 32 hours of synthetic seismograms computed with the spectral element method without accounting for gravity for four different models: 1D mantle and crust (blue), amplitude of the difference caused by adding topography and Moho topography (orange), 3D variations in seismic wave speeds according to S20RTS (green) and variations in density scaled from S-wave wave speed with a factor 0.3 (red).

displacement eigenfunctions: while vertical displacement across density contrasts directly perturbs the gravitational potential (e.g. Rayleigh and Stoneley modes), the perturbation is smaller for horizontal displacements where the density change is only due to the normal strain (e.g. ScS modes). That said, the ICB Stoneley and core modes are of lower importance in many applications focused on the mantle, as they cannot be easily excited directly by an earthquake in the crust or upper mantle. The Cowling approximation can be considered sufficiently accurate for frequencies above 5-10 mHz in most applications.

While not yet common, it is in principle possible to compute long period spectra using time domain methods (e.g. *van Driel and Nissen-Meyer*, 2014; *Nissen-Meyer et al.*, 2014). Fig. 4.2 shows amplitude spectra for the vertical component seismogram recorded at the black forest observatory in Germany for the Tohoku Oki event. The spectra are computed from 32 hours of elastic 3D time domain spectral element wave propagation and ignore the effects of gravity, which we are addressing in the following. The incremental change from addition of surface and Moho topography, 3D velocities and density from S20RTS (*Ritsema et al.*, 1999) is computed as the absolute value of the complex difference of the spectra. Large phase shifts thus cause differences to exceed the 1D reference spectrum in amplitude. It is apparent that the strongest effect is from surface and Moho topography (including ellipticity) and the effect of lateral velocity variations is only marginally smaller. The effect of density however is an order of magnitude smaller, confirming the necessity for accurate modeling. As the dispersion error in time domain simulations accumulates over long propagation distances, correction for the dispersion error caused by the time stepping scheme (e.g. *Koene et al.*, 2018) is an attractive alternative to more accurate time integration (e.g. *Nissen-Meyer et al.*, 2008).

Two main challenges arise in including full self-gravitation in the 3D spectral el-

ement method: while the purely elastic simulations can be formulated in a fully explicit way and only require the computation of matrix-vector products, self-gravitation couples a Poisson equation into the system that needs to be solved in each time step. The cost of solving this system exceeds the cost of the elastic terms by far (*Chaljub et al.*, 2007), rendering this unpractical, in particular for inverse problems. Secondly, the spatial domain of the equation extends to the full space, with a boundary condition at infinity that cannot be treated directly by a standard space-discretized method.

We address both these issues in an effort towards the inclusion of the full physics for long period seismology in an efficient spectral element method. In section 4.2 we introduce the problem in quantitative terms and detail the steps towards an efficient solution. In section 4.3 we then apply these methods to the Poisson problem using the wavefield from a purely elastic simulation as a test case.

4.2 Methods

4.2.1 Problem Statement

The Poisson equation defining the perturbed gravitational potential is given by (e.g. *Chaljub and Valette*, 2004)

$$\nabla^2\psi = \begin{cases} -4\pi G\nabla\cdot(\rho\mathbf{u}) & \text{in } \Omega_e \\ 0 & \text{in } \mathbb{R}^3 \setminus \Omega_e, \end{cases} \tag{4.1}$$

where G is the gravitational constant, ρ is the mass density $\mathbf{u}$ is the seismic displacement and Earth is denoted by Ω_e. ψ vanishes at infinite distance from Earth and is continuous everywhere including at Earth's discontinuities and surface. The normal derivative of ψ is discontinuous at these interfaces and the jump is controlled by

$$[\nabla\psi\cdot\hat{\mathbf{n}}]_\Sigma = -4\pi G[\rho\mathbf{u}\cdot\hat{\mathbf{n}}]_\Sigma. \tag{4.2}$$

In the fluid parts, the seismic displacement can be computed from the displacement potential(s). The right hand side of eq. (4.1) – referred to as RHS in the following – has two contributions: 1) the change of density due to compression or dilation of the medium and 2) the displacement of material with heterogeneous density, including motion perpendicular to internal discontinuities and the free surface.

4.2.2 Boundary Conditions

One difficulty for the numerical solution of Poisson's equation is that the domain is the full $\mathbb{R}^3$ with a homogeneous Dirichlet boundary condition that needs to be applied at infinity. *Chaljub and Valette* (2004) approach this problem using a Dirichlet-to-Neumann operator to derive a Robin-type boundary condition at a spherical boundary large enough to compensate for Earth's non-spherical shape. This method requires computation of the spherical harmonic transform of the potential at this boundary in each iteration to couple it to the analytical solution in the outer domain. As an alternative, *Gharti and Tromp* (2017); *Gharti et al.* (2018) propose to use infinite elements to virtually extent the domain by mapping one face of the finite elements to infinity. The efficacy of this method is based on the fact that the potential decays with distance and this can be accommodated in the space of test functions. To maintain the convergence order, a Gauss-Radau quadrature rule is then used in the radial direction which avoids the evaluation of the basis polynomials on the outer boundary. In contrast, we use the same quadrature in all elements both in the interior and exterior domain.

Here we argue for a different approach: it is the low-order terms of the solution that are most sensitive to the outer boundary condition, as they decay with low powers of $1/r$. Higher-order terms decay quickly with distance from Earth's surface. We thus use the analytical solution given by the multipole expansion to derive the Neumann boundary condition at a finite radius. This is similar to the approach by *Chaljub and Valette* (2004) but instead of computing the spherical harmonic expansion over the surface of the domain in each iteration of the conjugate gradient solver, it requires computation of the expansion of the RHS of eq. (4.1) over the volume of the Earth only once per time step. The Neumann boundary condition only determines the potential up to an additive constant in contrast to a Dirichlet condition at infinity, however, the resulting forces in the wave equation only require the gradient of the potential and are insensitive to such a constant. While in theory a Dirichlet condition may be preferred, it requires the splitting of the solution into a homogeneous and inhomogeneous solution, elimination of the degrees of freedom on the surface from the linear system or introduction of a penalty term on the boundary. As we found no convergence issues with the Neumann condition, it is the preferred solution due to its simplicity.

The Neumann boundary condition can be written as

$$\nabla\psi \cdot \mathbf{n} = g, \qquad \text{on } \partial\Omega, \tag{4.3}$$

where Ω with $\Omega_e \subset \Omega \subset \mathbb{R}^3$ denotes the finite computational domain. As the RHS of eq. (4.1) is compactly supported within Earth, the exterior field can be expanded

into the multipole series in powers of $1/r$

$$\psi = \sum_{l=0}^{\infty} \sum_{m=-l}^{l} \sqrt{\frac{4\pi}{2l+1}} \frac{q_{lm}}{r^{l+1}} Y_{lm} \qquad \text{in } \mathbb{R}^3 \setminus \Omega_e, \tag{4.4}$$

where Y_{lm} are the complex valued spherical harmonic functions and q_{lm} are the spherical multipole moments,

$$q_{lm} = \sqrt{\frac{4\pi}{2l+1}} \int_{\Omega_e} G\nabla \cdot (\rho \mathbf{u})\, r^l\, Y_{lm}^*\, \mathrm{d}V. \tag{4.5}$$

The radial derivative needed to obtain the Neumann boundary condition according to eq. (4.3) if we assume Ω to be spherical can then be calculated directly:

$$g = -\sum_{l=0}^{\infty} \sum_{m=-l}^{l} \sqrt{\frac{4\pi}{2l+1}} (l+1) \frac{q_{lm}}{r^{l+2}} Y_{lm}. \tag{4.6}$$

For the problem to be well-posed, the Neumann boundary condition needs to fulfill the compatibility condition, i.e. we need to demonstrate that

$$\int_{\partial\Omega} g\, \mathrm{d}S = -4\pi \int_{\Omega_e} G\nabla \cdot (\rho \mathbf{u})\, \mathrm{d}V. \tag{4.7}$$

As the surface integral over spherical harmonics vanishes for all terms other than the monopole term with $l = 0$, it can be shown with the help of eq. (4.5) and (4.6) that g indeed satisfies the compatibility condition and

$$\int_{\partial\Omega} g\, \mathrm{d}S = -4\pi q_{00}. \tag{4.8}$$

In practice, the multipole expansion needs to be truncated to a maximum degree $l_{\max}$. Fig. 4.3 shows the maximum angular degree of the exterior solution as a function of the radius based on a threshold ε of the multipole expansion (4.4):

$$\frac{1}{r^{l+1}} = \varepsilon. \tag{4.9}$$

This relation can be used both to determine the $l_{\max}$ for the boundary condition given the domain size as well as the lateral element size in the exterior domain.

Similar to the truncation of the series we employ here, infinite elements also incorporate terms up to a maximum power of $1/r$ only and the exponent is equal to the polynomial order of the Lagrange basis in radial direction in the layer of infinite elements (eq. 25-27, *Gharti et al.*, 2018), and this order can be chosen independently of the polynomial order in the volume elements. With a polynomial order of 2,

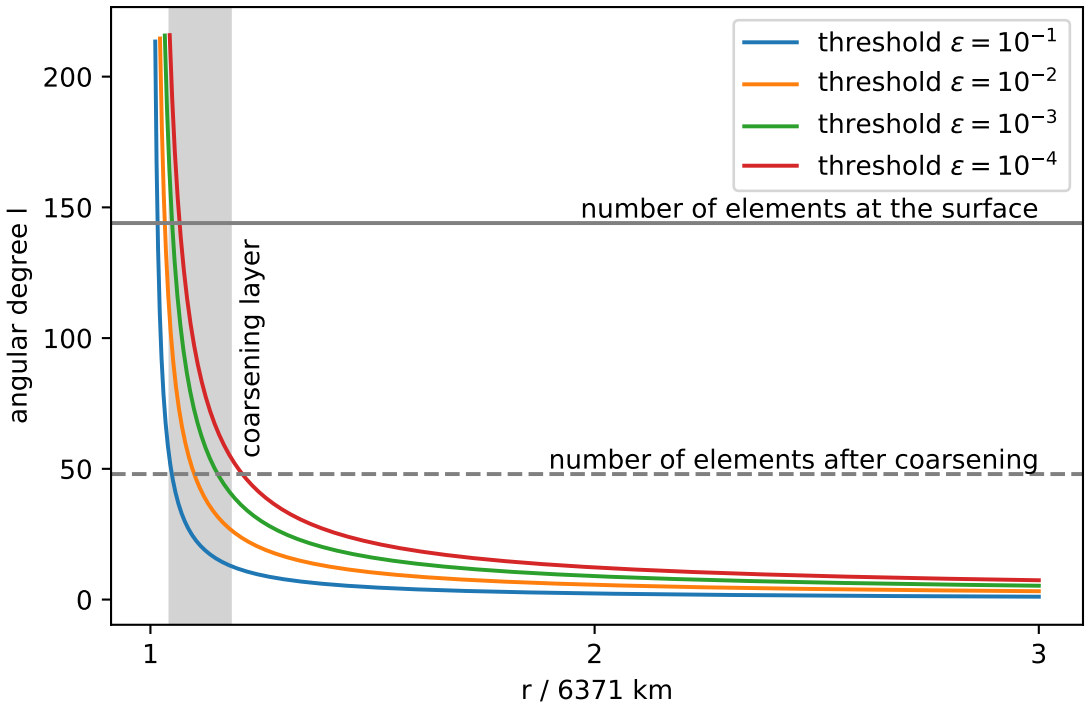

Figure 4.3: Maximum angular degree of the perturbed gravitational potential as a function of the radius for a range of threshold values ε. The number of elements in lateral direction and location of the coarsening layer of the mesh in Fig. 4.4 are indicated in grey.

however, as used in the numerical examples by *Gharti and Tromp* (2017) and *Gharti et al.* (2018), a significant buffer layer of normal spectral elements between the Earth's surface and the infinite elements is hence needed to achieve the required accuracy for the perturbed gravitational potential at all angular degrees present in the solution. Unfortunately, the authors are not aware of a quantitative test of infinite elements for high angular degrees, but assume that the required size of the domain and hence the total number of elements needed in the mesh will be similar to the one needed with the truncation of the Neumann boundary condition at the same angular degree.

4.2.3 Discretization

In order to apply the spectral-element method (SEM, *Patera*, 1984; *Chaljub et al.*, 2007) to the Poisson equation, it needs to be written in the weak form. This is achieved by multiplication of eq. (4.1) with a test function φ and integration by parts:

$$\int_\Omega \nabla\psi \cdot \nabla\varphi \,\mathrm{d}V = -4\pi G \int_{\Omega_e} (\rho\mathbf{u}) \cdot \nabla\varphi \,\mathrm{d}V + \int_{\partial\Omega} \nabla\psi \cdot \hat{\mathbf{n}}\varphi \,\mathrm{d}S. \tag{4.10}$$

The surface integral over $\partial\Omega$ on the right hand side and surface integrals over internal interfaces vanish due to the jump condition eq. (4.2). The jump condition is hence readily and implicitly included in the weak form, which is equivalent to the strong form of the equation provided that it holds for all test functions φ from an appropriately chosen set. The last term can be identified with the Neumann boundary condition:

$$\int_{\partial\Omega} \nabla\psi \cdot \hat{\mathbf{n}}\varphi \,\mathrm{d}S = \int_{\partial\Omega} g\varphi \,\mathrm{d}S. \tag{4.11}$$

We then subdivide the domain into hexahedral elements and use the standard SEM with Gauss quadrature on the Gauss-Lobatto-Legendre (GLL) points with Lagrangian interpolation functions to write the eq. (4.10) in matrix form:

$$\mathbf{K}\boldsymbol{\psi} = \mathbf{f}. \tag{4.12}$$

Here $\mathbf{K}$ is the stiffness matrix, $\boldsymbol{\psi}$ is the vector of degrees of freedom and the right hand side $\mathbf{f}$ contains both the density perturbation and the Neumann boundary condition.

For this study, we explicitly compute $\mathbf{K}$ and assemble it as a sparse matrix. While most codes that aim at optimal performance avoid this assembly and use matrix-free implementations, we chose the matrix-based approach for its simplicity, allowing for an implementation in Python and relying on available libraries to achieve acceptable performance in the solver for the purpose of this paper. For a production code that would couple directly to the seismic simulation, a large part of the implementation is equivalent to acoustic wave propagation that can hence be reused. Here we only discuss performance in terms of number of iterations and not in terms of actual runtime, so that this less efficient implementation can be ignored.

4.2.4 Meshing

Cubed sphere meshing (*Ronchi et al.*, 1996) in combination with deformed regularly gridded cube and lateral refinements by doubling or tripling layers has been established as the standard method in numerical global seismic wave propagation (e.g. *Komatitsch and Tromp*, 2002a; *Chaljub and Valette*, 2004). This approach can naturally be extended to also include the outer domain as shown in Fig. 4.4. While doubling layers in theory allow to better approximate the desired element size based on the S-wave length, we find tripling layers to be easier to locate. This is because fewer refinements are need to achieve the same change in element size and tripling layers only span one element in radial direction compared to three elements for the doubling on the full sphere due to the continuity conditions at the boundaries of the

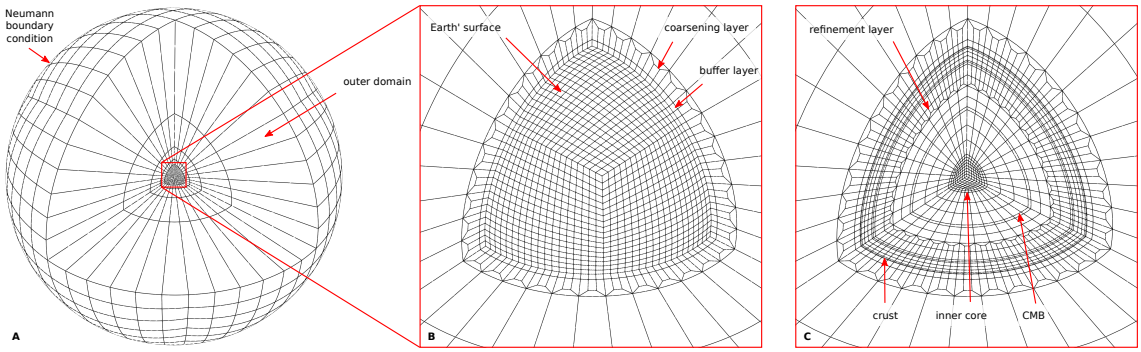

Figure 4.4: Cubed sphere mesh including the outer domain resolving seismic waves at 200 s with 2 elements per wavelength. (A) overview (B) zoom to the red box and (C) a view into the interior of Earth. This mesh is build with tripling layers, doubling layers can also be used but are more difficult to locate for very long period meshes.

cubed sphere chunks (see (Fig. 4 *Komatitsch and Tromp*, 2002a)). The resulting meshes have very similar numbers of elements for long period meshes. Furthermore, the smallest elements that determine the time step due to the Courant-Friedrichs-Lewy (CFL) condition are always located in the crust in this application, as the radial element size is constrained by the crustal thickness to have an element boundary conforming with the Moho. Also note that we employ elements that approximate the spherical shape with polynomials at the same order as the test functions so that much fewer elements are required to achieve acceptable accuracy (*van Driel et al.*, 2020, Fig. 8-9).

While the element size within Earth is constrained by the local S-wave length and we assume this to be a conservative choice for the perturbed potential, there is no such constraint on the element size in the exterior domain. As can be seen from Fig. 4.3, the lateral complexity of the perturbed potential decays rapidly with increasing distance from Earth's surface and this can be accounted for by coarsening the mesh using a tripling layer in the same way as in the mantle. Furthermore, the potential decreases monotonically as a function of the radius in the exterior domain. While the decay can be on short distances just above the free surface, the complexity is extremely low at larger radii. This suggests that the radial element size needs to be smaller close to Earth's surface and can then increase rapidly with distance.

To accommodate these constraints, we extend the mesh with a first layer of approximately isotropic elements, where the size is given by the S-wave length in the crust. This buffer layer is followed by a coarsening layer that increases the lateral element size by a factor of three. Finally, we add a configurable number of elements that increase in size with distance, where the radial nodes are computed as $r_i = r_0 + h_0 \cdot \mathrm{dr}^i$. Here r_0 and h_0 are the radius and lateral element size of the preceding layer of elements and dr is a parameter to tune the element growth rate to the complexity of the solution. For the range of number of elements in radial direction (up to about 10) and values for dr between 1.3 and 3, this keeps the aspect

ratio of the elements in an acceptable range to avoid potential ill-conditioning of the system.

We will determine the necessary domain size as well as an appropriate element shape empirically in section 4.3.1. With this meshing approach the number of elements in the outer domain is only a fraction of the total number of elements (21% for the mesh shown in Fig. 4.4 where the exterior domain has a radius 14.5 times the Earth radius). One third of these are located in the first layer above Earth's surface that is needed in any case to include topography in the approach by *Chaljub and Valette* (2004) or the infinite elements in the approach by *Gharti and Tromp* (2017). This shows that the potential gains from using the infinite element method instead of adaptive mesh refinement and the Neumann boundary discussion as discussed here are relatively small, even if a higher polynomial order in the radial direction was used in the infinite elements to avoid the additional buffer layers discussed above.

4.2.5 Initial Solution

The number of iterations needed to solve the Poisson equation can be significantly reduced if a suitable initial solution is known. In the case of the self-gravitation, the right hand side is computed from the time-dependent displacement, which only changes marginally between time steps. For global simulations at long period, this is even more pronounced because the crust is much thinner than the wavelength. The explicit time-stepping used in the spectral element method is then limited by the CFL condition to values smaller than approximately 0.5 s, with the exact value depending on the crustal velocity and thickness model as well as the surface topography resolution. On the other hand, solutions from preceding time steps are only known to finite numerical accuracy and this may render extrapolation unstable for high order schemes.

Here, we compare three extrapolation methods: First, we use the solution of the previous time step as initial solution,

$$\psi_i = \psi_{i-1}, \tag{4.13}$$

where the index indicates the time step.

Second, linear extrapolation can be written as

$$\psi_i = 2\psi_{i-1} - \psi_{i-2}, \tag{4.14}$$

and finally a quadratic extrapolation is given by

$$\psi_i = 3\psi_{i-1} - 3\psi_{i-2} + \psi_{i-3}. \tag{4.15}$$

We evaluate these in a numerical experiment in section 4.3.1.

4.2.6 Multigrid Solver

The convergence rate of iterative solvers depends on the scale length of the solution, with a higher convergence rate typically associated to the shorter wavelength component of the solution (e.g. *Wesseling*, 1992). Combining multiple discretizations that vary in their spatial resolution, this can be exploited to speed up the overall convergence. In the case discussed here, the element size is dictated by the S-wave velocity and the solution to the Poisson equation is dominated by longer scale components, which suggests that a multigrid approach may improve the convergence significantly. As we work with fully unstructured meshes, no straightforward coarsening of the mesh exists, in contrast to the hierarchical meshes often uses (e.g. *Bank et al.*, 1988; *May and Knepley*, 2011). However, the polynomial basis we employ typically has a polynomial degree $p = 4$. Thus, bases with lower polynomial orders on the same mesh can then be used to create a coarser spatial discretization (e.g. *Craig and Zienkiewicz*, 1985; *Foresti et al.*, 1989; *Helenbrook et al.*, 2003; *Bello-Maldonado and Fischer*, 2019).

For two polynomial spaces P_m and P_n with different orders m and n, the projection of an element φ_m from P_m into P_n is defined as the solution to

$$\varphi_n = \arg\min_{\varphi \in P_n} \frac{1}{2} \|\varphi - \varphi_m\|^2_{L^2(\Omega)}. \tag{4.16}$$

This is a strictly convex problem with a unique solution satisfying

$$(\varphi_n, \varphi) = (\varphi_m, \varphi) \quad \text{for all } \varphi \in P_n, \tag{4.17}$$

where

$$(f, g) = \int_\Omega f(\mathbf{x}) g(\mathbf{x}) \, d\mathbf{x} \tag{4.18}$$

denotes the L^2 inner product on Ω. Because the lower-order polynomial space is a subset of the higher-order space, the mapping to higher orders is exact and we simply obtain $\varphi_n = \varphi_m$ for $n \geq m$. However, in case $n < m$, the projection requires the solution of the linear system defined by eq. (4.17) with the Gram matrix

$$\mathbf{G}^n_{ij} = (\varphi^i_n, \varphi^j_n), \tag{4.19}$$

for basis vectors $\varphi^i_n, \varphi^j_n \in P_n$ and a right hand side $\mathbf{b}$ defined by

$$b_i = (\varphi_m, \varphi^i_n). \tag{4.20}$$

Here it is important to use exact integrals and not the Gauss-Lobatto quadrature rule as used by the spectral-element method, because the latter is only exact up to order $2n-1$ and thus not suitable for computing eq. (4.18).

In the following we require the projection to lower orders only for the RHS of eq. (4.1). The RHS is allowed to be discontinuous at element boundaries, so we can use the locally optimal projection in each element. Furthermore, because the 3D SEM basis is formed by the tensor product of the 1D basis, the 3D mapping matrices are obtained by solving the linear system mentioned above in 1D and applying the resulting projection to the three dimensions subsequently. In the following, we refer to the mapping of the 3D SEM basis from order m to n as $\mathbf{P}^{mn}$.

In the application discussed here, a good initial solution is available from the extrapolation from previous time steps, see previous section. Hence, the residual only needs to be reduced by a small factor and this allows to apply a simplified multigrid approach with N stages, going through each stage exactly once. We denote the full resolution as stage 0 and indicate the stage with an upper index on all variables. The Poisson equation to be solved can then be written in the form

$$\mathbf{K}^0 \boldsymbol{\psi}^0 = \mathbf{f}^0. \tag{4.21}$$

Assuming that a good initial solution $\boldsymbol{\psi}_0^0$ is available, the residual is defined as

$$\boldsymbol{\epsilon}^0 = \mathbf{f}^0 - \mathbf{K}^0 \boldsymbol{\psi}_0^0. \tag{4.22}$$

Due to the linearity of the equation, the residual can be used as a right hand side to solve for the correction to the initial solution. To improve the convergence rate, we first solve this equation at lower polynomial order and use the result as an initial solution in the next higher order stage. This process is iterated until reaching the highest resolution stage. In each stage n of the multigrid starting at the coarsest discretization we hence first compute the right hand side by restricting the residual to the polynomial order of this stage:

$$\boldsymbol{\epsilon}^n = \mathbf{P}^{0n} \boldsymbol{\epsilon}^0. \tag{4.23}$$

Note that the right hand side does not need to be continuous across element boundaries so the restriction to the lower order is local to each element. Then, the solution is smoothed using several conjugate gradient iterations to reduce the error on

$$\mathbf{K}^n \boldsymbol{\psi}_{\boldsymbol{\epsilon}^n}^n = \boldsymbol{\epsilon}^n, \tag{4.24}$$

where the subscript on $\boldsymbol{\psi}$ indicates on which stage and corresponding right hand side it was computed and the superscript indicates the discretization stage. While

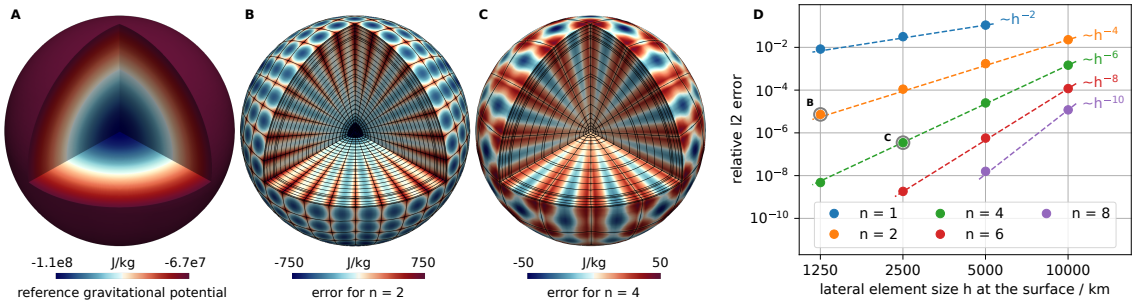

Figure 4.5: Verification of the numerical implementation by comparison to the semi-analytical solution of the gravitational potential in PREM, shown in A. B and C show the difference of the numerical to the analytical solution for polynomial order $n = 2$ and $n = 4$, respectively, and using different element sizes. D shows the convergence rates with respect to mesh refinement for a range of polynomial orders n, the gray circles indicate the two examples shown in B and C.

on the coarsest stage we use a zero initial solution, the initial solution for the other stages is computed by interpolation:

$$\boldsymbol{\psi}^{n-1}_{\boldsymbol{\epsilon}^n} = \mathbf{P}^{nn-1}\boldsymbol{\psi}^{n}_{\boldsymbol{\epsilon}^n}. \tag{4.25}$$

Ultimately, the final solution at the full resolution is obtained by correcting the initial solution $\boldsymbol{\psi}^0_0$ accordingly:

$$\boldsymbol{\psi}^0 = \boldsymbol{\psi}^0_0 + \boldsymbol{\psi}^0_{\boldsymbol{\epsilon}^0}. \tag{4.26}$$

4.2.7 Solver Verification

To verify the correct implementation of our numerical solver, we compute the gravitational potential for the 1D PREM density and compare it to the semi-analytic solution obtained by numerical integration over the radius of the planet (e.g. *Dahlen and Tromp*, 1998). While the homogeneous Dirichlet condition at infinity was assumed to require a large computational domain in previous work (*Gharti and Tromp*, 2017), we apply the Neumann boundary condition for the monopole term (the only non-zero term in the multipole expansion in this 1D example) directly at Earth's surface. While this offsets the potential by a constant relative to a solution with homogeneous Dirichlet condition at infinity, the absolute value of the potential has no physical significance. The resulting gravitational force is given by the gradient of the potential, rendering the force invariant under the addition of a constant to the potential. To measure the quality of the numerical solution, we hence subtract the mean value from the difference to the analytical solution, see Fig. 4.5.

For a finite element based method, the more difficult challenge in this test case is the accurate representation of the spherical shape. While analytical mappings between the reference coordinates in each element and the physical coordinates could be used in this exactly spherical case (compare e.g. *Chaljub and Valette*, 2004;

Nissen-Meyer et al., 2007), we prefer a more generic approach using polynomial approximations to be able to include topography at a later stage. The accuracy of approximating the sphere by polynomials on the GLL points with relatively few elements is demonstrated by *van Driel et al.* (2020). Here, we use the same polynomial order for the shape representation as for the test functions, i.e. we use isoparametric elements. This choice is the reason that for polynomial orders $n \geq 2$ the convergence rate seen in Fig. 2.7D is approximately $n + 2$: not only is the solution represented more accurately, but additionally the accuracy in representing the spherical shape improves with increased order and decreased element size.

In the first order shape representation $n = 1$ that is commonly used in seismology, when placing the nodes of the elements on the planet's surface, the volume of the sphere is systematically underestimated. This explains the particularly slow convergence.

On the other hand, the meshes in the Poisson problem are designed for seismic wave propagation primarily, and assuming a crustal S-wave velocity of 3.2 km/s, the lateral element size at the surface is 1600 km when using two elements per wavelength at 1 mHz. Using $n = 4$ for the shape approximation is hence a conservative choice to avoid errors in the potential and $n = 2$ is likely sufficient for meshes designed for shorter periods.

4.3 Application to Seismic Waves

To verify our approach, we consider the Poisson problem where the right hand side is computed from a purely elastic seismic wave propagation ignoring the coupling between the gravitational potential and the seismic displacement. Although self-gravitation has a significant effect on the longest period modes, we consider this to be a realistic test case to evaluate the performance of the Poisson solver separately. A snapshot from such a simulation is shown in Fig. 4.6.

The seismic simulation is based on the mesh shown in Fig. 4.4, designed to resolve S-waves at 200 s with 2 elements per wavelength in the PREM velocity model and uses the Salvus wave-propagation software package (*Afanasiev et al.*, 2019). This results in a total of 105K elements, 21% of which are in the exterior domain. The source is the centroid solution of the Tohoku Oki earthquake with a half-duration of 100 s and the snapshot is taken 900 s after the quake. With a time step of 0.34 s governed by the stability condition for elements in the crust, the computational time was 16 s on two Nvidia Titan X GPUs. In the fluid part of the core, the displacement shown in A is computed as the gradient of the displacement potential times the density. From the displacement, we compute the RHS according to eq. 4.1 and then solve the discrete system (eq. 4.12) using the conjugate gradient method

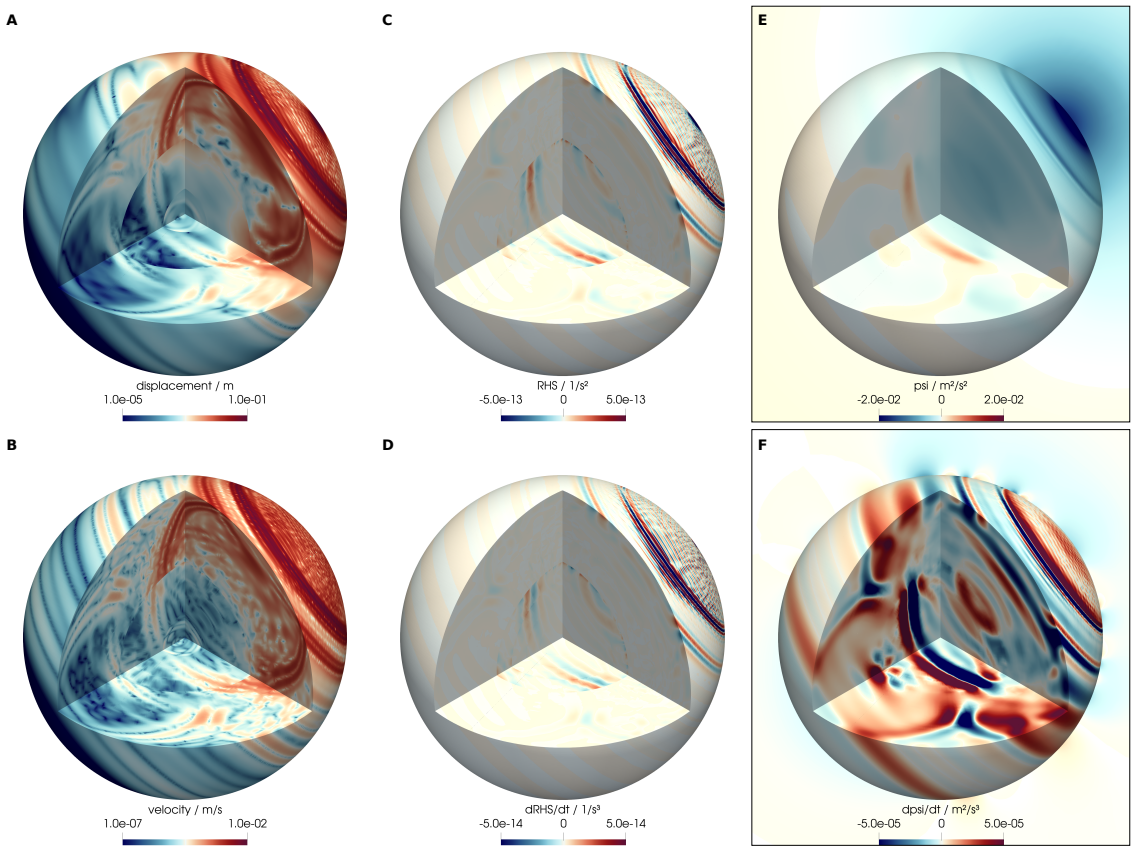

Figure 4.6: Snapshots of the absolute value of displacement (A), RHS (C) and resulting potential (E) as well as their time derivatives (B, D, F) 900 s after the Tohoku Oki earthquake computed in the mesh shown in Fig. 4.4. Note that the visible element boundaries in the RHS are expected, as it is not continuous. E and F include a slice through the center of the planet and perpendicular do the line of sight in the external part of the domain. The color scales are logarithmic in A and B and linear in C-F.

with a diagonal Jacobi preconditioner and homogeneous Neumann conditions for simplicity. We use the same mesh (within the volume of the Earth) and polynomial order as in the elastic simulation, resulting in a total of approximately 800 iterations to achieve a residual of 10^{-5}, which was determined by *Chaljub and Valette* (2004) as sufficiently accurate.

Fig. 4.6 shows both the fields as well as their time derivatives. While the potential is dominated by the static displacement close to the source, the time derivative also shows significant contributions from Rayleigh and P-waves. Love and S-waves have a very small contribution to the right hand side of eq. (4.1) as they have no associated divergence and only contribute by translating material with a density gradient. However, at the free surface and the core mantle boundary, P to S converted phases are clearly visible both in the RHS and the resulting potential. These observations confirm the expectations discussed in Fig 4.1.

In the following subsections, we use several time steps around this snapshot to evaluate the efficiency of the numerical approach described in section 4.2.

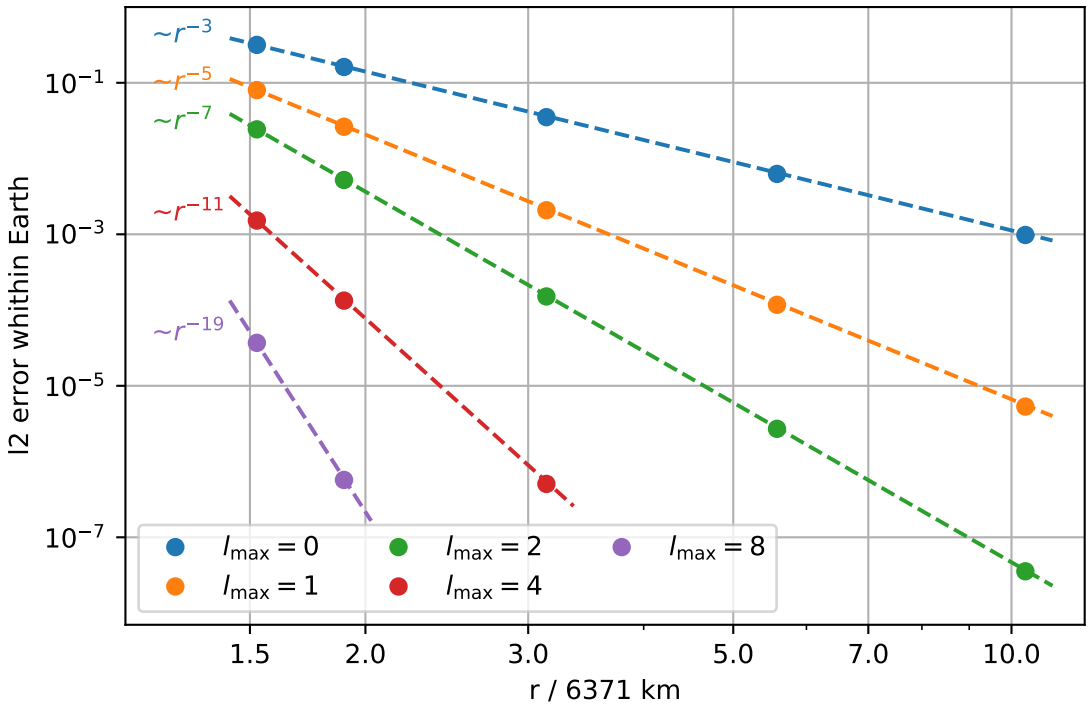

Figure 4.7: Convergence of the solution within the Earth as a function of the exterior domain radius and the maximum degree used in the multipole expansion for the Neumann boundary condition.

4.3.1 Boundary Condition Verification

To verify the Neumann boundary conditions introduced in section 4.2.2 and choose appropriate values for the exterior domain radius and maximum degree $l_{\max}$ in the multipole expansion of the RHS, we perform a convergence test, see Fig. 4.7. The reference solution was calculated with $l_{\max} = 16$ and a radius of r =38.1·6371 km, so that the error due to the finite domain size can be neglected. The element growth parameter is constant dr = 1.4 for all cases (see the following subsection and Fig 4.8).

This test shows empirically, that the L^2 error within the volume of the Earth computed relative to the reference solution converges depending on the radius of the computational domain r_Ω as $r_\Omega^{-(2l_{\max}+3)}$. Due to this fast convergence, relatively low values for both r_Ω and $l_{\max}$ lead to sufficient accuracy of the solution. A final choice depends on the trade-off between using more elements or more expansion coefficients, but $r_\Omega \approx 3r_{\text{Earth}}$ and $l_{\max} = 4$ appear to be reasonable values.

Higher values of $l_{\max}$ were suggested by *Chaljub and Valette* (2004), presumably because in their numerical tests they assumed a spherical Earth and applied the boundary condition directly on the free surface. As can be seen from Fig. 4.7, it is likely more efficient to extent the domain to some degree rather than just increasing $l_{\max}$: the cost of the multipole expansion scales with $l_{\max}^2$ and the number of elements scales subproportionally with r_Ω due to the increasing radial element

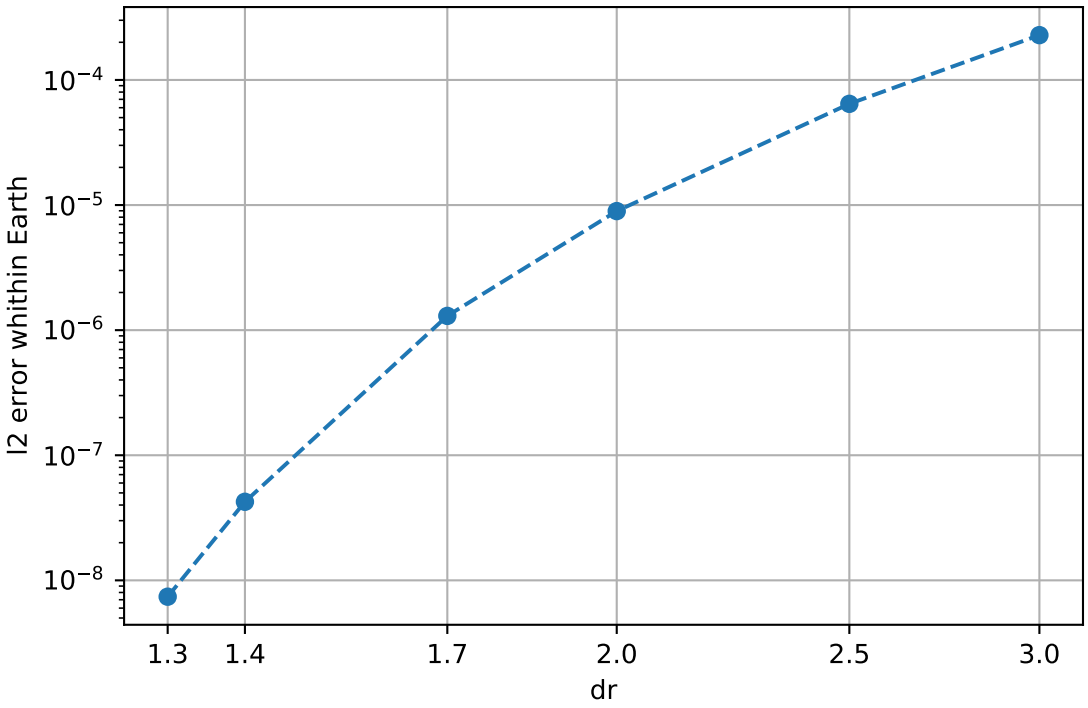

Figure 4.8: Convergence tests for the radial element growth rate dr in the outer domain.

size even without a coarsening layer.

4.3.2 Exterior Mesh Verification

Fig. 4.7 also gives an indication for the required lateral resolution as a function of the radius, confirming our assumption that lateral coarsening can be applied relatively close to Earth's surface. The remaining question particularly concerns the radial element size in the exterior domain. Fig. 4.8 shows the L^2 error computed within Earth relative to a reference solution computed with dr $= 1.2$. In all cases, the exterior domain had 8 elements in radial direction and $l_{\max} = 16$, to ensure that the boundary condition does not contribute to the error.

The result suggests that dr should be chosen slightly below a value of 2 to achieve an accuracy of 10^{-5}, i.e. a bit less aggressive than what was used to generate the mesh in Fig. 4.4

4.3.3 Accuracy of initial solutions

To evaluate the accuracy of the three different extrapolation schemes discussed in section 4.9, we compute the perturbed potential corresponding to four consecutive time steps to a residual of 10^{-5} and then compare the extrapolation from the preceding one, two or three steps, respectively, to the numerical solution of the last one.

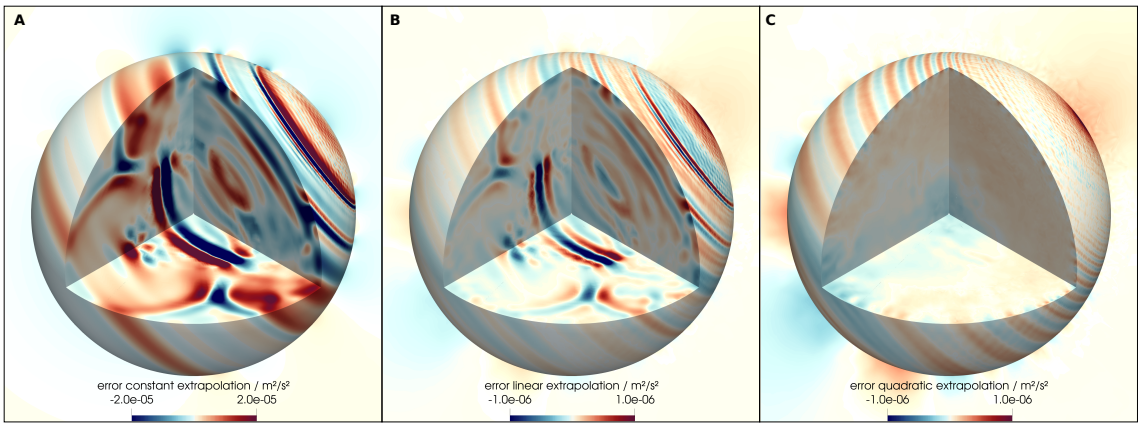

Figure 4.9: Accuracy of constant (A), linear (B) and quadratic (C) extrapolation in terms of the difference relative to the numerical solution of the potential in the next time step. See Fig. 4.6(E) for the potential itself and note the different color scales in (A) vs (B) and (C), the corresponding residuals are shown in Fig. 4.10.

The time between two steps in this case is 0.34 s using a single crustal layer with a thickness of 25 km. For applications with crustal thickness variations the CFL condition will dictate a smaller time step, which will improve the extrapolation relative to the results discussed here.

The error level of the extrapolated potential is about three orders of magnitude below the field itself for the constant extrapolation and one order of magnitude lower for linear and quadratic extrapolation. Quadratic extrapolation is most accurate for body waves at depth and surface waves, but less so for body waves at the free surface. The near source region is likely dominated by numerical noise introduced by the point source approximation at this accuracy level and hence does not behave physically in the extrapolation. To quantify this visual impression and evaluate the quality of the extrapolated field as initial solution, we compute the residual for 20 consecutive time steps preceding the one discussed above. The cumulative distribution of these residuals is shown in Fig. 4.10 for the linear and quadratic scheme. The residuals for the constant extrapolation are beyond the scale of the figure and take values of approximately $1.2 \cdot 10^{-3}$, almost two orders of magnitude above the other two schemes. The figure shows the result both for a single discretization at fourth order ($p = 4$) and the multigrid scheme (mg). The quadratic extrapolation appears to perform slightly better than the linear scheme in both cases, however, probably less than expected from the visual impression in Fig. 4.9. Additionally, the performance of the linear scheme is much more predictable for the multigrid approach with significantly less variance of the residual over the iterations.

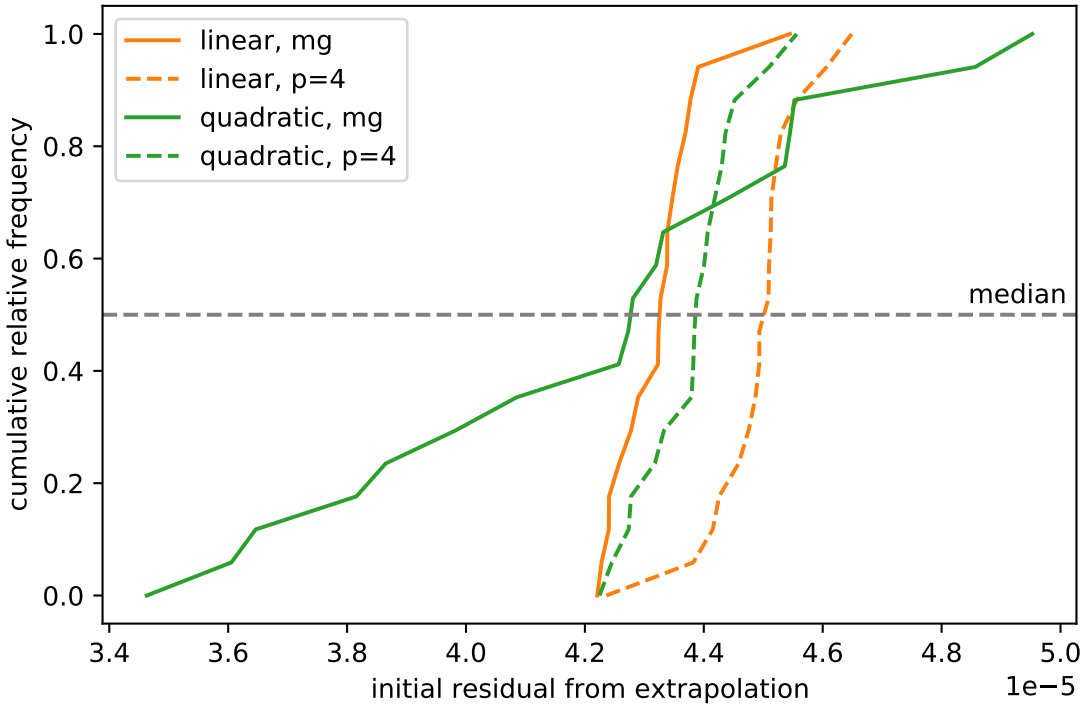

Figure 4.10: Cumulative distribution of the initial residual from linear and quadratic extrapolation. For constant extrapolation, the value is consistently around $1.2 \cdot 10^{-3}$ and not shown here. Importantly, the efficacy of the extrapolation also depends on the spatial scheme.

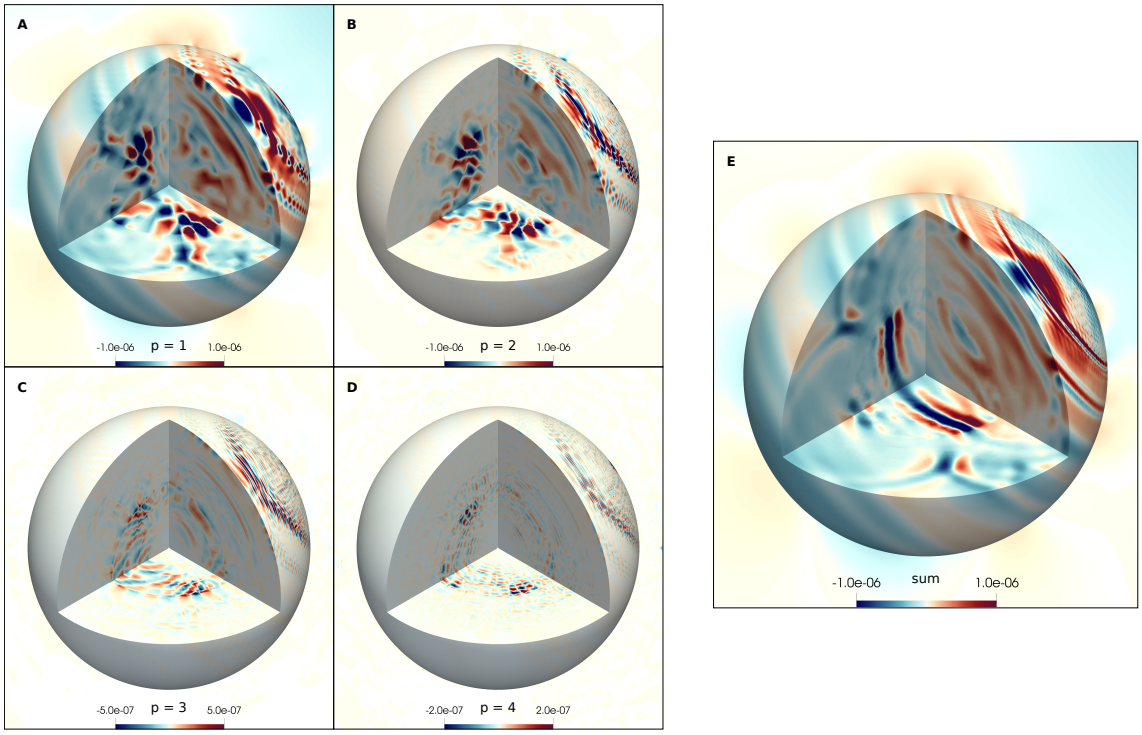

Figure 4.11: (A-D) Contributions and sum (E) of the four stages of the multigrid solver over polynomial orders $p = 1$ to 4 using linear extrapolation. (E) hence shows the difference between the initial solution and the final solution.

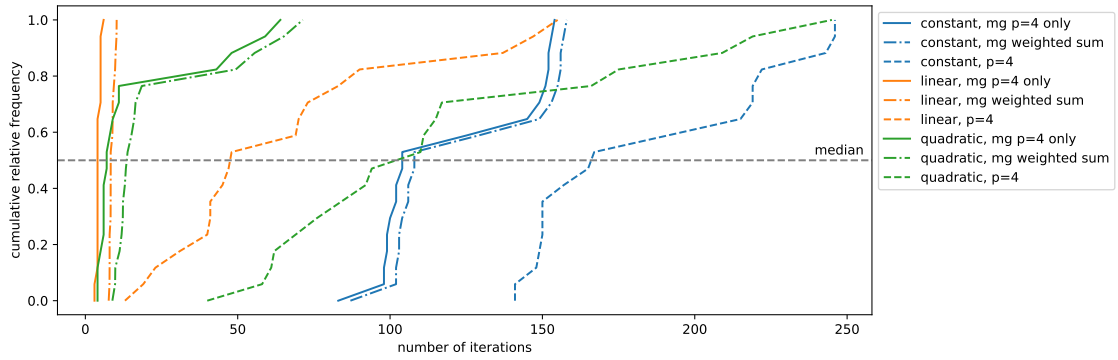

Figure 4.12: Cumulative distribution of the number of iterations needed to reach a residual of 10^{-5} for constant, linear and quadratic time extrapolation and using the four stage multigrid method as well as just the highest order (4). For the multigrid method, both the number of iterations at the highest order as well as a weighted sum over all stages based on a FLOP count estimate is shown.

4.3.4 Efficiency of MG

The final crucial component of our approach is the polynomial multigrid method introduced in section 4.2.6. Fig. 4.11 shows how the four different stages contribute to the final solution starting from a linearly extrapolated initial solution. In the stages using polynomial orders $p = 1$ to $p = 3$, we empirically chose the convergence criterion to be the relative residual of 0.01, 0.05 and 0.05 solving for the update of the initial solution using the residual as the RHS. In the last step, we converge to a residual of 10^{-5} in terms of the full potential. While all the long-scale structure of the solution in particular in the exterior domain is readily present in the first stage, the higher orders are needed for a detailed representation of the body and surface waves. Also, the amplitude of the solution in each stage is significantly reduced for the higher-order stages by up to an order of magnitude.

To quantify the performance gained by using multiple stages, we compare the number of iterations required using different time extrapolation schemes as well as the multigrid and the fourth order system. For the multigrid scheme, we consider both the number of iterations at the highest resolution as it dominates the computational cost, as well as a weighted sum of the iterations in all stages. The weighting is estimated from the leading order scaling in the number of FLOPs in a matrix free implementation of the stiffness terms as would be used in a production code, i.e. p^4.

Fig. 4.12 shows cumulative distributions of these numbers of iterations; in all cases, the linear extrapolation performs better than both the quadratic and the constant one. Additionally, as already seen in the residual, the quadratic extrapolation again exhibits the largest variance, making the linear extrapolation the best choice. The median value for the multigrid method with linear extrapolation is 5 iterations in the highest order and 8.2 iterations in the weighted sum. This confirms about a

factor 5 improvement in the performance by using multigrid in comparison to the same extrapolation used with fourth order only, which is comparable to previous results (e.g. *Barker and Kolev*, 2021).

The linear extrapolation itself leads to a factor 3 reduction in cost in comparison to the constant extrapolation for the fourth order approach and to a factor 10 for the multigrid approach. This however mostly suggests that the simplified multigrid approach we use here with a single cycle through the different orders is not a good choice if the initial solution has a higher residual. With higher initial residuals, we expect cycling through the stages multiple times to be more efficient.

As a reference, for a zero initial solution and using fourth order, the number of iterations are approximately 700 to 900. *Chaljub et al.* (2007) report a range of 50 to 100 iterations, though using wavefields with significantly lower frequency (dominant frequency of 1 mHz vs 5 mHz used here, corresponding to 443K vs 6.8M degrees of freedom for the potential). They also use a spatially variable polynomial order from 2 to 10 to improve the condition number of the matrix and do not specify the initial solution, so that a comparison to their numbers requires careful interpretation.

4.4 Conclusions & Outlook

In summary, linear extrapolation together with the simplified multigrid approach reduces the cost of solving the Poisson equation for the perturbed gravitational potential significantly. As the elastic stiffness terms in the wave propagation are about an order of magnitude more expensive than the stiffness term in the Poisson equation, the reduction to a cost equivalent to less than ten iterations means that the cost for the Poisson solver is on the same order of magnitude as the elastic terms and no longer dominates the numerical cost. All computations in this paper both for the wave propagation and the Poisson equation were run on a workstation.

Future work includes the implementation of the presented method into a production software with direct coupling between the gravitational and elastic forces as well as its verification against established solutions. In order to apply this method to full waveform based tomography at normal mode frequencies, classical methods of extracting information from the seismograms (*Laske and Widmer-Schnidrig*, 2015) need to be revised and adapted for this framework and the corresponding adjoint sources need to be derived. The check pointing approach used for the computation of gradients in the adjoint method (*Komatitsch et al.*, 2016) needs to be verified for simulations with very high numbers of time steps and potentially extended to use multiple levels (*Walther and Griewank*, 2004). In any case, the work presented here constitutes an important step towards the inclusion of full self-gravitation in routine calculations of long period seismograms.

Chapter 5

Conclusions and outlook

An important goal to this day in the geophysics community is to determine the structure of planets with great rigour. In this thesis, we emphasized the importance of long period seismic signals that are especially sensitive to density variations due to self-gravitation. We focused specifically on modernizing the computational methods of normal modes using spectral elements, as well as improving Earth's density and attenuation structure in a probabilistic, self-consistent inversion setting. In consequence, we improved the estimation of density in planets.

To advance our understanding of the formation and evolution of the Earth and terrestrial planets, knowledge of their composition and structure are of fundamental importance. Because density information is contained in the normal mode spectra at relatively small amplitudes, accurate implementation of the underlying physics is required (*Akbarashrafi et al.*, 2018). In this project we overcame some of the methodological deficiencies that beset former modelling techniques for normal modes by leveraging the high accuracy provided by the spectral element method (*Kemper et al.*, 2021). Our method avoids numerical instabilities often encountered in the classical method of radial integration. The *Python*-based implementation of the normal mode spectral element method (spectral element normal mode code; *specnm*) is available open source as benefit to the community.

An important feature of our code is the general mesh generation based solely on the input model which allows for the calculation of normal modes for general symmetric bodies, such as planets, moons (*Kemper et al.*, 2021) and even special stars. This is due to the fact that the theory of free oscillations is applicable to model variable stars like β Cepheids whose luminosity varies due to radial oscillations (*Nolet*, 2008). One output of our code are spherical symmetric eigenfunctions describing the displacement in depths that can be employed as input for (full) coupling codes (*Yang and Tromp*, 2015) which in turn would benefit greatly from the high accuracy our method provides. A rather speculative idea is to look into the full coupling of inner core spheroidal and inner core toroidal modes to see if the exotic inner core toroidal modes (*Dahlen and Tromp*, 1998) have an influence on inner core and full

planet spheroidal modes. For the same reason, the calculation of splitting functions could potentially increase in accuracy. In addition, any kind of surface wave phase and group velocity study that depends on the mode description could greatly benefit from the improved accuracy in the description of boundary modes, i.e. the higher fundamental branch accuracy.

The main result of the probabilistically inverted models from chapter 3 are a series of interesting and important observations. The mantle P- and S-wave velocities are respectively slightly faster and slower relative to PREM(*Dziewonski and Anderson*, 1981). The outer-core P-wave velocity is slower than PREM on account of a different velocity gradient, whereas inner-core velocity structure is similar. In terms of density, we find that the mantle is less dense and the outer core more dense than PREM, while the inner core is similar to PREM. These changes are partly caused by the geodetic data. The laboratory-based visco-elastic model we set up resolves the anelastic response of Earth's mantle from long-period seismic (100 s) to tidal (18.6 yrs) periods, accounting for both normal-mode and tidal dissipation measurements. We verified our inferred mantle seismic velocity structure by computing P- and S-wave travel times and comparing these to the observations of globally-averaged P- and S-wave travel times from the reprocessed ISC catalog. The comparison results in an excellent match that is partly superior to that of PREM. To further refine the seismic P-wave velocity structure of the outer core, we also considered multiple core-mantle-boundary underside-reflected body wave travel time data. While the match to the underside reflections clearly improves as a result of a steeper velocity gradient in the outer core, subtle differences persist that appear to support a change in velocity gradient in the outermost core, evocative of a stably stratified layer.

The improved density estimates from our models regarding Earth's inner core boundary give insights into the generation of Earth geomagnetic field by the core dynamo which is driven by compositional convection. Especially, we find a lower ICB density difference in contrast to earlier predictions in between 0.3–0.5 g/cm^3 which suggests that the geodynamo purely driven by the heterogeneity associated with light-element partitioning is not strong enough to explain Earth magnetic field. Thus our finding supports the additional source of exsolution of solids from the liquid outer core. Better knowledge of the upper most outer core density would also improve our understanding of the composition of the stably stratified layer suggested by SmKS travel times.

To improve the results of the Gibbs energy minimization used by PerpleX (*Connolly*, 2009) within the mantle the thermodynamic databases should be improved (*Khan et al.*, 2021b). Our parameterization employing the isentropic Vinet-EoS is unable to represent thin layers of the outer core, which may correspond to stably stratified regions at either the innermost or outermost boundaries of the outer core.

For this matter an updated equation of state or a full thermodynamic database is needed. It would be especially important to have laboratory measurements for iron-silicate mixtures at outermost outer core conditions (e.g., *Hirose et al.*, 2017). To generate proper seismic profiles for the inner core, the thermodynamic databases for iron mixtures at very high temperatures and pressures (e.g., *Saxena and Eriksson*, 2015) have to be established. Another important aspect for improvement regarding density could involve the use of other long-period data from measurements of the Slichter mode and the Chandler wobble together with improved synthetics for those data types. Regarding the anelastic modelling, a way to improve would be to properly set up a shear attenuation model for the inner core, as well as a whole planet compression attenuation model. While anisotropy can trade off with isotropic structure as evidenced in numerous tomography models, we did not consider it in our Earth inversion as these studies rarely agree. In the Earth anisotropy has been reported to exist not only in the upper mantle (e.g., *Ekström and Dziewonski*, 1998; *Lebedev et al.*, 2009; *Russell et al.*, 2019), but also deeper, e.g., in the D" region (*Restivo and Helffrich*, 2006; *Beghein et al.*, 2008), at the ICB (*Helffrich and Mainprice*, 2019), and the inner core (*Woodhouse et al.*, 1986; *Morelli et al.*, 1986; *Tromp*, 1993; *Durek and Romanowicz*, 1999; *Beghein and Trampert*, 2003; *Wookey and Helffrich*, 2008; *Deuss*, 2014). Hence, new radial structure models should include transversal anisotropy in these regions. For the future measurements of normal modes splitting functions it certainly is important to include the effects of full coupling into the fitting process to improve the parameters especially for Stoneley modes (*Robson et al.*, 2022).

An improved understanding of the interior structure of the Earth and other rocky planets can be related to the differentiation process that happened early during planet formation and therefore has a strong impact on the early solar system evolution models (e.g., *Nimmo and Kleine*, 2015; *Rubie et al.*, 2015). The better insight into the dynamical evolution of our solar system might then be used to understand the evolution of other systems and the genesis of exo-planets (e.g., *Dorn et al.*, 2015; *Bonsor et al.*, 2020; *Adibekyan et al.*, 2021).

The overarching goal in numerical seismology in this regard is to achieve full three-dimensional time stepping of long period waves, i.e. normal modes. The main challenge in the description is that the gravity potential extends to infinity outside of the planet, which we tackle by using a multipole expansion for the associated boundary conditions together with adaptive meshing and higher order shape mapping to reduce the number of elements needed significantly. These enhancements allow for the solving of the three-dimensional gravity equations with a cost comparable to that for the solving of the elastic wave equation. In the future, this may lead to three-dimensional wave simulations with direct coupling between the gravitational and elastic forces.

Appendix A

A.1 Normal mode density sensitivity

Normal modes show a higher sensitivity to density mainly due to gravity interaction of the long period modes described mathematically by a coupling of the ordinary differential equations with a Poisson equation for the gravity potential φ. In first order perturbation theory the radial integral of the change in density, while holding the wave velocities VP, VS and the discontinuities d constant, is given by (Eq. 9.26, *Dahlen and Tromp*, 1998):

$$2\omega \int_0^R \rho \left(\frac{\partial \omega}{\partial \rho}\right)_{\mathrm{VP,VS},d} \mathrm{d}r = \int_0^R [4\pi G\rho^2 U^2 + \rho(UP' + kr^{-1}VP)]r^2 \,\mathrm{d}r \qquad (A.1)$$
$$- 8\pi G \int_0^R \int_r^R \rho\tilde{\rho}\tilde{U}(2\tilde{U} - k\tilde{V})\tilde{r}^{-1} \,\mathrm{d}\tilde{r} r^2 \,\mathrm{d}r.$$

The right hand side is either proportional to the gravity constant G or the P eigenfunction that incorporates perturbations in the gravity potential itself for full gravity spheroidal modes. Note that there are no toroidal eigenfunctions W present, which shows that they are in general not more sensitive to density ρ than travelling waves.

A.2 Spectral element normal mode code

A.2.1 Equations from the literature

This sections includes the equations used in the derivations in the main part of the paper, copied from *Dahlen and Tromp* (1998) for completeness. Toroidal first order equations:

$$\partial_r W = r^{-1}W + L^{-1}T, \qquad (A.2)$$
$$\partial_r T = [-\omega^2\rho + (k^2 - 2)Nr^{-2}]W - 3r^{-1}T. \qquad (A.3)$$

Spheroidal first order equations:

$$\partial_r U = -2C^{-1}Fr^{-1}U + kC^{-1}Fr^{-1}V + C^{-1}R, \qquad (A.4)$$

$$\partial_r V = -kr^{-1}U + r^{-1}V + L^{-1}S, \tag{A.5}$$

$$\partial_r P = -4\pi G\rho U - (l+1)r^{-1}P + B, \tag{A.6}$$

$$\begin{aligned}\partial_r R = &[-\omega^2\rho - 4\rho g r^{-1} + 4(A - N - C^{-1}F^2)r^{-1}]U \\ &+[k\rho g r^{-1} - 2k(A - N - C^{-1}F^2)r^{-2}]V \\ &-2(1 - C^{-1}F)r^{-1}T_U + kr^{-1}T_V \\ &-(l+1)\rho r^{-1}P + \rho T_P,\end{aligned} \tag{A.7}$$

$$\begin{aligned}\partial_r S = &[k\rho g r^{-1} - 2k(A - N - C^{-1}F^2)r^{-2}]U \\ &-[\omega^2\rho + 2Nr^{-2} - k^2(A - C^{-1}F^2)r^{-2}]V \\ &-kC^{-1}Fr^{-1}T_U - 3r^{-1}T_V + k\rho r^{-1}P,\end{aligned} \tag{A.8}$$

$$\begin{aligned}\partial_r B = &-4\pi G(l+1)\rho r^{-1}U + 4\pi G k\rho r^{-1}V \\ &+(l-1)r^{-1}T_P.\end{aligned} \tag{A.9}$$

A.2.2 Weak form of the radial ODEs

This section includes some additional derivations and equations for the symmetric weak form as described in the main part of the paper. Radial equation with eigenfunction $U(r)$ and its test function $\tilde{U}(r)$. The included traction $T_U(V = 0)$ is the same as for spheroidal modes setting the V eigenfunction to zero:

$$\begin{aligned}\omega^2 \int_\Omega \rho U\tilde{U}r^2\,\mathrm{d}r = &-\left[T_U(V=0)\tilde{U}r^2\right]_0^{r_{\mathrm{surf}}} + \left[T_U(V=0)\tilde{U}r^2\right]_-^+ \\ &+\int_\Omega Cr^2\partial_r U\partial_r\tilde{U}\,\mathrm{d}r \\ &+\int_\Omega 2Fr(U\partial_r\tilde{U} + \partial_r U\tilde{U})\,\mathrm{d}r \\ &+\int_\Omega [4(A-N) - 4\rho g r]U\tilde{U}\,\mathrm{d}r.\end{aligned} \tag{A.10}$$

Full gravity spheroidal equation with eigenfunctions $U(r), V(r), P(r)$ and its symmetric counterparts $\tilde{U}(r), \tilde{V}(r), \tilde{P}(r)$:

$$\begin{aligned}\omega^2 \int_\Omega \rho(U\tilde{U} + V\tilde{V})r^2\,\mathrm{d}r = &\\ &-\left[T_U\tilde{U}r^2\right]_0^{r_{\mathrm{surf}}} - \left[T_V\tilde{V}r^2\right]_0^{r_{\mathrm{surf}}} - \left[T_P\tilde{P}r^2\right]_0^{r_{\mathrm{surf}}} \\ &+\left[T_U\tilde{U}r^2\right]_-^+ + \left[T_V\tilde{V}r^2\right]_-^+ + \left[T_P\tilde{P}r^2\right]_-^+ \\ &+\int_\Omega L(kU - V + r\partial_r V)(k\tilde{U} - \tilde{V} + r\partial_r\tilde{V})\,\mathrm{d}r\end{aligned} \tag{A.11}$$

$$
\begin{aligned}
&+ \int_\Omega (A-N)(2U-kV)(2\tilde{U}-k\tilde{V})\,\mathrm{d}r \\
&- \int_\Omega Fr[2(\partial_r U\tilde{U} + U\partial_r\tilde{U}) - k(V\partial_r\tilde{U} + \partial_r U\tilde{V})]\,\mathrm{d}r \\
&+ \int_\Omega \rho g r[-4U\tilde{U} + k(V\tilde{U} + U\tilde{V})]\,\mathrm{d}r \\
&+ \int_\Omega Cr^2\partial_r U\partial_r\tilde{U}\,\mathrm{d}r \\
&+ \int_\Omega N(k^2-2)V\tilde{V}\,\mathrm{d}r \\
&+ \int_\Omega \rho r^2(\partial_r P\tilde{U} + P\partial_r\tilde{U})\,\mathrm{d}r \\
&+ \int_\Omega 4\pi G\rho^2 r^2 U\tilde{U}\,\mathrm{d}r \\
&+ \int_\Omega k\rho r(P\tilde{V} + V\tilde{P})\,\mathrm{d}r \\
&+ \int_\Omega (4\pi G)^{-1} r^2\partial_r P\partial_r\tilde{P}\,\mathrm{d}r \\
&+ \int_\Omega (l+1)(4\pi G)^{-1} r(P\partial_r\tilde{P} + \partial_r P\tilde{P})\,\mathrm{d}r \\
&+ \int_\Omega (l+1)^2(4\pi G)^{-1} P\tilde{P}\,\mathrm{d}r
\end{aligned}
$$

Note that the left hand side does not include $P(r)$ or $\tilde{P}(r)$, hence the mass matrix is positive semi definite.

A.3 Self-consistent models of the Earth from long-period seismic and tidal constraints

A.4 Theoretical background

To compute normal mode and tidal responses for comparison with data, we employ spectral element discretization of the underlying differential equations. In the following, we briefly summarise the governing equations. For details the reader is referred to *Bagheri et al.* (2019) for body tides and to *Kemper et al.* (2021) for normal modes. In what follows, the radial domains and the boundaries are denoted by Ω and Σ, respectively, while subscripts S and F refer to solid and fluid, respectively, and superscripts $\pm$ indicate on which side of a discontinuity a term is evaluated, where $(+)$ designates radially outer $(+)$ or inner $(-)$ side.

A.4.1 Tides

The quasi-static momentum equation (*Al-Attar and Tromp*, 2014) in weak form is given by

$$
\begin{aligned}
0 = & \underbrace{\int_{\Omega_\mathrm{S}} \kappa \nabla\cdot\mathbf{u}\nabla\cdot\tilde{\mathbf{u}}\,\mathrm{d}V}_{\mathbf{1}} + \underbrace{\int_{\Omega_\mathrm{S}} 2\mu\mathbf{d}:\tilde{\mathbf{d}}\,\mathrm{d}V}_{\mathbf{2}} \\
& + \underbrace{\frac{1}{2}\int_{\Omega_\mathrm{S}} \rho\left\{[\nabla(\mathbf{u}\cdot\nabla\Phi)\cdot\tilde{\mathbf{u}} + \nabla(\tilde{\mathbf{u}}\cdot\nabla\Phi)\cdot\mathbf{u}] - [\nabla\cdot\mathbf{u}\nabla\Phi\cdot\tilde{\mathbf{u}} + \nabla\cdot\tilde{\mathbf{u}}\nabla\Phi\cdot\mathbf{u}]\right\}\mathrm{d}V}_{\mathbf{3}} \\
& + \underbrace{\int_{\Omega_\mathrm{S}} \rho(\nabla\varphi\cdot\tilde{\mathbf{u}} + \mathbf{u}\cdot\nabla\tilde{\varphi} + \nabla\psi\cdot\tilde{\mathbf{u}})\,\mathrm{d}V}_{\mathbf{4}} + \underbrace{\int_{\Omega_\mathrm{F}} g^{-1}(\varphi+\psi)\tilde{\varphi}\partial_n\rho\,\mathrm{d}V}_{\mathbf{5}} \\
& + \underbrace{(4\pi G)^{-1}\int_{\mathbb{R}^3} \nabla\varphi\cdot\nabla\tilde{\varphi}\,\mathrm{d}V}_{\mathbf{6}} \\
& + \underbrace{\int_{\Sigma_\mathrm{FS}} \rho^- g\hat{\mathbf{n}}\cdot\mathbf{u}\hat{\mathbf{n}}\cdot\tilde{\mathbf{u}}\,\mathrm{d}S}_{\star} - \underbrace{\int_{\Sigma_\mathrm{SF}} \rho^+ g\hat{\mathbf{n}}\cdot\mathbf{u}\hat{\mathbf{n}}\cdot\tilde{\mathbf{u}}\,\mathrm{d}S}_{\star} \\
& + \underbrace{\int_{\Sigma_\mathrm{FS}} \rho^-(\varphi\tilde{\mathbf{u}} + \mathbf{u}\tilde{\varphi})\cdot\hat{\mathbf{n}}\,\mathrm{d}S}_{\star} - \underbrace{\int_{\Sigma_\mathrm{SF}} \rho^+(\varphi\tilde{\mathbf{u}} + \mathbf{u}\tilde{\varphi})\cdot\hat{\mathbf{n}}\,\mathrm{d}S}_{\star} \\
& + \underbrace{\int_{\Sigma_\mathrm{FS}} \rho^-\psi\tilde{\mathbf{u}}\cdot\hat{\mathbf{n}}\,\mathrm{d}S}_{\star} - \underbrace{\int_{\Sigma_\mathrm{SF}} \rho^+\psi\tilde{\mathbf{u}}\cdot\hat{\mathbf{n}}\,\mathrm{d}S}_{\star},
\end{aligned}
\tag{A.12}
$$

where, κ and μ are bulk and shear moduli, respectively, ρ is density, $\mathbf{u}$ is the displacement vector, $\mathbf{d} = \mathbf{e} - \frac{1}{3}\mathrm{tr}(\mathbf{e})\mathbf{I}$ is the deviatoric strain tensor, Φ and φ are the equilibrium and perturbed gravitational potentials, respectively, ψ is the tidal potential, G is the gravitational constant, and $g = ||\mathbf{g}||$ is the scalar gravitational acceleration at the boundary. $\tilde{\mathbf{u}}$, $\tilde{\varphi}$, and $\tilde{\mathbf{d}}$ are suitably-defined regular time-independent test functions.

The individual integral terms that make up the weak form (Eq. A.12) will be briefly explained in the following. Term 1: material contraction or dilatation given by the divergence of the displacement $\mathbf{u}$. The amplitude of this contraction or dilatation is given by a multiplication with the bulk modulus κ of the material. Term 2: Second contraction of the deviatoric strain tensor, representing the strength of the shear forces acting in the material that for historical reasons are multiplied by a factor 2 and become dimensionalised through multiplication with μ. Term 3: Interaction of displacement $\mathbf{u}$ and gravity potential φ. The forces generated by this

interaction cancel each other (+ and − terms) in the equilibrium state. Terms 4 & 5: Hydrostatic equilibrium terms as solutions of the underlying Poisson's equation that behave differently in solid Ω_{S} and fluid domains Ω_{F}. Term 6: Gradient of the gravitational potential, i.e., the gravitational force field. The potential extends outside of the planet into space but decays as $1/r$ and equals zero at infinity. The rest of the terms ($\star$) are boundary terms (on Σ) that have to be introduced to satisfy solid-fluid interactions of the gravitational acceleration g, the displacement $\mathbf{u}$, the gravity potential φ, and the tidal potential ψ.

A.4.2 Normal modes

To compute normal-mode centre frequencies and global quality factors, we use the spectral-element-based code `specnm` described in *Kemper et al.* (2021). Theoretically, the treatment of normal modes is given by expanding the displacement field in the wave equation in vector spherical harmonics, which gives rise to ordinary differential equations depending on radius r (*Dahlen and Tromp*, 1998). Normal modes are classified in two types as toroidal T (SH or Love wave interference) or spheroidal S (P-SV or Rayleigh wave interference) modes, where the latter are affected by gravity. We denote the toroidal displacement eigenfunctions as W and the spheroidal displacement eigenfunctions as U and V. Since spheroidal oscillations also involve changes in density, and therefore perturbations in the gravitational potential, we define the function P through an additional coupled second-order ordinary differential equation (ODE) based on Poisson's equation. In terms of the tidal gravity potential φ, P is given by the radial gravity potential $P = \varphi \cdot \hat{\mathbf{e}}_r$, where $\hat{\mathbf{e}}_r$ is the unit vector in radial direction. Note that all parameters are implicitly assumed to be functions of radius.

Assuming transversely isotropic media, the deformation of the Earth can be parameterised by the five Love parameters A, C, L, N, and F (*Love*, 1927) together with the density ρ,

$$A = \rho V_{PH}^2, \tag{A.13}$$

$$C = \rho V_{PV}^2, \tag{A.14}$$

$$L = \rho V_{SV}^2, \tag{A.15}$$

$$N = \rho V_{SH}^2, \tag{A.16}$$

$$F = \frac{\eta}{A - 2L}, \tag{A.17}$$

where η provides a rule of how the velocity evolves as the incidence angle varies between horizontal and vertical. In the isotropic case $A = C$, $L = N$, and $\eta = 1$. The tractions associated with toroidal (T_W) and spheroidal (T_U, T_V, and T_P) normal

modes are defined as (*Dahlen and Tromp*, 1998)

$$T_W = L(\partial_r W - r^{-1}W), \tag{A.18}$$
$$T_U = C\partial_r U + Fr^{-1}(2U - kV), \tag{A.19}$$
$$T_V = L(\partial_r V - r^{-1}V + kr^{-1}U), \tag{A.20}$$
$$T_P = \partial_r P + 4\pi G\rho U + (l+1)r^{-1}P, \tag{A.21}$$

where k is the wavenumber. The second order ODE for the description of toroidal modes with associated eigenfunction W and symmetric counterpart $\tilde{W}$ is, in the weak form, given by (*Kemper et al.*, 2021):

$$\begin{aligned}\omega^2 \int_\Omega \rho W\tilde{W}r^2 \,\mathrm{d}r = &-\left[T_W\tilde{W}r^2\right]_{r_0}^{r_{\mathrm{surf}}} + \sum_{r\in d}\left[T_W\tilde{W}r^2\right]_-^+ \\ &+ \int_\Omega T_W(r^2\partial_r\tilde{W} + 2r\tilde{W})\,\mathrm{d}r \\ &+ \int_\Omega N(k^2-2)W\tilde{W}\,\mathrm{d}r \\ &- \int_\Omega 3rT_W\tilde{W}\,\mathrm{d}r,\end{aligned} \tag{A.22}$$

where d denotes internal discontinuities. The toroidal normal modes are only affected by the radial density distribution ρ and the two elastic parameters L and N that depend on shear shear modulus μ and ρ.

The symmetrized weak form in the spheroidal case reads (*Kemper et al.*, 2021)

$$\begin{aligned}\omega^2 \int_\Omega \rho(U\tilde{U} + V\tilde{V}) r^2 \,\mathrm{d}r = &- \left[T_U \tilde{U} r^2\right]_0^{r_{\mathrm{surf}}} - \left[T_V \tilde{V} r^2\right]_0^{r_{\mathrm{surf}}} - \left[T_P \tilde{P} r^2\right]_0^{r_{\mathrm{surf}}} \\ &+ \left[T_U \tilde{U} r^2\right]_-^+ + \left[T_V \tilde{V} r^2\right]_-^+ + \left[T_P \tilde{P} r^2\right]_-^+ \\ &+ \int_\Omega L(kU - V + r\partial_r V)(k\tilde{U} - \tilde{V} + r\partial_r \tilde{V}) \,\mathrm{d}r \\ &+ \int_\Omega (A - N)(2U - kV)(2\tilde{U} - k\tilde{V}) \,\mathrm{d}r \\ &- \int_\Omega Fr[2(\partial_r U\tilde{U} + U\partial_r \tilde{U}) - k(V\partial_r \tilde{U} + \partial_r U\tilde{V})] \,\mathrm{d}r \\ &+ \int_\Omega \rho g r[-4U\tilde{U} + k(V\tilde{U} + U\tilde{V})] \,\mathrm{d}r \\ &+ \int_\Omega Cr^2 \partial_r U \partial_r \tilde{U} \,\mathrm{d}r \\ &+ \int_\Omega N(k^2 - 2) V\tilde{V} \,\mathrm{d}r \\ &+ \int_\Omega \rho r^2 (\partial_r P\tilde{U} + P\partial_r \tilde{U}) \,\mathrm{d}r \\ &+ \int_\Omega 4\pi G \rho^2 r^2 U\tilde{U} \,\mathrm{d}r \\ &+ \int_\Omega k\rho r(P\tilde{V} + V\tilde{P}) \,\mathrm{d}r \\ &+ \int_\Omega (4\pi G)^{-1} r^2 \partial_r P \partial_r \tilde{P} \,\mathrm{d}r \\ &+ \int_\Omega (l+1)(4\pi G)^{-1} r(P\partial_r \tilde{P} + \partial_r P\tilde{P}) \,\mathrm{d}r \\ &+ \int_\Omega (l+1)^2 (4\pi G)^{-1} P\tilde{P} \,\mathrm{d}r. \end{aligned} \tag{A.23}$$

A special case of the spheroidal modes are given by setting the angular degree to zero $l = 0$. The radial weak form includes the eigenfunction $U(r)$ and its test function $\tilde{U}(r)$. The traction $T_U(V = 0)$ is the same as for spheroidal modes setting the V eigenfunction to zero (*Kemper et al.*, 2021):

$$\begin{aligned}\omega^2 \int_\Omega \rho U\tilde{U} r^2 \,\mathrm{d}r = &- \left[T_U \tilde{U} r^2\right]_0^{r_{\mathrm{surf}}} + \left[T_U \tilde{U} r^2\right]_-^+ \\ &+ \int_\Omega Cr^2 \partial_r U \partial_r \tilde{U} \,\mathrm{d}r \\ &+ \int_\Omega 2Fr(U\partial_r \tilde{U} + \partial_r U\tilde{U}) \,\mathrm{d}r \\ &+ \int_\Omega [4(A - N) - 4\rho g r] U\tilde{U} \,\mathrm{d}r. \end{aligned} \tag{A.24}$$

Note that all boundary conditions are implicitly fulfilled through the weak form (see

Kemper et al. (2021) for details).

A.4.3 Normal-mode anelastic correction

As a consequence of the Kramers-Kronig relations and causality, attenuation of elastic waves is directly related to the frequency dependence of the elastic moduli, that is, physical dispersion. This results in a weakly non-linear eigenvalue problem that we solve as described in *Kemper et al.* (2021). Physical dispersion is accounted for by evaluating the model parameters at the frequency of the mode. Assuming the quality factors Q to be independent of frequency ω within the seismic frequency band and the five elastic Love parameters to be specified at a given frequency ω_0 in a model of interest, the elastic parameters can be evaluated at any frequency ω using the logarithmic relation (*Dahlen and Tromp*, 1998)

$$x(r,\omega) \propto x(r,\omega_0) \ln\left(\frac{\omega}{\omega_0}\right), \tag{A.25}$$

where x is any of the Love parameters $\{C, F, N, L, A\}$.

A.5 The extended Burgers model

The frequency-dependent complex compliance $J(\omega)$ for the Extended Burgers Model (EBM) is defined by

$$J(\omega) = J_1(\omega) + iJ_2(\omega), \tag{A.26}$$

where the storage J_1 and loss compliance J_2 for are given by

$$\begin{aligned} J_1(\omega) =& J_U(r)\Bigg\{1 + \frac{\alpha\Delta_B}{\tau_H^\alpha - \tau_L^\alpha}\int_{\tau_L}^{\tau_H}\frac{\tau^{\alpha-1}}{1+\omega^2\tau^2}\,\mathrm{d}\tau \\ &+\frac{\Delta_P}{\sigma\sqrt{2\pi}}\int_0^\infty \frac{\exp\{-\frac{1}{2}[\ln(\tau/\tau_P)/\sigma]^2\}}{\tau(1+\omega^2\tau^2)}\,\mathrm{d}\tau\Bigg\}, \end{aligned} \tag{A.27}$$

$$\begin{aligned} J_2(\omega) =& J_U(r)\Bigg\{\frac{\omega\alpha\Delta_B}{\tau_H^\alpha - \tau_L^\alpha}\int_{\tau_L}^{\tau_H}\frac{\tau^{\alpha}}{1+\omega^2\tau^2}\,\mathrm{d}\tau \\ &+\frac{\omega\Delta_P}{\sigma\sqrt{2\pi}}\int_0^\infty \frac{\exp\{-\frac{1}{2}[\ln(\tau/\tau_P)/\sigma]^2\}}{1+\omega^2\tau^2}\,\mathrm{d}\tau + \frac{1}{\omega\tau_M}\Bigg\}. \end{aligned} \tag{A.28}$$

In this, the infinite-frequency unrelaxed compliance J_U is defining the elastic behaviour, while the anelastic behavior consists of a broad plateau and an absorption band. The former is generally represented by a log-normal distribution with relax-

Table A.1: Fixed mantle attenuation input parameters for the extended Burgers model used in our inversions (*Lau and Faul*, 2019).

Parameter	Symbol	Value
Upper mantle		
Activation energy	E_a	3.75×10^5 Jmol^{-1}
Activation volume	V_a	6.0×10^{-6} m^{3}mol^{-1}
Grainsize	d_g	1.0×10^{-2} m
Reference grainsize	d_{gR}	13.4×10^{-6} m
Reference temperature	T_R	1173.15 K
Reference pressure	P_R	0.2×10^9 Pa
Viscous grainsize exponent	m_{M}	3
Anelastic grainsize exponents	$m_{\mathrm{H,L,P}}$	1.31
Burgers element strength	Δ_B	1.04
Peak height	Δ_P	0.057
Lower mantle		
Activation energy	E_a	2.86×10^5 Jmol^{-1}
Activation volume	V_a	4.8×10^{-6} m^{3}mol^{-1}
Burgers element strength	Δ_B	1.9
Peak height	Δ_P	0.03

ation strength Δ_P centered at τ_P with width σ. The other absorption band, with relaxation strength Δ_B, is delimited by lower and upper cutoff times τ_L and τ_H, whose frequency dependence is determined by the exponent α. In the EBM, the Maxwell relaxation time τ_M dominates the dissipation at long periods. The equations for the relaxation times τ_i for the subscript $i \in \{H, L, P, M\}$ is defined by:

$$\tau_i(d_g, E^*, T, V^*, P) = \tau_{iR} \left(\frac{d_g}{d_{gR}}\right)^{m_i} \exp\left[\left(\frac{E^*}{R}\right)\left(\frac{1}{T} - \frac{1}{T_R}\right) + \left(\frac{V^*}{R}\right)\left(\frac{P}{T} - \frac{P_R}{T_R}\right)\right], \tag{A.29}$$

where R=8.314 Jmol^{-1}K^{-1} is the gas constant, T temperature, P pressure, d_g grainsize, E^* activation energy, and V^* activation volume. Subscript R denotes the parameters in the reference, i.e., laboratory, state. All necessary parameter values are listed in Table A.1.

A.6 Normal-mode data

The normal-mode data employed in this study are compiled below in Tables A.2–A.15.

Table A.2: Normal mode spheroidal data collection for cluster upper mantle modes with observed frequency f_{obs} in μHz and global quality factors Q with respective uncertainties. Data collected from references MW: *Masters and Widmer* (1995), RS: *Resovsky and Ritzwoller* (1998), DE: *Deuss et al.* (2013), PREM: *Dziewonski and Anderson* (1981).

${}_n\mathrm{S}_l$	f_{obs}	f_{err}	Q_{obs}	Q_{err}	ref.	${}_n\mathrm{S}_l$	f_{obs}	f_{err}	Q_{obs}	Q_{err}	ref.
${}_0\mathrm{S}_{11}$	1861.90	1.60	294	4	DE	${}_0\mathrm{S}_{12}$	1989.73	0.60	295	3	DE
${}_0\mathrm{S}_{13}$	2112.02	0.80	294	3	DE	${}_0\mathrm{S}_{14}$	2230.47	0.80	294	2	DE
${}_0\mathrm{S}_{15}$	2345.45	1.20	285	3	DE	${}_0\mathrm{S}_{16}$	2457.50	0.60	274	2	DE
${}_0\mathrm{S}_{17}$	2566.53	1.00	262	2	DE	${}_0\mathrm{S}_{18}$	2672.46	0.12	296	5	RS
${}_0\mathrm{S}_{19}$	2776.86	2.00	256	2	DE	${}_0\mathrm{S}_{20}$	2878.36	3.20	238	4	DE
${}_0\mathrm{S}_{21}$	2977.48	12.20	239	3	DE	${}_0\mathrm{S}_{22}$	3074.60	0.15	N/A	N/A	MW
${}_0\mathrm{S}_{23}$	3170.65	0.10	259	5	MW	${}_0\mathrm{S}_{24}$	3265.60	0.10	251	4	MW
${}_0\mathrm{S}_{25}$	3359.42	0.56	207	5	PREM	${}_0\mathrm{S}_{26}$	3452.20	0.60	202	5	PREM
${}_0\mathrm{S}_{27}$	3543.46	0.63	203	5	PREM	${}_0\mathrm{S}_{28}$	3634.91	0.66	199	5	PREM
${}_0\mathrm{S}_{29}$	3725.37	0.69	191	5	PREM	${}_0\mathrm{S}_{30}$	3815.48	0.73	188	5	PREM
${}_0\mathrm{S}_{31}$	3905.95	0.76	184	5	PREM	${}_0\mathrm{S}_{32}$	3995.37	0.80	180	5	PREM
${}_0\mathrm{S}_{33}$	4083.63	0.83	177	5	PREM	${}_0\mathrm{S}_{34}$	4173.27	0.87	173	5	PREM
${}_0\mathrm{S}_{35}$	4262.57	0.91	172	5	PREM	${}_0\mathrm{S}_{36}$	4351.80	0.95	170	5	PREM
${}_0\mathrm{S}_{37}$	4441.09	0.99	167	5	PREM	${}_0\mathrm{S}_{38}$	4530.83	1.03	162	5	PREM
${}_0\mathrm{S}_{39}$	4620.00	1.07	161	5	PREM	${}_0\mathrm{S}_{40}$	4709.21	1.11	159	5	PREM
${}_0\mathrm{S}_{41}$	4800.08	1.15	156	5	PREM	${}_0\mathrm{S}_{42}$	4888.54	1.20	155	5	PREM
${}_0\mathrm{S}_{43}$	4977.60	1.24	154	5	PREM	${}_0\mathrm{S}_{44}$	5068.17	1.28	152	5	PREM
${}_0\mathrm{S}_{45}$	5157.03	1.33	151	5	PREM	${}_0\mathrm{S}_{46}$	5247.69	1.38	147	5	PREM
${}_0\mathrm{S}_{47}$	5338.17	1.43	144	5	PREM	${}_0\mathrm{S}_{48}$	5428.59	1.47	139	5	PREM
${}_0\mathrm{S}_{49}$	5519.98	1.52	136	5	PREM	${}_0\mathrm{S}_{50}$	5609.15	1.57	133	5	PREM
${}_0\mathrm{S}_{51}$	5702.55	1.63	134	5	PREM	${}_0\mathrm{S}_{52}$	5794.08	1.68	136	5	PREM
${}_0\mathrm{S}_{53}$	5882.70	1.73	139	5	PREM	${}_0\mathrm{S}_{54}$	5983.01	1.79	136	5	PREM
${}_0\mathrm{S}_{55}$	6065.02	1.84	134	5	PREM	${}_0\mathrm{S}_{56}$	6167.51	1.90	133	5	PREM
${}_0\mathrm{S}_{57}$	6245.71	1.95	131	5	PREM	${}_0\mathrm{S}_{58}$	6339.14	2.01	N/A	N/A	PREM
${}_0\mathrm{S}_{59}$	6435.83	2.07	N/A	N/A	PREM	${}_0\mathrm{S}_{60}$	6525.71	2.13	N/A	N/A	PREM
${}_0\mathrm{S}_{61}$	6614.19	2.19	N/A	N/A	PREM	${}_0\mathrm{S}_{62}$	6704.21	2.25	N/A	N/A	PREM
${}_0\mathrm{S}_{63}$	6796.25	2.31	N/A	N/A	PREM	${}_0\mathrm{S}_{64}$	6898.45	4.29	N/A	N/A	PREM

Table A.3: Normal mode spheroidal data collection for cluster upper mantle modes with observed frequency f_{obs} in μHz and global quality factors Q with respective uncertainties. Data collected from references MW: *Masters and Widmer* (1995), RS: *Resovsky and Ritzwoller* (1998), DE: *Deuss et al.* (2013), PREM: *Dziewonski and Anderson* (1981).

${}_n\mathrm{S}_l$	f_{obs}	f_{err}	Q_{obs}	Q_{err}	ref.	${}_n\mathrm{S}_l$	f_{obs}	f_{err}	Q_{obs}	Q_{err}	ref.
${}_0\mathrm{S}_{66}$	7081.15	4.52	N/A	N/A	PREM	${}_0\mathrm{S}_{67}$	7156.66	5.64	N/A	N/A	PREM
${}_0\mathrm{S}_{68}$	7249.53	5.79	N/A	N/A	PREM	${}_0\mathrm{S}_{69}$	7342.68	6.48	N/A	N/A	PREM
${}_0\mathrm{S}_{70}$	7436.05	6.64	N/A	N/A	PREM	${}_0\mathrm{S}_{71}$	7530.69	7.38	N/A	N/A	PREM
${}_0\mathrm{S}_{72}$	7608.03	7.53	N/A	N/A	PREM	${}_0\mathrm{S}_{73}$	7722.01	7.76	N/A	N/A	PREM
${}_0\mathrm{S}_{74}$	7819.22	7.34	N/A	N/A	PREM	${}_0\mathrm{S}_{75}$	7918.28	6.90	N/A	N/A	PREM
${}_0\mathrm{S}_{76}$	7997.44	19.23	127	15	PREM	${}_0\mathrm{S}_{80}$	8367.50	21.06	N/A	N/A	PREM
${}_0\mathrm{S}_{85}$	8832.36	23.47	N/A	N/A	PREM	${}_0\mathrm{S}_{90}$	9298.87	26.01	N/A	N/A	PREM
${}_1\mathrm{S}_{16}$	3341.00	1.00	N/A	N/A	MW	${}_1\mathrm{S}_{17}$	3495.50	1.00	N/A	N/A	MW
${}_1\mathrm{S}_{18}$	3642.50	1.50	N/A	N/A	MW	${}_1\mathrm{S}_{19}$	3794.00	1.50	N/A	N/A	MW
${}_1\mathrm{S}_{20}$	3944.50	2.50	N/A	N/A	MW	${}_1\mathrm{S}_{21}$	4093.50	2.50	N/A	N/A	MW
${}_1\mathrm{S}_{22}$	4228.50	3.50	N/A	N/A	MW	${}_1\mathrm{S}_{23}$	4379.00	2.00	N/A	N/A	MW
${}_1\mathrm{S}_{24}$	4525.00	3.00	N/A	N/A	MW	${}_1\mathrm{S}_{25}$	4670.50	3.00	N/A	N/A	MW
${}_1\mathrm{S}_{26}$	4812.50	3.00	N/A	N/A	MW	${}_1\mathrm{S}_{27}$	4956.00	6.00	N/A	N/A	MW
${}_1\mathrm{S}_{28}$	5088.00	5.00	N/A	N/A	MW	${}_1\mathrm{S}_{30}$	5378.50	4.50	N/A	N/A	MW
${}_1\mathrm{S}_{31}$	5512.50	4.50	N/A	N/A	MW	${}_1\mathrm{S}_{32}$	5657.00	8.00	N/A	N/A	MW
${}_1\mathrm{S}_{33}$	5798.00	6.00	N/A	N/A	MW	${}_1\mathrm{S}_{36}$	6200.00	7.00	N/A	N/A	MW
${}_1\mathrm{S}_{37}$	6338.00	6.00	N/A	N/A	MW	${}_1\mathrm{S}_{38}$	6482.00	9.00	N/A	N/A	MW
${}_1\mathrm{S}_{40}$	6739.00	7.00	N/A	N/A	MW	${}_2\mathrm{S}_{6}$	1681.10	1.20	236	1	DE
${}_2\mathrm{S}_{7}$	1865.11	1.00	228	4	DE	${}_2\mathrm{S}_{8}$	2049.39	0.60	202	2	DE
${}_2\mathrm{S}_{9}$	2228.57	3.00	186	2	DE	${}_2\mathrm{S}_{10}$	2403.09	0.20	186	2	DE
${}_2\mathrm{S}_{11}$	2572.24	3.60	178	2	DE	${}_2\mathrm{S}_{12}$	2737.15	0.40	175	2	DE
${}_2\mathrm{S}_{13}$	2899.78	0.80	175	2	DE	${}_2\mathrm{S}_{14}$	3062.00	1.50	N/A	N/A	MW
${}_2\mathrm{S}_{27}$	5736.50	2.50	N/A	N/A	MW	${}_2\mathrm{S}_{28}$	5904.00	2.00	N/A	N/A	MW
${}_2\mathrm{S}_{29}$	6068.50	2.50	N/A	N/A	MW	${}_2\mathrm{S}_{30}$	6230.50	2.50	N/A	N/A	MW
${}_2\mathrm{S}_{31}$	6388.50	2.00	N/A	N/A	MW	${}_2\mathrm{S}_{32}$	6548.50	4.00	N/A	N/A	MW
${}_2\mathrm{S}_{35}$	7015.00	3.50	N/A	N/A	MW	${}_2\mathrm{S}_{36}$	7166.50	3.00	N/A	N/A	MW
${}_2\mathrm{S}_{37}$	7314.50	3.50	N/A	N/A	MW	${}_2\mathrm{S}_{38}$	7476.00	4.00	N/A	N/A	MW

Table A.4: Normal mode spheroidal data collection for cluster upper mantle modes with observed frequency f_{obs} in μHz and global quality factors Q with respective uncertainties. Data collected from references MW: *Masters and Widmer* (1995), RS: *Resovsky and Ritzwoller* (1998), DE: *Deuss et al.* (2013), PREM: *Dziewonski and Anderson* (1981).

${}_n\mathrm{S}_l$	f_{obs}	f_{err}	Q_{obs}	Q_{err}	ref.	${}_n\mathrm{S}_l$	f_{obs}	f_{err}	Q_{obs}	Q_{err}	ref.
${}_2\mathrm{S}_{39}$	7627.00	4.00	N/A	N/A	MW	${}_2\mathrm{S}_{40}$	7776.00	4.00	N/A	N/A	MW
${}_2\mathrm{S}_{41}$	7917.50	6.00	N/A	N/A	MW	${}_2\mathrm{S}_{42}$	8065.00	8.00	N/A	N/A	MW
${}_2\mathrm{S}_{43}$	8213.00	7.00	N/A	N/A	MW	${}_2\mathrm{S}_{44}$	8367.00	6.00	N/A	N/A	MW
${}_2\mathrm{S}_{45}$	8515.00	8.00	N/A	N/A	MW	${}_2\mathrm{S}_{46}$	8682.00	6.00	N/A	N/A	MW
${}_3\mathrm{S}_{47}$	9729.00	6.00	N/A	N/A	MW	${}_3\mathrm{S}_{48}$	9877.00	6.00	N/A	N/A	MW

Table A.5: Normal mode spheroidal data collection for cluster general mantle modes with observed frequency f_{obs} in μHz and global quality factors Q with respective uncertainties. Data collected from references MW: *Masters and Widmer* (1995), RS: *Resovsky and Ritzwoller* (1998), DE: *Deuss et al.* (2013).

${}_n\text{S}_l$	f_{obs}	f_{err}	Q_{obs}	Q_{err}	ref.	${}_n\text{S}_l$	f_{obs}	f_{err}	Q_{obs}	Q_{err}	ref.
${}_0\text{S}_8$	1412.81	0.40	342	2	DE	${}_0\text{S}_9$	1577.56	0.40	330	2	DE
${}_0\text{S}_{10}$	1725.65	0.11	343	5	RS	${}_1\text{S}_2$	679.91	1.00	327	5	DE
${}_1\text{S}_3$	939.98	1.20	303	5	DE	${}_1\text{S}_4$	1172.89	1.00	298	3	DE
${}_1\text{S}_5$	1370.09	0.60	331	3	DE	${}_3\text{S}_{12}$	3361.40	0.45	N/A	N/A	MW
${}_3\text{S}_{13}$	3506.20	0.70	N/A	N/A	MW	${}_3\text{S}_{14}$	3655.40	0.60	N/A	N/A	MW
${}_3\text{S}_{15}$	3809.80	0.80	N/A	N/A	MW	${}_3\text{S}_{16}$	3965.60	1.50	N/A	N/A	MW
${}_3\text{S}_{17}$	4124.30	0.90	N/A	N/A	MW	${}_3\text{S}_{18}$	4284.00	1.00	N/A	N/A	MW
${}_3\text{S}_{19}$	4447.00	1.00	N/A	N/A	MW	${}_3\text{S}_{20}$	4606.00	1.00	N/A	N/A	MW
${}_3\text{S}_{21}$	4771.00	1.50	N/A	N/A	MW	${}_3\text{S}_{22}$	4931.50	1.50	N/A	N/A	MW
${}_3\text{S}_{23}$	5092.50	2.00	N/A	N/A	MW	${}_3\text{S}_{24}$	5262.50	1.50	N/A	N/A	MW
${}_3\text{S}_{41}$	8816.50	2.50	N/A	N/A	MW	${}_3\text{S}_{42}$	8966.50	2.50	N/A	N/A	MW
${}_3\text{S}_{43}$	9120.50	2.00	N/A	N/A	MW	${}_3\text{S}_{44}$	9275.00	3.50	N/A	N/A	MW
${}_3\text{S}_{45}$	9424.00	4.50	N/A	N/A	MW	${}_3\text{S}_{46}$	9575.50	4.50	N/A	N/A	MW
${}_4\text{S}_{23}$	5858.50	3.50	N/A	N/A	MW	${}_4\text{S}_{24}$	6025.50	3.50	N/A	N/A	MW
${}_4\text{S}_{25}$	6199.00	3.00	N/A	N/A	MW	${}_4\text{S}_{26}$	6363.00	3.50	N/A	N/A	MW
${}_4\text{S}_{27}$	6532.00	2.00	N/A	N/A	MW	${}_4\text{S}_{28}$	6705.00	1.50	N/A	N/A	MW
${}_4\text{S}_{29}$	6870.00	2.00	N/A	N/A	MW	${}_4\text{S}_{30}$	7034.00	2.00	N/A	N/A	MW
${}_4\text{S}_{31}$	7200.00	2.00	N/A	N/A	MW	${}_4\text{S}_{32}$	7366.00	2.00	N/A	N/A	MW
${}_4\text{S}_{33}$	7532.00	1.50	N/A	N/A	MW	${}_4\text{S}_{34}$	7691.00	1.50	N/A	N/A	MW
${}_4\text{S}_{35}$	7856.00	1.50	N/A	N/A	MW	${}_4\text{S}_{36}$	8015.50	3.50	N/A	N/A	MW
${}_4\text{S}_{37}$	8177.50	3.00	N/A	N/A	MW	${}_4\text{S}_{38}$	8336.00	2.00	N/A	N/A	MW
${}_4\text{S}_{39}$	8492.50	3.00	N/A	N/A	MW	${}_5\text{S}_{11}$	4456.84	2.20	399	6	DE
${}_5\text{S}_{12}$	4695.73	0.60	443	4	DE	${}_5\text{S}_{13}$	4927.50	1.50	N/A	N/A	MW
${}_5\text{S}_{14}$	5134.93	1.20	403	3	DE	${}_5\text{S}_{15}$	5326.85	0.40	365	2	DE
${}_5\text{S}_{16}$	5502.43	2.00	324	2	DE	${}_5\text{S}_{17}$	5668.75	1.20	315	3	DE
${}_5\text{S}_{23}$	6635.00	3.50	N/A	N/A	MW	${}_5\text{S}_{24}$	6802.00	3.00	N/A	N/A	MW
${}_5\text{S}_{25}$	6964.50	3.50	N/A	N/A	MW	${}_5\text{S}_{26}$	7129.00	2.00	N/A	N/A	MW

Table A.6: Normal mode spheroidal data collection for cluster general mantle modes with observed frequency f_{obs} in μHz and global quality factors Q with respective uncertainties. Data collected from references MW: *Masters and Widmer* (1995), DE: *Deuss et al.* (2013).

${}_n\text{S}_l$	f_{obs}	f_{err}	Q_{obs}	Q_{err}	ref.	${}_n\text{S}_l$	f_{obs}	f_{err}	Q_{obs}	Q_{err}	ref.
${}_5\text{S}_{28}$	7450.50	2.00	N/A	N/A	MW	${}_5\text{S}_{29}$	7616.00	2.50	N/A	N/A	MW
${}_5\text{S}_{30}$	7776.50	2.50	N/A	N/A	MW	${}_5\text{S}_{31}$	7939.00	1.50	N/A	N/A	MW
${}_5\text{S}_{32}$	8098.00	5.00	N/A	N/A	MW	${}_5\text{S}_{33}$	8253.50	3.50	N/A	N/A	MW
${}_5\text{S}_{34}$	8410.00	4.00	N/A	N/A	MW	${}_5\text{S}_{35}$	8570.50	3.50	N/A	N/A	MW
${}_5\text{S}_{36}$	8726.50	3.50	N/A	N/A	MW	${}_5\text{S}_{37}$	8882.50	2.00	N/A	N/A	MW
${}_5\text{S}_{38}$	9035.50	4.50	N/A	N/A	MW	${}_5\text{S}_{39}$	9195.00	4.50	N/A	N/A	MW
${}_5\text{S}_{40}$	9335.50	3.00	N/A	N/A	MW	${}_5\text{S}_{41}$	9512.50	4.50	N/A	N/A	MW
${}_5\text{S}_{42}$	9666.00	3.00	N/A	N/A	MW	${}_5\text{S}_{43}$	9826.00	7.00	N/A	N/A	MW
${}_6\text{S}_{9}$	3964.99	0.80	320	3	DE	${}_6\text{S}_{10}$	4211.02	0.60	376	2	DE
${}_6\text{S}_{15}$	5601.23	2.60	289	3	DE	${}_6\text{S}_{16}$	5811.50	2.50	N/A	N/A	MW
${}_6\text{S}_{17}$	6026.50	2.00	N/A	N/A	MW	${}_6\text{S}_{18}$	6235.66	1.60	327	2	DE
${}_6\text{S}_{19}$	6453.50	2.50	N/A	N/A	MW	${}_6\text{S}_{20}$	6659.50	2.00	N/A	N/A	MW
${}_6\text{S}_{21}$	6859.00	2.00	N/A	N/A	MW	${}_6\text{S}_{22}$	7053.50	2.50	N/A	N/A	MW
${}_6\text{S}_{23}$	7241.00	2.00	N/A	N/A	MW	${}_6\text{S}_{24}$	7418.50	2.00	N/A	N/A	MW
${}_6\text{S}_{25}$	7590.00	1.50	N/A	N/A	MW	${}_6\text{S}_{26}$	7756.00	4.00	N/A	N/A	MW
${}_6\text{S}_{27}$	7929.00	7.00	N/A	N/A	MW	${}_6\text{S}_{28}$	8094.00	5.00	N/A	N/A	MW
${}_6\text{S}_{29}$	8257.50	4.00	N/A	N/A	MW	${}_6\text{S}_{30}$	8417.00	6.00	N/A	N/A	MW
${}_6\text{S}_{31}$	8589.00	5.00	N/A	N/A	MW	${}_6\text{S}_{32}$	8755.00	5.00	N/A	N/A	MW
${}_6\text{S}_{33}$	8929.00	6.00	N/A	N/A	MW	${}_6\text{S}_{34}$	9100.00	10.00	N/A	N/A	MW
${}_6\text{S}_{36}$	9420.00	6.00	N/A	N/A	MW	${}_6\text{S}_{37}$	9597.50	6.50	N/A	N/A	MW
${}_7\text{S}_{23}$	7598.00	3.50	N/A	N/A	MW	${}_7\text{S}_{24}$	7788.00	5.00	N/A	N/A	MW
${}_7\text{S}_{25}$	7968.00	3.50	N/A	N/A	MW	${}_7\text{S}_{26}$	8152.00	8.00	N/A	N/A	MW
${}_7\text{S}_{27}$	8347.00	6.00	N/A	N/A	MW	${}_7\text{S}_{28}$	8536.00	9.00	N/A	N/A	MW
${}_7\text{S}_{31}$	9107.00	8.00	N/A	N/A	MW	${}_7\text{S}_{33}$	9464.00	9.00	N/A	N/A	MW
${}_7\text{S}_{34}$	9651.00	5.00	N/A	N/A	MW	${}_7\text{S}_{35}$	9827.00	9.00	N/A	N/A	MW
${}_{10}\text{S}_{16}$	7423.00	2.50	N/A	N/A	MW	${}_{10}\text{S}_{17}$	7672.66	1.40	381	5	DE
${}_{10}\text{S}_{18}$	7936.38	2.20	415	6	DE	${}_{10}\text{S}_{19}$	8196.75	1.80	413	2	DE

Table A.7: Normal mode spheroidal data collection for cluster general mantle modes with observed frequency f_{obs} in μHz and global quality factors Q with respective uncertainties. Data collected from references MW: *Masters and Widmer* (1995), DE: *Deuss et al.* (2013).

${}_n\text{S}_l$	f_{obs}	f_{err}	Q_{obs}	Q_{err}	ref.	${}_n\text{S}_l$	f_{obs}	f_{err}	Q_{obs}	Q_{err}	ref.
${}_{10}\text{S}_{20}$	8446.05	3.20	389	3	DE	${}_{10}\text{S}_{21}$	8671.33	3.60	333	2	DE
${}_{10}\text{S}_{22}$	8868.00	7.00	N/A	N/A	MW	${}_{11}\text{S}_{23}$	9332.85	5.00	320	4	DE
${}_{11}\text{S}_{24}$	9570.47	4.80	360	3	DE	${}_{11}\text{S}_{25}$	9808.51	2.60	373	8	DE

Table A.8: Normal mode spheroidal data collection for cluster lower mantle modes with observed frequency f_{obs} in μHz and global quality factors Q with respective uncertainties. Data collected from references MW: *Masters and Widmer* (1995), DE: *Deuss et al.* (2013).

${}_n\text{S}_l$	f_{obs}	f_{err}	Q_{obs}	Q_{err}	ref.	${}_n\text{S}_l$	f_{obs}	f_{err}	Q_{obs}	Q_{err}	ref.
${}_0\text{S}_6$	1037.54	0.80	358	4	DE	${}_0\text{S}_7$	1230.98	0.60	350	3	DE
${}_2\text{S}_1$	404.17	0.80	414	70	DE	${}_3\text{S}_6$	2548.80	1.60	296	8	DE
${}_3\text{S}_7$	2685.78	4.20	283	7	DE	${}_3\text{S}_8$	2819.25	0.60	275	2	DE
${}_3\text{S}_9$	2951.39	0.60	260	4	DE	${}_3\text{S}_{10}$	3081.50	1.00	N/A	N/A	MW
${}_3\text{S}_{11}$	3220.60	0.70	N/A	N/A	MW	${}_4\text{S}_2$	1721.41	1.00	485	18	DE
${}_4\text{S}_3$	2048.27	0.20	520	7	DE	${}_4\text{S}_4$	2278.30	0.60	292	3	DE
${}_4\text{S}_5$	2411.12	0.60	287	5	DE	${}_4\text{S}_{10}$	3864.50	2.00	N/A	N/A	MW
${}_4\text{S}_{11}$	4009.00	2.00	N/A	N/A	MW	${}_4\text{S}_{12}$	4150.00	2.00	N/A	N/A	MW
${}_4\text{S}_{13}$	4294.00	2.00	N/A	N/A	MW	${}_4\text{S}_{14}$	4433.00	1.50	N/A	N/A	MW
${}_4\text{S}_{15}$	4583.00	1.50	N/A	N/A	MW	${}_4\text{S}_{16}$	4730.00	2.50	N/A	N/A	MW
${}_4\text{S}_{17}$	4882.50	2.00	N/A	N/A	MW	${}_4\text{S}_{18}$	5043.00	2.50	N/A	N/A	MW
${}_4\text{S}_{19}$	5201.00	2.00	N/A	N/A	MW	${}_4\text{S}_{20}$	5362.00	2.50	N/A	N/A	MW
${}_4\text{S}_{21}$	5525.00	2.00	N/A	N/A	MW	${}_4\text{S}_{22}$	5694.00	2.50	N/A	N/A	MW
${}_5\text{S}_2$	2090.47	1.20	358	7	DE	${}_5\text{S}_3$	2168.68	1.20	310	5	DE
${}_5\text{S}_4$	2379.18	0.80	531	7	DE	${}_5\text{S}_5$	2703.39	0.20	568	5	DE
${}_5\text{S}_6$	3011.03	1.00	547	7	DE	${}_5\text{S}_7$	3291.63	0.80	579	13	DE
${}_5\text{S}_8$	3525.91	0.40	463	4	DE	${}_5\text{S}_{18}$	5831.00	3.00	N/A	N/A	MW
${}_5\text{S}_{19}$	5989.50	2.00	N/A	N/A	MW	${}_5\text{S}_{20}$	6152.00	3.00	N/A	N/A	MW
${}_5\text{S}_{21}$	6312.50	2.00	N/A	N/A	MW	${}_5\text{S}_{22}$	6480.00	6.00	N/A	N/A	MW
${}_6\text{S}_8$	3737.50	1.00	N/A	N/A	MW	${}_6\text{S}_{14}$	5409.00	2.00	N/A	N/A	MW
${}_7\text{S}_5$	3657.54	0.40	514	5	DE	${}_7\text{S}_6$	3955.63	0.40	557	3	DE
${}_7\text{S}_7$	4234.38	0.60	446	2	DE	${}_7\text{S}_8$	4449.42	2.60	381	5	DE
${}_7\text{S}_9$	4614.45	2.80	333	4	DE	${}_7\text{S}_{10}$	4763.50	4.50	N/A	N/A	MW
${}_7\text{S}_{11}$	4915.50	3.00	N/A	N/A	MW	${}_7\text{S}_{12}$	5068.50	2.50	N/A	N/A	MW
${}_7\text{S}_{17}$	6611.00	4.50	N/A	N/A	MW	${}_7\text{S}_{19}$	6919.00	7.00	N/A	N/A	MW
${}_7\text{S}_{20}$	7085.00	5.00	N/A	N/A	MW	${}_7\text{S}_{21}$	7238.50	4.50	N/A	N/A	MW
${}_7\text{S}_{22}$	7416.00	6.00	N/A	N/A	MW	${}_8\text{S}_6$	4430.29	0.60	402	3	DE

Table A.9: Normal mode spheroidal data collection for cluster lower mantle modes with observed frequency f_{obs} in μHz and global quality factors Q with respective uncertainties. Data collected from references MW: *Masters and Widmer* (1995), DE: *Deuss et al.* (2013).

${}_nS_l$	f_{obs}	f_{err}	Q_{obs}	Q_{err}	ref.	${}_nS_l$	f_{obs}	f_{err}	Q_{obs}	Q_{err}	ref.
${}_8S_7$	4646.44	3.20	332	10	DE	${}_8S_{10}$	5503.01	0.80	489	3	DE
${}_8S_{11}$	5715.50	3.00	N/A	N/A	MW	${}_8S_{22}$	8135.00	8.00	N/A	N/A	MW
${}_9S_2$	3230.92	1.60	439	11	DE	${}_9S_{10}$	5606.09	4.60	323	5	DE
${}_9S_{11}$	5882.36	1.00	391	3	DE	${}_9S_{12}$	6183.66	0.80	448	4	DE
${}_9S_{13}$	6480.68	1.00	503	3	DE	${}_9S_{14}$	6764.71	0.60	499	5	DE
${}_9S_{15}$	7025.29	2.00	436	5	DE	${}_9S_{16}$	7238.00	3.00	N/A	N/A	MW
${}_9S_{18}$	7551.00	5.00	N/A	N/A	MW	${}_{10}S_{13}$	6871.00	9.00	N/A	N/A	MW
${}_{10}S_{15}$	7202.00	5.00	N/A	N/A	MW	${}_{11}S_9$	6431.87	1.00	614	9	DE
${}_{11}S_{10}$	6705.57	2.20	431	5	DE	${}_{11}S_{11}$	6915.00	9.00	N/A	N/A	MW
${}_{11}S_{17}$	8265.00	8.00	N/A	N/A	MW	${}_{11}S_{20}$	8715.00	10.00	N/A	N/A	MW
${}_{11}S_{22}$	9101.50	4.50	N/A	N/A	MW	${}_{12}S_6$	5643.85	3.00	262	6	DE
${}_{12}S_7$	5852.44	2.00	409	4	DE	${}_{12}S_8$	6132.06	1.20	559	5	DE
${}_{12}S_{12}$	7448.91	0.80	557	3	DE	${}_{12}S_{13}$	7769.84	2.20	552	3	DE
${}_{12}S_{14}$	8090.28	1.80	515	9	DE	${}_{12}S_{15}$	8404.52	1.80	528	5	DE
${}_{13}S_{16}$	8744.85	5.60	388	3	DE	${}_{13}S_{17}$	9055.50	4.00	N/A	N/A	MW
${}_{13}S_{18}$	9363.72	2.20	490	3	DE	${}_{13}S_{19}$	9664.48	2.80	501	4	DE
${}_{13}S_{20}$	9954.47	2.00	478	4	DE	${}_{15}S_{15}$	9592.15	2.20	467	13	DE
${}_{15}S_{16}$	9921.12	3.20	515	5	DE	${}_{16}S_{14}$	9299.32	19.00	314	6	DE
${}_{18}S_9$	8735.00	7.00	N/A	N/A	MW	${}_{22}S_1$	7822.62	0.60	944	12	DE

A.7 Radial and toroidal mode misfits

In the following, we show the data misfits to the radial and toroidal modes and quality factors. Toroidal mode centre frequency and quality factor misfits are shown in Figure A.1 and Figure A.4, respectively. Radial centre frequency misfits are shown in Figure A.2, whereas radial quality factor misfits are shown in figure A.5.

A.8 Integration of equations of state

To get a thermodynamically consistent core we are starting with the pressure at the CMB p_{CMB} which is a result of our mantle pressure integration. For the outer core, this pressure is then used to generate the volume V by finding the unique zero of the Vinet equation of state (Eq. 13) subtracted by the input pressure. In the inner core the procedure is analogous, but using equation (17) subtracted by the input pressure to generate the strain ϵ. We find the roots of the equations by using Brent's method as implemented in the python package scipy (*Virtanen et al.*, 2020). The main difference between the inner core and the outer core are the boundary conditions. In addition to the pressure at the ICB, the inner core equation system has to fulfill the boundary condition at the zero radius that the gravity acceleration g has to

Table A.10: Normal mode spheroidal data for clusters full planet modes and inner core modes with observed frequency f_{obs} in μHz and global quality factors Q with respective uncertainties. Data collected from references MW: *Masters and Widmer* (1995), DE: *Deuss et al.* (2013), MAE: *Mäkinen and Deuss* (2013).

${}_n\text{S}_l$	f_{obs}	f_{err}	Q_{obs}	Q_{err}	ref.	${}_n\text{S}_l$	f_{obs}	f_{err}	Q_{obs}	Q_{err}	ref.
${}_0\text{S}_2$	309.48	0.40	477	177	DE	${}_0\text{S}_3$	468.46	0.80	405	14	DE
${}_0\text{S}_4$	646.78	0.60	373	9	DE	${}_0\text{S}_5$	839.99	0.80	364	5	DE
${}_1\text{S}_6$	1521.48	0.80	400	5	DE	${}_1\text{S}_7$	1654.56	1.20	416	5	DE
${}_1\text{S}_8$	1797.86	0.60	422	3	DE	${}_1\text{S}_{14}$	2973.36	15.00	291	9	DE
${}_2\text{S}_3$	1242.83	0.60	444	11	MAE	${}_2\text{S}_4$	1379.51	0.60	388	2	DE
${}_2\text{S}_5$	1515.23	0.60	313	2	DE	${}_3\text{S}_1$	944.29	0.80	874	34	DE
${}_3\text{S}_2$	1106.16	3.20	270	7	MAE	${}_4\text{S}_1$	1411.80	1.00	380	12	DE
${}_6\text{S}_1$	1983.33	0.36	293	29	RS	${}_6\text{S}_3$	2821.70	0.60	459	8	DE
${}_8\text{S}_1$	2872.63	0.20	1000	15	DE	${}_8\text{S}_5$	4165.03	0.80	653	5	MAE
${}_9\text{S}_3$	3555.60	1.40	626	18	MAE	${}_9\text{S}_4$	3878.28	1.80	428	9	MAE
${}_9\text{S}_6$	4618.88	3.40	349	7	DE	${}_9\text{S}_8$	5138.47	1.20	494	4	DE
${}_9\text{S}_9$	5378.00	3.50	N/A	N/A	MW	${}_{10}\text{S}_8$	5735.00	7.00	N/A	N/A	MW
${}_{10}\text{S}_9$	5939.00	4.50	N/A	N/A	MW	${}_{10}\text{S}_{10}$	6186.47	4.20	340	7	DE
${}_{10}\text{S}_{11}$	6446.00	6.00	N/A	N/A	MW	${}_{10}\text{S}_{12}$	6682.50	3.00	N/A	N/A	MW
${}_{11}\text{S}_1$	3687.69	11.80	581	20	DE	${}_{11}\text{S}_4$	4765.94	1.40	682	11	MAE
${}_{11}\text{S}_5$	5072.81	0.60	622	6	MAE	${}_{11}\text{S}_6$	5348.93	0.80	399	7	DE
${}_{11}\text{S}_{12}$	7142.97	8.20	372	8	DE	${}_{11}\text{S}_{13}$	7411.50	2.00	N/A	N/A	MW
${}_{11}\text{S}_{14}$	7679.55	10.40	361	13	DE	${}_{12}\text{S}_{10}$	6860.00	5.00	N/A	N/A	MW
${}_{12}\text{S}_{11}$	7133.44	0.80	508	6	DE	${}_{12}\text{S}_{16}$	8686.69	2.20	425	7	DE
${}_{12}\text{S}_{17}$	8928.22	2.80	370	10	DE	${}_{13}\text{S}_1$	4494.50	1.80	609	13	MAE
${}_{13}\text{S}_2$	4844.54	0.40	930	8	MAE	${}_{13}\text{S}_3$	5193.78	1.60	885	21	MAE
${}_{13}\text{S}_6$	6157.53	2.00	535	8	MAE	${}_{13}\text{S}_{15}$	8472.67	12.60	337	32	DE
${}_{14}\text{S}_4$	5542.04	5.60	693	14	DE	${}_{14}\text{S}_7$	6769.37	4.80	324	4	DE
${}_{14}\text{S}_8$	7042.54	5.60	416	6	DE	${}_{14}\text{S}_9$	7344.53	2.40	545	4	DE
${}_{14}\text{S}_{13}$	8729.83	1.40	474	5	DE	${}_{14}\text{S}_{14}$	8981.50	1.60	368	6	DE
${}_{15}\text{S}_3$	6031.13	1.60	747	8	MAE	${}_{15}\text{S}_4$	6323.64	5.40	405	7	MAE
${}_{15}\text{S}_{11}$	8132.00	6.00	N/A	N/A	MW	${}_{15}\text{S}_{12}$	8427.74	2.60	553	9	DE

Table A.11: Normal mode spheroidal data for clusters full planet modes and inner core modes with observed frequency f_{obs} in μHz and global quality factors Q with respective uncertainties. Data collected from references MW: *Masters and Widmer* (1995), DE: *Deuss et al.* (2013), MAE: *Mäkinen and Deuss* (2013).

${}_n\text{S}_l$	f_{obs}	f_{err}	Q_{obs}	Q_{err}	ref.	${}_n\text{S}_l$	f_{obs}	f_{err}	Q_{obs}	Q_{err}	ref.
${}_{16}\text{S}_5$	6830.56	1.40	506	8	MAE	${}_{16}\text{S}_6$	7149.10	1.80	590	6	DE
${}_{16}\text{S}_7$	7470.18	2.40	634	8	DE	${}_{16}\text{S}_{10}$	8433.36	1.60	697	12	DE
${}_{16}\text{S}_{11}$	8730.13	5.40	444	11	DE	${}_{17}\text{S}_1$	6128.91	4.80	420	19	DE
${}_{17}\text{S}_8$	7802.59	7.80	427	13	DE	${}_{17}\text{S}_{12}$	9148.44	1.20	434	10	DE
${}_{17}\text{S}_{13}$	9428.47	1.60	533	4	DE	${}_{17}\text{S}_{14}$	9698.54	6.00	472	5	DE
${}_{17}\text{S}_{15}$	9932.67	10.40	335	3	DE	${}_{18}\text{S}_3$	6888.89	2.00	699	10	MAE
${}_{18}\text{S}_4$	7238.53	0.80	986	9	MAE	${}_{18}\text{S}_6$	7956.81	5.20	394	14	DE
${}_{19}\text{S}_{10}$	9351.14	1.00	616	5	DE	${}_{19}\text{S}_{11}$	9644.79	4.60	588	11	DE
${}_{20}\text{S}_1$	6953.80	2.80	688	12	MAE	${}_{20}\text{S}_5$	8465.52	3.00	580	23	DE
${}_{21}\text{S}_6$	8848.80	5.00	542	6	MAE	${}_{21}\text{S}_7$	9171.18	4.20	664	7	DE
${}_{23}\text{S}_4$	8936.44	2.20	710	8	DE	${}_{23}\text{S}_5$	9289.93	0.80	883	6	DE
${}_{25}\text{S}_1$	8656.67	7.80	787	18	DE	${}_{25}\text{S}_2$	9025.19	0.80	745	11	MAE
${}_{27}\text{S}_2$	9872.16	4.60	747	7	MAE						

Table A.12: Normal mode radial data collection with observed frequency f_{obs} in μHz and global quality factors Q with respective uncertainties. Data collected from reference (*Talavera-Soza and Deuss*, 2020).

${}_n\text{S}_l$	f_{obs}	f_{err}	Q_{obs}	Q_{err}
${}_0\text{S}_0$	814.60	0.00	5982	211
${}_1\text{S}_0$	1631.56	0.12	1856	144
${}_2\text{S}_0$	2509.30	0.22	1788	122
${}_3\text{S}_0$	3271.98	0.06	1242	80
${}_4\text{S}_0$	4106.51	0.12	1157	86
${}_5\text{S}_0$	4886.72	0.19	1008	13
${}_6\text{S}_0$	5742.11	0.57	1077	111
${}_7\text{S}_0$	6583.56	0.55	883	87
${}_8\text{S}_0$	7429.66	0.40	1198	139
${}_9\text{S}_0$	8268.27	0.25	965	63
${}_{11}\text{S}_0$	9893.37	0.35	1053	93

Table A.13: Normal mode toroidal collection with observed frequency f_{obs} in μHz and global quality factors Q with respective uncertainties. Data collected from references MW: *Masters and Widmer* (1995), RS: *Resovsky and Ritzwoller* (1998), SN: *Schneider and Deuss* (2020).

${}_n\mathrm{T}_l$	f_{obs}	f_{err}	Q_{obs}	Q_{err}	ref.	${}_n\mathrm{T}_l$	f_{obs}	f_{err}	Q_{obs}	Q_{err}	ref.
${}_0\mathrm{T}_2$	377.30	0.80	N/A	N/A	MW	${}_0\mathrm{T}_3$	587.60	0.70	N/A	N/A	MW
${}_0\mathrm{T}_4$	766.00	0.15	268	22	RS	${}_0\mathrm{T}_5$	928.37	0.10	254	16	RS
${}_0\mathrm{T}_6$	1079.08	0.10	249	34	RS	${}_0\mathrm{T}_7$	1221.00	0.10	207	11	RS
${}_0\mathrm{T}_8$	1356.55	0.17	201	10	RS	${}_0\mathrm{T}_9$	1487.07	0.17	191	15	RS
${}_0\mathrm{T}_{10}$	1613.67	0.41	175	19	RS	${}_0\mathrm{T}_{11}$	1737.42	0.20	171	10	RS
${}_0\mathrm{T}_{12}$	1858.82	0.17	168	10	RS	${}_0\mathrm{T}_{13}$	1977.88	0.18	162	10	RS
${}_0\mathrm{T}_{14}$	2095.43	0.18	158	10	RS	${}_0\mathrm{T}_{15}$	2211.16	0.40	155	10	RS
${}_1\mathrm{T}_1$	1235.58	0.48	268	30	RS	${}_1\mathrm{T}_2$	1319.29	0.17	302	19	SN
${}_1\mathrm{T}_3$	1438.45	0.08	299	7	SN	${}_1\mathrm{T}_4$	1585.09	0.22	290	34	RS
${}_1\mathrm{T}_5$	1750.19	0.13	303	9	SN	${}_1\mathrm{T}_6$	1925.25	0.12	277	7	SN
${}_1\mathrm{T}_7$	2103.40	0.06	289	3	SN	${}_1\mathrm{T}_8$	2279.49	0.19	270	30	RS
${}_1\mathrm{T}_9$	2452.41	0.23	252	13	RS	${}_1\mathrm{T}_{10}$	2619.00	2.00	N/A	N/A	MW
${}_1\mathrm{T}_{11}$	2783.00	1.00	N/A	N/A	MW	${}_1\mathrm{T}_{13}$	3099.07	0.10	236	3	SN
${}_1\mathrm{T}_{14}$	3253.52	0.06	227	2	SN	${}_1\mathrm{T}_{15}$	3407.00	1.50	N/A	N/A	MW
${}_1\mathrm{T}_{16}$	3560.50	1.00	N/A	N/A	MW	${}_1\mathrm{T}_{17}$	3710.00	1.00	N/A	N/A	MW
${}_1\mathrm{T}_{19}$	4006.00	2.00	N/A	N/A	MW	${}_1\mathrm{T}_{20}$	4152.00	2.50	N/A	N/A	MW
${}_1\mathrm{T}_{21}$	4295.00	1.00	N/A	N/A	MW	${}_1\mathrm{T}_{22}$	4440.00	2.00	N/A	N/A	MW
${}_1\mathrm{T}_{23}$	4580.00	2.00	N/A	N/A	MW	${}_1\mathrm{T}_{24}$	4721.00	2.00	N/A	N/A	MW
${}_1\mathrm{T}_{25}$	4859.50	2.00	N/A	N/A	MW	${}_1\mathrm{T}_{27}$	5129.00	2.00	N/A	N/A	MW
${}_1\mathrm{T}_{28}$	5264.50	2.00	N/A	N/A	MW	${}_1\mathrm{T}_{29}$	5399.50	2.50	N/A	N/A	MW
${}_1\mathrm{T}_{30}$	5527.50	1.50	N/A	N/A	MW	${}_2\mathrm{T}_2$	2232.80	0.27	235	31	RS
${}_2\mathrm{T}_3$	2295.28	0.22	236	7	SN	${}_2\mathrm{T}_4$	2379.09	0.15	233	18	RS
${}_2\mathrm{T}_5$	2484.87	0.15	245	5	SN	${}_2\mathrm{T}_7$	2753.00	0.33	247	12	SN
${}_2\mathrm{T}_8$	2912.57	0.08	267	3	SN	${}_2\mathrm{T}_{10}$	3267.50	3.50	N/A	N/A	MW
${}_2\mathrm{T}_{11}$	3456.00	2.50	N/A	N/A	MW	${}_2\mathrm{T}_{12}$	3640.50	2.50	N/A	N/A	MW
${}_2\mathrm{T}_{13}$	3830.52	0.21	271	7	SN	${}_2\mathrm{T}_{14}$	4013.81	0.24	301	8	SN
${}_2\mathrm{T}_{15}$	4192.69	0.22	287	7	SN	${}_2\mathrm{T}_{16}$	4368.75	0.53	258	15	SN

Table A.14: Normal mode toroidal collection with observed frequency f_{obs} in μHz and global quality factors Q with respective uncertainties. Data collected from references MW: *Masters and Widmer* (1995), RS: *Resovsky and Ritzwoller* (1998), SN: *Schneider and Deuss* (2020).

${}_n\mathrm{T}_l$	f_{obs}	f_{err}	Q_{obs}	Q_{err}	ref.	${}_n\mathrm{T}_l$	f_{obs}	f_{err}	Q_{obs}	Q_{err}	ref.
${}_2\mathrm{T}_{18}$	4710.00	2.50	N/A	N/A	MW	${}_2\mathrm{T}_{20}$	5044.50	4.00	N/A	N/A	MW
${}_2\mathrm{T}_{21}$	5202.00	2.50	N/A	N/A	MW	${}_2\mathrm{T}_{22}$	5366.00	2.50	N/A	N/A	MW
${}_2\mathrm{T}_{23}$	5525.50	2.50	N/A	N/A	MW	${}_2\mathrm{T}_{24}$	5684.50	4.00	N/A	N/A	MW
${}_2\mathrm{T}_{25}$	5843.00	3.50	N/A	N/A	MW	${}_2\mathrm{T}_{26}$	6001.00	4.50	N/A	N/A	MW
${}_2\mathrm{T}_{27}$	6151.00	6.00	N/A	N/A	MW	${}_2\mathrm{T}_{28}$	6309.50	3.50	N/A	N/A	MW
${}_2\mathrm{T}_{29}$	6464.50	3.00	N/A	N/A	MW	${}_2\mathrm{T}_{30}$	6609.00	3.50	N/A	N/A	MW
${}_2\mathrm{T}_{31}$	6763.00	4.50	N/A	N/A	MW	${}_2\mathrm{T}_{32}$	6911.00	4.50	N/A	N/A	MW
${}_2\mathrm{T}_{33}$	7066.00	4.00	N/A	N/A	MW	${}_2\mathrm{T}_{34}$	7214.00	6.00	N/A	N/A	MW
${}_2\mathrm{T}_{35}$	7362.00	4.00	N/A	N/A	MW	${}_2\mathrm{T}_{36}$	7505.00	5.00	N/A	N/A	MW
${}_2\mathrm{T}_{37}$	7653.00	3.00	N/A	N/A	MW	${}_2\mathrm{T}_{38}$	7797.00	4.00	N/A	N/A	MW
${}_2\mathrm{T}_{39}$	7943.50	3.00	N/A	N/A	MW	${}_2\mathrm{T}_{40}$	8089.00	5.00	N/A	N/A	MW
${}_2\mathrm{T}_{41}$	8230.00	8.00	N/A	N/A	MW	${}_2\mathrm{T}_{42}$	8370.00	10.00	N/A	N/A	MW
${}_2\mathrm{T}_{43}$	8507.00	8.00	N/A	N/A	MW	${}_2\mathrm{T}_{44}$	8661.00	9.00	N/A	N/A	MW
${}_2\mathrm{T}_{45}$	8785.00	6.00	N/A	N/A	MW	${}_2\mathrm{T}_{46}$	8932.00	7.00	N/A	N/A	MW
${}_2\mathrm{T}_{47}$	9069.00	8.00	N/A	N/A	MW	${}_2\mathrm{T}_{48}$	9204.00	8.00	N/A	N/A	MW
${}_2\mathrm{T}_{49}$	9333.00	5.00	N/A	N/A	MW	${}_2\mathrm{T}_{50}$	9475.00	10.00	N/A	N/A	MW
${}_2\mathrm{T}_{51}$	9615.00	10.00	N/A	N/A	MW	${}_2\mathrm{T}_{52}$	9745.00	10.00	N/A	N/A	MW
${}_3\mathrm{T}_1$	3200.08	1.73	203	52	SN	${}_3\mathrm{T}_7$	3603.68	0.24	286	8	SN
${}_3\mathrm{T}_9$	3843.00	5.00	N/A	N/A	MW	${}_3\mathrm{T}_{10}$	3990.00	5.00	N/A	N/A	MW
${}_3\mathrm{T}_{12}$	4317.00	6.00	N/A	N/A	MW	${}_3\mathrm{T}_{13}$	4482.00	7.00	N/A	N/A	MW
${}_3\mathrm{T}_{16}$	5051.39	0.23	273	6	SN	${}_3\mathrm{T}_{17}$	5234.00	8.00	N/A	N/A	MW
${}_3\mathrm{T}_{18}$	5414.00	7.00	N/A	N/A	MW	${}_3\mathrm{T}_{19}$	5607.00	4.50	N/A	N/A	MW
${}_3\mathrm{T}_{20}$	5785.00	8.00	N/A	N/A	MW	${}_3\mathrm{T}_{21}$	5955.00	6.00	N/A	N/A	MW
${}_3\mathrm{T}_{22}$	6120.00	6.00	N/A	N/A	MW	${}_3\mathrm{T}_{23}$	6299.00	6.00	N/A	N/A	MW
${}_3\mathrm{T}_{25}$	6622.50	3.50	N/A	N/A	MW	${}_3\mathrm{T}_{26}$	6791.00	7.00	N/A	N/A	MW
${}_3\mathrm{T}_{27}$	6946.50	3.50	N/A	N/A	MW	${}_3\mathrm{T}_{28}$	7113.50	3.50	N/A	N/A	MW
${}_3\mathrm{T}_{29}$	7273.00	4.50	N/A	N/A	MW	${}_3\mathrm{T}_{30}$	7439.00	4.50	N/A	N/A	MW

Figure A.1: Toroidal frequency misfits for models shown in section (6.2). The observed center frequency of the modes was set to zero for displaying the different modes in one plot and the corresponding measured frequencies can be looked up in the table contained in section S1.

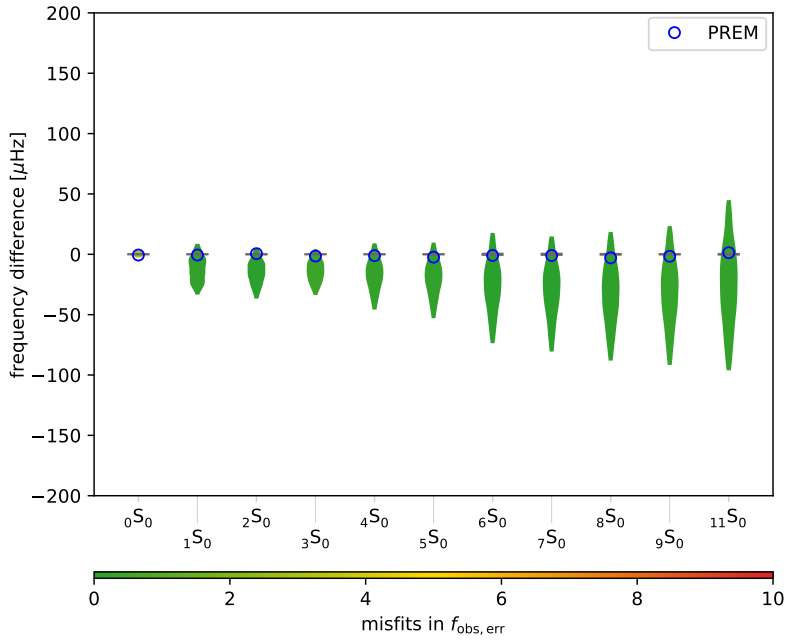

Figure A.2: Radial frequency misfits for models shown in section (6.2). The observed center frequency of the modes was set to zero for displaying the different modes in one plot and the corresponding measured frequencies can be looked up in the tables contained in section S1.

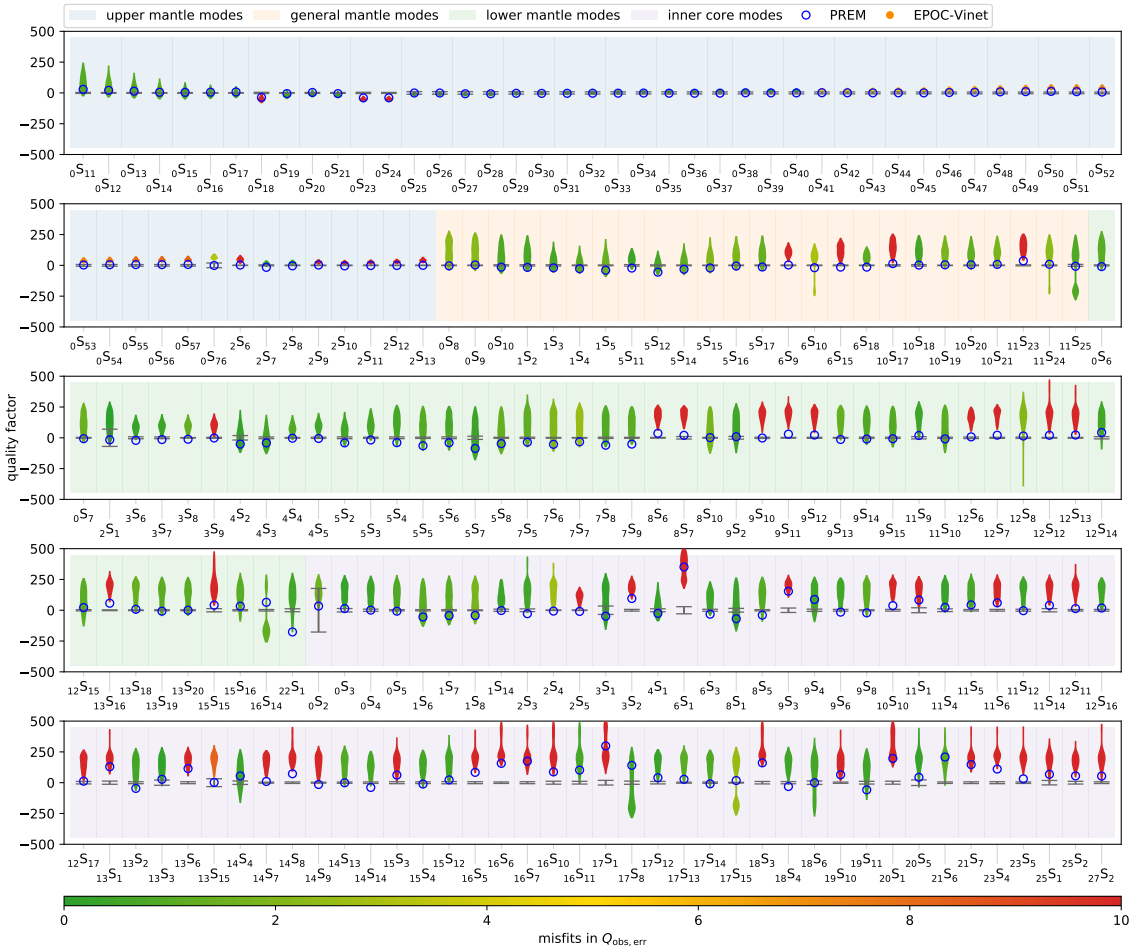

Figure A.3: Spheroidal quality factor data fit. The observed quality factor is located at zero of each violin. Color coding indicates the distance of the mean of the probability density function to the observed quality factor in multiples of the observational uncertainties. Observed spheroidal quality factors are compiled in Tables (S1–S11) and observational uncertainties span the breadth of the black horizontal bars. Blue circles indicate predictions based on PREM.

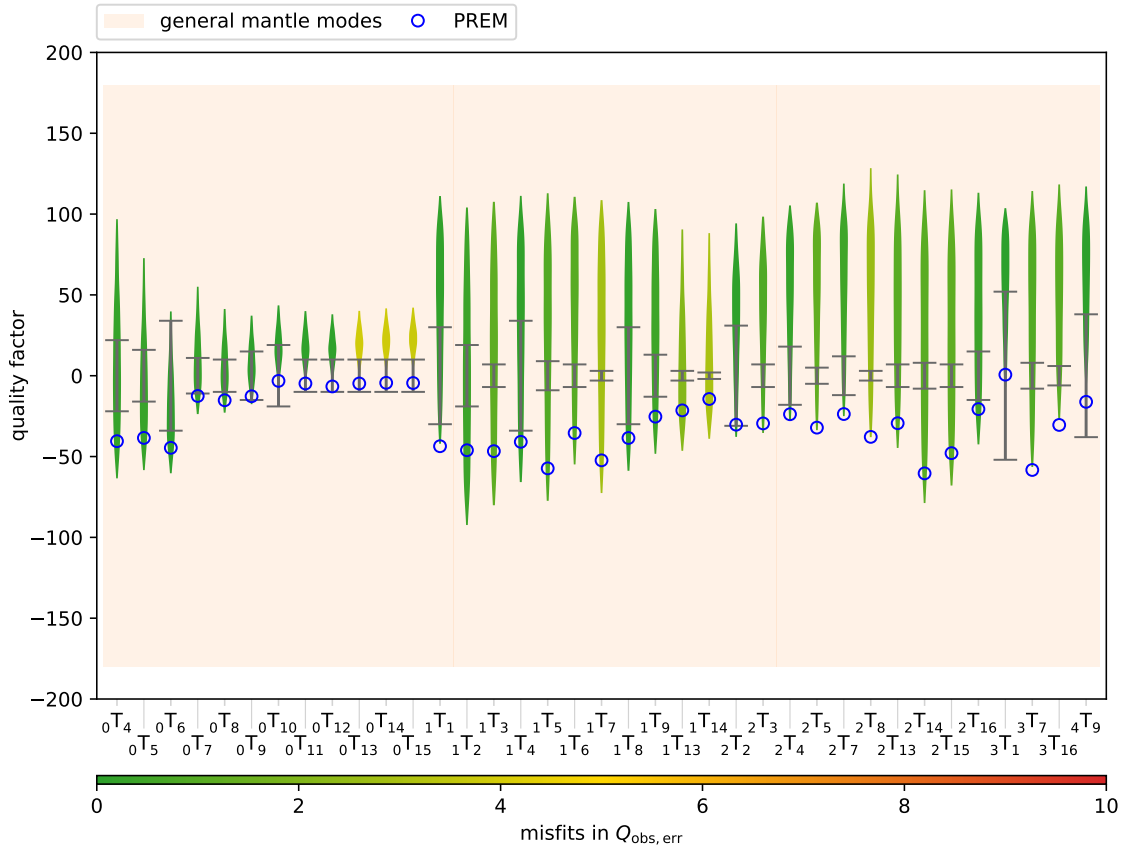

Figure A.4: Toroidal quality factor misfits for models shown in section (6.2). The observed quality factor of the modes was set to zero for displaying the different modes in one plot and the corresponding measured quality factors can be looked up in the table contained in section S1.

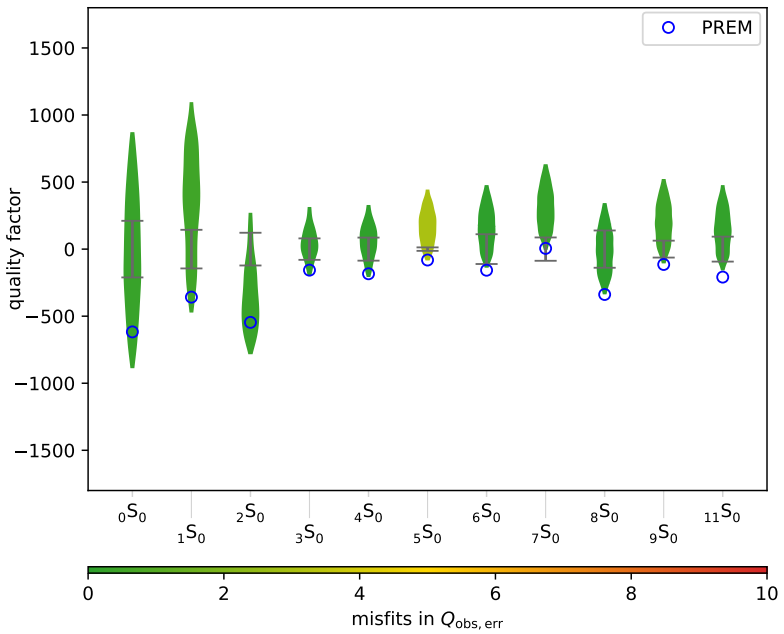

Figure A.5: Radial quality factor misfits for models shown in section (6.2). The observed center frequency of the modes was set to zero for displaying the different modes in one plot and the corresponding measured frequencies can be looked up in the table contained in section S1.

Table A.15: Normal mode toroidal collection with observed frequency f_{obs} in μHz and global quality factors Q with respective uncertainties. Data collected from references MW: *Masters and Widmer* (1995), RS: *Resovsky and Ritzwoller* (1998), SN: *Schneider and Deuss* (2020).

${}_n\mathrm{T}_l$	f_{obs}	f_{err}	Q_{obs}	Q_{err}	ref.	${}_n\mathrm{T}_l$	f_{obs}	f_{err}	Q_{obs}	Q_{err}	ref.
${}_3\mathrm{T}_{31}$	7605.00	5.00	N/A	N/A	MW	${}_3\mathrm{T}_{32}$	7757.50	4.50	N/A	N/A	MW
${}_3\mathrm{T}_{33}$	7914.50	4.50	N/A	N/A	MW	${}_3\mathrm{T}_{34}$	8080.00	5.00	N/A	N/A	MW
${}_3\mathrm{T}_{36}$	8395.00	10.00	N/A	N/A	MW	${}_3\mathrm{T}_{37}$	8548.00	5.00	N/A	N/A	MW
${}_3\mathrm{T}_{38}$	8697.00	8.00	N/A	N/A	MW	${}_3\mathrm{T}_{39}$	8858.00	8.00	N/A	N/A	MW
${}_3\mathrm{T}_{40}$	9020.00	10.00	N/A	N/A	MW	${}_3\mathrm{T}_{41}$	9166.00	8.00	N/A	N/A	MW
${}_3\mathrm{T}_{42}$	9323.00	8.00	N/A	N/A	MW	${}_3\mathrm{T}_{43}$	9472.00	7.00	N/A	N/A	MW
${}_3\mathrm{T}_{44}$	9615.00	7.00	N/A	N/A	MW	${}_3\mathrm{T}_{45}$	9782.00	9.00	N/A	N/A	MW
${}_3\mathrm{T}_{46}$	9926.00	7.00	N/A	N/A	MW	${}_4\mathrm{T}_{9}$	4775.37	1.86	237	38	SN
${}_4\mathrm{T}_{10}$	4885.00	5.00	N/A	N/A	MW	${}_4\mathrm{T}_{11}$	4993.50	4.50	N/A	N/A	MW
${}_4\mathrm{T}_{12}$	5116.00	6.00	N/A	N/A	MW	${}_4\mathrm{T}_{13}$	5243.00	7.00	N/A	N/A	MW
${}_4\mathrm{T}_{14}$	5384.50	4.00	N/A	N/A	MW	${}_4\mathrm{T}_{15}$	5538.00	7.00	N/A	N/A	MW
${}_4\mathrm{T}_{16}$	5709.00	7.00	N/A	N/A	MW	${}_4\mathrm{T}_{17}$	5870.00	9.00	N/A	N/A	MW
${}_4\mathrm{T}_{21}$	6594.00	6.00	N/A	N/A	MW	${}_4\mathrm{T}_{24}$	7159.00	8.00	N/A	N/A	MW
${}_4\mathrm{T}_{26}$	7512.00	6.00	N/A	N/A	MW	${}_4\mathrm{T}_{27}$	7694.00	7.00	N/A	N/A	MW
${}_4\mathrm{T}_{28}$	7863.00	8.00	N/A	N/A	MW	${}_4\mathrm{T}_{30}$	8195.00	10.00	N/A	N/A	MW
${}_4\mathrm{T}_{32}$	8548.00	7.00	N/A	N/A	MW	${}_4\mathrm{T}_{33}$	8718.00	4.50	N/A	N/A	MW
${}_4\mathrm{T}_{34}$	8873.00	6.00	N/A	N/A	MW	${}_4\mathrm{T}_{35}$	9050.00	5.00	N/A	N/A	MW
${}_4\mathrm{T}_{36}$	9210.00	8.00	N/A	N/A	MW	${}_4\mathrm{T}_{37}$	9390.00	7.00	N/A	N/A	MW
${}_4\mathrm{T}_{39}$	9679.00	9.00	N/A	N/A	MW						

be zero. For the inner core structure, we therefore integrate the pressure and the gravity acceleration up from a suitable starting value at the zero radius ($p_{(r=0)}$=350 GPa, $g_{(r=0)}$=0) and minimize the difference of the integrated pressure and gravity acceleration at the ICB to the actual ICB pressure and gravity acceleration that we get from the outer core calculations (p_{ICB}, g_{ICB}). This leads to a refined value for the pressure at zero radius $p_{(r=0),ref}$ which is then used to integrate the ODEs up to the ICB, where in each integration step the equation system (18) can be used to produce the radial inner core seismic properties.

A.9 Normal-mode clustering

A.9.1 Kinetic energy clustering

To determine the number of clusters for the normal-mode data set, we computed the sum of the squared error estimate as a function of cluster number. The result is shown in Figure A.6, which indicates an optimal value for six clusters. The six cluster centers are listed in table A.16.

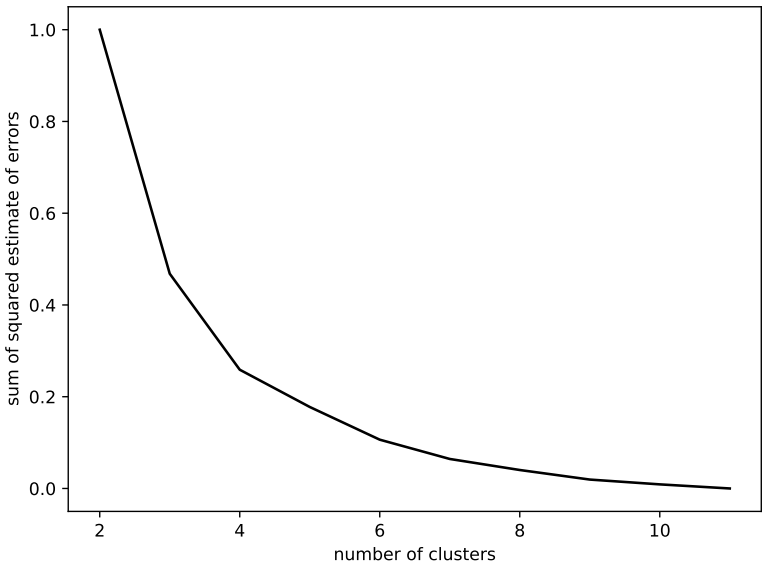

Figure A.6: Sum of squared estimate of errors for different cluster numbers (normalized). Using the elbow method to determine the number of clusters gives us a number of clusters of six for the spheroidal normal modes (sse=0.07).

Table A.16: The six cluster centers indicated by id we got from applying the KMeans algorithm to the kinetic energies in Earth regions. Number of modes (#) counts the modes in the cluster of the synthetic spheroidal spectrum of isotropic PREM (*Dziewonski and Anderson*, 1981) up to 10 mHz frequency. Note that core-mantle-boundary (CMB) Stoneley modes, while shown here, are not considered in the inversion.

id	upper mantle	lower mantle	CMB Stoneley	outer core	inner core	#
0	0.95	0.04	0	0	0	247
1	0.52	0.46	0.06	0.01	0	186
2	0.36	0.55	0.24	0.07	0.01	275
3	0.02	0.31	0.96	0.59	0	45
4	0.02	0.03	0.02	0.15	0.8	102
5	0.24	0.33	0.3	0.37	0.05	166

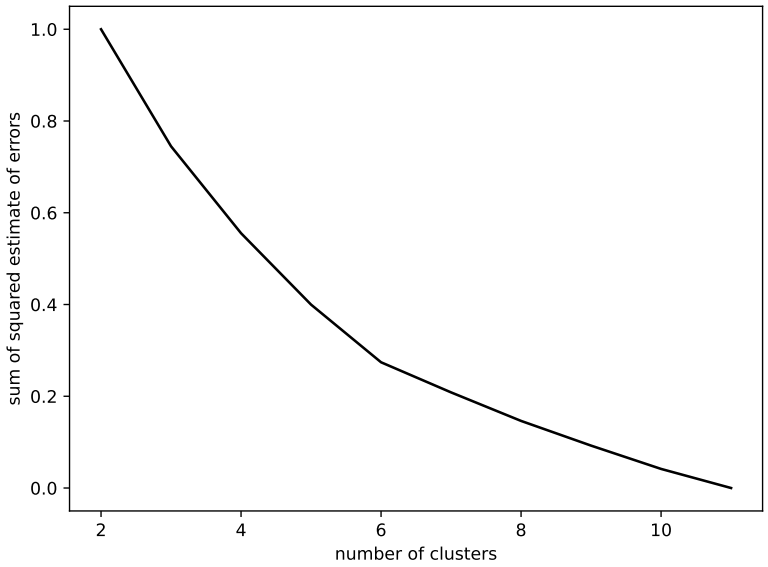

Figure A.7: Sum of squared estimate of errors for different cluster numbers (normalized). Using the elbow method to determine the number of clusters gives us a number of clusters of six for the normal mode anelastic sensitivity kernels.

A.9.2 Anelastic sensitivity clustering

To determine the number of clusters needed to determine the anelastic sensitivity kernels, we computed the sum of the squared error estimate as a function of cluster number. The result is shown in Figure A.7, which indicates an optimal value for six clusters. The six cluster centers are shown in Figure A.8.

A.10 Density robustness in the outer core

A comparison the density models inverted with the full data set and without geodetic constraints are shown in Figure A.10.

A.11 Radial model uncertainty ranges

Radial profiles of sampled seismic properties indicating the uncertainty ranges in the form of credible intervals, relative to the mean radial model, are shown in Figures S9–S12.

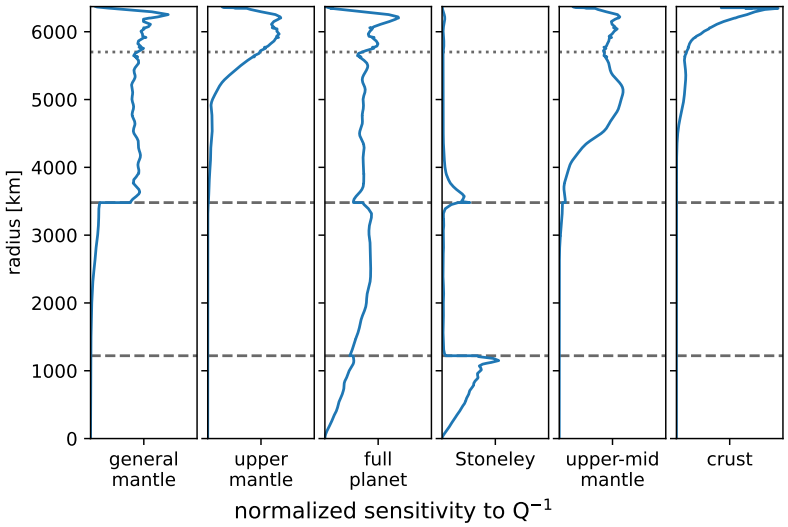

Figure A.8: The six cluster centers we got from applying the KMeans algorithm to the anelastic sensitivity kernels.

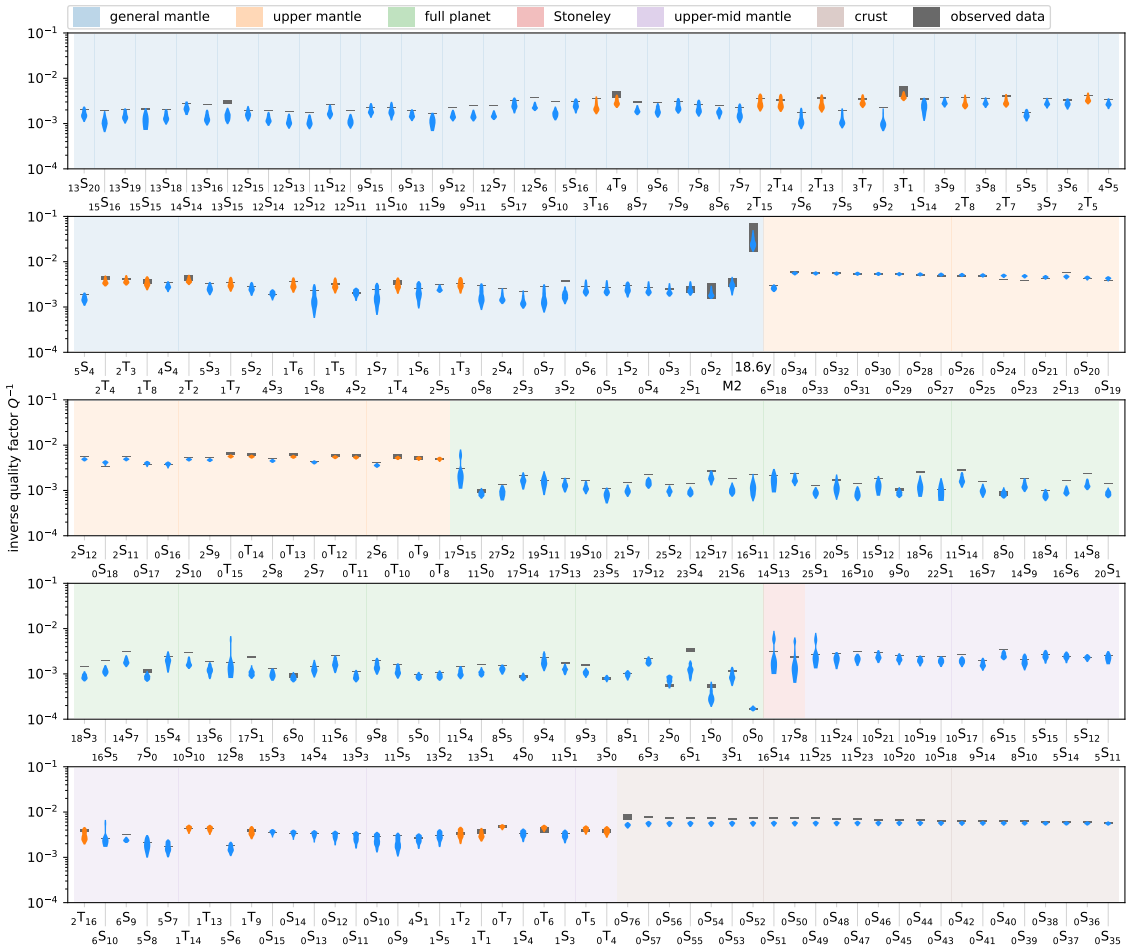

Figure A.9: Depiction of the spectrum of inverse quality factors for normal modes, grouped together via anelastic clustering. The inverse quality factors are compared to the observed inverse quality factors of the M2 tide and the 18.6 year nutation of the Earth that are clustered together with the general mantle cluster due to their similar sensitivity kernels.

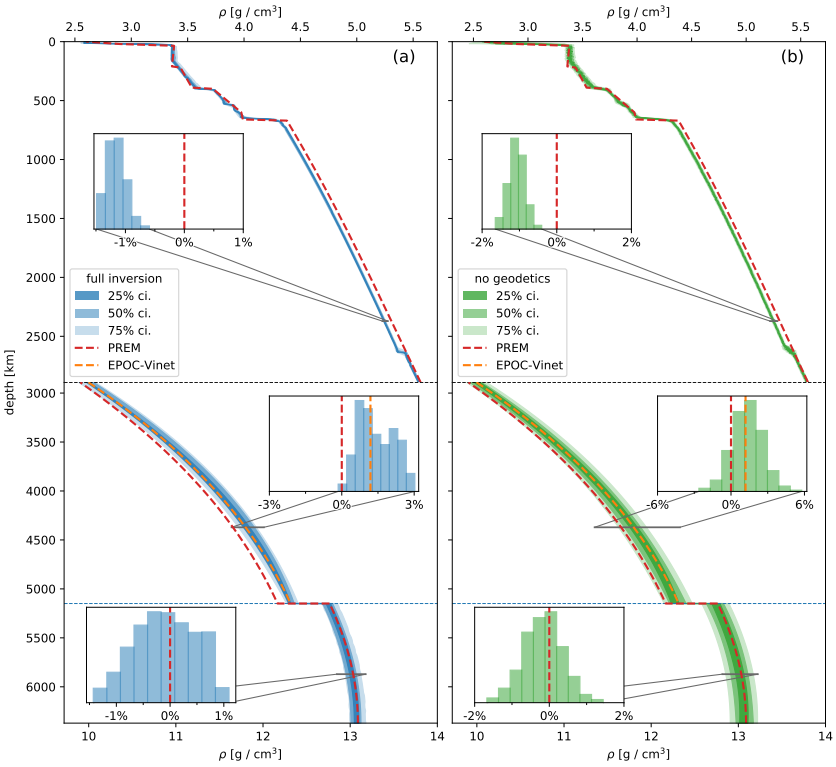

Figure A.10: Density comparison analysis. The plots show inverted density profiles obtained from inversion of different datasets: (a) full dataset, (b) without geodetic data. Sampled models are shown using probability contours in the form of credible intervals (ci).

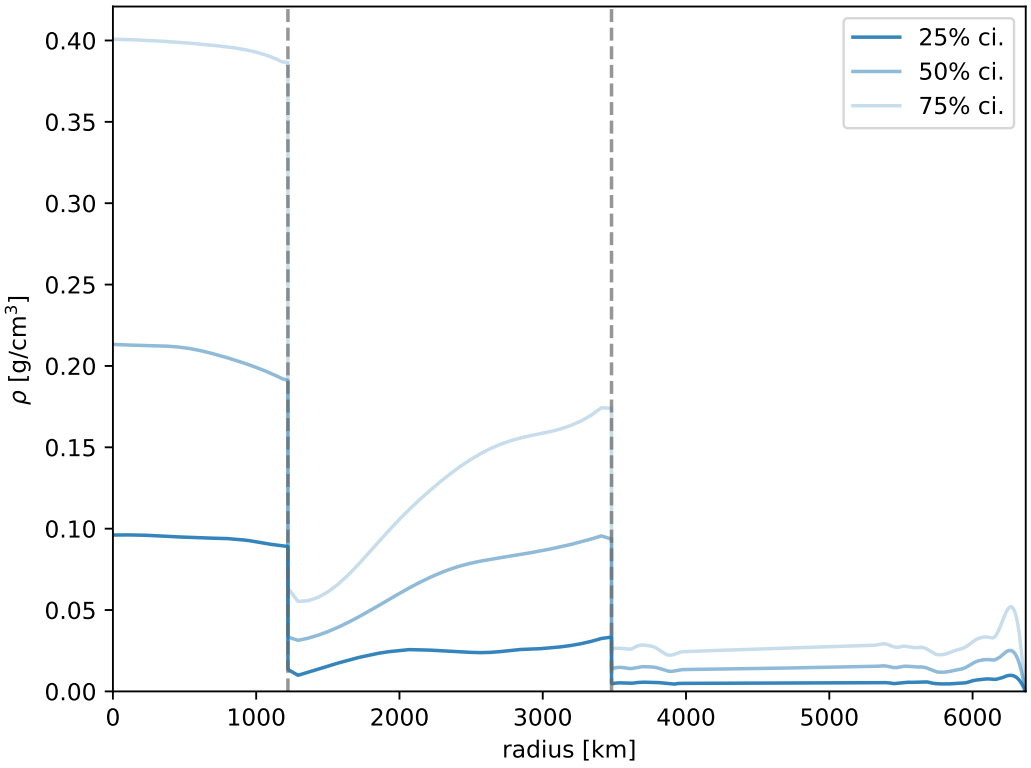

Figure A.11: Radial density sensitivity profiles. Sensitivities are shown using probability contours in the form of credible intervals (ci).

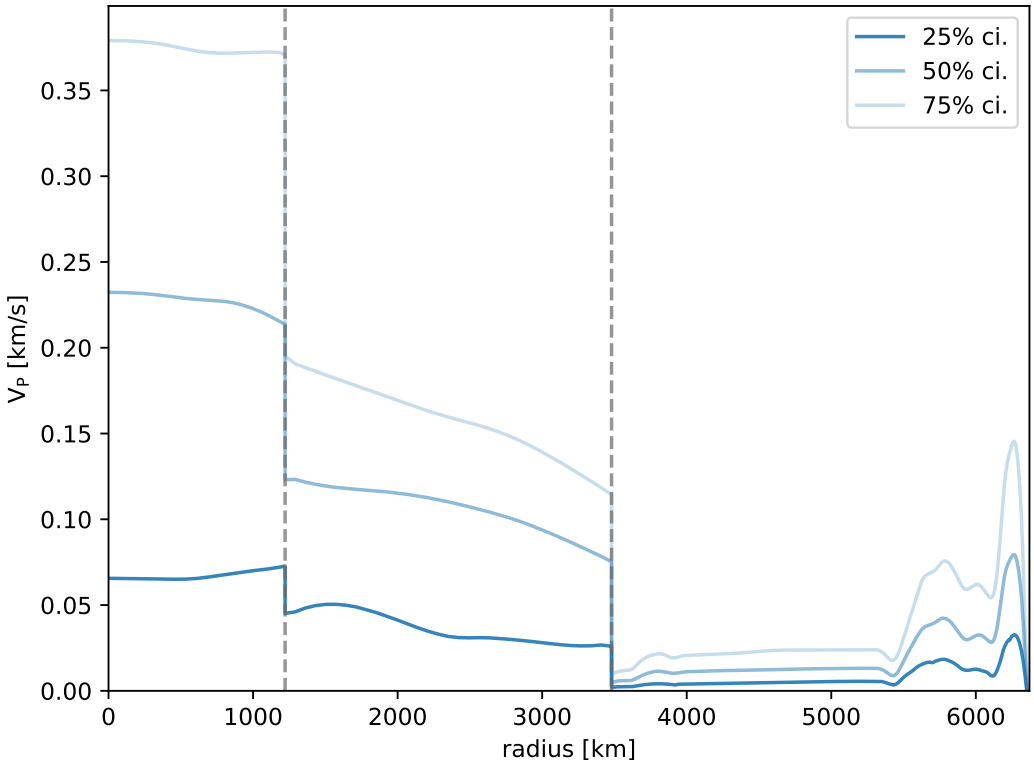

Figure A.12: Radial P-wave velocity sensitivity profiles. Sensitivities are shown using probability contours in the form of credible intervals (ci).

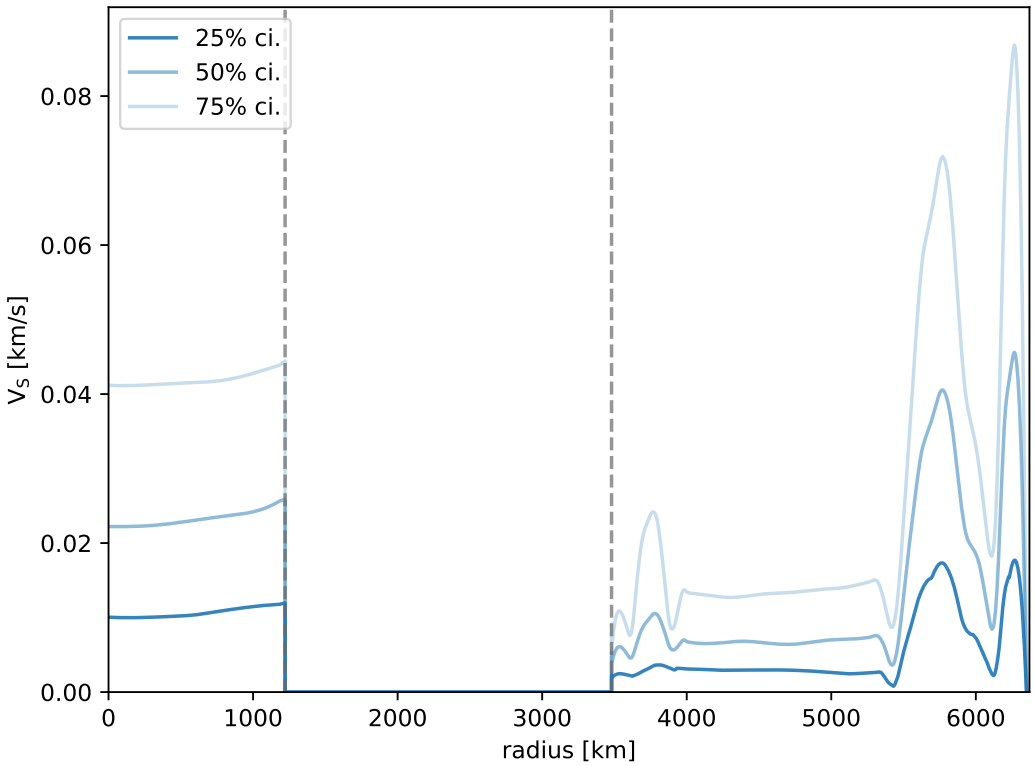

Figure A.13: Radial S-wave velocity sensitivity profiles. Sensitivities are shown using probability contours in the form of credible intervals (ci).

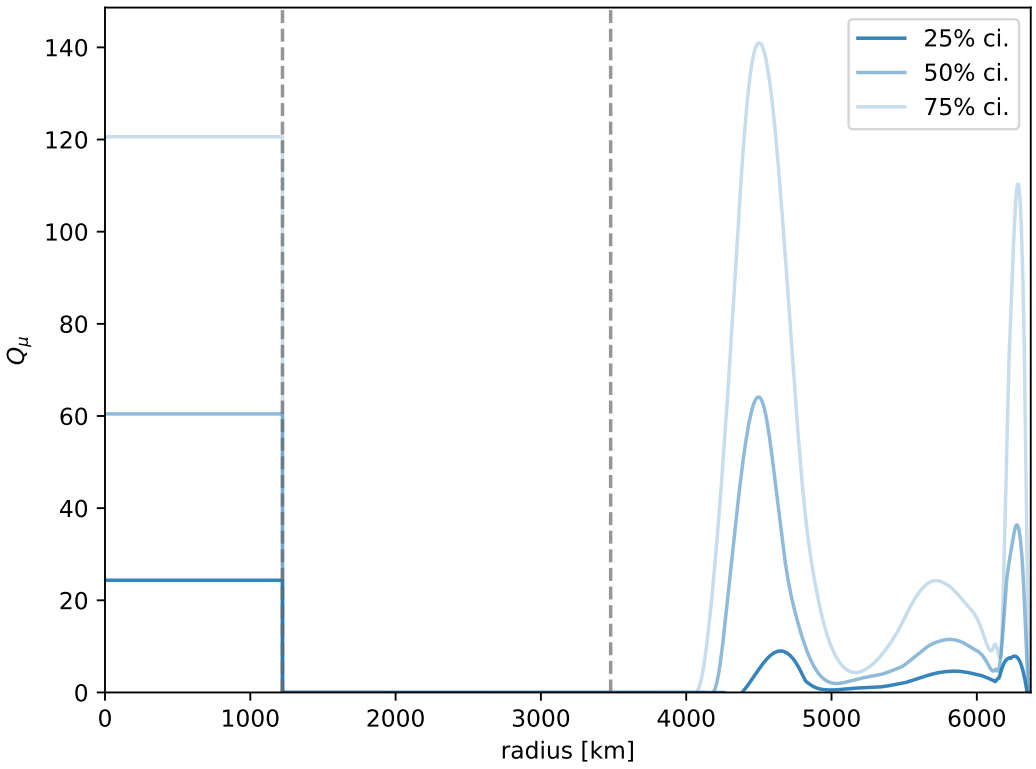

Figure A.14: Radial shear attenuation Q_μ sensitivity profiles. Sensitivities are shown using probability contours in the form of credible intervals (ci).

Bibliography

Abers, G. A., K. Fischer, G. Hirth, D. Wiens, T. Plank, B. K. Holtzman, C. McCarthy, and E. Gazel (2014), Reconciling mantle attenuation-temperature relationships from seismology, petrology, and laboratory measurements, *Geochemistry, Geophysics, Geosystems*, *15*(9), 3521–3542. (Cited on p.: 58)

Adibekyan, V., C. Dorn, S. G. Sousa, N. C. Santos, B. Bitsch, G. Israelian, C. Mordasini, S. C. Barros, E. Delgado Mena, O. D. Demangeon, et al. (2021), A compositional link between rocky exoplanets and their host stars, *Science*, *374*(6565), 330–332. (Cited on p.: 113)

Afanasiev, M., C. Boehm, M. van Driel, L. Krischer, M. Rietmann, D. A. May, M. G. Knepley, and A. Fichtner (2019), Modular and flexible spectral-element waveform modelling in two and three dimensions, *Geophysical Journal International*, *216*(3), 1675–1692. (Cited on p.: 56, 103)

Agnew, D. C. (2005), Earth tides: an introduction, *University of California, San Diego*. (Cited on p.: 16)

Akbarashrafi, F., D. Al-Attar, A. Deuss, J. Trampert, and A. P. Valentine (2018), Exact free oscillation spectra, splitting functions and the resolvability of Earth's density structure, *Geophysical Journal International*, *213*(1), 58–76, doi:10.1093/gji/ggx539. (Cited on p.: 12, 56, 86, 91, 111)

Aki, K., and P. Richards (2002), *Quantitative seismology, second edition*, vol. 1, 2nd ed., University Science Books. (Cited on p.: 9)

Al-Attar, D. (2007), A solution of the elastodynamic equation in an anelastic earth model, *Geophys. J. Int.*, *171*(2), 755–760, doi:10.1111/j.1365-246X.2007.03517.x. (Cited on p.: 42)

Al-Attar, D., and J. Tromp (2013), Sensitivity kernels for viscoelastic loading based on adjoint methods, *Geophysical Journal International*, *196*(1), 34–77, doi:10.1093/gji/ggt395. (Cited on p.: 32)

Al-Attar, D., and J. Tromp (2014), Sensitivity kernels for viscoelastic loading based on adjoint methods, *Geophysical Journal International*, *196*(1), 34–77. (Cited on p.: 117)

Al-Attar, D., and J. H. Woodhouse (2008), Calculation of seismic displacement fields in self-gravitating earth models—applications of minors vectors and symplectic structure, *Geophysical Journal International*, *175*(3), 1176–1208. (Cited on p.: 14)

Al-Attar, D., J. H. Woodhouse, and A. Deuss (2012), Calculation of normal mode spectra in laterally heterogeneous earth models using an iterative direct solution method, *Geophysical Journal International*, *189*(2), 1038–1046, doi: 10.1111/j.1365-246X.2012.05406.x. (Cited on p.: 13, 27, 56, 86)

Al-Attar, D., O. Crawford, A. P. Valentine, and J. Trampert (2018), Hamilton's principle and normal mode coupling in an aspherical planet with a fluid core, *Geophys. J. Int.*, *214*(1), 485–507. (Cited on p.: 91)

Alexandrakis, C., and D. W. Eaton (2010), Precise seismic-wave velocity atop Earth's core: No evidence for outer-core stratification, *Physics of the Earth and Planetary Interiors*, *180*(1-2), 59–65. (Cited on p.: 79)

Alfe, D., G. Price, and M. Gillan (2000), Thermodynamic stability of Fe/O solid solution at inner-core conditions, *Geophysical research letters*, *27*(16), 2417–2420. (Cited on p.: 83)

Alfè, D., M. Gillan, and G. D. Price (2002), Composition and temperature of the Earth's core constrained by combining ab initio calculations and seismic data, *Earth and Planetary Science Letters*, *195*(1-2), 91–98. (Cited on p.: 82)

Alterman, Z., H. Jarosch, and C. L. Pekeris (1959), Oscillation of the Earth, *Proceedings of the Royal Society of London. Series A. Mathematical and Physical Sciences*, *252*, doi:10.1098/rspa.1959.0138. (Cited on p.: 14, 27)

Amestoy, P., I. S. Duff, J. Koster, and J.-Y. L'Excellent (2001), A Fully Asynchronous Multifrontal Solver Using Distributed Dynamic Scheduling, *SIAM Journal on Matrix Analysis and Applications*, *23*(1), 15–41. (Cited on p.: 39)

Anderson, D. L., and J. W. Given (1982), Absorption band Q model for the Earth, *Journal of Geophysical Research: Solid Earth*, *87*(B5), 3893–3904. (Cited on p.: 57)

Anderson, D. L., and R. Hart (1978), Q of the Earth, *Journal of Geophysical Research: Solid Earth*, *83*(B12), 5869–5882. (Cited on p.: 78)

Anderson, D. L., and J. B. Minster (1979), The frequency dependence of Q in the Earth and implications for mantle rheology and Chandler wobble, *Geophysical Journal International*, *58*(2), 431–440. (Cited on p.: 56, 57)

Anderson, D. L., W. Miller, G. Latham, Y. Nakamura, M. Toksöz, A. Dainty, F. Duennebier, A. R. Lazarewicz, R. Kovach, and T. Knight (1977), Seismology on mars, *Journal of Geophysical Research*, *82*(28), 4524–4546. (Cited on p.: 9)

Anderson, J., G. Schubert, R. Jacobson, E. Lau, W. Moore, and W. Sjogren (1998), Europa's differentiated internal structure: Inferences from four Galileo encounters, *Science*, *281*(5385), 2019–2022. (Cited on p.: 51)

Anderson, O. L., V. Dehant, K. Creager, S. Karato, and S. Zatman (2003), The three-dimensional phase diagram of iron, *Earth's Core: Dynamics, Structure, Rotation, Geodyn. Ser*, *31*, 83–104. (Cited on p.: 82)

Antonangeli, D., J. Siebert, J. Badro, D. L. Farber, G. Fiquet, G. Morard, and F. J. Ryerson (2010), Composition of the Earth's inner core from high-pressure sound velocity measurements in Fe–Ni–Si alloys, *Earth and Planetary Science Letters*, *295*(1-2), 292–296. (Cited on p.: 82)

Arveson, S. M., J. Deng, B. B. Karki, and K. K. Lee (2019), Evidence for Fe-Si-O liquid immiscibility at deep Earth pressures, *Proceedings of the National Academy of Sciences*, *116*(21), 10,238–10,243. (Cited on p.: 79)

Babuška, I., and J. Osborn (1991), Eigenvalue problems, in *Finite Element Methods (Part 1)*, *Handbook of Numerical Analysis*, vol. 2, pp. 641 – 787, Elsevier, doi: 10.1016/S1570-8659(05)80042-0. (Cited on p.: 46)

Badro, J., G. Fiquet, F. Guyot, E. Gregoryanz, F. Occelli, D. Antonangeli, and M. d'Astuto (2007), Effect of light elements on the sound velocities in solid iron: Implications for the composition of Earth's core, *Earth and Planetary Science Letters*, *254*(1-2), 233–238. (Cited on p.: 82)

Badro, J., A. S. Côté, and J. P. Brodholt (2014), A seismologically consistent compositional model of Earth's core, *Proceedings of the National Academy of Sciences*, *111*(21), 7542–7545. (Cited on p.: 82, 89)

Badro, J., J. P. Brodholt, H. Piet, J. Siebert, and F. J. Ryerson (2015), Core formation and core composition from coupled geochemical and geophysical constraints, *Proceedings of the National Academy of Sciences*, *112*(40), 12,310–12,314. (Cited on p.: 82, 89)

Bagheri, A., A. Khan, D. Al-Attar, O. Crawford, and D. Giardini (2019), Tidal response of Mars constrained from laboratory-based viscoelastic dissipation models and geophysical data, *Journal of Geophysical Research: Planets*, *124*(11), 2703–2727. (Cited on p.: 16, 17, 57, 63, 67, 85, 116)

Banerdt, W. B., S. E. Smrekar, D. Banfield, D. Giardini, M. Golombek, C. L. Johnson, P. Lognonné, A. Spiga, T. Spohn, C. Perrin, et al. (2020), Initial results from the InSight mission on Mars, *Nature Geoscience*, *13*(3), 183–189. (Cited on p.: 9, 50)

Bank, R. E., T. F. Dupont, and H. Yserentant (1988), The hierarchical basis multigrid method, *Numer. Math.*, *52*(4), 427–458. (Cited on p.: 100)

Barker, A. T., and T. Kolev (2021), Matrix-free preconditioning for high-order H(curl) discretizations, *Numer. Linear Algebr. with Appl.*, *28*(2), 1–17. (Cited on p.: 110)

Bazhanova, Z. G., A. R. Oganov, and O. Gianola (2012), Fe–C and Fe–H systems at pressures of the Earth's inner core, *Physics-Uspekhi*, *55*(5), 489. (Cited on p.: 82)

Beghein, C., and J. Trampert (2003), Robust normal mode constraints on inner-core anisotropy from model space search, *Science*, *299*(5606), 552–555. (Cited on p.: 113)

Beghein, C., J. Resovsky, and R. D. Van Der Hilst (2008), The signal of mantle anisotropy in the coupling of normal modes, *Geophysical Journal International*, *175*(3), 1209–1234. (Cited on p.: 86, 113)

Bellis, C., and B. Holtzman (2014), Sensitivity of seismic measurements to frequency-dependent attenuation and upper mantle structure: An initial approach, *Journal of Geophysical Research: Solid Earth*, *119*(7), 5497–5517. (Cited on p.: 58)

Bello-Maldonado, P. D., and P. F. Fischer (2019), Scalable Low-Order Finite Element Preconditioners for High-Order Spectral Element Poisson Solvers, *SIAM J. Sci. Comput.*, *41*(5), S2–S18. (Cited on p.: 100)

Belonoshko, A. B., N. V. Skorodumova, S. Davis, A. N. Osiptsov, A. Rosengren, and B. Johansson (2007), Origin of the low rigidity of the Earth's inner core, *science*, *316*(5831), 1603–1605. (Cited on p.: 82)

Ben-Menahem, A., and S. J. Singh (1981), *Seismic waves and sources*, Springer New York Inc. (Cited on p.: 17)

Benioff, H., and B. Gutenberg (1952), The response of strain and pendulum seismographs to surface waves, *Bulletin of the Seismological Society of America*, *42*(3), 229–237. (Cited on p.: 13)

Benjamin, D., J. Wahr, R. D. Ray, G. D. Egbert, and S. D. Desai (2006), Constraints on mantle anelasticity from geodetic observations, and implications for the J2 anomaly, *Geophysical Journal International*, *165*(1), 3–16, doi: 10.1111/j.1365-246X.2006.02915.x. (Cited on p.: 58, 61, 84, 179)

Biggin, A., R. Bono, D. Meduri, C. Sprain, C. Davies, R. Holme, and P. Dubrovine (2020), Quantitative estimates of average geomagnetic axial dipole dominance in deep geological time, *Nature Comm.*, *11*, doi:{https://doi.org/10.1038/s41467-020-19794-7}. (Cited on p.: 83)

Birch, F. (1952), Elasticity and constitution of the Earth's interior, *Journal of Geophysical Research (1896-1977)*, *57*(2), 227–286, doi:10.1029/JZ057i002p00227. (Cited on p.: 65)

Birch, F. (1964), Density and composition of mantle and core, *Journal of geophysical research*, *69*(20), 4377–4388. (Cited on p.: 64, 82)

Bissig, F., A. Khan, M. van Driel, S. C. Stähler, D. Giardini, M. Panning, M. Drilleau, P. Lognonné, T. V. Gudkova, V. N. Zharkov, A.-C. Plesa, and W. B. Banerdt (2018), On the Detectability and Use of Normal Modes for Determining Interior Structure of Mars, *Space Science Reviews*, *214*(8), 114, doi: 10.1007/s11214-018-0547-9. (Cited on p.: 50)

Bissig, F., A. Khan, B. Tauzin, P. A. Sossi, F. D. Munch, and D. Giardini (2021), Multifrequency inversion of Ps and Sp receiver functions: Methodology and application to USArray data, *Journal of Geophysical Research: Solid Earth*, *126*(2), e2020JB020,350. (Cited on p.: 62, 75)

Bissig, F., A. Khan, and D. Giardini (2022a), Evidence for basalt enrichment in the mantle transition zone from inversion of triplicated P-and S-waveforms, *Earth and Planetary Science Letters*, *580*, 117,387. (Cited on p.: 75)

Bissig, F., A. Khan, and D. Giardini (2022b), Joint inversion of PP and SS precursor w av ef orms and R ayleigh w av e phase velocities for global mantle transition zone structure, *Geophysical Journal International*, pp. 1–24, doi:10.1093/gji/ggac451. (Cited on p.: 75)

Bolt, B. A., and D. R. Brillinger (1979), Estimation of uncertainties in eigenspectral estimates from decaying geophysical time series, *Geophysical Journal International*, *59*(3), 593–603. (Cited on p.: 19)

Bolt, B. A., and J. S. Derr (1969), Free bodily vibrations of the terrestrial planets, *Vistas in Astronomy*, *11*, 69–102. (Cited on p.: 50)

Bonsor, A., P. J. Carter, M. Hollands, B. T. Gänsicke, Z. Leinhardt, and J. H. Harrison (2020), Are exoplanetesimals differentiated?, *Monthly Notices of the Royal Astronomical Society*, *492*(2), 2683–2697. (Cited on p.: 113)

Bouffard, M., G. Choblet, S. Labrosse, and J. Wicht (2019), Chemical Convection and Stratification in the Earth's Outer Core, *Frontiers in Earth Science*, *7*, doi:10.3389/feart.2019.00099. (Cited on p.: 79)

Bozdağ, E., D. Peter, M. Lefebvre, D. Komatitsch, J. Tromp, J. Hill, N. Podhorszki, and D. Pugmire (2016), Global adjoint tomography: First-generation model, *Geophys. J. Int.*, *207*(3), 1739–1766. (Cited on p.: 90)

Brodholt, J., and J. Badro (2017), Composition of the low seismic velocity E' layer at the top of Earth's core, *Geophysical Research Letters*, *44*(16), 8303–8310. (Cited on p.: 79, 82, 89)

Buffett, B. (2014), Geomagnetic fluctuations reveal stable stratification at the top of the Earth's core, *Nature*, *507*(7493), 484–487. (Cited on p.: 79)

Buffett, B. A., and C. T. Seagle (2010), Stratification of the top of the core due to chemical interactions with the mantle, *Journal of Geophysical Research: Solid Earth*, *115*(B4), doi:10.1029/2009JB006751. (Cited on p.: 79)

Buland, R., and F. Gilbert (1978), Improved resolution of complex eigenfrequencies in analytically continued seismic spectra, *Geophysical Journal International*, *52*(3), 457–470. (Cited on p.: 19)

Buland, R., and F. Gilbert (1984), Computation of free oscillations of the earth, *Journal of Computational Physics*, *54*(1), 95 – 114, doi:10.1016/0021-9991(84)90141-4. (Cited on p.: 28, 37, 39, 40, 41)

Bullen, K. E. (1963), An Index of Degree of Chemical Inhomogeneity in the Earth, *Geophysical Journal*, *7*(5), 584–592, doi:10.1111/j.1365-246X.1963.tb03823.x. (Cited on p.: 87)

Butler, R., and D. L. Anderson (1978), Equation of state fits to the lower mantle and outer core, *Physics of the Earth and Planetary Interiors*, *17*(2), 147–162, doi:10.1016/0031-9201(78)90056-0. (Cited on p.: 87)

Cammarano, F., B. Romanowicz, L. Stixrude, and C. Lithgow-Bertelloni (2009), Inferring the thermochemical structure of the upper mantle from seismic data, *Geophys. J. Int.*, *179*, 1169–1185, doi:10.1111/j.1365-246X.2009.04338.x. (Cited on p.: 75)

Cao, A., and B. Romanowicz (2004), Hemispherical transition of seismic attenuation at the top of the Earth's inner core, *Earth and Planetary Science Letters*, *228*(3-4), 243–253. (Cited on p.: 82)

Cao, A., and B. Romanowicz (2009), Constraints on shear wave attenuation in the Earth's inner core from an observation of PKJKP, *Geophysical research letters*, *36*(9). (Cited on p.: 78)

Cao, A., B. Romanowicz, and N. Takeuchi (2005), An observation of PKJKP: inferences on inner core shear properties, *Science*, *308*(5727), 1453–1455. (Cited on p.: 76)

Caracas, R., P. D. Asimow, A. S. Wolf, J.-P. Harvey, A. Martin, and M. Torrent (2015), Refining the chemical composition of the inner core with multicomponent alloys: from first-principles to thermodynamics and seismology, in *AGU Fall Meeting Abstracts*, vol. 2015, pp. MR33D–02. (Cited on p.: 82)

Chaljub, E., and B. Valette (2004), Spectral element modelling of three-dimensional wave propagation in a self-gravitating Earth with an arbitrarily stratified outer core, *Geophysical Journal International*, *158*(1), 131–141. (Cited on p.: 15, 28, 91, 93, 94, 97, 99, 102, 104, 105)

Chaljub, E., D. Komatitsch, J. P. Vilotte, Y. Capdeville, B. Valette, and G. Festa (2007), Spectral-Element Analysis in Seismology, in *Adv. Geophys.*, *Advances in Geophysics*, vol. 48, edited by R.-S. Wu, V. Maupin, and R. Dmowska, chap. 7, pp. 365–419, Elsevier. (Cited on p.: 93, 96, 110)

Chambat, F., and B. Valette (2001), Mean radius, mass, and inertia for reference Earth models, *Physics of the Earth and Planetary Interiors*, *124*(3-4), 237–253. (Cited on p.: 61, 179)

Chree, C. (1889), The equations of an isotropic elastic solid in polar and cylindrical co-ordinates their solution and application, *Transactions of the Cambridge Philosophical Society*, *14*, 250. (Cited on p.: 10)

Cobden, L., S. Goes, F. Cammarano, and J. A. D. Connolly (2008), Thermochemical interpretation of one-dimensional seismic reference models for the upper mantle: Evidence for bias due to heterogeneity, *Geophys. J. Int.*, *175*(2), 627–648, doi: 10.1111/j.1365-246X.2008.03903.x. (Cited on p.: 75)

Cohen, G. C., and S. Pernet (2017), *Finite element and discontinuous Galerkin methods for transient wave equations*, Springer. (Cited on p.: 35, 46)

Connolly, J. A. D. (2009), The geodynamic equation of state: What and how, *Geochemistry, Geophysics, Geosystems*, *10*(10), doi:10.1029/2009GC002540. (Cited on p.: 57, 62, 112)

Connolly, J. A. D., and A. Khan (2016), Uncertainty of mantle geophysical properties computed from phase equilibrium models, *Geophysical Research Letters*, *43*(10), 5026–5034, doi:10.1002/2016GL068239. (Cited on p.: 63, 88)

Cowling, T. G. (1941), The non-radial oscillations of polytropic stars, *Monthly Notices of the Royal Astronomical Society*, *101*, 367. (Cited on p.: 31)

Craig, A. W., and O. C. Zienkiewicz (1985), A multigrid algorithm using a hierarchical finite element basis, in *Multigrid Methods Integr. Differ. Equations*, pp. 301–312, Clarendon Press, Oxford. (Cited on p.: 100)

Crary, A. (1954), Seismic studies on Fletcher's ice island, T-3, *Eos, Transactions American Geophysical Union*, *35*(2), 293–300. (Cited on p.: 52)

Crawford, J. M., W. E. Doty, and M. R. Lee (1960), Continuous signal seismograph, *Geophysics*, *25*(1), 95–105. (Cited on p.: 9)

Creager, K. C. (1999), Large-scale variations in inner core anisotropy, *Journal of Geophysical Research: Solid Earth*, *104*(B10), 23,127–23,139, doi:10.1029/1999JB900162. (Cited on p.: 87)

Dahlen, F. (1982), The effect of data windows on the estimation of free oscillation parameters, *Geophysical Journal International*, *69*(2), 537–549. (Cited on p.: 18, 20)

Dahlen, F. A. (1968), The normal modes of a rotating, elliptical Earth, *Geophysical Journal International*, *16*(4), 329–367. (Cited on p.: 12)

Dahlen, F. A., and J. Tromp (1998), *Theoretical Global Seismology*, pbk. ed., Princeton University Press, Princeton, New Jersey. (Cited on p.: 11, 18, 22, 29, 30, 31, 32, 37, 38, 39, 41, 42, 43, 45, 46, 48, 59, 102, 111, 114, 118, 119, 121, 183)

Davies, G. F., and A. M. Dziewonski (1975), Homogeneity and constitution of the Earth's lower mantle and outer core, *Physics of the Earth and Planetary Interiors*, *10*(4), 336–343. (Cited on p.: 57, 65, 66)

de Wit, R., P. Käufl, A. Valentine, and J. Trampert (2014), Bayesian inversion of free oscillations for Earth's radial (an) elastic structure, *Physics of the Earth and Planetary Interiors*, *237*, 1–17. (Cited on p.: 56)

Deuss, A. (2008), Normal mode constraints on shear and compressional wave velocity of the Earth's inner core, *Earth and Planetary Science Letters*, *268*(3-4), 364–375. (Cited on p.: 56, 76)

Deuss, A. (2014), Heterogeneity and anisotropy of Earth's inner core, *Annual Review of Earth and Planetary Sciences*, *42*, 103–126. (Cited on p.: 113)

Deuss, A., J. H. Woodhouse, H. Paulssen, and J. Trampert (2000), The observation of inner core shear waves, *Geophys. J. Int.*, *142*(1), 67–73. (Cited on p.: 76, 78)

Deuss, A., J. Ritsema, and H. van Heijst (2013), A new catalogue of normal-mode splitting function measurements up to 10 mHz, *Geophysical Journal International*, *193*(2), 920–937, doi:10.1093/gji/ggt010. (Cited on p.: 18, 20, 21, 56, 58, 59, 60, 85, 123, 124, 125, 126, 127, 128, 129, 130, 179, 180, 181)

Dorn, C., A. Khan, K. Heng, J. A. Connolly, Y. Alibert, W. Benz, and P. Tackley (2015), Can we constrain the interior structure of rocky exoplanets from mass and radius measurements?, *Astronomy & Astrophysics*, *577*, A83. (Cited on p.: 113)

Drake, M. J., and K. Righter (2002), Determining the composition of the Earth, *Nature*, *416*(6876), 39–44. (Cited on p.: 55, 74)

Durek, J. J., and G. Ekström (1996), A radial model of anelasticity consistent with long-period surface-wave attenuation, *Bulletin of the Seismological Society of America*, *86*(1A), 144–158. (Cited on p.: 78)

Durek, J. J., and B. Romanowicz (1999), Inner core anisotropy inferred by direct inversion of normal mode spectra, *Geophysical Journal International*, *139*(3), 599–622. (Cited on p.: 113)

Dziewonski, A., and F. Gilbert (1971), Solidity of the inner core of the Earth inferred from normal mode observations, *Nature*, *234*(5330), 465–466. (Cited on p.: 14)

Dziewonski, A., and B. Romanowicz (2015), 1.01 - Deep Earth Seismology: An Introduction and Overview, in *Treatise on Geophysics (Second Edition)*, edited by G. Schubert, second edition ed., pp. 1–28, Elsevier, Oxford, doi:10.1016/B978-0-444-53802-4.00001-4. (Cited on p.: 58)

Dziewonski, A., A. Hales, and E. Lapwood (1975), Parametrically simple Earth models consistent with geophysical data, *Physics of the Earth and Planetary Interiors*, *10*(1), 12–48. (Cited on p.: 23)

Dziewonski, A., T.-a. Chou, and J. H. Woodhouse (1981), Determination of earthquake source parameters from waveform data for studies of global and regional seismicity, *J. Geophys. Res.*, *86*(B4), 2825. (Cited on p.: 11, 23, 183)

Dziewonski, A. M., and D. L. Anderson (1981), Preliminary reference Earth model, *Physics of the earth and planetary interiors*, *25*(4), 297–356. (Cited on p.: 17, 18, 19, 20, 25, 27, 38, 46, 55, 56, 58, 59, 60, 61, 77, 82, 91, 112, 123, 124, 137, 179, 180, 182, 183, 184, 189)

Ekström, G., and A. M. Dziewonski (1998), The unique anisotropy of the Pacific upper mantle, *Nature*, *394*(6689), 168–172. (Cited on p.: 113)

Enescu, D., and B. Enescu (1999), Possible cause-effect relationships between Vrancea (Romania) earthquakes and some global geophysical phenomena, *Natural Hazards*, *19*(2), 233–245. (Cited on p.: 16)

Engdahl, E. R., R. van der Hilst, and R. Buland (1998), Global teleseismic earthquake relocation with improved travel times and procedures for depth determination, *Bulletin of the Seismological Society of America*, *88*(3), 722–743. (Cited on p.: 76, 79, 189)

Fabrichnaya, O., K. Saxena, P. Richet, and E. F. Westrum (2004), Thermodynamic Data, Models, and Phase Diagrams in Multicomponent Oxide Systems, in *Thermodynamic Data, Models, and Phase Diagrams in Multicomponent Oxide Systems*, Springer, Heidelberg, doi:doi:10.1007/978-3-662-10504-7. (Cited on p.: 87)

Faul, U., and I. Jackson (2015), Transient creep and strain energy dissipation: An experimental perspective, *Annual Review of Earth and Planetary Sciences*, *43*, 541–569. (Cited on p.: 17)

Faul, U., J. Fitz Gerald, and I. Jackson (2004), Shear wave attenuation and dispersion in melt-bearing olivine polycrystals: 2. Microstructural interpretation and seismological implications, *Journal of Geophysical Research: Solid Earth*, *109*(6), B06,202 1–20, doi:10.1029/2003JB002407. (Cited on p.: 88)

Fearn, D. R., D. E. Loper, and P. H. Roberts (1981), Structure of the Earth's inner core, *Nature*, *292*(5820), 232–233. (Cited on p.: 79)

Fichtner, A., B. L. Kennett, H. Igel, and H.-P. Bunge (2009), Full seismic waveform tomography for upper-mantle structure in the Australasian region using adjoint methods, *Geophys. J. Int.*, *179*(3), 1703–1725. (Cited on p.: 90)

Foresti, S., G. Brussino, S. Hassanzadeh, and V. Sonnad (1989), Multilevel solution method for the p-version of finite elements, *Comput. Phys. Commun.*, *53*(1-3), 349–355. (Cited on p.: 100)

Frame, D., R. He, I. Ipsen, D. Lee, D. Lee, and E. Rrapaj (2018), Eigenvector Continuation with Subspace Learning, *Phys. Rev. Lett.*, *121*(3), doi:10.1103/PhysRevLett.121.032501. (Cited on p.: 45)

French, S., and B. A. Romanowicz (2014), Whole-mantle radially anisotropic shear velocity structure from spectral-element waveform tomography, *Geophysical Journal International*, *199*(3), 1303–1327. (Cited on p.: 9, 27, 55, 90)

Frohlich, C. (2006), *Deep Earthquakes*, Cambridge University Press, doi:10.1017/CBO9781107297562. (Cited on p.: 13)

Frohlich, C., and Y. Nakamura (2009), The physical mechanisms of deep moonquakes and intermediate-depth earthquakes: How similar and how different?, *Physics of the Earth and Planetary Interiors*, *173*(3), 365–374, doi:10.1016/j.pepi.2009.02.004. (Cited on p.: 16)

Garnero, E. J. (2000), Heterogeneity of the lowermost mantle, *Annual Review of Earth and Planetary Sciences*, *28*(1), 509–537. (Cited on p.: 81)

Gharti, H. N., and J. Tromp (2017), A spectral-infinite-element solution of Poisson's equation: an application to self gravity, *arxiv.org*, pp. 1–15. (Cited on p.: 94, 96, 99, 102)

Gharti, H. N., J. Tromp, and S. Zampini (2018), Spectral-infinite-element simulations of gravity anomalies, *Geophys. J. Int.*, *215*(2), 1098–1117. (Cited on p.: 94, 95, 96)

Giardini, D., X.-D. Li, and J. H. Woodhouse (1987), Three-dimensional structure of the Earth from splitting in free-oscillation spectra, *Nature*, *325*(6103), 405. (Cited on p.: 9, 12, 27)

Giardini, D., X.-D. Li, and J. H. Woodhouse (1988), Splitting functions of long-period normal modes of the Earth, *Journal of Geophysical Research: Solid Earth*, *93*(B11), 13,716–13,742. (Cited on p.: 12, 58)

Giardini, D., P. Lognonné, W. B. Banerdt, W. T. Pike, U. Christensen, S. Ceylan, J. F. Clinton, M. van Driel, S. C. Stähler, M. Böse, et al. (2020), The seismicity of Mars, *Nature Geoscience*, *13*(3), 205–212. (Cited on p.: 9)

Gilbert, F. (1971), The diagonal sum rule and averaged eigenfrequencies, *Geophysical Journal International*, *23*(1), 119–123. (Cited on p.: 17)

Gilbert, F., and G. E. Backus (1966), Propagator Matrices In Elastic Wave And Vibration Problems, *GEOPHYSICS*, *31*(2), 326–332, doi:10.1190/1.1439771. (Cited on p.: 15)

Gilbert, F., and A. M. Dziewonski (1975), An application of normal mode theory to the retrieval of structural parameters and source mechanisms from seismic spectra, *Philosophical Transactions of the Royal Society of London. Series A, Mathematical and Physical Sciences*, *278*(1280), 187–269. (Cited on p.: 22)

Goulty, N. R. (1979), Tidal triggering of deep moonquakes, *Physics of the Earth and Planetary Interiors*, *19*(1), 52–58, doi:10.1016/0031-9201(79)90089-X. (Cited on p.: 16)

Grayver, A. V., F. D. Munch, A. V. Kuvshinov, A. Khan, T. J. Sabaka, and L. Tøffner-Clausen (2017), Joint inversion of satellite-detected tidal and magnetospheric signals constrains electrical conductivity and water content of the upper mantle and transition zone, *Geophysical research letters*, *44*(12), 6074–6081. (Cited on p.: 74)

Gribb, T. T., and R. F. Cooper (1998), Low-frequency shear attenuation in polycrystalline olivine: Grain boundary diffusion and the physical significance of the Andrade model for viscoelastic rheology, *Journal of Geophysical Research: Solid Earth*, *103*(B11), 27,267–27,279. (Cited on p.: 17, 57)

Gubbins, D., and C. Davies (2013), The stratified layer at the core–mantle boundary caused by barodiffusion of oxygen, sulphur and silicon, *Physics of the Earth and Planetary Interiors*, *215*, 21–28. (Cited on p.: 79)

Gubbins, D., T. Masters, and J. Jacobs (1979), Thermal evolution of the Earth's core, *Geophysical Journal International*, *59*(1), 57–99. (Cited on p.: 55)

Gudkova, T., V. Zharkov, and S. Lebedev (1993), Theoretical spectrum of free oscillations of Mars., *Solar System Research*, *27*(2), 129–148. (Cited on p.: 50)

Hager, B. H., R. W. Clayton, M. A. Richards, R. P. Comer, and A. M. Dziewonski (1985), Lower mantle heterogeneity, dynamic topography and the geoid, *Nature*, *313*(6003), 541–545. (Cited on p.: 55)

Hastings, W. K. (1970), Monte Carlo sampling methods using Markov chains and their applications, *Biometrika*, *57*(1), 97–109. (Cited on p.: 22)

Havlin, C., B. K. Holtzman, and E. Hopper (2021), Inference of thermodynamic state in the asthenosphere from anelastic properties, with applications to North American upper mantle, *Physics of the Earth and Planetary Interiors*, *314*, 106,639, doi:https://doi.org/10.1016/j.pepi.2020.106639. (Cited on p.: 57, 88)

He, Y., S. Sun, D. Y. Kim, B. G. Jang, H. Li, and H.-k. Mao (2022), Superionic iron alloys and their seismic velocities in Earth's inner core, *Nature*, *602*(7896), 258–262. (Cited on p.: 89)

Helenbrook, B., D. Mavriplis, and H. Atkins (2003), Analysis of "p"-Multigrid for Continuous and Discontinuous Finite Element Discretizations, in *16th AIAA Comput. Fluid Dyn. Conf.*, pp. 1–6, American Institute of Aeronautics and Astronautics, Reston, Virigina. (Cited on p.: 100)

Helffrich, G. (2014), Outer core compositional layering and constraints on core liquid transport properties, *Earth and Planetary Science Letters*, *391*, 256–262. (Cited on p.: 79)

Helffrich, G., and S. Kaneshima (2004), Seismological Constraints on Core Composition from Fe-O-S Liquid Immiscibility, *Science*, *306*, 2239=–2242. (Cited on p.: 79)

Helffrich, G., and S. Kaneshima (2010), Outer-core compositional stratification from observed core wave speed profiles, *Nature*, *468*(7325), 807–810, doi:10.1038/nature09636. (Cited on p.: 79)

Helffrich, G., and D. Mainprice (2019), Anisotropy at the inner core boundary, *Geophysical Research Letters*, *46*(21), 11,959–11,967. (Cited on p.: 82, 113)

Hernandez, V., J. E. Roman, and V. Vidal (2005), SLEPc: A Scalable and Flexible Toolkit for the Solution of Eigenvalue Problems, *ACM Trans. Math. Softw.*, *31*(3), 351–362, doi:10.1145/1089014.1089019. (Cited on p.: 28, 39)

Hirose, K., G. Morard, R. Sinmyo, K. Umemoto, J. Hernlund, G. Helffrich, and S. Labrosse (2017), Crystallization of silicon dioxide and compositional evolution of the Earth's core, *Nature*, *543*(7643), 99–102. (Cited on p.: 82, 83, 113)

Hirose, K., B. Wood, and L. Vočadlo (2021), Light elements in the Earth's core, *Nature Reviews Earth & Environment*, *2*(9), 645–658. (Cited on p.: 56, 64, 82)

Huang, D., J. Badro, J. Brodholt, and Y. Li (2019), Ab initio molecular dynamics investigation of molten Fe–Si–O in Earth's core, *Geophysical Research Letters*, *46*(12), 6397–6405. (Cited on p.: 82)

Igel, H. (2017), *Computational seismology: a practical introduction*, Oxford University Press. (Cited on p.: 15, 35)

Irifune, T. (1994), Absence of an aluminous phase in the upper part of the Earth's lower mantle, *Nature*, *370*(6485), 131–133. (Cited on p.: 62)

Irifune, T., Y. Higo, T. Inoue, Y. Kono, H. Ohfuji, and K. Funakoshi (2008), Sound velocities of majorite garnet and the composition of the mantle transition region, *Nature*, *451*, 814–817, doi:10.1038/nature06551. (Cited on p.: 75)

Irving, J. C. E., S. Cottaar, and V. Lekić (2018), Seismically determined elastic parameters for Earth's outer core, *Science Advances*, *4*(6), doi:10.1126/sciadv.aar2538. (Cited on p.: 24, 25, 27, 56, 57, 58, 59, 64, 65, 70, 73, 77, 79, 184, 189)

Ishii, M., and J. Tromp (1999), Normal-mode and free-air gravity constraints on lateral variations in velocity and density of Earth's mantle, *Science*, *285*(5431), 1231–1236. (Cited on p.: 13, 14, 27, 55, 58, 90)

Ivins, E. R., L. Caron, S. Adhikari, and E. Larour (2021), Notes on a compressible extended Burgers model of rheology, *Geophysical Journal International*, *228*(3), 1975–1991, doi:10.1093/gji/ggab452. (Cited on p.: 57)

Jackson, I., and U. H. Faul (2010), Grainsize-sensitive viscoelastic relaxation in olivine: Towards a robust laboratory-based model for seismological application, *Physics of the Earth and Planetary Interiors*, *183*(1), 151–163, doi:10.1016/j.pepi.2010.09.005, special Issue on Deep Slab and Mantle Dynamics. (Cited on p.: 57, 63)

Jackson, I., and S. M. Rigden (1998), Composition and temperature of the Earth's mantle: Seismological models interpreted through experimental studies of Earth materials, *The Earth's Mantle: Composition, Structure and Evolution*, pp. 405–460. (Cited on p.: 74)

Jackson, I., J. D. Fitz Gerald, U. H. Faul, and B. H. Tan (2002), Grain-size-sensitive seismic wave attenuation in polycrystalline olivine, *Journal of Geophysical Research: Solid Earth*, *107*(B12), ECV–5. (Cited on p.: 57)

Jackson, I., S. Webb, L. Weston, and D. Boness (2005), Frequency dependence of elastic wave speeds at high temperature: a direct experimental demonstration, *Physics of the Earth and Planetary Interiors*, *148*(1), 85–96. (Cited on p.: 88)

Jaerisch, P. (1880), Vibrations in a sphere, *JF Math (Crelle)*, *88*, 131–145. (Cited on p.: 10)

Jagoda, M., and M. Rutkowska (2013), Estimation of the Love and Shida numbers: h2, l2 using SLR data for the low satellites, *Advances in Space Research*, *52*(4), 633–638. (Cited on p.: 61)

Jagoda, M., M. Rutkowska, K. Kraszewska, and C. Suchocki (2018), Time changes of the potential Love tidal parameters k2 and k3, *Studia Geophysica et Geodaetica*, *62*(4), 586–595. (Cited on p.: 61, 179)

Javoy, M., E. Kaminski, F. Guyot, D. Andrault, C. Sanloup, M. Moreira, S. Labrosse, A. Jambon, P. Agrinier, A. Davaille, et al. (2010), The chemical composition of the Earth: Enstatite chondrite models, *Earth and Planetary Science Letters*, *293*(3-4), 259–268. (Cited on p.: 55)

Jeffreys, H. (1967), Radius of the earth's core, *Nature*, *215*(5108), 1365–1366. (Cited on p.: 17)

Jeffreys, H., and K. Bullen (1940), Seismological Tables, *British Association Seismological Committee, London*. (Cited on p.: 22, 23)

Ji, Q., and L. Zhao (2022), Automatic measurement and quality control of S3KS-SKKS differential traveltimes and the influence of mantle heterogeneity, *Geophysical Journal International*, *229*(2), 1448–1461, doi:10.1093/gji/ggac001. (Cited on p.: 81)

Jobert, G. (1957), Influence de la structure de la croûte sur les déformations causées par les marées océaniques (II), in *Annales de Geophysique*, vol. 13, p. 83. (Cited on p.: 10)

Jobert, N. (1956), Evaluation de la periode d'oscillation d'une sphere elastique heterogene, par application du principe de Rayleigh-(vibrations propres de rotation), *Comptes rendus hebdomadaires des seances de l'Academie des Sciences*, *243*(17), 1230–1232. (Cited on p.: 10)

Jobert, N. (1961), Calcul approché de la période des oscillations spheroïdales de la terre, *Geophysical Journal International*, *4*(Supplement_1), 242–258. (Cited on p.: 10)

Kanamori, H. (1976), Re-examination of the earth's free oxcillations excited by the Kamchatka earthquake of November 4, 1952, *Physics of the Earth and Planetary Interiors*, *11*(3), 216–226, doi:10.1016/0031-9201(76)90066-2. (Cited on p.: 13)

Kanamori, H., and D. L. Anderson (1977), Importance of physical dispersion in surface wave and free oscillation problems: Review, *Reviews of Geophysics*, *15*(1), 105–112, doi:10.1029/RG015i001p00105. (Cited on p.: 17)

Kaneshima, S. (2018), Array analyses of SmKS waves and the stratification of Earth's outermost core, *Physics of the Earth and Planetary Interiors*, *276*, 234–246. (Cited on p.: 79, 80, 81, 190)

Kaneshima, S., and T. Matsuzawa (2015), Stratification of earth's outermost core inferred from SmKS array data, *Progress in Earth and Planetary Science*, *2*(1), 1–15. (Cited on p.: 79)

Karato, S.-i. (2014), Does partial melting explain geophysical anomalies?, *Physics of the Earth and Planetary Interiors*, *228*, 300–306. (Cited on p.: 88)

Karato, S.-I., and S. Karato (2003), *The dynamic structure of the deep earth: an interdisciplinary approach*, Princeton University Press. (Cited on p.: 17)

Karato, S.-I., and H. Spetzler (1990), Defect microdynamics in minerals and solid-state mechanisms of seismic wave attenuation and velocity dispersion in the mantle, *Reviews of Geophysics*, *28*(4), 399–421. (Cited on p.: 56)

Kasahara, J. (2002), Tides, earthquakes, and volcanoes, *Science*, *297*(5580), 348–349. (Cited on p.: 16)

Katsura, T. (2022), A Revised Adiabatic Temperature Profile for the Mantle, *Journal of Geophysical Research: Solid Earth*, *127*(2), e2021JB023,562, doi:10.1029/2021JB023562, e2021JB023562 2021JB023562. (Cited on p.: 73, 74, 77, 189)

Kelvin, L. (1863), Dynamical Problem Regarding Elastic Spheroid Shell; On the Rigidity of the Earth', *Philosophical Transactions of the Royal Society of London, Treatise on Natural Philosophy*, *2*, 837. (Cited on p.: 10)

Kemper, J., M. van Driel, F. Munch, A. Khan, and D. Giardini (2021), A spectral element approach to computing normal modes, *Geophysical Journal International*, *229*(2), 915–932, doi:10.1093/gji/ggab476. (Cited on p.: 18, 19, 56, 59, 67, 111, 116, 118, 119, 120, 121, 183, 184)

Kennett, B. (2006), On seismological reference models and the perceived nature of heterogeneity, *Physics of the Earth and Planetary Interiors*, *159*(3-4), 129–139. (Cited on p.: 23)

Kennett, B. (2020), Radial earth models revisited, *Geophysical Journal International*, *222*(3), 2189–2204. (Cited on p.: 22, 23, 24, 25, 79, 184, 189)

Kennett, B., and E. Engdahl (1991), Traveltimes for global earthquake location and phase identification, *Geophysical Journal International*, *105*(2), 429–465. (Cited on p.: 23, 25, 184)

Kennett, B. L., E. Engdahl, and R. Buland (1995), Constraints on seismic velocities in the Earth from traveltimes, *Geophysical Journal International*, *122*(1), 108–124. (Cited on p.: 23, 24, 25, 76, 184)

Kennett, B. L. N. (1998), On the density distribution within the Earth, *Geophysical Journal International*, *132*(2), 374–382, doi:10.1046/j.1365-246x.1998.00451.x. (Cited on p.: 14, 56)

Khan, A., J. Connolly, and N. Olsen (2006), Constraining the composition and thermal state of the mantle beneath Europe from inversion of long-period electromagnetic sounding data, *Journal of Geophysical Research: Solid Earth*, *111*(B10). (Cited on p.: 74, 87)

Khan, A., J. Connolly, and S. R. Taylor (2008), Inversion of seismic and geodetic data for the major element chemistry and temperature of the Earth's mantle, *J. Geophys. Res.*, *113*(B09308), 1–20, doi:10.1029/2007JB005239. (Cited on p.: 55)

Khan, A., L. Boschi, and J. Connolly (2009), On mantle chemical and thermal heterogeneities and anisotropy as mapped by inversion of global surface wave

data, *Journal of Geophysical Research: Solid Earth*, *114*(B9). (Cited on p.: 62, 75, 179)

Khan, A., A. Zunino, and F. Deschamps (2011), The thermo-chemical and physical structure beneath the North American continent from Bayesian inversion of surface-wave phase velocities, *Journal of Geophysical Research: Solid Earth*, *116*(B9). (Cited on p.: 14, 58)

Khan, A., A. Zunino, and F. Deschamps (2013), Upper mantle compositional variations and discontinuity topography imaged beneath Australia from Bayesian inversion of surface-wave phase velocities and thermochemical modeling, *Journal of Geophysical Research: Solid Earth*, *118*(10), 5285–5306, doi:10.1002/jgrb.50304. (Cited on p.: 14, 55, 75)

Khan, A., C. Liebske, A. Rozel, A. Rivoldini, F. Nimmo, J. Connolly, A.-C. Plesa, and D. Giardini (2018), A geophysical perspective on the bulk composition of Mars, *Journal of Geophysical Research: Planets*, *123*(2), 575–611. (Cited on p.: 51, 57, 63)

Khan, A., S. Ceylan, M. van Driel, D. Giardini, P. Lognonné, H. Samuel, N. C. Schmerr, S. C. Stähler, A. C. Duran, Q. Huang, D. Kim, A. Broquet, C. Charalambous, J. F. Clinton, P. M. Davis, M. Drilleau, F. Karakostas, V. Lekic, S. M. McLennan, R. R. Maguire, C. Michaut, M. P. Panning, W. T. Pike, B. Pinot, M. Plasman, J.-R. Scholz, R. Widmer-Schnidrig, T. Spohn, S. E. Smrekar, and W. B. Banerdt (2021a), Upper mantle structure of Mars from InSight seismic data, *Science*, *373*(6553), 434–438, doi:10.1126/science.abf2966. (Cited on p.: 50)

Khan, D., C. Liebske, and J. A. D. Connolly (2021b), An Algorithm for Thermodynamic Parameter Optimization: Application to the Martian Mantle, *Geochemistry, Geophysics, Geosystems*, *22*(5), e2020GC009,399, doi:https://doi.org/10.1029/2020GC009399, e2020GC009399 2020GC009399. (Cited on p.: 87, 112)

Khurana, K., M. Kivelson, D. Stevenson, G. Schubert, C. Russell, R. Walker, and C. Polanskey (1998), Induced magnetic fields as evidence for subsurface oceans in Europa and Callisto, *Nature*, *395*(6704), 777–780. (Cited on p.: 51)

Knapmeyer-Endrun, B., M. P. Panning, F. Bissig, R. Joshi, A. Khan, D. Kim, V. Lekić, B. Tauzin, S. Tharimena, M. Plasman, N. Compaire, R. F. Garcia, L. Margerin, M. Schimmel, É. Stutzmann, N. Schmerr, E. Bozdağ, A.-C. Plesa, M. A. Wieczorek, A. Broquet, D. Antonangeli, S. M. McLennan, H. Samuel, C. Michaut, L. Pan, S. E. Smrekar, C. L. Johnson, N. Brinkman, A. Mittelholz, A. Rivoldini, P. M. Davis, P. Lognonné, B. Pinot, J. Scholz, S. Stähler, M. Knapmeyer, M. van Driel, D. Giardini, and W. B. Banerdt (2021), Thickness

and structure of the martian crust from InSight seismic data, *Science*, *373*(6553), 438–443, doi:10.1126/science.abf8966. (Cited on p.: 50)

Knopoff, L. (1964), Earth tides as a triggering mechanism for earthquakes, *Bulletin of the Seismological Society of America*, *54*(6A), 1865–1870. (Cited on p.: 16, 17)

Koelemeijer, P., A. Deuss, and J. Ritsema (2013), Observations of core-mantle boundary Stoneley modes, *Geophysical Research Letters*, *40*(11), 2557–2561, doi: 10.1002/grl.50514. (Cited on p.: 58, 86)

Koelemeijer, P., A. Deuss, and J. Ritsema (2017), Density structure of Earth's lowermost mantle from Stoneley mode splitting observations, *Nat. Commun.*, *8*(May), 1–10. (Cited on p.: 90)

Koene, E. F. M., J. O. A. Robertsson, F. Broggini, and F. Andersson (2018), Eliminating time dispersion from seismic wave modeling, *Geophys. J. Int.*, *213*(1), 169–180. (Cited on p.: 92)

Komatitsch, D., and J. Tromp (2002a), Spectral-element simulations of global seismic wave propagation-I. Validation, *Geophys. J. Int.*, *149*(1), 390–412. (Cited on p.: 97, 98)

Komatitsch, D., and J. Tromp (2002b), Spectral-element simulations of global seismic wave propagation-II. Three-dimensional models, oceans, rotation and self-gravitation, *Geophys. J. Int.*, *150*(2), 303–318. (Cited on p.: 91)

Komatitsch, D., Z. Xie, E. Bozdağ, E. S. de Andrade, D. Peter, Q. Liu, and J. Tromp (2016), Anelastic sensitivity kernels with parsimonious storage for adjoint tomography and full waveform inversion, *Geophys. J. Int.*, *206*(3), 1467–1478. (Cited on p.: 110)

Koper, K. D., and M. Dombrovskaya (2005), Seismic properties of the inner core boundary from PKiKP/P amplitude ratios, *Earth and Planetary Science Letters*, *237*(3-4), 680–694. (Cited on p.: 82)

Koper, K. D., and M. L. Pyle (2004), Observations of PKiKP/PcP amplitude ratios and implications for Earth structure at the boundaries of the liquid core, *Journal of Geophysical Research: Solid Earth*, *109*(B3). (Cited on p.: 82, 83)

Kovach, R. L., and C. F. Chyba (2001), Seismic detectability of a subsurface ocean on Europa, *Icarus*, *150*(2), 279–287. (Cited on p.: 52)

Ksanfomaliti, L., V. Zubkova, N. Morozov, and E. Petrova (1982), Microseisms at the VENERA-13 and VENERA-14 Landing Sites, *Soviet Astronomy Letters*, *8*, 241. (Cited on p.: 9)

Lamb, H. (1881), On the Vibrations of an Elastic Sphere, *Proceedings of the London Mathematical Society*, *s1-13*(1), 189–212, doi:10.1112/plms/s1-13.1.189. (Cited on p.: 10, 27)

Landeau, M., P. Olson, R. Deguen, and B. Hirsch (2016), Core merging and stratification following giant impact, *Nature Geoscience*, *9*(1), 786–789, doi:10.1038/ngeo2808. (Cited on p.: 79)

Lapwood, E., and T. Usami (1981), *Free Oscillations of the Earth*, Cambridge Monographs on Mechanics, Cambridge University Press. (Cited on p.: 10)

Laske, G., and R. Widmer-Schnidrig (2015), *Theory and Observations: Normal Mode and Surface Wave Observations*, 117–167 pp., Elsevier B.V. (Cited on p.: 110)

Latham, G. V., M. Ewing, F. Press, G. Sutton, J. Dorman, Y. Nakamura, N. Toksöz, R. Wiggins, J. Derr, and F. Duennebier (1970), Passive seismic experiment, *Science*, *167*(3918), 455–457. (Cited on p.: 9)

Lau, H. C., and U. H. Faul (2019), Anelasticity from seismic to tidal timescales: Theory and observations, *Earth and Planetary Science Letters*, *508*, 18–29. (Cited on p.: 57, 58, 74, 78, 83, 84, 122, 180)

Lau, H. C., J. Austermann, B. K. Holtzman, C. Havlin, A. J. Lloyd, C. Book, and E. Hopper (2021), Frequency Dependent Mantle Viscoelasticity via the Complex Viscosity: cases from Antarctica, *Journal of Geophysical Research: Solid Earth*, *126*(11), e2021JB022,622. (Cited on p.: 57)

Lay, T. (2015), 1.22 - Deep Earth Structure: Lower Mantle and D", in *Treatise on Geophysics (Second Edition)*, second edition ed., pp. 683–723, Elsevier, Oxford, doi:https://doi.org/10.1016/B978-0-444-53802-4.00019-1. (Cited on p.: 74)

Lebedev, S., J. Boonen, and J. Trampert (2009), Seismic structure of Precambrian lithosphere: new constraints from broad-band surface-wave dispersion, *Lithos*, *109*(1-2), 96–111. (Cited on p.: 113)

Lehoucq, R. B., D. C. Sorensen, and C. Yang (1998), *ARPACK users' guide: solution of large-scale eigenvalue problems with implicitly restarted Arnoldi methods*, vol. 6, Siam. (Cited on p.: 39)

Lei, W., Y. Ruan, E. Bozdağ, D. Peter, M. Lefebvre, D. Komatitsch, J. Tromp, J. Hill, N. Podhorszki, and D. Pugmire (2020), Global adjoint tomography—model GLAD-M25, *Geophys. J. Int.*, *223*(1), 1–21, doi:10.1093/gji/ggaa253. (Cited on p.: 9, 27, 90)

Lekić, V., and B. Romanowicz (2011), Inferring upper-mantle structure by full waveform tomography with the spectral element method, *Geophys. J. Int.*, *185*(2), 799–831. (Cited on p.: 90)

Lekić, V., J. Matas, M. Panning, and B. Romanowicz (2009), Measurement and implications of frequency dependence of attenuation, *Earth and Planetary Science Letters*, *282*(1-4), 285–293. (Cited on p.: 58, 84)

Li, W.-J., Z. Li, C.-J. Mo, Z. Ma, X.-T. He, C. Wang, and P. Zhang (2023), Self-diffusion coefficient and sound velocity of Fe-Ni-O fluid: Implications for the stratification of Earth's outer core, *Physics of the Earth and Planetary Interiors*, *335*, 106,983, doi:10.1016/j.pepi.2023.106983. (Cited on p.: 79)

Li, Y., L. Vočadlo, and J. P. Brodholt (2018), The elastic properties of hcp-Fe alloys under the conditions of the Earth's inner core, *Earth and Planetary Science Letters*, *493*, 118–127. (Cited on p.: 82)

Lin, J.-F., D. L. Heinz, A. J. Campbell, J. M. Devine, and G. Shen (2002), Iron-Silicon Alloy in Earth's Core?, *Science*, *295*(5553), 313–315, doi:10.1126/science.1066932. (Cited on p.: 82)

Liu, H.-P., D. L. Anderson, and H. Kanamori (1976), Velocity dispersion due to anelasticity; implications for seismology and mantle composition, *Geophysical Journal International*, *47*(1), 41–58. (Cited on p.: 56)

Lognonné, P. (1991), Normal modes and seismograms in an anelastic rotating Earth, *Journal of Geophysical Research: Solid Earth*, *96*(B12), 20,309–20,319. (Cited on p.: 27)

Lognonné, P., J. G. Beyneix, W. B. Banerdt, S. Cacho, J. F. Karczewski, and M. Morand (1996), Ultra broad band seismology on InterMarsNet, *Planetary and space science*, *44*(11), 1237–1249. (Cited on p.: 50)

Loper, D. E. (1978), The gravitationally powered dynamo, *Geophysical Journal International*, *54*(2), 389–404. (Cited on p.: 55)

Loper, D. E. (2000), A model of the dynamical structure of Earth's outer core, *Physics of the Earth and Planetary Interiors*, *117*(1), 179–196, doi:https://doi.org/10.1016/S0031-9201(99)00096-5. (Cited on p.: 79)

Love, A. (1927), A Treatise on the Theory of Elasticity, *Cambridge Univ. Press, Cambridge, ed*, *4*, 15. (Cited on p.: 10, 16, 118)

Ma, X., and H. Tkalčić (2022), CCMOC: A new view of the Earth's outer core through the global coda correlation wavefield, *Physics of the Earth and Planetary Interiors*, p. 106957, doi:10.1016/j.pepi.2022.106957. (Cited on p.: 79)

Maitra, M., and D. Al-Attar (2019), A non-perturbative method for gravitational potential calculations within heterogeneous and aspherical planets, *Geophys. J. Int.*, *219*(2), 1043–1055. (Cited on p.: 91)

Marchenko, A. N., and P. Schwintzer (2003), Estimation of the Earth's tensor of inertia from recent global gravity field solutions, *Journal of Geodesy*, *76*(9), 495–509, doi:10.1007/s00190-002-0280-7. (Cited on p.: 61, 179)

Martorell, B., J. Brodholt, I. G. Wood, and L. Vočadlo (2013), The effect of nickel on the properties of iron at the conditions of Earth's inner core: Ab initio calculations of seismic wave velocities of Fe–Ni alloys, *Earth and Planetary Science Letters*, *365*, 143–151. (Cited on p.: 82)

Masters, G., and F. Gilbert (1983), Attenuation in the earth at low frequencies, *Philosophical Transactions of the Royal Society of London. Series A, Mathematical and Physical Sciences*, *308*(1504), 479–522. (Cited on p.: 19)

Masters, G., and D. Gubbins (2003), On the resolution of density within the Earth, *Physics of the Earth and Planetary Interiors*, *140*(1), 159–167, doi:10.1016/j.pepi.2003.07.008, geophysical and Geochemical Evolution of the Deep Earth. (Cited on p.: 13, 56, 58, 82, 88)

Masters, G., J. Woodhouse, and G. Freeman (2011), Mineos v1.0.2 [software]. (Cited on p.: 14, 15, 28, 46)

Masters, T., and R. Widmer (1995), Free oscillations: frequencies and attenuations, *Global Earth Physics: a handbook of physical constants*, *1*, 104. (Cited on p.: 13, 19, 20, 58, 60, 123, 124, 125, 126, 127, 128, 129, 130, 131, 132, 136, 179, 180, 181)

Matas, J., J. Bass, Y. Ricard, E. Mattern, and M. S. T. Bukowinski (2007), On the bulk composition of the lower mantle: predictions and limitations from generalized inversion of radial seismic profiles, *Geophysical Journal International*, *170*(2), 764–780, doi:10.1111/j.1365-246X.2007.03454.x. (Cited on p.: 74, 87)

May, D. A., and M. G. Knepley (2011), Optimal, scalable forward models for computing gravity anomalies, *Geophys. J. Int.*, *187*(1), 161–177. (Cited on p.: 100)

McCarthy, C., and Y. Takei (2011), Anelasticity and viscosity of partially molten rock analogue: Toward seismic detection of small quantities of melt, *Geophysical Research Letters*, *38*(18), doi:10.1029/2011GL048776. (Cited on p.: 88)

Metropolis, N., A. W. Rosenbluth, M. N. Rosenbluth, A. H. Teller, and E. Teller (1953), Equation of state calculations by fast computing machines, *The journal of chemical physics*, *21*(6), 1087–1092. (Cited on p.: 22)

Montagner, J.-P., and B. L. N. Kennett (1996), How to reconcile body-wave and normal-mode reference earth models, *Geophysical Journal International*, *125*(1), 229–248, doi:10.1111/j.1365-246X.1996.tb06548.x. (Cited on p.: 55)

Morelli, A., A. M. Dziewonski, and J. H. Woodhouse (1986), Anisotropy of the inner core inferred from PKIKP travel times, *Geophysical Research Letters*, *13*(13), 1545–1548. (Cited on p.: 113)

Mosegaard, K., and A. Tarantola (1995), Monte Carlo sampling of solutions to inverse problems, *Journal of Geophysical Research: Solid Earth*, *100*(B7), 12,431–12,447. (Cited on p.: 66, 67)

Moucha, R., A. Forte, J. Mitrovica, and A. Daradich (2007), Lateral variations in mantle rheology: implications for convection related surface observables and inferred viscosity models, *Geophysical Journal International*, *169*(1), 113–135. (Cited on p.: 55)

Moulik, P., and G. Ekström (2016), The relationships between large-scale variations in shear velocity, density, and compressional velocity in the Earth's mantle, *Journal of Geophysical Research: Solid Earth*, *121*(4), 2737–2771. (Cited on p.: 55, 76)

Munch, F. D., A. Khan, B. Tauzin, M. van Driel, and D. Giardini (2020), Seismological evidence for thermo-chemical heterogeneity in Earth's continental mantle, *Earth and Planetary Science Letters*, *539*, 116,240. (Cited on p.: 62, 75)

Murakami, M., Y. Ohishi, N. Hirao, and K. Hirose (2012), A perovskitic lower mantle inferred from high-pressure, high-temperature sound velocity data, *Nature*, *485*(7396), 90–94. (Cited on p.: 74)

Mäkinen, A. M., and A. Deuss (2013), Normal mode splitting function measurements of anelasticity and attenuation in the Earth's inner core, *Geophysical Journal International*, *194*(1), 401–416, doi:10.1093/gji/ggt092. (Cited on p.: 59, 60, 129, 130, 179, 181)

Nakagawa, T. (2018), On the thermo-chemical origin of the stratified region at the top of the Earth's core, *Physics of the Earth and Planetary Interiors*, *276*, 172–181. (Cited on p.: 79)

Nakagawa, T., P. J. Tackley, F. Deschamps, and J. A. D. Connolly (2009), Incorporating self-consistently calculated mineral physics into thermochemical mantle convection simulations in a 3-D spherical shell and its influence on seismic anomalies in Earth's mantle, *Geochemistry, Geophysics, Geosystems*, *10*(3), doi:10.1029/2008GC002280. (Cited on p.: 75)

Nakajima, Y., S. Araki, D. Kinoshita, K. Hirose, S. Tateno, S. I. Kawaguchi, and N. Hirao (2020), New pressure-induced phase transition to Co2Si-type Fe2P, *American Mineralogist: Journal of Earth and Planetary Materials*, *105*(11), 1752–1755. (Cited on p.: 82)

Nakamura, Y. (2003), New identification of deep moonquakes in the Apollo lunar seismic data, *Physics of the Earth and Planetary Interiors*, *139*(3-4), 197–205. (Cited on p.: 9)

Ness, F. N., C. J. Harrison, and B. L. Slichter (1961), Observations of the free oscillations of the Earth, *Journal of Geophysical Research*, *66*, doi:10.1029/JZ066i002p00621. (Cited on p.: 13)

Nimmo, F. (2015), Thermal and compositional evolution of the core, *Treatise on Geophysics*, *9*, 201–219. (Cited on p.: 83)

Nimmo, F., and T. Kleine (2015), *Early Differentiation and Core Formation*, chap. 5, pp. 83–102, American Geophysical Union (AGU), doi:10.1002/9781118860359.ch5. (Cited on p.: 113)

Nissen-Meyer, T., A. Fournier, and F. A. Dahlen (2007), A two-dimensional spectral-element method for computing spherical-earth seismograms - I. Moment-tensor source, *Geophys. J. Int.*, *168*(3), 1067–1092. (Cited on p.: 36, 103)

Nissen-Meyer, T., A. Fournier, and F. A. Dahlen (2008), A 2-D spectral-element method for computing spherical-earth seismograms - II. Waves in solid-fluid media, *Geophys. J. Int.*, *174*(3), 873–888. (Cited on p.: 92)

Nissen-Meyer, T., M. van Driel, S. C. Stähler, K. Hosseini, S. Hempel, L. Auer, A. Colombi, and A. Fournier (2014), AxiSEM: broadband 3-D seismic wavefields in axisymmetric media, *Solid Earth*, *5*(1), 425–445. (Cited on p.: 32, 92)

Nolet, G. (2008), *A Breviary of Seismic Tomography: Imaging the Interior of the Earth and Sun*, Cambridge University Press, doi:10.1017/CBO9780511984709. (Cited on p.: 13, 14, 27, 111)

Nowick, A., and D. Berry (1972), Anelastic relaxation in crystalline solids, acad, *Press, New York*. (Cited on p.: 63)

Okal, E. A., and D. L. Anderson (1978), Theoretical models for Mars and their seismic properties, *Icarus*, *33*(3), 514–528. (Cited on p.: 50)

Panning, M., V. Lekic, M. Manga, F. Cammarano, and B. Romanowicz (2006), Long-period seismology on Europa: 2. Predicted seismic response, *Journal of Geophysical Research: Planets*, *111*(E12). (Cited on p.: 52)

Panning, M. P., P. Lognonné, W. B. Banerdt, R. Garcia, M. Golombek, S. Kedar, B. Knapmeyer-Endrun, A. Mocquet, N. A. Teanby, J. Tromp, et al. (2017), Planned products of the Mars structure service for the InSight mission to Mars, *Space Science Reviews*, *211*(1-4), 611–650. (Cited on p.: 52)

Park, J., T.-R. A. Song, J. Tromp, E. Okal, S. Stein, G. Roult, E. Clevede, G. Laske, H. Kanamori, P. Davis, et al. (2005), Earth's free oscillations excited by the 26 December 2004 Sumatra-Andaman earthquake, *Science*, *308*(5725), 1139–1144. (Cited on p.: 14)

Park, J. J. (1986), Synthetic seismograms from coupled free oscillations: Effects of lateral structure and rotation, *J. Geophys. Res.*, *91*(B6), 6441, doi:10.1029/JB091iB06p06441. (Cited on p.: 43)

Patera, A. T. (1984), A spectral element method for fluid dynamics: Laminar flow in a channel expansion, *J. Comput. Phys.*, *54*(3), 468–488. (Cited on p.: 96)

Peale, S. J., P. Cassen, and R. T. Reynolds (1979), Melting of Io by tidal dissipation, *Science*, *203*(4383), 892–894. (Cited on p.: 16)

Pedregosa, F., G. Varoquaux, A. Gramfort, V. Michel, B. Thirion, O. Grisel, M. Blondel, P. Prettenhofer, R. Weiss, V. Dubourg, J. Vanderplas, A. Passos, D. Cournapeau, M. Brucher, M. Perrot, and E. Duchesnay (2011), Scikit-learn: Machine Learning in Python, *Journal of Machine Learning Research*, *12*, 2825–2830. (Cited on p.: 59)

Pekeris, C., and H. Jarosch (1958), The free oscillations of the earth. Contributions in Geophysics in Honor of Beno Gutenberg. (Cited on p.: 10)

Piazzoni, A. S., G. Steinle-Neumann, H.-P. Bunge, and D. Dolejš (2007), A mineralogical model for density and elasticity of the Earth's mantle, *Geochemistry, Geophysics, Geosystems*, *8*(11), doi:10.1029/2007GC001697. (Cited on p.: 87)

Poirier, J.-P. (1994), Light elements in the Earth's outer core: a critical review, *Physics of the earth and planetary interiors*, *85*(3-4), 319–337. (Cited on p.: 64, 82)

Poisson, S. (1829), Mémoire sur l'équilibre et le Mouvement des Corps élastiques, *Mémoires l'Académie R. des Sci. l'Institut Fr.*, *8*, 357–570. (Cited on p.: 10, 27)

Qu, T., I. Jackson, and U. H. Faul (2021), Low-Frequency Seismic Properties of Olivine-Orthopyroxene Mixtures, *Journal of Geophysical Research: Solid Earth*, *126*(10), e2021JB022,504, doi:https://doi.org/10.1029/2021JB022504, e2021JB022504 2021JB022504. (Cited on p.: 57, 63)

Randall, M. J. (1976), Attenuative dispersion and frequency shifts of the earth's free oscillations, *Physics of the Earth and Planetary Interiors*, *12*(1), P1–P4. (Cited on p.: 17)

Ray, R. D., R. J. Eanes, and F. G. Lemoine (2001), Constraints on energy dissipation in the Earth's body tide from satellite tracking and altimetry, *Geophysical Journal International*, *144*(2), 471–480, doi:10.1046/j.1365-246x.2001.00356.x. (Cited on p.: 61, 179)

Resovsky, J., and J. Trampert (2003), Using probabilistic seismic tomography to test mantle velocity–density relationships, *Earth and Planetary Science Letters*, *215*(1-2), 121–134. (Cited on p.: 56)

Resovsky, J., J. Trampert, and R. Van der Hilst (2005), Error bars for the global seismic Q profile, *Earth and Planetary Science Letters*, *230*(3-4), 413–423. (Cited on p.: 78)

Resovsky, J. S., and M. H. Ritzwoller (1998), New and refined constraints on three-dimensional Earth structure from normal modes below 3 mHz, *Journal of Geophysical Research: Solid Earth*, *103*(B1), 783–810, doi:10.1029/97JB02482. (Cited on p.: 13, 20, 58, 59, 60, 123, 124, 125, 131, 132, 136, 179, 180, 181)

Resovsky, J. S., and M. H. Ritzwoller (1999), Regularization uncertainty in density models estimated from normal mode data, *Geophysical research letters*, *26*(15), 2319–2322. (Cited on p.: 27)

Resovsky, J. S., and J. Trampert (2002), Reliable mantle density error bars: an application of the neighbourhood algorithm to normal-mode and surface wave data, *Geophysical Journal International*, *150*(3), 665–672. (Cited on p.: 56)

Restivo, A., and G. Helffrich (2006), Core—mantle boundary structure investigated using SKS and SKKS polarization anomalies, *Geophysical Journal International*, *165*(1), 288–302, doi:10.1111/j.1365-246X.2006.02901.x. (Cited on p.: 113)

Ringwood, A. E. (1975), Composition and Petrology of the Earth's Mantle, *MacGraw-Hill*, *618*. (Cited on p.: 62, 74)

Ritsema, J., H. J. van Heijst, and J. H. Woodhouse (1999), Complex Shear Wave Velocity Structure Imaged Beneath Africa and Iceland, *Science*, *286*, 1925–1929. (Cited on p.: 92)

Ritsema, J., H. J. Van Heijst, and J. H. Woodhouse (2004), Global transition zone tomography, *Journal of Geophysical Research: Solid Earth*, *109*(B2). (Cited on p.: 55)

Ritsema, J., W. Xu, L. Stixrude, and C. Lithgow-Bertelloni (2009), Estimates of the transition zone temperature in a mechanically mixed upper mantle, *Earth and Planetary Science Letters*, *277*(1-2), 244–252. (Cited on p.: 62, 75)

Rivoldini, A., T. Van Hoolst, O. Verhoeven, A. Mocquet, and V. Dehant (2011), Geodesy constraints on the interior structure and composition of Mars, *Icarus*, *213*(2), 451–472. (Cited on p.: 66)

Robson, A., H. C. Lau, P. Koelemeijer, and B. Romanowicz (2022), An analysis of core–mantle boundary Stoneley mode sensitivity and sources of uncertainty, *Geophysical Journal International*, *228*(3), 1962–1974. (Cited on p.: 59, 76, 86, 113)

Robson, A. J., and B. Romanowicz (2019), New normal mode constraints on bulk inner core velocities and density, *Physics of the Earth and Planetary Interiors*, *295*, 106,310, doi:10.1016/j.pepi.2019.106310. (Cited on p.: 56, 59, 82, 83)

Romanowicz, B. (2001), Can we resolve 3D density heterogeneity in the lower mantle?, *Geophysical research letters*, *28*(6), 1107–1110. (Cited on p.: 13)

Romanowicz, B., and B. Mitchell (2015), 1.25—deep earth structure: Q of the Earth from crust to core, *Treatise on geophysics*, *1*, 789–827. (Cited on p.: 57, 78)

Ronchi, C., R. Iacono, and P. Paolucci (1996), The "cubed sphere": a new method for the solution of partial differential equations in spherical geometry, *J. Comput. Phys.*, *114*(124), 93–114. (Cited on p.: 97)

Rubie, D., S. Jacobson, A. Morbidelli, D. O'Brien, E. Young, J. de Vries, F. Nimmo, H. Palme, and D. Frost (2015), Accretion and differentiation of the terrestrial planets with implications for the compositions of early-formed Solar System bodies and accretion of water, *Icarus*, *248*, 89–108, doi:10.1016/j.icarus.2014.10.015. (Cited on p.: 113)

Rubie, D. C., D. J. Frost, U. Mann, Y. Asahara, F. Nimmo, K. Tsuno, P. Kegler, A. Holzheid, and H. Palme (2011), Heterogeneous accretion, composition and core–mantle differentiation of the Earth, *Earth and Planetary Science Letters*, *301*(1-2), 31–42. (Cited on p.: 82)

Russell, J. B., J. B. Gaherty, P.-Y. P. Lin, D. Lizarralde, J. A. Collins, G. Hirth, and R. L. Evans (2019), High-resolution constraints on Pacific upper mantle petrofabric inferred from surface-wave anisotropy, *Journal of Geophysical Research: Solid Earth*, *124*(1), 631–657. (Cited on p.: 113)

Saito, M. (1988), DISPER80 [software]. (Cited on p.: 15)

Sakamaki, T., E. Ohtani, H. Fukui, S. Kamada, S. Takahashi, T. Sakairi, A. Takahata, T. Sakai, S. Tsutsui, D. Ishikawa, et al. (2016), Constraints on Earth's inner core composition inferred from measurements of the sound velocity of hcp-iron in extreme conditions, *Science Advances*, *2*(2), e1500,802. (Cited on p.: 82, 89)

Saxena, S., and G. Eriksson (2015), Thermodynamics of Fe–S at ultra-high pressure, *Calphad*, *51*, 202 – 205, doi:10.1016/j.calphad.2015.09.009. (Cited on p.: 113)

Schneider, S., and A. Deuss (2020), A new catalogue of toroidal-mode overtone splitting function measurements, *Geophysical Journal International*, *225*(1), 329–341, doi:10.1093/gji/ggaa567. (Cited on p.: 58, 59, 60, 131, 132, 136, 179, 181)

Schuster, A. (1897), On lunar and solar periodicities of earthquakes, *Proceedings of the Royal Society of London*, *61*(369-377), 455–465, doi:10.1098/rspl.1897.0060. (Cited on p.: 16)

Scott, D. (1982), The advantages of inverted operators in Rayleigh–Ritz approximations, *SIAM Journal on Scientific and Statistical Computing*, *3*(1), 68–75. (Cited on p.: 39)

Shearer, P., and G. Masters (1990), The density and shear velocity contrast at the inner core boundary, *Geophysical Journal International*, *102*(2), 491–498. (Cited on p.: 82)

Shearer, P. M. (1994), Constraints on inner core anisotropy from PKP (DF) travel times, *Journal of Geophysical Research: Solid Earth*, *99*(B10), 19,647–19,659. (Cited on p.: 87)

Shearer, P. M. (2009), *Introduction to Seismology*, Cambridge University Press. (Cited on p.: 9)

Shen, Z., Y. Ai, Y. He, and M. Jiang (2016), Using pre-critical PKiKP–PcP phases to constrain the regional structures of the inner core boundary beneath East Asia, *Physics of the Earth and Planetary Interiors*, *252*, 37–48. (Cited on p.: 82)

Shi, J., R. Li, Y. Xi, Y. Saad, and V. Maarten (2018), Computing planetary interior normal modes with a highly parallel polynomial filtering eigensolver, in *SC18: International Conference for High Performance Computing, Networking, Storage and Analysis*, pp. 894–906, IEEE. (Cited on p.: 11, 183)

Simmons, N. A., S. C. Myers, C. Morency, A. Chiang, and D. R. Knapp (2021), SPiRaL: A multi-resolution global tomography model of seismic wave speeds and radial anisotropy variations in the crust and mantle, *Geophys. J. Int.*, doi:10.1093/gji/ggab277. (Cited on p.: 9, 27)

Slichter, L. B. (1961), The Fundamental Free Mode Of The Earth's Inner Core, *Proceedings of the National Academy of Sciences of the United States of America*, *47*(2), 186. (Cited on p.: 28)

Smith, S. W. (1972), The Anelasticity of the Mantle, in *The Upper Mantle*, *Developments in Geotectonics*, vol. 4, edited by A. Ritsema, pp. 601–622, Elsevier, doi:10.1016/B978-0-444-41015-3.50037-9. (Cited on p.: 19)

Smith, S. W. (1987), IRIS—A university consortium for seismology, *Reviews of Geophysics*, *25*(6), 1203–1207. (Cited on p.: 13)

Snieder, R., and C. Sens-Schönfelder (2021), Local coupling and conversion of surface waves due to Earth's rotation. Part 1: theory, *Geophys. J. Int.*, *225*(1), 158–175, doi:10.1093/gji/ggaa587. (Cited on p.: 43)

Song, X. (1997), Anisotropy of the Earth's inner core, *Reviews of geophysics*, *35*(3), 297–313. (Cited on p.: 87)

Sottili, G., S. Martino, D. M. Palladino, A. Paciello, and F. Bozzano (2007), Effects of tidal stresses on volcanic activity at Mount Etna, Italy, *Geophysical Research Letters*, *34*(1), doi:10.1029/2006GL028190. (Cited on p.: 16)

Sparks, R. (1981), Triggering of volcanic eruptions by Earth tides, *Nature*, *290*(5806), 448–448. (Cited on p.: 16)

Špičáková, H., J. Böhm, P. M. Cerveira, and H. Schuh (2009), Determination of degree-2 Love and Shida numbers from VLBI, *Bulletin d'Information des Marées Terrestres*, *1*(145), 11,679–11,685. (Cited on p.: 61, 179)

Stacey, F., and P. Davis (2004), High pressure equations of state with applications to the lower mantle and core, *Physics of the Earth and Planetary interiors*, *142*(3-4), 137–184. (Cited on p.: 24)

Stähler, S. C., M. P. Panning, S. D. Vance, R. D. Lorenz, M. van Driel, T. Nissen-Meyer, and S. Kedar (2018), Seismic wave propagation in icy ocean worlds, *Journal of Geophysical Research: Planets*, *123*(1), 206–232. (Cited on p.: 47)

Stähler, S. C., A. Khan, W. B. Banerdt, P. Lognonné, D. Giardini, S. Ceylan, M. Drilleau, A. C. Duran, R. F. Garcia, Q. Huang, D. Kim, V. Lekic, H. Samuel, M. Schimmel, N. Schmerr, D. Sollberger, É. Stutzmann, Z. Xu, D. Antonangeli, C. Charalambous, P. M. Davis, J. C. E. Irving, T. Kawamura, M. Knapmeyer, R. Maguire, A. G. Marusiak, M. P. Panning, C. Perrin, A.-C. Plesa, A. Rivoldini, C. Schmelzbach, G. Zenhäusern, É. Beucler, J. Clinton, N. Dahmen, M. van Driel, T. Gudkova, A. Horleston, W. T. Pike, M. Plasman, and S. E. Smrekar

(2021), Seismic detection of the martian core, *Science*, *373*(6553), 443–448, doi: 10.1126/science.abi7730. (Cited on p.: 47, 50, 51)

Stixrude, L., and C. Lithgow-Bertelloni (2005a), Thermodynamics of mantle minerals—I. Physical properties, *Geophysical Journal International*, *162*(2), 610–632. (Cited on p.: 62, 87)

Stixrude, L., and C. Lithgow-Bertelloni (2005b), Mineralogy and elasticity of the oceanic upper mantle: Origin of the low-velocity zone, *Journal of Geophysical Research: Solid Earth*, *110*(B3). (Cited on p.: 88)

Stixrude, L., and C. Lithgow-Bertelloni (2011), Thermodynamics of mantle minerals-II. Phase equilibria, *Geophysical Journal International*, *184*(3), 1180–1213. (Cited on p.: 62, 87)

Stixrude, L., and C. Lithgow-Bertelloni (2021), Thermal expansivity, heat capacity and bulk modulus of the mantle, *Geophysical Journal International*, *228*(2), 1119–1149, doi:10.1093/gji/ggab394. (Cited on p.: 87)

Stoneley, R. (1924), Elastic waves at the surface of separation of two solids, *Proceedings of the Royal Society of London. Series A, Containing Papers of a Mathematical and Physical Character*, *106*(738), 416–428. (Cited on p.: 28)

Sundberg, M., and R. F. Cooper (2010), A composite viscoelastic model for incorporating grain boundary sliding and transient diffusion creep; correlating creep and attenuation responses for materials with a fine grain size, *Philosophical Magazine*, *90*(20), 2817–2840. (Cited on p.: 17, 57)

Tackley, P. J., S. Xie, T. Nakagawa, and J. W. Hernlund (2005), Numerical and laboratory studies of mantle convection: Philosophy, accomplishments, and thermochemical structure and evolution, *GEOPHYSICAL MONOGRAPH-AMERICAN GEOPHYSICAL UNION*, *160*(83), 2190. (Cited on p.: 87)

Tagawa, S., K. Ohta, K. Hirose, C. Kato, and Y. Ohishi (2016), Compression of Fe–Si–H alloys to core pressures, *Geophysical Research Letters*, *43*(8), 3686–3692. (Cited on p.: 82)

Tagawa, S., H. Gomi, K. Hirose, and Y. Ohishi (2022), High-Temperature Equation of State of FeH: Implications for Hydrogen in Earth's Inner Core, *Geophysical Research Letters*, *49*(5), e2021GL096,260, doi:10.1029/2021GL096260. (Cited on p.: 82)

Takafuji, N., K. Hirose, M. Mitome, and Y. Bando (2005), Solubilities of O and Si in liquid iron in equilibrium with (Mg, Fe) SiO3 perovskite and the light elements in the core, *Geophysical Research Letters*, *32*(6). (Cited on p.: 82)

Takei, Y. (2017), Effects of Partial Melting on Seismic Velocity and Attenuation: A New Insight from Experiments, *Annual Review of Earth and Planetary Sciences*, *45*(1), 447–470, doi:10.1146/annurev-earth-063016-015820. (Cited on p.: 88)

Takei, Y., F. Karasawa, and H. Yamauchi (2014), Temperature, grain size, and chemical controls on polycrystal anelasticity over a broad frequency range extending into the seismic range, *Journal of Geophysical Research: Solid Earth*, *119*(7), 5414–5443. (Cited on p.: 57)

Takeuchi, H. (1959), Torsional oscillations of the Earth and some related problems, *Geophysical Journal International*, *2*(2), 89–100. (Cited on p.: 10)

Takeuchi, H., and M. Saito (1972), Seismic surface waves, *Methods in computational physics*, *11*, 217–295. (Cited on p.: 15, 29, 41, 42, 46)

Talavera-Soza, S., and A. Deuss (2020), New measurements of long-period radial modes using large earthquakes, *Geophysical Journal International*, *224*(2), 1211–1224, doi:10.1093/gji/ggaa499. (Cited on p.: 58, 59, 60, 130, 179, 181)

Tamrazyan, G. P. (1968), Principal regularities in the distribution of major earthquakes relative to solar and lunar tides and other cosmic forces, *Icarus*, *9*(1-3), 574–592. (Cited on p.: 16)

Tanaka, S. (2007), Possibility of a low P-wave velocity layer in the outermost core from global SmKS waveforms, *Earth and Planetary Science Letters*, *259*(3-4), 486–499. (Cited on p.: 78)

Tanaka, S., M. Ohtake, and H. Sato (2002), Evidence for tidal triggering of earthquakes as revealed from statistical analysis of global data, *Journal of Geophysical Research: Solid Earth*, *107*(B10), ESE–1. (Cited on p.: 16)

Tanaka, S., H. Sato, S. Matsumura, and M. Ohtake (2006), Tidal triggering of earthquakes in the subducting Philippine Sea plate beneath the locked zone of the plate interface in the Tokai region, Japan, *Tectonophysics*, *417*(1-2), 69–80. (Cited on p.: 16)

Tang, V., L. Zhao, and S.-H. Hung (2015), Seismological evidence for a non-monotonic velocity gradient in the topmost outer core, *Scientific reports*, *5*(1), 8613, doi:doi.org/10.1038/srep08613. (Cited on p.: 79)

Tape, C., Q. Liu, A. Maggi, and J. Tromp (2009), Adjoint tomography of the southern California crust., *Science*, *325*(5943), 988–92. (Cited on p.: 90)

Tapley, B., J. Ries, S. Bettadpur, D. Chambers, M. Cheng, F. Condi, B. Gunter, Z. Kang, P. Nagel, R. Pastor, et al. (2005), GGM02–An improved Earth gravity field model from GRACE, *Journal of Geodesy*, *79*(8), 467–478. (Cited on p.: 55)

Tarantola, A. (2005), *Inverse problem theory and methods for model parameter estimation*, SIAM. (Cited on p.: 21)

Tarantola, A., and B. Valette (1982), Generalized nonlinear inverse problems solved using the least squares criterion, *Reviews of Geophysics*, *20*(2), 219–232. (Cited on p.: 20)

Tauzin, B., L. Waszek, M. D. Ballmer, J. C. Afonso, and T. Bodin (2022), Basaltic reservoirs in the Earth's mantle transition zone, *Proceedings of the National Academy of Sciences*, *119*(48), e2209399,119, doi:10.1073/pnas.2209399119. (Cited on p.: 75)

Taylor, S. R. (1980), Refractory and moderately volatile element abundances in the earth, moon and meteorites., *Lunar and Planetary Science Conference Proceedings*, *1*, 333–348. (Cited on p.: 74)

Thomas, A. M., R. M. Nadeau, and R. Bürgmann (2009), Tremor-tide correlations and near-lithostatic pore pressure on the deep San Andreas fault, *Nature*, *462*(7276), 1048–1051, doi:10.1038/nature08654. (Cited on p.: 16)

Thomson, W. (1863), On the Rigidity of the Earth, *Philos. Trans. R. Soc. London*, *153*, 573–582. (Cited on p.: 27)

Tian, D., M. Lv, S. Wei, S. M. Dorfman, and P. M. Shearer (2020), Global variations of Earth's 520- and 560-km discontinuities, *Earth Planet. Sci. Lett.*, *552*, doi:10.1016/j.epsl.2020.116600. (Cited on p.: 75)

Tkalčić, H., and T.-S. Pham (2018), Shear properties of Earth's inner core constrained by a detection of J waves in global correlation wavefield, *Science*, *362*(6412), 329–332. (Cited on p.: 76, 78)

Tkalčić, H., B. L. Kennett, and V. F. Cormier (2009), On the inner—outer core density contrast from PKiKP/PcP amplitude ratios and uncertainties caused by seismic noise, *Geophysical Journal International*, *179*(1), 425–443. (Cited on p.: 82)

Trampert, J., F. Deschamps, J. Resovsky, and D. Yuen (2004), Probabilistic tomography maps chemical heterogeneities throughout the lower mantle, *Science*, *306*(5697), 853–856. (Cited on p.: 13, 27)

Tromp, J. (1993), Support for anisotropy of the Earth's inner core from free oscillations, *Nature*, *366*(6456), 678–681. (Cited on p.: 113)

Tromp, J. (2001), Inner-core anisotropy and rotation, *Annual Review of Earth and Planetary Sciences*, *29*(1), 47–69. (Cited on p.: 87)

Tromp, J., and F. A. Dahlen (1990), Free oscillations of a spherical anelastic earth, *Geophysical Journal International*, *103*(3), 707–723, doi:10.1111/j.1365-246X.1990.tb05682.x. (Cited on p.: 42)

Tromp, J., and E. Zanzerkia (1995), Toroidal splitting observations from the great 1994 Bolivia and Kuril Islands earthquakes, *Geophysical research letters*, *22*(16), 2297–2300. (Cited on p.: 21)

Umemoto, K., and K. Hirose (2020), Chemical compositions of the outer core examined by first principles calculations, *Earth and Planetary Science Letters*, *531*, 116,009. (Cited on p.: 82, 89)

Valette, B. (1987), Spectre des oscillations libres de la Terre: aspects mathématiques et géophysiques, Ph.D. thesis, Paris 6. (Cited on p.: 41)

van Driel, M., and T. Nissen-Meyer (2014), Seismic wave propagation in fully anisotropic axisymmetric media, *Geophys. J. Int.*, *199*(2), 880–893. (Cited on p.: 92)

van Driel, M., C. Boehm, L. Krischer, and M. Afanasiev (2020), Accelerating numerical wave propagation using wavefield adapted meshes. Part I: forward and adjoint modelling, *Geophys. J. Int.*, *221*(3), 1580–1590, doi:10.1093/gji/ggaa058. (Cited on p.: 98, 103)

van Driel, M., J. Kemper, and C. Boehm (2021), On the modelling of self-gravitation for full 3-D global seismic wave propagation, *Geophysical Journal International*, *227*(1), 632–643, doi:10.1093/gji/ggab237. (Cited on p.: 54)

van Gerven, L., F. Deschamps, and R. D. van der Hilst (2004), Geophysical evidence for chemical variations in the Australian Continental Mantle, *Geophysical Research Letters*, *31*(17). (Cited on p.: 55)

van Tent, R., A. Deuss, S. Kaneshima, and C. Thomas (2020), The signal of outermost-core stratification in body-wave and normal-mode data, *Geophysical Journal International*, *223*(2), 1338–1354. (Cited on p.: 56, 59, 74)

Vance, S. D., M. P. Panning, S. Stähler, F. Cammarano, B. G. Bills, G. Tobie, S. Kamata, S. Kedar, C. Sotin, W. T. Pike, et al. (2018), Geophysical investigations of habitability in ice-covered ocean worlds, *Journal of Geophysical Research: Planets*, *123*(1), 180–205. (Cited on p.: 51)

Varga, P., and E. Grafarend (2019), Influence of tidal forces on the triggering of seismic events, *Geodynamics and Earth Tides Observations from Global to Micro Scale*, pp. 55–63. (Cited on p.: 16)

Vinet, P., J. Ferrante, J. Rose, and J. Smith (1987), Compressibility of Solids, *J. Geophys. Res.*, *92*, 9319–9325. (Cited on p.: 64)

Virieux, J., and S. Operto (2009), An overview of full-waveform inversion in exploration geophysics, *Geophysics*, *74*(6), WCC1. (Cited on p.: 90)

Virieux, J., A. Asnaashari, R. Brossier, L. Métivier, A. Ribodetti, and W. Zhou (2017), An introduction to full waveform inversion, in *Encycl. Explor. Geophys.*, pp. R1–1–R1–40, Society of Exploration Geophysicists. (Cited on p.: 90)

Virtanen, P., R. Gommers, T. E. Oliphant, M. Haberland, T. Reddy, D. Cournapeau, E. Burovski, P. Peterson, W. Weckesser, J. Bright, S. J. van der Walt, M. Brett, J. Wilson, K. J. Millman, N. Mayorov, A. R. J. Nelson, E. Jones, R. Kern, E. Larson, C. J. Carey, İ. Polat, Y. Feng, E. W. Moore, J. VanderPlas, D. Laxalde, J. Perktold, R. Cimrman, I. Henriksen, E. A. Quintero, C. R. Harris, A. M. Archibald, A. H. Ribeiro, F. Pedregosa, P. van Mulbregt, and SciPy 1.0 Contributors (2020), SciPy 1.0: Fundamental Algorithms for Scientific Computing in Python, *Nature Methods*, *17*, 261–272, doi:10.1038/s41592-019-0686-2. (Cited on p.: 128)

Vočadlo, L. (2007), Ab initio calculations of the elasticity of iron and iron alloys at inner core conditions: Evidence for a partially molten inner core?, *Earth and Planetary Science Letters*, *254*(1-2), 227–232. (Cited on p.: 82)

Wahr, J. M., M. T. Zuber, D. E. Smith, and J. I. Lunine (2006), Tides on Europa, and the thickness of Europa's icy shell, *Journal of Geophysical Research: Planets*, *111*(E12), doi:10.1029/2006JE002729. (Cited on p.: 16)

Walther, A., and A. Griewank (2004), Advantages of Binomial Checkpointing for Memory-reduced Adjoint Calculations, in *Numer. Math. Adv. Appl.*, 1, pp. 834–843, Springer Berlin Heidelberg, Berlin, Heidelberg. (Cited on p.: 110)

Warner, M., A. Ratcliffe, T. Nangoo, J. Morgan, A. Umpleby, N. Shah, V. Vinje, I. Štekl, L. Guasch, C. Win, G. Conroy, and A. Bertrand (2013), Anisotropic 3D full-waveform inversion, *Geophysics*, *78*(2). (Cited on p.: 90)

Waszek, L., and A. Deuss (2015), Anomalously strong observations of PKiKP/PcP amplitude ratios on a global scale, *Journal of Geophysical Research: Solid Earth*, *120*(7), 5175–5190. (Cited on p.: 82)

Waszek, L., B. Tauzin, N. C. Schmerr, M. D. Ballmer, and J. C. Afonso (2021), A poorly mixed mantle transition zone and its thermal state inferred from seismic waves, *Nature Geoscience*, *14*(12), 949–955. (Cited on p.: 75)

Weidner, D. J. (1985), A mineral physics test of a pyrolite mantle, *Geophysical Research Letters*, *12*(7), 417–420. (Cited on p.: 74)

Wesseling, P. (1992), *An Introduction to Multigrid Methods*, Wiley, New York, New York, USA. (Cited on p.: 100)

Widmer, R., G. Masters, and F. Gilbert (1991), Spherically symmetric attenuation within the Earth from normal mode data, *Geophysical journal international*, *104*(3), 541–553. (Cited on p.: 78)

Wiggins, R. A. (1976), A fast, new computational algorithm for free oscillations and surface waves, *Geophysical Journal International*, *47*(1), 135–150, doi:10.1111/j.1365-246X.1976.tb01266.x. (Cited on p.: 28, 37, 40, 41)

Wilke, C. O. (2019), *Fundamentals of data visualization: a primer on making informative and compelling figures*, O'Reilly Media. (Cited on p.: 70)

Williamson, E. D., and L. H. Adams (1923), Density distribution in the Earth, *Journal of the Washington academy of sciences*, *13*(19), 413–428. (Cited on p.: 55)

Wood, B. J. (2008), Accretion and core formation: constraints from metal–silicate partitioning, *Philosophical Transactions of the Royal Society A: Mathematical, Physical and Engineering Sciences*, *366*(1883), 4339–4355. (Cited on p.: 82)

Wood, B. J., J. Wade, and M. R. Kilburn (2008), Core formation and the oxidation state of the Earth: Additional constraints from Nb, V and Cr partitioning, *Geochimica et Cosmochimica Acta*, *72*(5), 1415–1426. (Cited on p.: 82)

Woodhouse, J., and A. Deuss (2015), Earth's Free Oscillations, in *Treatise on Geophysics (Second Edition)*, edited by G. Schubert, second edition ed., pp. 79 – 115, Elsevier, Oxford, doi:10.1016/B978-0-444-53802-4.00002-6. (Cited on p.: 12, 13, 15, 27, 29)

Woodhouse, J. H. (1988), The Calculation of Eigenfrequencies and Eigenfunctions of the Free Oscillations of the Earth and the Sun, in *Seismol. algorithms*, pp. 321–370. (Cited on p.: 15, 28, 46, 53)

Woodhouse, J. H., and A. M. Dziewonski (1984), Mapping the upper mantle: Three-dimensional modeling of Earth structure by inversion of seismic waveforms, *Journal of Geophysical Research: Solid Earth*, *89*(B7), 5953–5986. (Cited on p.: 27)

Woodhouse, J. H., D. Giardini, and X.-D. Li (1986), Evidence for inner core anisotropy from free oscillations, *Geophysical Research Letters*, *13*(13), 1549–1552. (Cited on p.: 12, 87, 113)

Wookey, J., and G. Helffrich (2008), Inner-core shear-wave anisotropy and texture from an observation of PKJKP waves, *Nature*, *454*, 873–877. (Cited on p.: 76, 78, 87, 113)

Wu, W., and J. C. Irving (2020), Array-Based Iterative Measurements of Travel Times and Their Constraints on Outermost Core Structure, *Journal of Geophysical Research: Solid Earth*, *125*(3), e2019JB018,162. (Cited on p.: 79, 81)

Xu, W., C. Lithgow-Bertelloni, L. Stixrude, and J. Ritsema (2008), The effect of bulk composition and temperature on mantle seismic structure, *Earth and Planetary Science Letters*, *275*(1-2), 70–79. (Cited on p.: 62, 75)

Xu, Y., T. J. Shankland, and B. T. Poe (2000), Laboratory-based electrical conductivity in the Earth's mantle, *Journal of Geophysical Research: Solid Earth*, *105*(B12), 27,865–27,875. (Cited on p.: 74)

Yamauchi, H., and Y. Takei (2016), Polycrystal anelasticity at near-solidus temperatures, *J. Geophys. Res.*, *121*(11), 7790–7820. (Cited on p.: 88)

Yan, J., M. D. Ballmer, and P. J. Tackley (2020), The evolution and distribution of recycled oceanic crust in the Earth's mantle: Insight from geodynamic models, *Earth Planet. Sci. Lett.*, *537*(116171), doi:10.1016/j.epsl.2020.116171. (Cited on p.: 75, 87)

Yang, H., J. M. R. Muir, and F. Zhang (2022), Iron Hydride in the Earth's Inner Core and Its Geophysical Implications, *Geochemistry, Geophysics, Geosystems*, *23*(12), e2022GC010,620, doi:10.1029/2022GC010620, e2022GC010620 2022GC010620. (Cited on p.: 82)

Yang, H.-Y., and J. Tromp (2015), Synthetic free-oscillation spectra: an appraisal of various mode-coupling methods, *Geophysical Journal International*, *203*(2), 1179–1192. (Cited on p.: 12, 86, 111)

Yokoo, S., K. Hirose, S. Tagawa, G. Morard, and Y. Ohishi (2022), Stratification in planetary cores by liquid immiscibility in Fe-SH, *Nature communications*, *13*(1), 1–8. (Cited on p.: 79)

Zábranová, E., L. Hanyk, and C. Matyska (2017), Matrix eigenvalue method for free-oscillations modelling of spherical elastic bodies, *Geophysical Journal International*, *211*, 1254–1271, doi:10.1093/gji/ggx353. (Cited on p.: 28, 30, 37, 40, 43, 45, 48, 179)

Zahnle, K., L. Dones, and H. F. Levison (1998), Cratering rates on the Galilean satellites, *Icarus*, *136*(2), 202–222. (Cited on p.: 52)

Zheng, Y., F. Nimmo, and T. Lay (2015), Seismological implications of a lithospheric low seismic velocity zone in Mars, *Physics of the Earth and Planetary Interiors*, *240*, 132–141. (Cited on p.: 50)

Zhu, H., E. Bozdağ, D. Peter, and J. Tromp (2012), Structure of the European upper mantle revealed by adjoint tomography, *Nat. Geosci.*, *5*(7), 493–498. (Cited on p.: 90)

Zhu, M., S. Sun, Y. Zhou, and Q. Wu (2022), Mantle Q structure from S, SS, SSS and SSSS amplitude measurements, *Geophysical Journal International*, *231*(1), 703–716, doi:10.1093/gji/ggac217. (Cited on p.: 78)

List of Tables

List of Figures

Acknowledgements

To be honest, delving into normal mode seismology wasn't the path I had envisioned for myself as a young theoretical physicist. However, to my surprise, the theory revealed a captivating mathematical essence that gradually won me over. I am genuinely grateful for the invaluable lessons learned in both scientific and personal realms and I will always fondly remember my time at ETH Zürich. This work would not have been possible without the help and support of numerous people.

First of all, I am grateful to Martin van Driel for giving me deep insights into (computational) seismology and being an understanding supervisor during the major part of this thesis. Not only did he advance my *Python* and code development skills, but also improved my general problem solving approach. I thank Amir Khan for bestowing me with his immense experience in the inversion part of this project. His handling of the English language is second to none and working on a manuscript with him can only be described as intense, but also highly rewarding. Being able to go hiking on high alpine routes (T4+) with my supervisors was an experience I cherish a lot. Furthermore, I extend my heartfelt gratitude to Domenico Giardini for granting me the opportunity to join and work in the Seismology and Geodynamics group.

I am deeply grateful for Yann Capdeville's exceptional patience in accommodating my defense date and serving as an invaluable external independent committee member. In addition, I thank Andreas Fichtner for officiating as chairperson. For financial support, I thank the Swiss National Science Foundation (SNF project 172508). For their help in all administrative issues, I thank Elisabeth Läderach, Sigrid Trindler, and Mirjam Kandler.

Personally, I thank for a plethora of reasons: Felix Bissig, Johannes Käufl, Dean Khan, Aurélia Meister, Rob Spaargaren, Adriaan Visser, and Cecilia Duran. Above all, I express my deepest and most heartfelt gratitude to my family for their unwavering support throughout this journey.: Josef & Felicitas, Viktoria, Rebekka, my uncles Eugen & Thomas, as well as my godmother Claudia.

Of course, the story will never be quite finished:
in describing the interior of the Earth, there will always be extra
decimal places to add as further significant evidence arises.

– The Earth's Density by K.E. Bullen on 29th June 1974